Nuclear Energy University Program Research
DOE Award Number: DE-NE0008443
Project 15-8623

CHARACTERIZATION OF CREEP-FATIGUE CRACK GROWTH IN ALLOY 709 AND PREDICTION OF SERVICE LIVES IN NUCLEAR REACTOR COMPONENTS

Final Report

Research Team
Faculty - University of Idaho
Dr. Gabriel Potirniche (PI),
Dr. Robert Stephens (Co-PI), Dr. Indrajit Charit (Co-PI)

Graduate Students - University of Idaho
Nicholas Shaber, Jose Ramirez, Martin Taylor, Harry Pugesek, Philip Malmquist

Distinguished Staff Scientist - Idaho National Laboratory
Dr. Michael Glazoff

Contact information
Gabriel Potirniche, gabrielp@uidaho.edu, (208) 885-4049
Mechanical Engineering Department, University of Idaho

4/30/2019

TABLE OF CONTENTS

1 ABSTRACT

This final report summarizes the activities and results that were obtained by the research team working on the project “Characterization of Creep-Fatigue Crack Growth in Alloy 709 and Prediction of Service Lives in Nuclear Reactor Components”, DOE-NEUP Project 15-8623. This project was mainly concerned with the creep-fatigue crack growth characterization of austenitic stainless-steel Fe-20Cr-25Ni (Alloy 709). For this purpose, an array of experimental and computational activities was performed. The main goal of these activities was to describe and predict the crack growth behavior in Alloy 709 under different conditions of applied loading and temperature.

Alloy 709 specimens were tested to describe both the uniaxial creep behavior and creep-fatigue crack growth rates at temperatures between 550°C and 700°C. Microstructure and fracture surface analysis was performed using several experimental techniques, and the defining features of crack growth propagation were identified and described. Thermodynamic and diffusion simulations were performed to understand the microstructure evolution of Alloy 709 at elevated temperatures, and to establish an aging schedule relevant for in-service conditions over extended periods. Experimental testing was performed on both as-received and aged Alloy 709 specimens.

Two computational methods were developed to predict crack growth rates and remaining lives in specimens loaded under either fatigue of creep-fatigue. The first computational technique was the finite element method, while the second was strip-yield modeling. Both methods relied on the prediction of crack growth rates using the concept of plasticity-induced crack closure. Crack-tip opening loads were computed and used to perform crack growth rate predictions. The computational predictions matched well with the experimental results. The strip-yield model was shown to be an excellent predictive tool not only for crack growth in austenitic SS Alloy 709, but also in 316 SS, martensitic Cr-Mo steels, Ni-based alloys and Al-based alloys.

The main conclusion of this study is that Alloy 709 exhibits excellent creep crack growth resistance at temperatures between 550°C and 700°C. In fact, the crack growth resistance of this alloy appears to be higher than that of 316 SS in similar testing conditions. Moreover, when creep loading with hold (dwell) times of 60s or 600s were intercalated every fatigue cycle, the crack growth rates did not change significantly. The conclusion is that the tests performed

revealed that the crack growth is insignificant during the creep portion of a loading cycle, as compared with the crack growth during the fatigue portion of the cycle. In general, Alloy 709 shows excellent resistance to creep deformations and creep crack growth up to 700°C.

1 PROJCT OBJECTIVES

The overall goal of this project was to measure and report the creep-fatigue crack growth rates in Alloy 709 under various creep-fatigue loading in accelerated test conditions and to use this knowledge to predict the fatigue life of fracture specimens. The uniaxial creep and creep-fatigue crack growth behavior were measured in the as-received and aged conditions. Computational techniques were developed to perform flaw evaluation procedure under creep-fatigue loading conditions.

Specifically, the project objectives are described as follows.

Objective 1: To perform testing and characterization of creep-fatigue crack growth rates in Alloy 709 in accelerated and service conditions, for material in as-received and aged conditions.

Objective 2: To perform microstructure analysis using electron back-scatter diffraction (EBSD) and transmission-electron microscopy (TEM) to describe the microstructure evolution and crack propagation mechanisms caused by creep-fatigue interactions.

Objective 3: To understand the kinetics of microstructure evolution during accelerated creep-fatigue testing and during service conditions by performing thermodynamics and kinetics simulations.

Objective 4: To incorporate the knowledge from the above steps into phenomenological equations implemented in a constitutive model for the finite element method.

Objective 5: To perform assessment of the damage evolution in the crack-tip process (plastic) zone during creep-fatigue loading using the finite element code ABAQUS.

Objective 6: To perform crack growth simulations in ABAQUS by taking advantage of the constitutive model developed.

Objective 7: To develop a strip-yield model for creep-fatigue crack growth and to simulate crack growth under various temperature and loading scenarios.

Objective 8: To propose a flaw evaluation technique based on experimental testing and numerical simulations for the assessment of the remaining service life in nuclear reactor components.

In this project, all research objectives have been achieved. To achieve these objectives, the research team has performed the following list of activities, and achieved the results as outlined below.

1) Two creep-fatigue testing frames were built at the University of Idaho and was used to perform creep-fatigue crack growth experiments. Each of the testing frames was equipped with high-temperature chambers capable of performing experiments up to 1100°C. High temperature extensometers were installed in order to measure load line displacement and crack opening during testing. A direct-current potential drop system was installed on each testing frame to measure crack lengths during crack growth. In the beginning of the project, the testing frames were calibrated and verified to ensure accuracy of data collected.

2) During the project, three different plates of different heats of Alloy 709 were received from Oak Ridge National Laboratory (ORNL). Uniaxial tension specimens with a round cross-section were machined out of each plate. These specimens were used to perform uniaxial creep tests at temperatures between 600°C and 700°C. In addition, compact-tension (CT) specimens were also machined from the received plates. The CT specimens were used for creep-fatigue crack growth testing. Both uniaxial creep and creep-crack growth testing was performed on as-received and aged Alloy 709 specimens. Two aging conditions were employed in this study, i.e., the specimens were exposed to 650°C for 3 months or 6 months. Post aging, the specimens were tested. Testing data included creep diagrams (i.e., strain rate versus applied stress) to determine the exponent in Norton creep law and identify the operating creep mechanisms. From the CT specimens crack growth rates versus applied stress intensity factor range (da/dN versus ΔK) were obtained for fatigue and creep-fatigue testing conditions at different load ratios $R = F_{min}/F_{max}$ and temperatures between 550°C and 750°C. Crack growth testing was also performed on 316 SS CT specimens and the results were compared with the results obtained from the testing of Alloy 709 specimens. In general, Alloy 709 exhibited better crack growth resistance than 316 SS at temperatures between 600°C and 700°C in laboratory air conditions.

3) Post-failure analysis was performed on fractured specimens using optical microscopy, scanning electron microscopy (SEM), scanning electron microscopy (TEM) and electron-

backscatter diffraction (EBSD). These analysis methods revealed important features of the crack surface profiles. The fracture mode was predominantly transgranular, resembling brittle fracture. A significant feature of the fracture surface for specimens tested under creep-fatigue was the presence of secondary cracking at the crack tip. This feature was not as noticeable in the case of fatigue crack growth specimens.

4) Thermodynamics and diffusion simulations using ThermoCalc and DICTRA with the goal of identifying the effects on aging on the Alloy 709 microstructure. TTT (time-temperature-transformation and CCT (continuous cooling transformation) diagrams for the precipitation of the phase(s) of interest were produced by performing simulations with these software. The composition and phase evolution for each of the three plates that were provided from ORNL were simulated as a function of temperature. From the thermodynamics simulations it was decided that aging the material at 650°C for 3 months and 6 months, would correspond to in-service conditions for 25 and 50 years at 550°C from the standpoint of SIGMA phase formation. The SIGMA phase is the most detrimental to the creep and creep-fatigue crack growth properties of this alloy.

5) The data that was obtained from the uniaxial creep testing of the as-received and aged material was incorporated in finite element modeling and simulations in the commercial software ABAQUS. Extensive parametric studies were performed to develop robust computational procedures from simulating stationary and growing cracks. Plastic and creep zones at the crack tip in CT specimens were simulated and measured. Load line displacements were simulated and compared with experimental values to ensure accuracy of the computational simulations.

6) A node-release method was developed in ABAQUS to simulate growing cracks in CT specimens. Plasticity-induced crack closure was simulated and computed during crack growth for both fatigue and creep-fatigue loading. The impact of creep deformations on the plasticity-induced crack closure and crack-tip opening loads were computed. The crack opening loads obtained from the computational simulations were used to perform predictions of crack growth rates. The computational predictions were compared with the experimentally measured data.

7) A strip-yield model was developed to simulate fatigue and creep-fatigue crack growth. The model is based on the weight function method to compute the stress intensity factor K and crack opening displacements (COD) for various types of fracture specimens. The model is able to reliably predict plasticity-induced crack closure and crack-opening loads. Based on these data, the model predicts crack growth rates (da/dN) as a function of applied stress intensity factor range (ΔK). The model is able to accurately predict crack growth rates under both fatigue and creep-fatigue loading in Alloy 709, and also in other materials, such as 316 SS, martensitic Cr-Mo steels, Ni-based alloys and Al-based alloys.

8) To evaluate flaw evolution, the strip-yield model was used to simulate crack growth under fatigue crack growth and creep-fatigue crack growth. The fatigue crack growth was under constant amplitude loading with a frequency of 15 Hz. The creep-fatigue crack growth tests were performed considering hold (dwell) times of 60s and 600s. The 600s hold times were intercalated at several ΔK values during the crack growth history. The strip-yield model was able to predict well both crack growth rates diagrams (da/dN versus ΔK), and crack length (a) versus number of cycles (N).

A detailed description of the tasks that were performed to accomplish each project objective along with the results obtained are described in detail in the following chapters. The technical results were included in presentations at conferences, peer-reviewed conference papers and journal papers. Some of the journal papers that resulted from this research have been published, while others are in preparation to be submitted as of the date of this final report submission.

3. INTRODUCTION

3.1. Background

As the world's energy consumption continues to rise, the need for more efficient nuclear and coal power plants has been an area of great importance. Generation IV reactors including Sodium-cooled Fast Reactors (SFR), Gas-cooled Fast Reactors (GFR), Lead-cooled Fast Reactors (LFR), Molten Salt Reactors (MSR), and Very High Temperature Reactors (VHTR), all require materials that can serve under high temperature, greater radiation doses and extremely corrosive environment. One of the important requirements for the structural materials used under such high temperature conditions for prolonger duration of time is superior high temperature mechanical properties. The SFR has a maximum operating temperature of 500°C – 550°C [1]. The life of these reactors are expected to last over 60 years. The increase in operating temperatures of nuclear plants has led to efforts in improving the creep resistance of austenitic stainless steels. Alloy 709, originally developed by Nippon Steel (Tokyo, Japan) and marketed as NF709, is a novel austenitic stainless steel based on a Fe-20Cr-25Ni base composition. It exhibits excellent high temperature creep, yield, and fatigue strength, with excellent corrosion resistance [2], [3]. However, fundamental information on the creep behavior of the alloy is still sparse.

3.2. Sodium-cooled Fast Reactors

The SFR is at the forefront of the Generation IV reactors considered in the US due to its reasonable coolant temperature and low pressure. A schematic SFR design is shown in Figure 3.1. The liquid sodium coolant allows a high power density with a low coolant volume, all at near atmospheric pressures [4]. The boiling point of liquid sodium is over 850°C so the operating temperature of 550°C allows a grace period of several hours in loss of coolant events [5]. Additionally there is no hydrogen generation from the sodium coolant which further increases the safety features of this design.

Sodium, however, chemically reacts with air and water which requires the coolant to be in a closed system. Keeping the coolant contained requires materials that can maintain excellent mechanical properties at high temperatures, such as sodium compatibility, weldability, easily machinable, and can handle irradiation doses of 10 – 200 displacements per atom (dpa) [6].

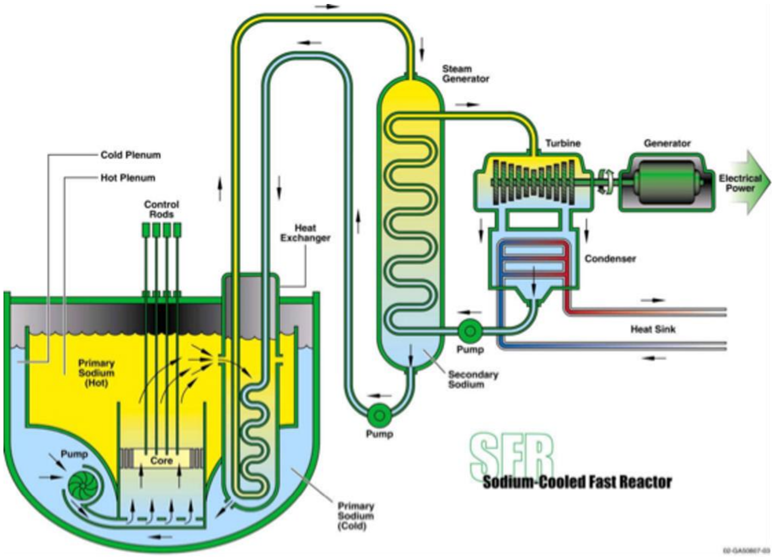

Figure 3.1. Power generation section of a Sodium-cooled Fast Reactor

3.3 Austenitic Stainless Steel

Austenitic stainless steels are used widely because of their corrosion resistance, high temperature strength, and economic feasibility of the alloys. Austenitic stainless steels are known for a wide variety of compositions but is primarily a Fe-Cr-Ni alloy. The chromium content is generally over 12 wt% for the alloy to form a passive chromium oxide film. Nickel also improves the corrosion resistance but primarily is used to increase the high temperature strength of the material and to stabilize austenite. The FCC lattice provides for a reduced diffusivity because of the close packed structure compared to ferritic steels with more open BCC lattice structure. A significant amount of research on optimizing the composition of austenitic stainless steels for high temperature applications have been carried out and there are a number of different grades of austenitic stainless steels available in the market [7].

Austenite, ferrite and martensite are the primary phases found in stainless steels. The phase of a stainless steel depends on the composition and the thermal process in preparing the material. Martensite forms when austenite is quenched rapidly leaving the material in a metastable phase that significantly increases the hardness of the material. The alloying elements generally fall under two categories, austenite stabilizers and ferrite stabilizers [8]. Austenite has a FCC crystal structure and is stabilized by N, C, Ni, Mn, and Cu. Ferrite has a BCC crystal structure and is stabilized with addition of Cr, Si, Mo, and Nb. The Schaeffler diagram is an empirical guide to determine what phase(s) to expect at a certain composition in stainless steels as described by nickel equivalent and chromium equivalent, shown in Figure 3.2. Note that Alloy 709 composition falls fully within the austenitic phase domain on the Schaeffler diagram.

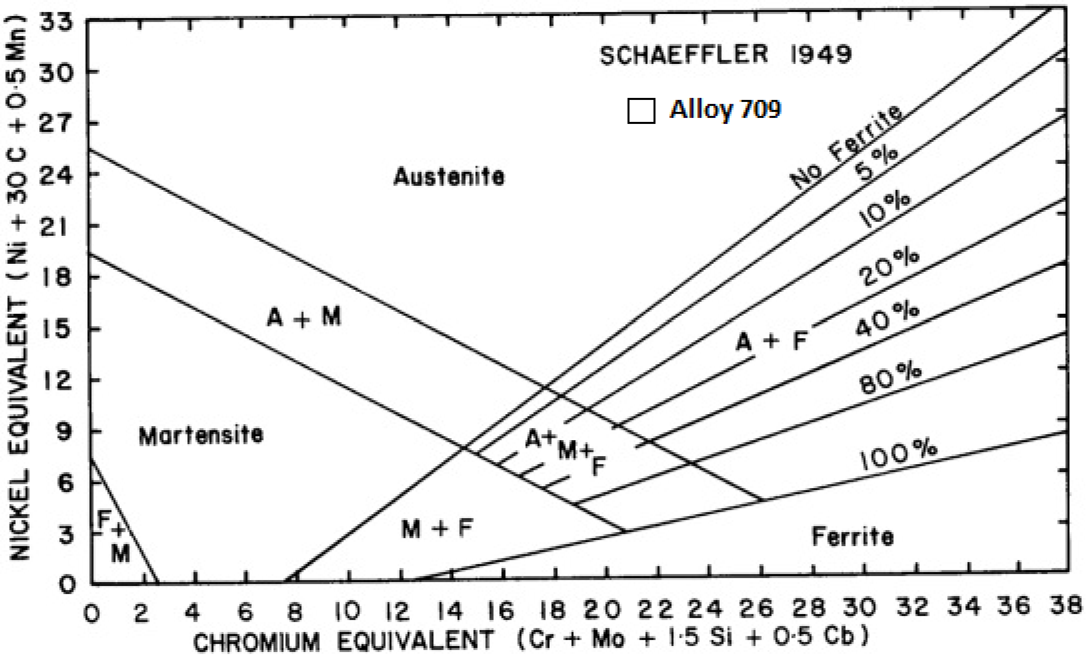

Figure 3.2. Schaeffler diagram showing the effect of the nickel and chromium content on the stability of austenite [9].

The more densely packed FCC structure of austenite increases the creep properties of the material making it the ideal phase for high temperature applications. The other alloying elements in common austenitic stainless steels have their advantages and disadvantages.

Chromium – a crucial alloying element in stainless steels that improves hardenability, strength, wear resistance, and increase the corrosion resistance. It can be found forming precipitates like M23C6, Cr2N, M6C, Z-phase, sigma phase, etc. [10], [11].

Nickel – is crucial for stabilizing austenite. It also aids in solid solution strengthening which increases the impact strength and toughness. Nickel also contributes to the corrosion resistance of the alloy. It also aids in hydrogen pick up.

Manganese – is added to increase the hardenability, ductility, and wear resistance of the stainless steel. It helps to prevent detrimental iron sulfides increasing the high temperature strength. Mn is a cheaper austenite stabilizer than Ni; so it can reduce the cost of the stainless steel [12]. The composition of Mn in high temperature stainless steels is kept low because it can decrease the creep rupture life.

Molybdenum – is often added to stainless steels because it increases the high temperature strength, improves creep resistance due to solid solution hardening, and can help in corrosion resistance particularly improving pitting resistance [13]. In some stainless steels tungsten is added over molybdenum because tungsten forms precipitates that have a slower response to creep along with imparting solid solution strengthening [10]. Also, tungsten in steel composition is known to create reduced activation steels.

Niobium – forms a very stable Nb(CN) precipitate that is beneficial for pinning mobile dislocations, and removing carbon from the matrix helping the corrosion resistance. Nb also has low neutron absorption cross-section (low activation) [10]. The Nb(CN) precipitates are very stable at high temperatures so they will often be found in 20Cr-25Ni-Nb after solution treating and quenching [11].

Silicon – helps to enhance oxidation resistance but when the concentration is over 0.7 wt%, potential spalling of the oxide layer can occur [8].

Carbon and Nitrogen – They are generally found in the interstitial sites of the iron lattice; they contribute to the strength of the material by forming precipitates that assist in precipitate strengthening of the material. The content of carbon, however, is generally made to be quite low for high temperature stainless steels because the carbon will form Cr rich precipitates on the grain boundaries leading to chromium depletion from solid solution causing the corrosion resistance of the alloy to decrease on the grain boundaries. High carbon content also contributes to poor weldability [10]. Nitrogen, similar to carbon, assists in strengthening the material by forming nitrides like NbN and TiN. However, high nitrogen content was shown to lead to intergranular stress corrosion cracking in austenitic stainless steels like 304 [14]. Figure 3.3 shows the effect of increasing nitrogen concentration on the flow stress of an austenitic Nb-microalloyed steel [15].

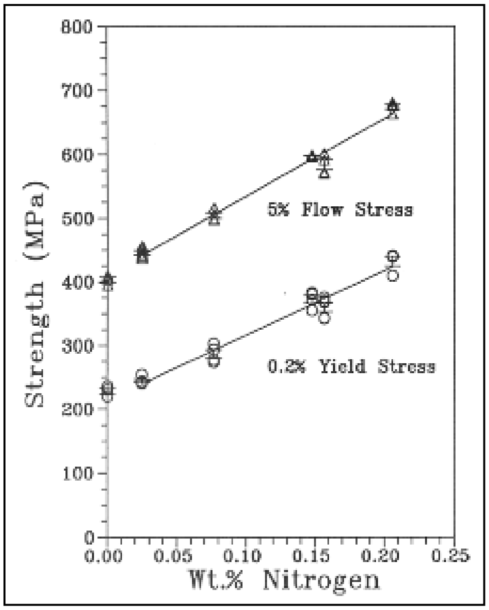

Figure 3.3. Strength as a function of nitrogen in steels [8], [15].

ASTI 300 series including type 304, a 18Cr-8Ni stainless steel, is a common series of stainless steels that is used for a wide variety of applications because of its good weldability, corrosion resistance, and strength. For higher temperatures 316 and 316L are typically used because they have better creep, high temperature strength and corrosion properties. They provide good pitting corrosion resistance at elevated temperatures.

20Cr-25Ni based stainless steels including Alloy 709 are being looked at for high temperature applications due to their superior creep resistance, high temperature strength, and corrosion resistance. Adding more Ni generally makes the alloy more expensive, but it helps the high temperature mechanical properties. The 20Cr-25Ni series of stainless steel might require more cost up-front but could save money down the road if the material can out last the other materials. The increase in Cr and Ni makes the alloy more corrosion resistant and increases the high temperature mechanical properties. Using the other alloying elements to create fine MX precipitates have been very beneficial for optimizing the 20Cr-25Ni series of stainless steels.

3.4 Creep Mechanisms

3.4.1 Overview of Creep

Creep is defined as time-dependent plasticity generally tested under a constant stress or load, often below the yield stress of the material, with the temperature typically being over $0.5T_m$

(with T_m being the melting temperature). Some studies have shown creep at temperatures of 0.09-0.21 T_m for certain alloys but generally for most materials creep begins to occur at 0.4-0.5 T_m [16][17][3]. It typically takes several years for well-engineered structural components to be affected by creep. This process, however, can be accelerated by increasing the temperature or applied stress to be able to see creep in shorter periods of time. This makes creep a primary concern for components at elevated temperatures for long periods of time.

There are generally three stages of creep that occur. They can easily be seen when plotting the plastic strain (ε_p) with the time (t) under constant load and temperature, shown in Figure 3.4. The first stage is known as the primary creep stage and is labeled "I" in Figure 3.4. In the primary creep region, the strain rate is not constant. In this case the strain rate decreases as the time and strain increase. This is due to strain hardening or a decrease in free or mobile dislocations [3]. An inverse case of primary creep has been found for certain alloys that experience solute drag with "3 power creep" [17]. In the secondary stage (labeled II), also called the steady-state creep stage, where the strain rate is constant [17]. The steady state is often attributed to the rate of dislocations being created, causing hardening, is equal to the rate of recovery, causing softening. It is a manifestation of a dynamic balance between strain hardening and recovery. The tertiary creep (labeled III) or accelerated creep is when the microstructure evolves, and damage evolution takes place.

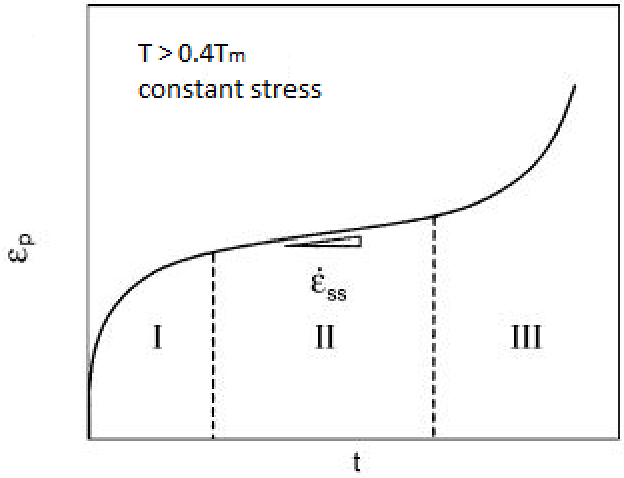

Figure 3.4. Typical creep curve under constant true-stress and temperature [17].

Microstructure evolution is usually dynamic recovery, dynamic recrystallization, coarsening of precipitates, or other phenomena. Damage evolution generally is caused by the formation of cracks and voids or cavities often on grain boundaries [3]. The testing conditions can cause a wide variety of creep curves with varying length of the primary, secondary and tertiary creep stages. Increasing the temperature and stress will result in more plastic strain over a period of time resulting in faster failure (Figure 3.5). Failure is typically the end of the creep curve.

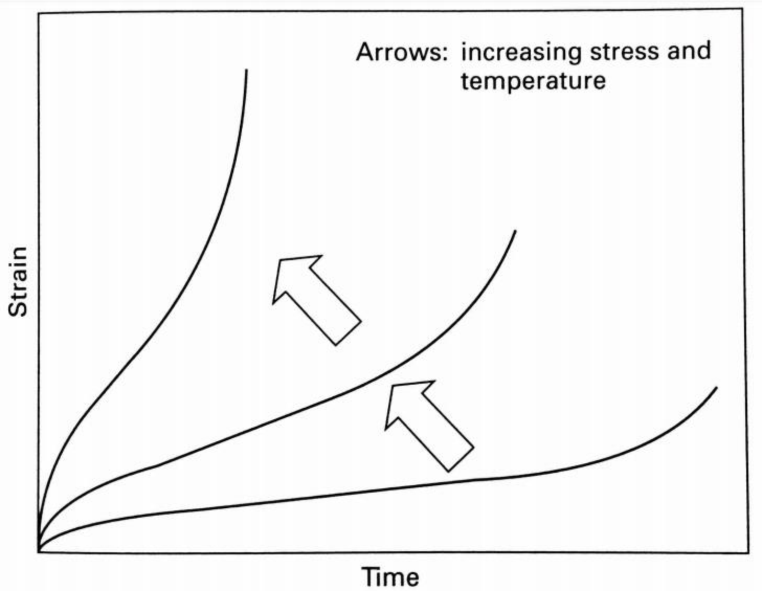

Figure 3.5. Schematic creep curves with increasing stress and temperature [3].

Some creep resistant steels and alloys under certain conditions do not have a clear steady state creep stage. In these instances, the creep curve will start with primary creep and move directly into tertiary creep. When this occurs the minimum creep rate can be defined as the moment the hardening in the primary is equivalent to the softening of the tertiary [3]. Research has shown that the microstructure during creep is constantly evolving for many creep resistant steels and alloys. This has led to many engineers and researchers preferring the term minimum creep rate over steady state creep rate because there is no true dynamic microstructural equilibrium for many materials [3]. Figure 3.6(a) and (b) show the creep curve and creep rate vs. time curve for a Grade 91 steel [18].

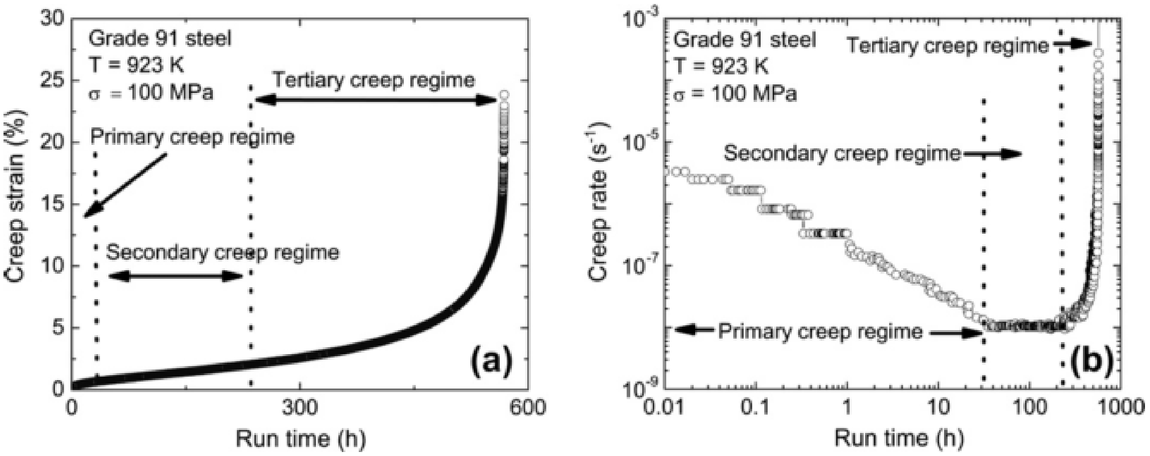

Figure 3.6. (a) A standard creep curve for Grade 91 steel, and (b) a creep rate vs. time showing the minimum creep rate being the same as the steady state creep rate [19].

A common equation to show the stress dependence of the minimum or steady state creep rate with the applied stress, is given by Norton's Law, equation (3.1)

$$\dot{\varepsilon}_{\min or\ ss} = A\sigma^n \tag{3.1}$$

$$A = A'\exp(-\frac{Q_c}{RT}) \tag{3.2}$$

where $\dot{\varepsilon}_{\min or\ ss}$is the minimum creep rate or steady state creep rate, *σ* is the applied stress, *n* is the stress exponent, $A'$is the parameter that includes grain size and test parameters, $Q_c$is the activation energy for creep, *R* is the universal gas constant, and *T* is the temperature in K [3]. The creep of materials can often be described by the Bird-Mukherjee-Dorn (BMD) equation.

$$\dot{\varepsilon} = A\frac{DEb}{kT}\left(\frac{\sigma}{E}\right)^n\left(\frac{b}{d}\right)^p \tag{3.3}$$

where $\dot{\varepsilon}$ is the steady state strain rate, σ the applied stress, *d* the grain diameter, *A* the material dependent constant depending on the operating mechanism, *E* the elastic modulus, *b* the Burgers vector, *k* the Boltzmann's constant, *n* is the stress exponent, *p* is the inverse grain size exponent, and *D* the diffusivity which is described by the equation:

$$D = D_o exp(-Q/RT) \tag{3.4}$$

where *Do* is the pre-exponential constant also known as the frequency factor, *Q* the appropriate activation energy, *R* the universal gas constant, and *T* the temperature in K [8]. The BMD equation was found to be accurate for most high stress low temperature conditions. However, when the alloy is particle-hardened, the BMD equation tends to result in high activation energy and stress exponent. Alloy 709 experiences a fair amount of particle hardening when stress change creep tests are used and the stress exponents (at 700°C, 725°C, and 750°C) and activation energy found for Alloy 709 by Alomari et al. [20] were high for this reason. The stress exponent found for Alloy 709 at 700°C and 600°C found with monotonic creep tests was not out of the 5 to 7 range for dislocation climb creep, shown in Chapter 3. Ennis et al. studied the high stress exponents in comparison to the precipitates that act as dislocation barriers [10], [21]. In this type of situation, the findings are generally rationalized to find true creep mechanism of the alloy lead to the threshold stress being considered. This lead to the BMD equation to be modified for a precipitate hardened alloy. The additional stress added to the dislocations due to the precipitates is considered in the modified BMD equation (3.5)

$$\frac{\dot{\varepsilon}_{ss}kT}{DEb} = A\left(\frac{\sigma-\sigma_{th}}{E}\right)^{n}\left(\frac{b}{d}\right)^{p} \tag{3.5}$$

where σ_{th} is the threshold stress and all other terms have been previously defined. The threshold stress is the stress below which no creep deformation takes place. This makes the effective stress (σ- σ_{th}) what is actually contributing to creep deformation in the material instead of the applied stress [10]. This will provide a better understanding of the actual creep mechanism occurring in the material. The resultant stress exponent and activation energy are often used to determine the mechanism of creep occurring in the material.

Table 3.1. Parametric dependence of various diffusion-controlled deformation mechanisms [22].

Creep Type	***n***	***p***	***Q***
Nabarro-Herring	1	2	QL
Coble	1	3	QGB
Harper-Dorn	1	0	QL
Grain Boundary Sliding	2	2	QGB
Solute Drag Dislocation Creep	3	0	QS
Dislocation Climb Creep	5	0	QL
Low Temperature Climb Creep	7	0	QC

where QL is lattice diffusion, QGB is grain boundary diffusion, QC is dislocation core diffusion, and QS is solute diffusion. These mechanisms will be discussed in more detail later in this chapter.

3.4.2. Dislocation Creep

For dislocation creep the movement of dislocations happens to be the rate-controlling mechanism [12]. There are two forms of dislocation creep, dislocation slip or glide and dislocation climb. Dislocations are line defects that move along the slip plane of the material, for FCC the slip plane is of type {111}. Additionally, dislocation movement requires the bonds between the atoms to break which requires high enough temperatures or stresses [23]. When the dislocations are moving in the matrix material, they are often gliding in the slip plane. The dislocation glide can be slowed by the presence of barriers in the material that prevent or slow the dislocations from moving. These barriers can be a variety of things, solute atoms, precipitates, grain boundaries or other dislocations. These strengthening mechanisms include solid solution strengthening, precipitation hardening, and grain boundary strengthening. The stress required to drive dislocation glide is on the order of one tenth the shear stress for most materials [23]. Figure 3.7 schematically shows the dislocation models of glide and climb.

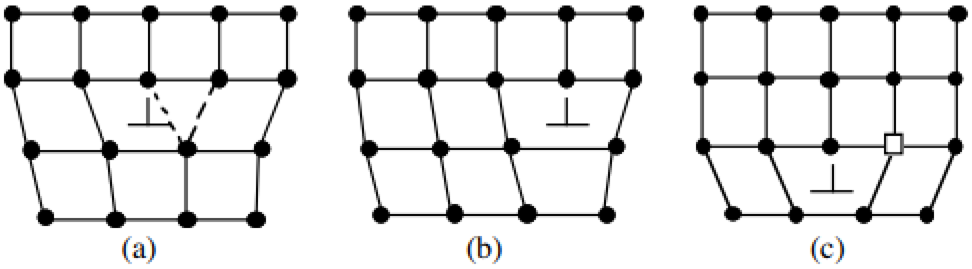

Figure 3.7. Dislocation glide (a) and (b) while (c) shows dislocation climb creating a vacancy.

When the dislocations meet with the barriers, they often cannot simply continue on the slip plane. Thus, the high temperatures will induce recovery of the pinned dislocations. As the material is strained more, the built-up strain energy and high temperature can be enough to drive the recovery process. The recovery process decreases the dislocation density by allowing the dislocations to move into low energy arrays that are often subgrain boundaries. For this to occur there must be dislocation climb and slip which goes along with self-diffusion in the lattice [23].

At high homologous temperatures the dislocations are able to climb towards each other and mutually annihilate. This process is aided by vacancy diffusion [22]. For this reason, it is often found that the activation energies for self-diffusion and creep are close to the same. As temperature increases, the atoms gain thermal energy and the vacancy concentration increases exponentially [23].

3.4.3. Grain-Boundary Sliding

The grain boundaries play an important role in creep deformation. Grain boundary sliding can occur at high temperatures which also can lead to the creation of vacancies [7]. The higher temperatures cause ductile materials grain boundaries soften allowing creep to occur through grain boundary sliding. Grain boundary sliding increases with temperature and grain boundary area. Where smaller grains significantly increase the grain boundary area so large grained materials are favored for creep resistance. At low temperatures grain boundaries prevent dislocation movement increasing the yield strength of the material, however at high temperatures they facilitate deformation by sliding [24]. The grain boundaries often act as a quasi-viscous material that flow at elevated temperatures.

3.4.4. Diffusion Creep

Diffusion creep is the creep mechanism that is caused by the flow of vacancies and interstitials through a crystal under the influence of applied stress causing grain boundary deformation. The diffusivity of a material increases with temperature which will lead to more deformation [7]. There are two major types of diffusion creep. As shown in Figure 3.8, the flow of vacancies through the grain boundaries is often called Coble creep, whereas the flow of vacancies through the grains is often called Nabarro-Herring creep. The vacancies migrate from grain boundaries in compression to grain boundaries in tension. The path the vacancies take, either through grain boundaries or through the grains, determines if it is Coble or Nabarro-Herring creep, respectively.

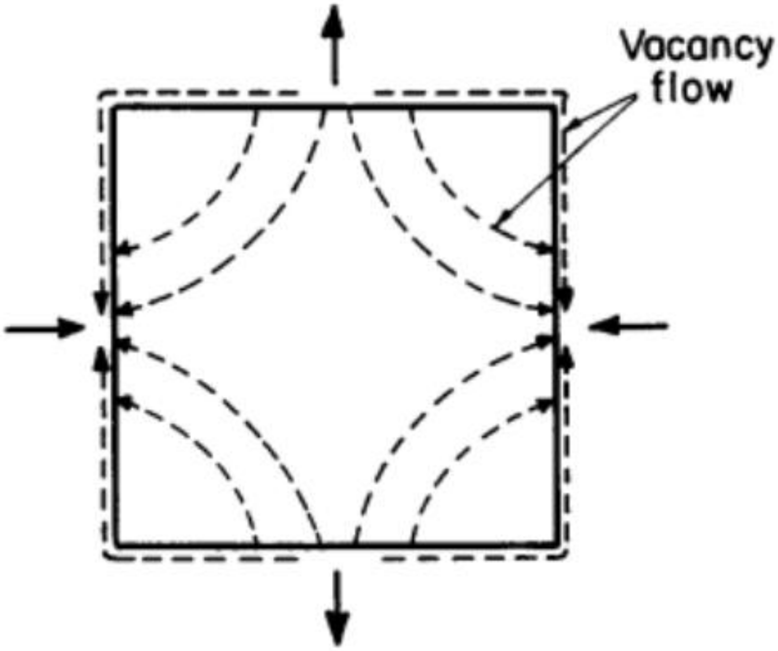

Figure 3.8. The principle of diffusion creep showing vacancy flow through the grains (Nabarro-Herring creep) and vacancy flow though the grain boundaries (Coble creep) [25].

3.5. References

[1] I. Charit and K. L. Murty, "Structural materials issues for the next generation fission reactors," Jom, vol. 62, no. 9. pp. 67–74, 2010.

[2] K. L. Murty and I. Charit, "Structural materials for Gen-IV nuclear reactors: Challenges and opportunities," J. Nucl. Mater., vol. 383, no. 1–2, pp. 189–195, 2008.

[3] F. Abe, T.-U. Kern, and R. Viswanathan, Creep-resistant steels, 1st ed. The Institute of Materials, Minerals, and Mining, 2008.

[4] OECD Nuclear Energy Agency, "Technology Roadmap Update for Generation IV Nuclear Energy Systems," Gen IV Int. Forum, pp. 1–66, 2014.

[5] IRSN, "Review of Generation IV Nuclear Energy Systems," 2015.

[6] T. Allen, J. Busby, M. Meyer, and D. Petti, "Material challenges for nuclear systems," Materials Today, vol. 13, no. 12. pp. 15–23, 2010.

[7] M. Farooq, "Strengthening and degradation mechanisms in austenitic stainless steels at elevated temperature," Royal Institute of Technology, 2013.

[8] S. McCormick, “Effect of heat treatment and creep deformation on the microstructural characteristics of ATI 20-25+Nb austenitic stainless steel,” University of Idaho, 2015.

[9] “Dissimilar welding metals,” WelderDestiny, 2016. [Online]. Available: https://www.welderdestiny.com/dissimilar-metals-welding.html.

[10] T. Shrestha, “Creep Deformation, Rupture Analysis, Heat Treatment and Residual Stress Measurement of Monolithic and Welded Grade 91 Steel for Power Plant,” University of Idaho, 2013.

[11] T. Sourmail and H. K. D. H. Bhadeshia, “Microstructural evolution in two variants of NF709 at 1023 and 1073 K,” Metall. Mater. Trans. A, vol. 36, no. 1, pp. 23–34, 2005.

[12] S. Abouzari, “Solid solution strengthening effect on creep strength of austenitic stainless steel,” Royal Institute of Technology, 2012.

[13] A. F. Padilha and P. R. Rios, “Decomposition of austenite in austenitic stainless steels,” ISIJ Int., vol. 42, no. 4, pp. 325–327, 2002.

[14] S. Roychowdhury, V. Kain, S. Neogy, D. Srivastava, G. K. Dey, and R. C. Prasad, “Understanding the effect of nitrogen in austenitic stainless steel on the intergranular stress corrosion crack growth rate in high temperature pure water,” Acta Mater., vol. 60, no. 2, pp. 610–621, 2012.

[15] G. Chen, W. Y. Yang, S. Z. Guo, and Z. Q. Sun, “Strain-induced precipitiaon of Nb(CN) during deformaiton of undercooled austenite in Nb-microalloyed HSLA steels,” in Materials Science Forum, vol. 475–479, Trans Tech Publications, 2005, pp. 105–108.

[16] L. A. Deibler, “Room temperature creep in metals and alloys,” no. September, 2014.

[17] M. E. Kassner, Fundamentals of Creep in Metals and Alloys, Second Edi. Elsevier Ltd., 2008.

[18] T. Shrestha, M. Basirat, I. Charit, G. P. Potirniche, K. K. Rink, and U. Sahaym, “Creep deformation mechanisms in modified 9Cr-1Mo steel,” J. Nucl. Mater., vol. 423, no. 1–3, pp. 110–119, 2012.

[19] T. Shrestha, M. Basirat, I. Charit, G. P. Potirniche, K. K. Rink, and U. Sahaym, “Creep deformation mechanisms in modified 9Cr-1Mo steel,” J. Nucl. Mater., vol. 423, no. 1–3, pp. 110–119, 2012.

[20] A. S. Alomari, N. Kumar, and K. L. Murty, “Investigation on Creep Mechanisms of Alloy 709,” ASME 2017 Nucl. Forum, p. V009T02A003, 2017.

[21] P. J. Ennis, A. Zielinska-Lipiec, O. Wachter, and A. Czyrska-Filemonowicz, "Microstructural stability and creep rupture strength of the martensitic steel P92 for advanced power plant," Acta Mater., vol. 45, no. 12, pp. 4901–4907, 1997.

[22] I. Charit and K. L. Murty, "Creep behavior of niobium-modified zirconium alloys," J. Nucl. Mater., vol. 374, no. 3, pp. 354–363, 2008.

[23] J. Pelleg, Creep in Ceramics, no. i. Springer International Publishing, 2017.

[24] S. L. Kakani and A. Kakani, Material science, vol. 1. New Age International Publishers, 2004.

[25] T. G. Langdon, "Creep at low stresses: An evaluation of diffusion creep and Harper-Dorn creep as viable creep mechanisms," Metall. Mater. Trans. A, vol. 33, no. 2, pp. 249–259, 2002.

4. MATERIAL CHARACTERIZATION

4.1. Introduction

Alloy 709 is a potential austenitic stainless steel for structural applications in sodium-cooled fast reactors. In this study, creep tests on Alloy 709 specimens were performed at a temperature of 700 °C under applied stresses in the range of 125 to 250 MPa. The alloy exhibited a brief primary, insignificant secondary and prolonged tertiary creep stages. A Norton stress exponent (n) of 5.9 was obtained from the creep plots. Microstructural analyses were carried out for both as-received and crept specimens using optical microscopy, electron backscattered diffraction, and transmission electron microscopy. The microstructures of the as-received and crept specimens were compared. Transgranular mode of fracture surfaces was observed by examining the creep-ruptured specimens using scanning electron microscopy. Based on the creep data and microstructural observations, possible creep deformation and failure mechanisms are elucidated.

Austenitic stainless steels are considered cost-effective materials if they have commensurate high temperature oxidation and creep resistance for prolonged duration under service conditions [1, 2]. Alloy 709 is a potential candidate material for structural applications in advanced nuclear reactors, particularly for sodium-cooled fast reactors (SFR). The steel has been down-selected from a list of other high temperature steels because of its superior high temperature properties including elevated temperature oxidation/corrosion resistance, creep strength, sodium compatibility and weldability [3]. A number of creep-resistant austenitic steels have been developed by modifying compositions of the 18/8 austenitic stainless steels. In 1980’s, the 20Cr-25Ni based austenitic steel was developed for its creep-resistance in fossil fired power plants [4]. However, Alloy 709 was originally developed by Nippon Steel (Tokyo, Japan), as NF709. This steel has a composition close to ATI 20+25Nb^{TM}. These steels contain Fe-20Cr-25Ni (wt%) base composition and the alloy composition is tailored in such a way that the austenitic phase is stabilized. The austenitic phase (close packed structure) is generally considered better for creep resistance compared to BCC ferritic phase (more open structure). The high Ni content in Alloy 709 provides enhanced stability to the steel at elevated temperatures (albeit it makes the steel more expensive) whereas high Cr content provides excellent high temperature corrosion/oxidation resistance. There are only a limited number of creep studies available in open literature on the creep behavior of Alloy 709. While it is likely that components will need to serve at temperatures around 550^{o}C, it is important to understand the creep behavior of this material at different temperatures.

The aim is to report on the 700^{o}C short-term creep behavior of Alloy 709 and to understand the characteristic microstructural evolution that takes place during creep deformation using different characterization tools. An attempt is also made to compare the obtained creep data from Alloy 709 with those of other austenitic stainless steels and to understand plausible operative creep deformation mechanisms.

4.2. Material and Procedures

An Alloy 709 plate with dimensions of 101.6 mm × 228.6 mm × 20.3 mm was received from the Oak Ridge National Laboratory (ORNL). The prior history of the as-received plate included hot-processing (forged and rolled) and annealing at 1100°C, followed by water quenching. The chemical composition of the Alloy 709 plate is given in Table 4.1.

Table 4.1. Chemical composition of Alloy 709 (in wt%)

C	Mn	Si	P	S	Cr	Ni	Mo	N	Ti	Nb	B	Fe
0.067	0.90	0.40	<0.005	<0.001	19.80	25.09	1.50	0.15	<0.01	0.26	0.0043	Bal.

Figure 4.1 shows a schematic of the plate showing the three primary orthogonal directions (rolling direction, transverse direction and normal direction). Sections from the Alloy 709 plate were cut and mounted in acrylic. Standard metallographic procedures involving sequential grinding and polishing were carried out. The final polish was taken to a 0.3 µm surface finish using alumina paste. After thoroughly rinsing the surface of these samples, Vickers hardness testing was performed using a LECO LM-100 microhardness tester on all three distinct faces (RD-TD, ND-RD and ND-TD) with very similar results. Six indentations were taken for each orthogonal plane. Essentially, no difference was observed in the Vickers hardness number (VHN) on the three orthogonal faces with VHN's of 177 ± 4 on the RD-TD, 179 ± 5 on the ND-RD plane, and 179 ± 4 on the ND-TD plane,

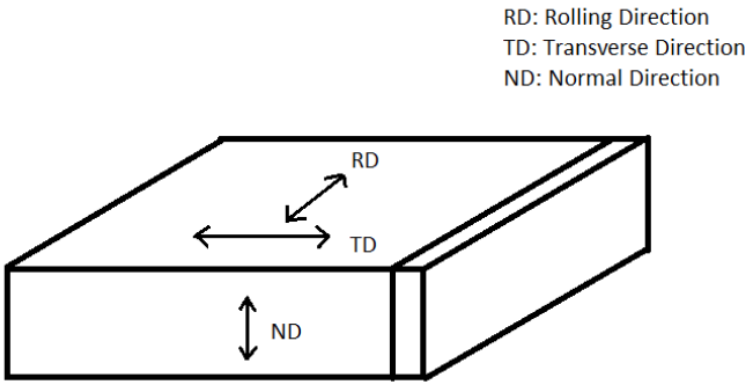

Figure 4.1. Schematic of the plate showing the rolling, transverse and the normal (thickness) directions.

The polished metallographic samples were then electrolytically etched with 10% (by mass) oxalic acid in deionized (DI) water at 6 V for 6-10 s, depending on the surface area of the specimen of interest [1]. Optical microscopy was conducted using an Olympus PMG-3 light microscope. The average grain size was determined from the metallographic images obtained using the mean linear intercept technique.

One section of the plate was machined into a round tensile specimen with a gauge length of 25.4 mm and a diameter of 6.53 mm. A tensile test was then performed at 700°C at a strain rate of 10^{-3} s^{-1} using an Instron 5982 Materials Testing System. Four sections were machined as round creep specimens with a gauge length of 25.4 mm and a diameter of 6.53 mm. Uniaxial constant-load creep tests were performed at 700 ± 1 °C with initial stresses ranging from 125 to 250 MPa using an Applied Test Systems 2335 lever arm (20:1) creep tester. Two Heidenhain ST-12 linear encoders measured the gauge elongation with an accuracy of ± 0.2 µm.

Samples were prepared for the transmission electron microscopy by grinding and polishing the samples until a thickness of approximately 100 µm thick or less was reached. Then a Gatan disc punch was used to obtain 3-mm diameter discs. Subsequently, electro-jet polishing on the disc samples were carried out using a Fischione Twin-Jet Polisher. A mixture of nitric acid (HNO_3) and methanol (CH_3OH) (1:9 ratio by vol.) was used as the electrolyte and the voltage used was around 30 V. Dry ice was used to keep the temperature of the electrolytic bath close to -40°C.

A JEOL 2010J transmission electron microscope (TEM) operated at an accelerating voltage of 200 kV was used to identify and study the characteristics of the second phase particles. Also, an energy dispersive spectroscopy (EDS) system attached to the TEM was used to carry out compositional analysis.

The polished metallographic samples were electro-etched and examined under a Zeiss Supra 35 Field Gun Emission Scanning Electron Microscope (FEG-SEM), revealing several of the precipitates and grain boundaries. Crept specimens were prepared either by sectioning along the loading direction exposing the grip and gauge sections, or cutting perpendicularly to the loading direction, exposing only the grip section. The specimens were then ground and polished down to 0.3 µm for SEM and EDS analyses. Vickers microhardness testing under 0.5 kgf load was carried out at several locations from the fracture tip to the grip region. At each location, six indentations were carried out.

Electron backscatter diffraction (EBSD) was obtained using the same sample preparation process listed above for the TEM samples except for the electro-jet polishing that was done for a shorter duration as a sample perforation is not required for EBSD. The surface- prepared disks were placed in the Zeiss Supra 35 FEG-SEM with the QUASOR^{TM} EBSD system. The sample stage was set at an angle of 70° with a working distance of about 16.5 mm. The SEM was operated at an accelerating voltage of 20 kV and put on high current mode. A binning of 8 pixel × 8 pixel was used in this study to obtain high enough resolution in the EBSD maps created.

ThermoCalc thermodynamic data can be passed on to the diffusion modeling software, DICTRA, and the data on the mobilities and driving forces from these two codes could be passed on to the microstructure evolution software, MICRESS. ThemoCalc was used in this work to determine what phases and precipitates are present at various temperatures and in what amount. The composition of Alloy 709 found in Table 4.1 was used for the ThermoCalc calculations.

4.3. Results and Discussion

4.3.1. Microstructural analysis of the as-received Alloy 709

A representative optical micrograph montage of the as-received Alloy 709 in all three orthogonal planes is shown in Figure 4.2. The microstructure consists of near equiaxed grains accompanied by a relatively high density of annealing twins. Grain sizes measured in all three orthogonal planes did not exhibit any significant difference and the mean grain size is estimated to be 38 ± 3 μm. Figure 4.3a shows a TEM image of the as-received material showing presence of annealing twins. A representative EDS spectrum from one of the dark-contrast second phase particles is shown in Figure 4.3b. While the EDS showed the presence of Nb, the N content could not be identified unambiguously in the EDS spectrum despite a peak presence of N. In the literature, NbN is found to be fine stable particles. The dark-contrast particles noted in the same TEM image are most likely NbN given the size and EDS spectrum of the particles. The other particles that contain Nb in Alloy 709 are NbC or Z phase (CrNbN). However, Z phase particles are typically rod-shaped and found to be in detectable amount only in materials exposed to high temperatures for a long duration, not in a solution annealed material.

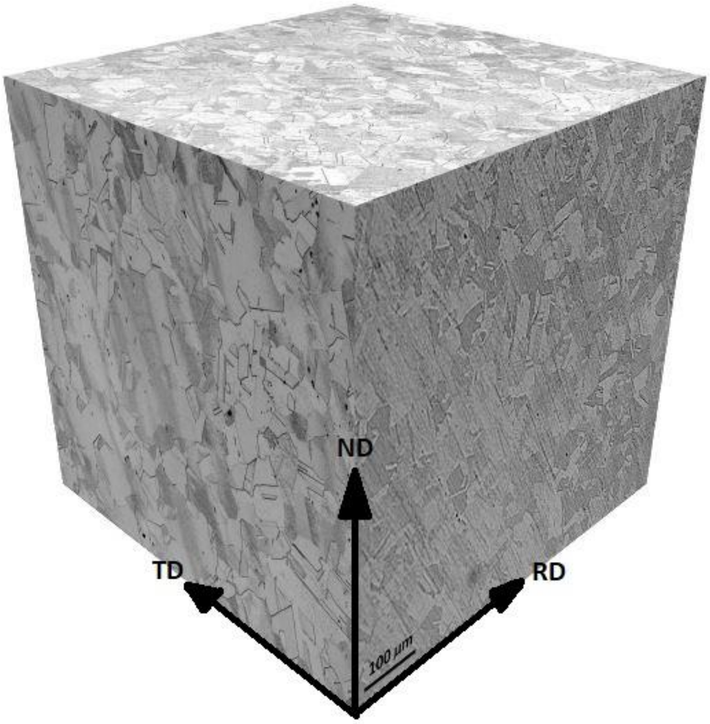

Figure 4.2. A three-dimensional representation of the optical micrographs in three orthogonal planes of the as-received Alloy 709 plate.

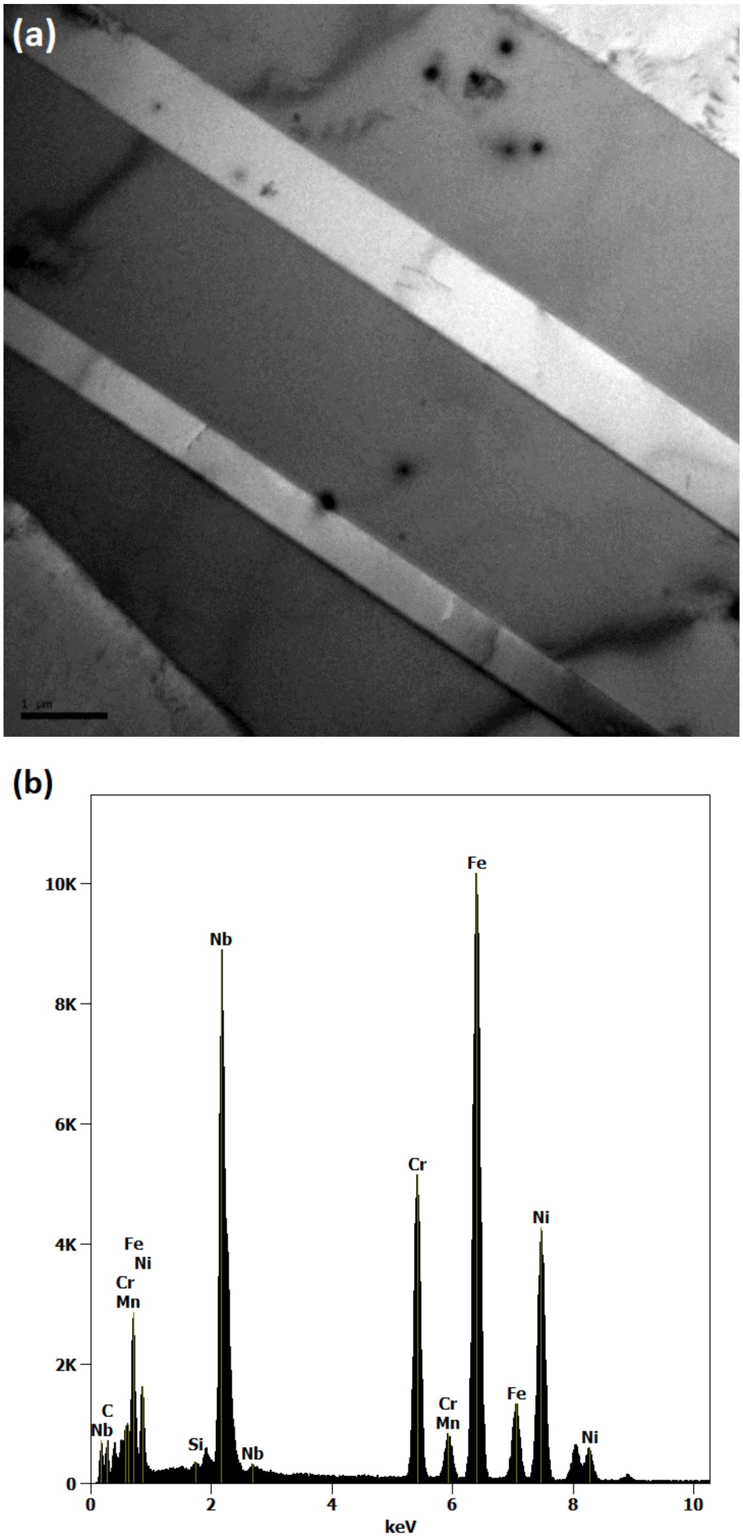

Figure 4.3. (a) A TEM bright field image of the as-received Alloy 709 showing annealing twins and dark-contrast globular second phase particles. (b) EDS spectrum of a dark particle.

4.3.2. Tensile behavior of the as-received Alloy 709 at 700°C

Tensile testing at 700°C was conducted to determine if the creep tests were performed at stresses around the yield strength. Two creep tests were conducted below the yield strength at 700°C and two tests at slightly above the yield strength in order obtain data in a reasonable period of time. The creep data will be reported in the next section. The true stress - true strain curve of Alloy 709 at 700°C at a strain rate of 10^{-3} s^{-1} (Figure 4.4). As common in austenitic stainless steels, the alloy exhibits a pronounced strain hardening regime. The stress-strain curve also exhibits slight indications of serrations right after yielding likely from dynamic strain aging (DSA).

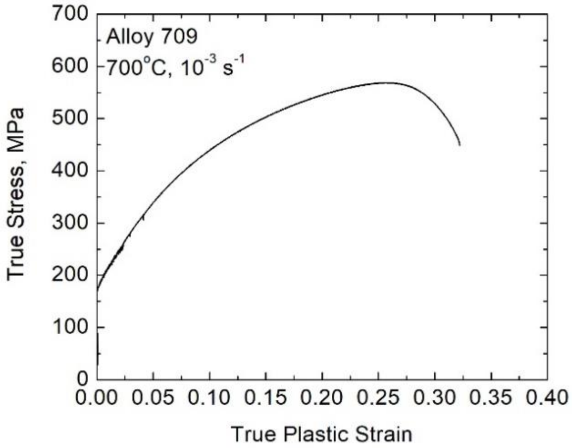

Figure 4.4. True stress - true strain curve for Alloy 709 at a temperature of 700°C and strain rate of 10^{-3} s^{-1}.

While DSA has largely been observed in mild steels as a result of interactions between mobile dislocations and interstitial impurities, it has also been observed in austenitic stainless steels like 316 SS where substitutional solutes modify such interactions. In 316 SS, it typically occurs at temperatures up to 600°C and strain rates in the range of 10^{-6} to 10^{-3} s^{-1} [5]. Alloy 709 exhibiting traces of DSA at 700°C is not unexpected as Alloy 709 is a more concentrated alloy with greater amounts of substitutional solutes being present in solid solution, such as Ni (10-14 wt% Ni in 316 SS as opposed to ~25 wt.% Ni in Alloy 709) leading sluggish diffusivity. Nevertheless, at lower temperatures (e.g. 600^{o}C) the DSA effect is expected to be more pronounced. Table 4.2 lists the measured engineering tensile properties (e.g. yield strength, ultimate tensile strength and the percentage elongation of failure) of Alloy 709 at 700°C. The large difference between the yield strength and ultimate tensile strength again confirms the significant extent of strain hardening.

Table 4.2. Tensile properties of Alloy 709 at 700°C.

Temperature	UTS (MPa)	YS (MPa)	Elongation
700 °C	449	178	46%

It is seen that the Alloy 709 maintained its yield strength at high temperatures making it attractive to structural applications under elevated temperatures. Other conventional austenitic stainless steels considered for structural applications in reactors have been found to have yield strengths below 178 MPa [6].

4.3.3. Creep tests at 700°C

A. Creep behavior of Alloy 709

The four accelerated creep tests were carried out on the as-received Alloy 709 specimens at 700°C. The corresponding creep curves are shown in Figure 4.5.a. The creep test at 125 MPa was performed up to 3,211 hours (without fracture) before unloading because of time constraint and the non-essentiality of the rupture life data for obtaining the Norton stress exponent. When initially loaded a small amount of instantaneous strain is created followed by a short primary and secondary stages, and a prolonged tertiary stage. As expected, the creep rate is found to rise with increasing applied stress from 125 MPa to 198 MPa. The higher stress tests were dominated by the tertiary creep zone. Figure 4.5.b shows the variation of creep rates as a function of time. The minimum creep rates are obtained from for each of the curves in Figure 4.5.b.

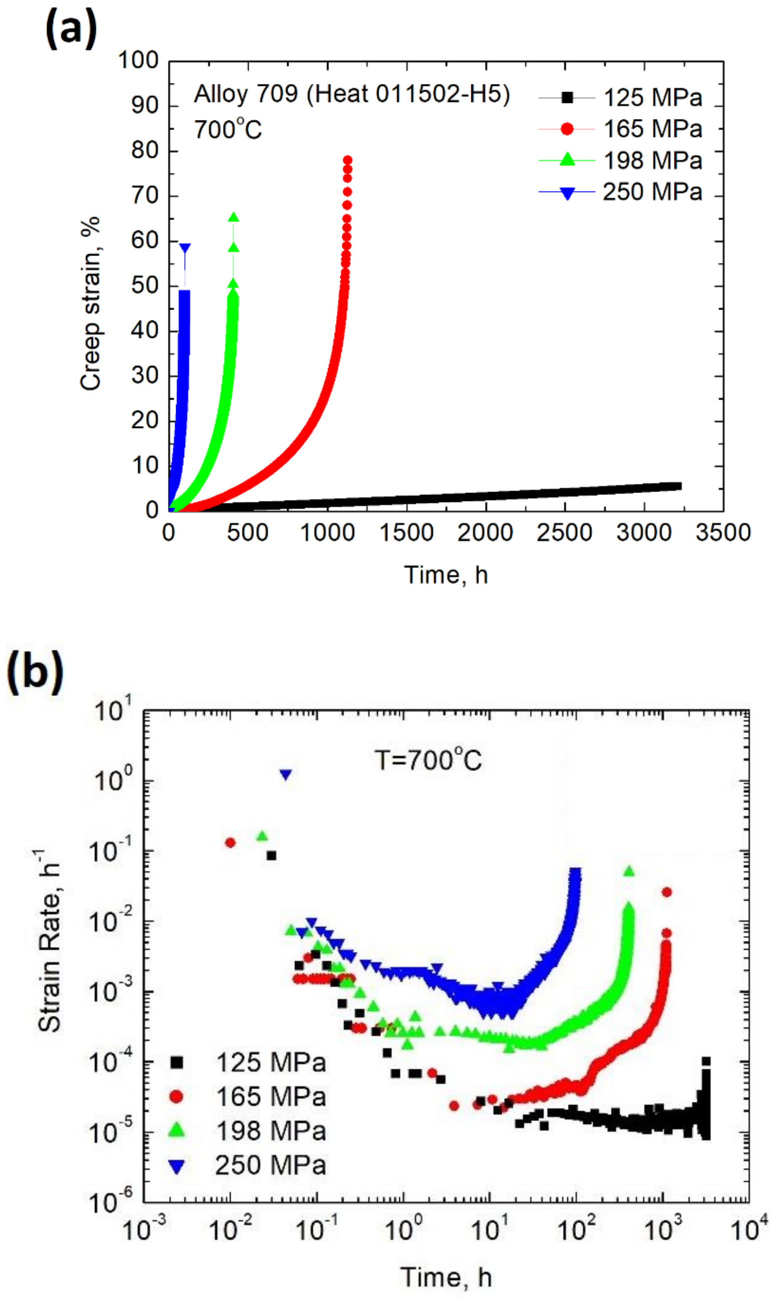

Figure 4.5. (a) Creep curves of the as-received Alloy 709 at 700°C under different applied stresses. (b) The corresponding variation of strain rate with time.

Table 4.3 shows the percentage elongation, percentage reduction in area and the minimum creep rates for the creep tests.

Table 4.3. Elongation, reduction in area, and minimum creep rate of Alloy 709 from various stresses at 700°C. (The symbol '*' means the sample did not rupture).

Applied Stress	125 MPa	165 MPa	198 MPa	250 MPa
% Elongation at Rupture	*	78%	65%	59%
%Reduction in Area	*	83%	81%	73%
Minimum Creep Rate, s^{-1}	4.17×10^{-9}	1.10×10^{-8}	6.10×10^{-8}	2.20×10^{-7}

The dependence of the minimum strain rate on the applied stress can be simply expressed by Norton's power law:

$$\dot{\varepsilon}_m = A\sigma^n, \tag{4.1}$$

where $\dot{\varepsilon}_m$ is the minimum creep rate, *A* is a material and temperature-dependent constant, σ is the applied stress, and *n* is the stress exponent). For this stress range and temperature, there was a single slope with an exponent of $n = 5.9$ from the double logarithmic plot of stress versus minimum creep rate as shown in Figure 4.6. This follows the experimental data obtained for NF709 steel from the datasheet.

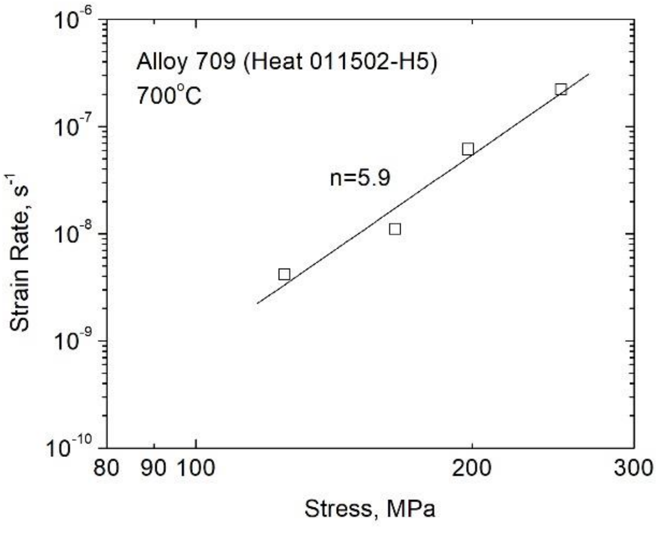

Figure 4.6. The variation of minimum creep rate as a function of stress for the as-received Alloy 709 at 700°C.

The stress exponent of 5.9 suggests that the creep mechanism at this temperature and stress range is most likely dislocation climb related. It is well known that a stress exponent between 4 and 7 indicates high temperature dislocation climb as the rate-controlling creep mechanism. However, because of the lack of additional data, it is not possible to unambiguously determine the creep mechanism at this point.

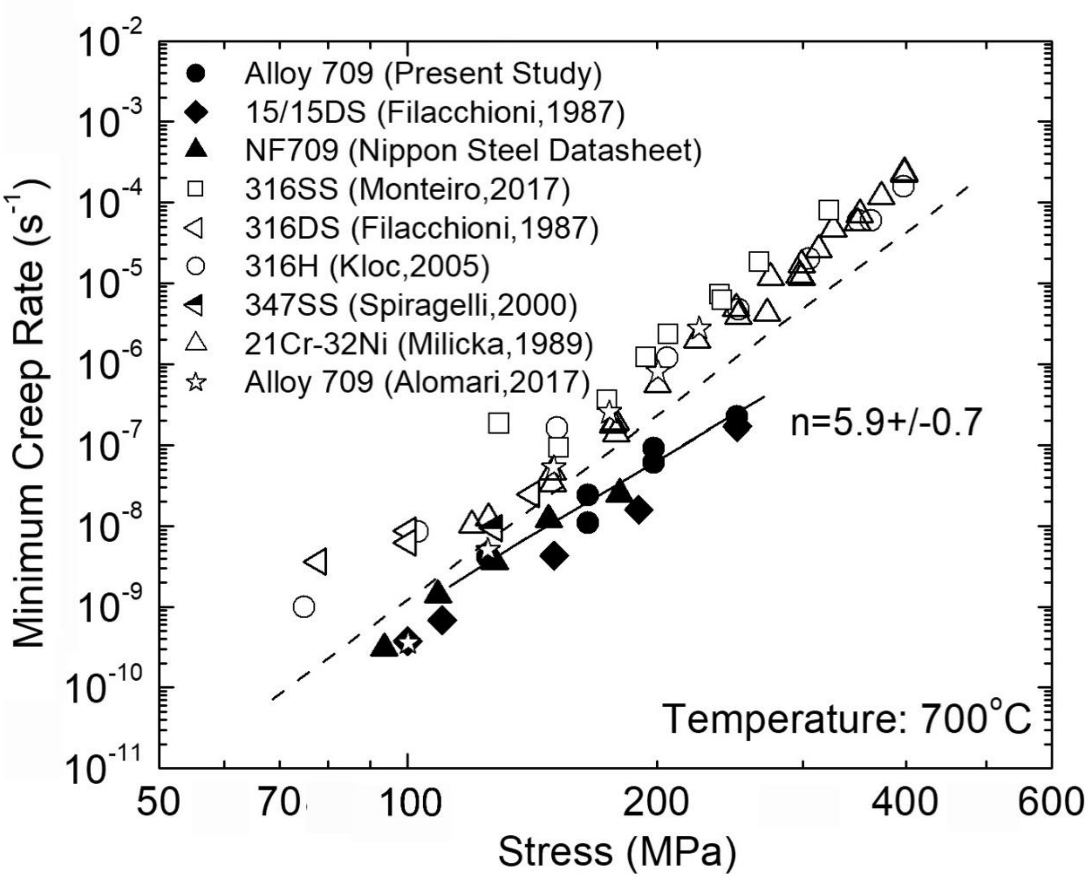

Figure 4.7. Comparison of minimum strain rates rate with applied stress at 700 °C for the as-received Alloy 709 at 700°C [7] - [13].

Figure 4.7 shows the double logarithmic plot of minimum creep rate versus applied stress in Alloy 709 at 700 ^{o}C. In the same plot, creep data of various 316 SS [7, 9] and 347 SS. Creep data from the NF709 datasheet from the Nippon Steel are also plotted as well as creep data of Alloy 709 obtained by Alomari et al. [10, 11] is also included. Also, some special austenitic stainless steels such as 15/15DS [8], 21Cr-32Ni [12] are also included. We note some difference between the creep data of the various 316 data; they lie rather all in the left side of the dashed line. We know that 316 steels are mainly based 16-18Cr—10-14Ni and 347 SS is based on 17-19Cr—9-13Ni. On the other hand, the creep data of Alloy 709, NF709 (Fe-20Cr-25Ni based composition) and 15/15DS data fall on the right side of the dashed line. In fact, the dashed line was constructed to delineate the difference between the creep strength of these alloys. It clearly shows that at least at 700 ^{o}C Alloy 709 maintains creep strength better than 316, 347 or 21Cr-32Ni austenitic stainless steels. The 15/15DS grade of austenitic stainless steel is a double-stabilized SS, slightly better creep strength than other grades even though it is very close to that of Alloy 709 of our study.

The data of Alomari et al. [11] cuts through the delineation line, which is not according to the overall trend. It is to note here that creep tests were done via stress-change experiments by Alomari and coworkers [11]. All the other studies conducted monotonic single stress creep tests. They also commented that threshold stress imparted by the particles led to the higher stress exponent values.

B. Fractography and optical metallography of creep ruptured specimens

Three of the tests (165, 198, and 250 MPa) were run up to rupture. A representative secondary electron SEM image of the specimen fracture surface tested at 700 ^{o}C under an applied stress of 198 MPa is shown in Figure 4.8.a. Transgranular mode of fracture was observed in all fractured specimens with dimple-like features in the center (Figure 4.8.b) and shear lips around the edges (Figure 4.8.c). The dimples are likely the result of the coalescence of microvoids [3]. The fracture surfaces show mostly ductile fracture, which corresponds to the significant ductility observed in Alloy 709.

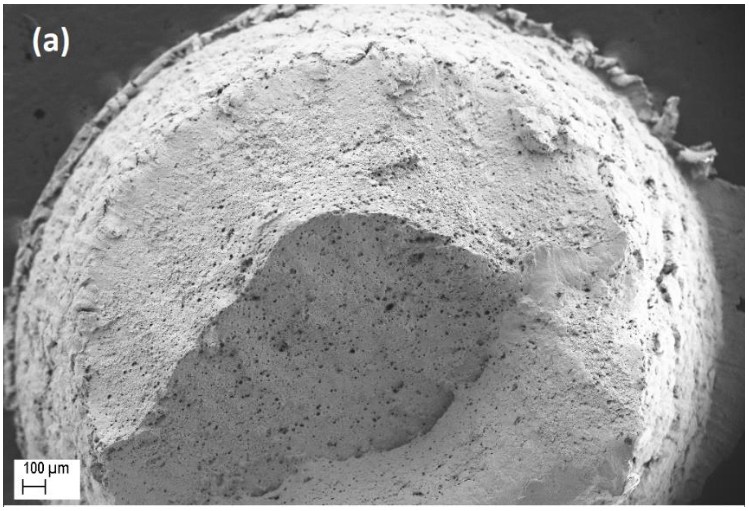

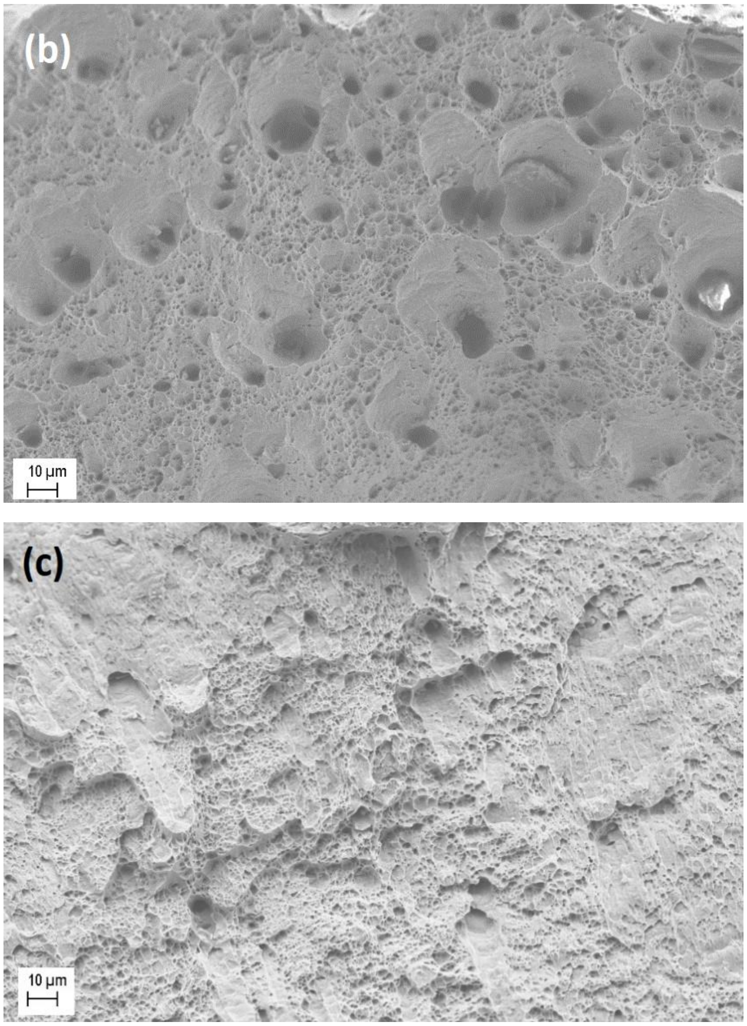

Figure 4.8. SEM images of the fracture surface of the crept Alloy 709 specimen tested under an applied stress of 165 MPa at 700°C: a) Ductile transgranular fracture with b) dimple-like features from microvoid coalescence and c) the presence of shear lip towards the outer edges.

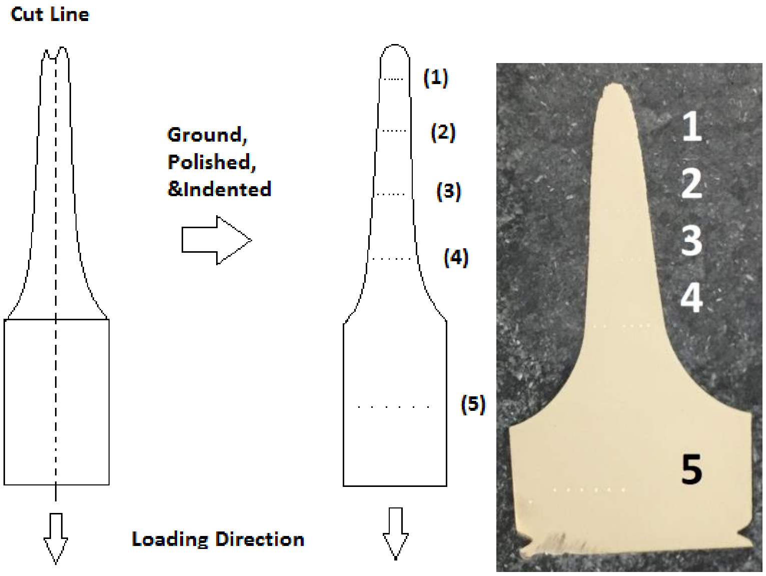

Figure 4.9. Schematic of the cut made on the crept specimen for hardness and microstructural analysis.

Six microindentations were taken to obtain average Vickers microhardness values at five different locations along the crept specimen section. Those microhardness values are listed in Table 4.4 along with the grain sizes measured from the corresponding optical micrographs.

Table 4.4. Vickers microhardness at the corresponding locations in Figure 4.9 for a crept Alloy 709 specimen (700 °C / 165 MPa).

Location Number	Section	Local True Strain $\ln(A_o/A)$	Vickers Hardness Number (VHN)	Average Grain Size (µm)
1	Gauge near fracture tip	1.4	246 ± 7	41.5
2	Gauge	0.9	230 ± 7	34.1
3	Gauge	0.6	219 ± 3	33.1
4	Gauge	0.2	211 ± 4	33.5
5	Grip	0	189 ± 8	34.0 (equiaxed)

After the microhardness values were obtained, the sample was polished again and electro-etched for optical microscopy and scanning electron microscopy (SEM). Optical microscopy revealed that the microhardness values increased with increasing grain size (Figure

4.10). The grains were the largest near the tip of the creep-ruptured specimen, but did show elongation and decreased with the smallest average grain size in the grip section. This suggests that the Hall-Petch relationship is not the main contributing factor for the increase in hardness but could still have an influence because of the elongated grains and the formation of subgrains shown in Figure 4.12. The grains in the gauge section were elongated in the strain direction while the grains in the grip section were equiaxed.

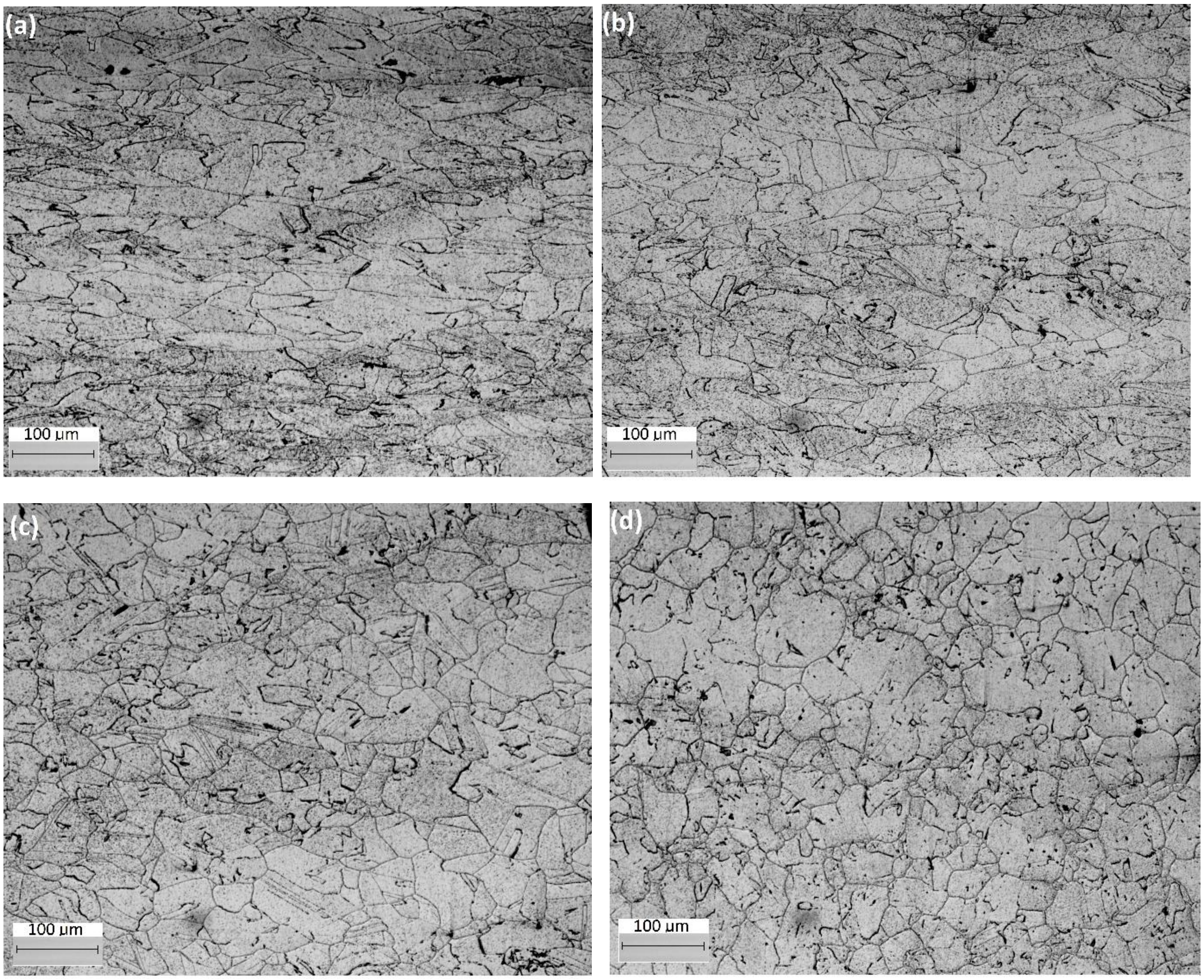

Figure 4.10. Optical micrographs of the crept Alloy 709 (700 °C / 165 MPa) specimen. (a) Corresponds to section 1 in Figure 2.9, (b) corresponds to section 2, (c) to section 3, and (d) to section 5 or the grip region.

The loading direction for Figure 4.10 is in the horizontal direction. It is also observed that the density of twins decreased from the as-received material after being exposed to 700°C. Both grip and gauge of the crept specimen are found to be decorated by grain boundary precipitates with dark contrast. Note that these precipitates are not cavities. Zhao et al. [4] reported the microstructural characteristics of a creep-rupture test conducted on NF709 alloy at 650 ^{o}C under an applied stress of 210 MPa for a total duration of 3,000 h. They also observed grain elongation along the applied stress direction and relatively equiaxed grains away from the fracture region similar to the present study. Furthermore, they also noted a hardness increase near the fracture region and the hardness falls while moving away from the gauge region toward the grip region.

C. Microstructural analysis of the crept specimen via EBSD and TEM

Both the grip and the gauge section of the crept (165 MPa / 700°C) specimen was cut perpendicularly to the loading direction and prepared for EBSD. The EBSD Euler maps as shown in Figure 4.11 revealed a more random variety of orientations in the grip section compared to   the crept gauge section. On the other hand, the grains were more aligned (i.e. the overall orientation spread became narrower) as evidenced by similarly color-coded domains that are also smaller in size. EBSD data were also analyzed to create grain boundary orientation maps as shown in Figure 4.12 from the same grip and gauge regions of the crept specimen. The EBSD map of grip region shows only a few low angle grain boundaries (2-15^{o}) along with the high angle grain boundaries. Conversely, the EBSD grain boundary angle map in the gauge region shows the presence of several low angle boundaries (<15^{o}) formed in the gauge section during creep deformation. The high density of these boundaries did not allow a good resolution of these boundaries. During creep, the whole specimen (including gauge and grip) was kept at about 700 ^{o}C for 1129 hours. The difference was that the gauge section experienced effects of both temperature and stress while the grip section saw only the effect of temperature, for the same time duration. The appearance of subgrain boundaries during creep deformation occurring via dislocation climb creep have been noted in several studies of other austenitic stainless steels [14]. The EBSD maps were taken of the ND-TD direction in which the loading direciton of the creep test were in the rolling direction.

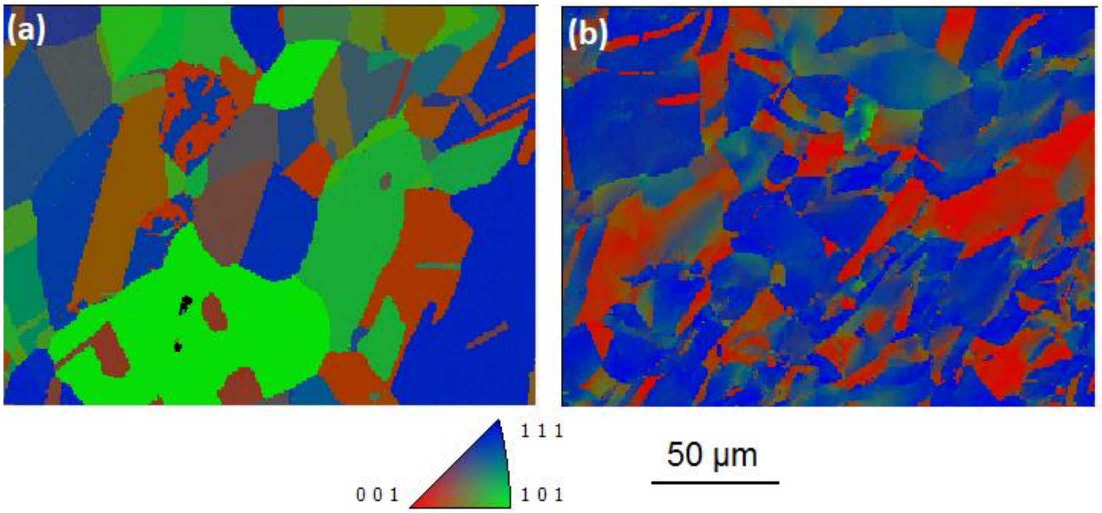

Figure 4.11. EBSD misorientation maps of the grip region (a) and gauge region (b) for the Alloy 709 specimen crept 165 MPa 700°C Alloy 709

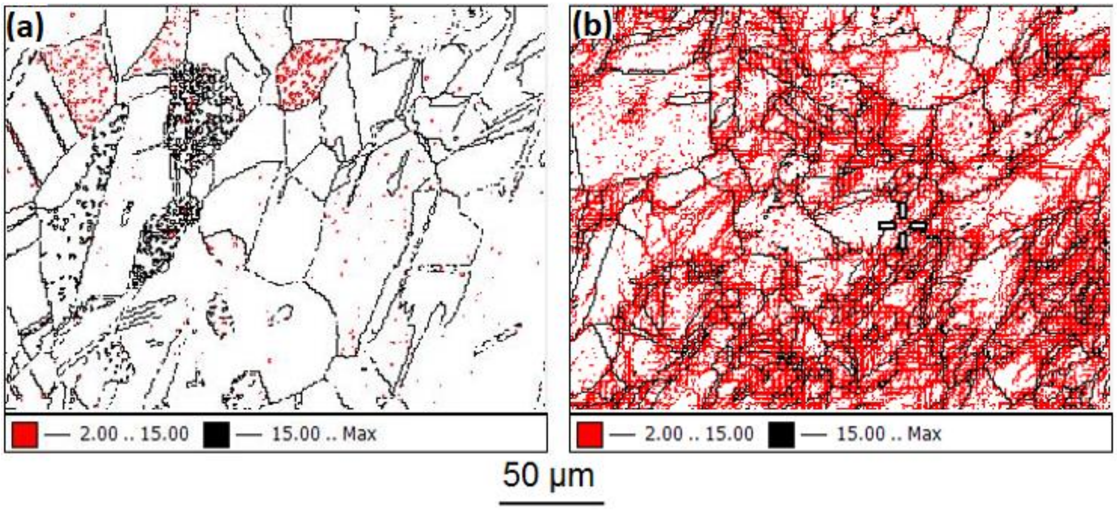

Figure 4.12. EBSD grain boundary angle maps of (a) the grip region and (b) the gauge region of the crept specimen (700°C / 165 MPa) of Alloy 709.

In order to further confirm these observations, TEM studies were performed on samples from both grip and gauge regions. Figure 4.13 (a) and (b) show bright field TEM images from the grip region of the crept sample. They do not show much activity of dislocations as can be expected of a statically annealed microstructure. In Figure 4.13 (b), one of the original twin boundaries in the microstructure could still be seen. However, in the gauge region as shown in Figure 4.14, the dislocation activity is quite evident. In both images 4.14 (a) and (b), formation of fine subgrains can be noted. It is important to recall that there was no such extensive formation of subgrains in the grip region of the crept specimen as well as the as-received Alloy 709 microstructure.

The grain size of the Alloy 709 is in the range of 30-40 μm, the fine grain-like structures (0.5-1.0 μm) observed in the TEM image (Figure 4.14) are indeed subgrains. These subgrains were formed more or less throughout the crept microstructure. Thus, it can be confirmed that the subgrains seen as shown in Figure 4.14 (b) were created because of the creep deformation. Also, the EBSD study discussed in the previous section already confirmed the presence of a high proportion of low angle boundaries. As subgrains have most of their boundaries composed by low angle boundaries which are essentially of low angle nature, confirming the observed high proportion of low angle boundaries by EBSD study in the previous section. Although annealing twins were not the focus of this study, they were all but gone in the gauge section under creep as noted by TEM as well as EBSD studies.

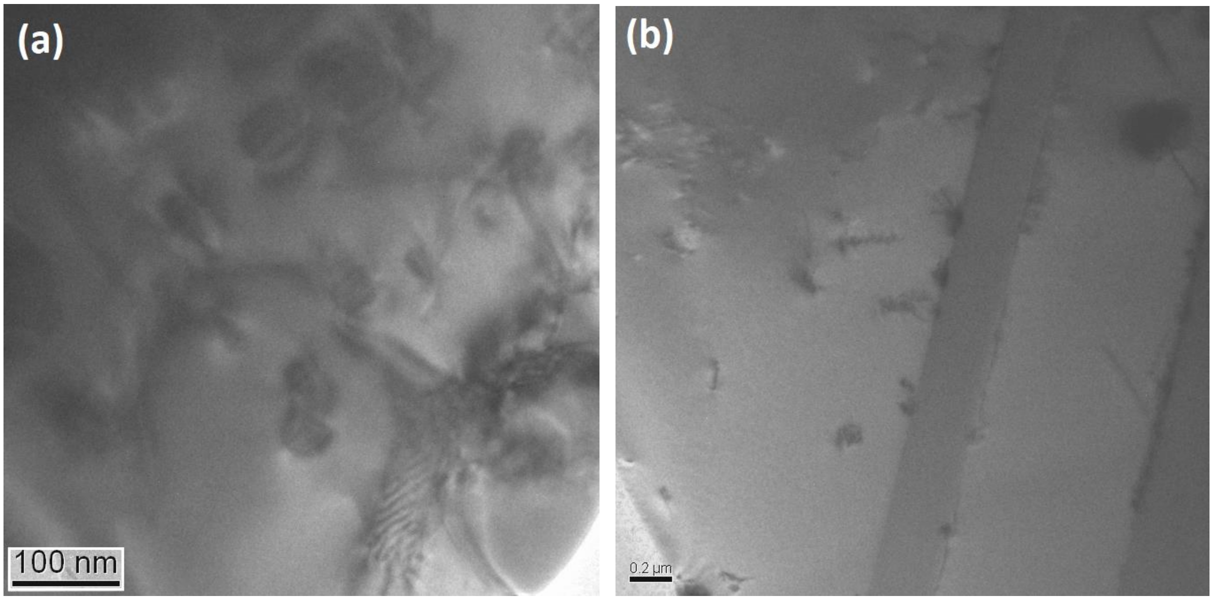

Figure 4.13. (a) and (b) Bright field TEM Image of the grip region of Alloy 709 crept at 700°C under an applied stress of 165 MPa.

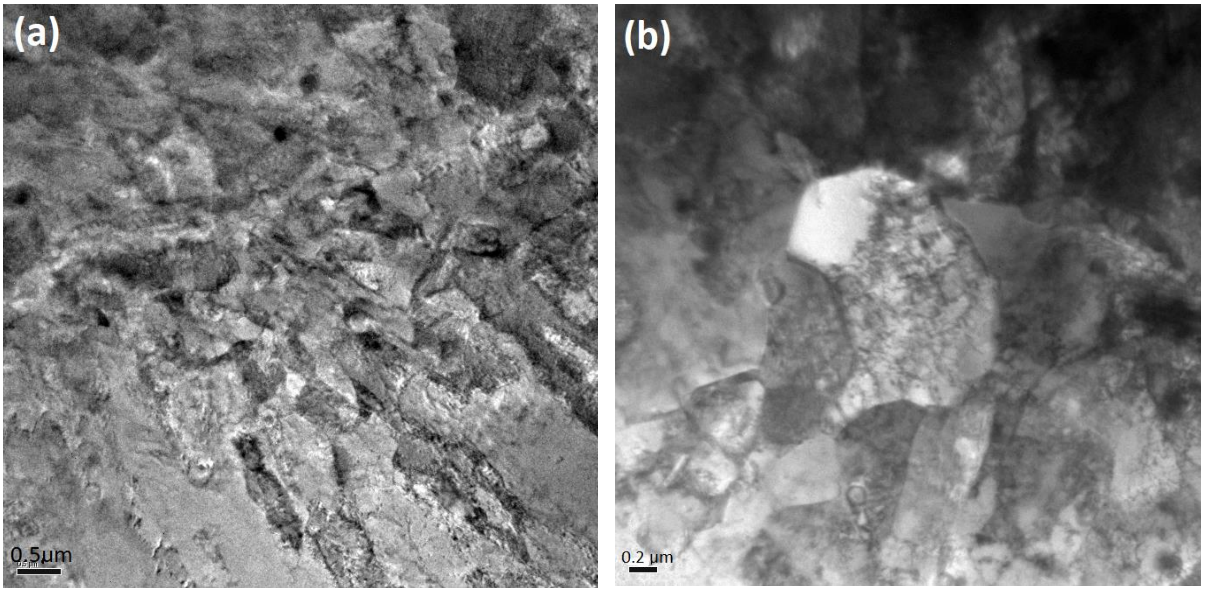

Figure 4.14. (a) and (b) Bright Field TEM images from the gauge section of Alloy 709 crept at a temperature of 700°C and an applied stress of 165 MPa.

The precipitates in the gauge region remained stable, especially the MX type precipitates. No G phase could be detected even though Zhang *et al.* [4] reported the presence of G phase in the crept NF709. However, their creep test temperature was lower at 650 ^{o}C but at the same temperature. Some precipitates formed on the grain and twin boundaries. These precipitates are most likely $M_{23}C_6$ type given that the starting material was in the solution annealed (1100 ^{o}C) condition; upon high temperature exposure these precipitates started to form preferentially on the grain boundaries and to some extent on twin boundaries.

Thermo-Calc^{TM} calculations were used to predict the presence of various precipitates and their amounts (in mole fraction and volume fraction) in Alloy 709 as a function of temperature shown in Figure 4.15. At 550°C, it is expected to see $M_{23}C_6$, MX, Z phase, and σ phase while at 700°C the mole fraction of σ phase decreases significantly. The σ phase is known to be detrimental for creep properties. However, studies suggest it fully forms after longer aging times (2,500 to 6,000 hours) [1, 15]. Future creep studies will be done on aged Alloy 709 based on the Thermo-Calc^{TM} results along with thermokinetics results from TC-Prisma^{TM}.

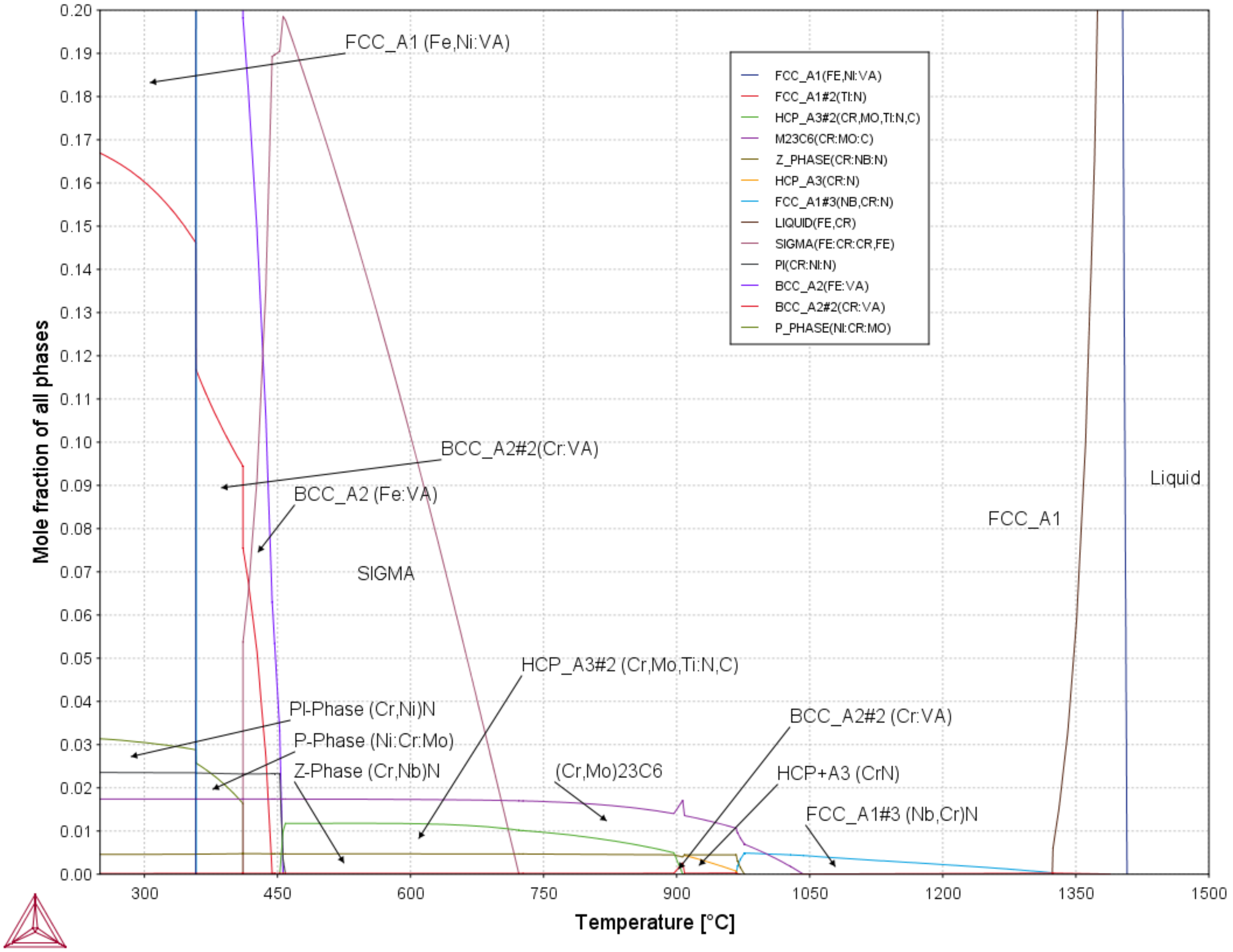

Figure 4.15. Thermo-Calc™ results of Alloy 709.

D. Relationship of substructural evolution and creep behavior

Subgrain formation is often found to accompany the traditional mechanisms such as recovery creep in the five power law creep regime [16]. During five-power creep new dislocations are generated and they rearrange themselves into low energy configurations because of long range stress fields between the dislocations. Additionally, the in-situ annihilation process where unlike dislocations get annihilated leaving dislocations of similar character left. These low energy configurations could be dislocation tangles, cell boundaries or subgrain boundaries. It has been determined from the TEM and EBSD studies that these low energy configurations of dislocation walls observed in the crept microstructure are essentially subgrain boundaries in the current study.

It is well established that the subgrain size is inversely related to the stress. Many studies developed a relation between the subgrain size (λ) and flow stress (σ) as shown in the following relation:

$$\lambda = \frac{BGb}{\sigma} \tag{4.2}$$

where b is the Burger's vector, G is the shear modulus of the material and B is a material-specific constant that is approximately 10 for many materials. There is an empirical relation between the applied stress (σ) and subgrain size (λ) under the steady state creep as shown below [17]:

$$\lambda = 10b\left(\frac{\sigma}{G}\right)^{-1} \tag{4.3}$$

At higher $\frac{\sigma}{G}$ values, the deformation mechanism changes causing the subgrain size dependence to change. However, this is not considered here as we could not discern any change in creep mechanism within the range of test conditions in the present study.

The magnitude of 'b' can be calculated from the lattice parameter (a) determined from the X-ray diffraction (XRD) pattern of the Alloy 709, assuming perfect dislocations of $a/2$ <110> type (Alloy 709 matrix having FCC lattice), the magnitude of 'b' is calculated. Then the elastic modulus (E) at 700 ^{o}C is taken as 148.9 GPa using material data sheet from Nippon Steel for NF709, and the shear modulus (G) is calculated using the following relation:

$$G = \frac{E}{2(1+\nu)} \tag{4.4}$$

where ν is the Poisson ratio (here taken as 0.33).

Now inputting G as 57,270 MPa, b of 0.253 nm (as obtained in the appendix) and σ value (165 MPa) in equation (4.2), the average subgrain size (λ) is calculated to be ~0.9 μm.

$$\lambda = \frac{10Gb}{\sigma} = \frac{10(57{,}270\ \text{MPa})(0.253\ nm)}{165\ \text{MPa}} = 0.878\ \text{nm} = \sim 0.9\ \mu\text{m} \tag{4.5}$$

Interestingly, the mean subgrain size measured from the TEM images of the crept specimen (700 ^{o}C / 165 MPa) was between 0.6 to 1 μm, which matches well with the predicted value from the above analysis. More microstructural examination of the other crept specimens may provide further information on the dependence of the subgrain size on the applied stress.

In the above analysis, the 'B' value is taken as 10. However, 'B' is a material-dependent constant and is found to vary depending on the stacking fault energy (SFE) with a smaller SFE giving a smaller 'B' value and vice-versa. However, further studies will be necessary to ascertain this variation.

4.4. Conclusions

This chapter reported the results and analyses of a preliminary investigation of the creep behavior of Alloy 709 that is currently being considered for use as a structural material for the sodium fast reactor. The following observations and conclusions were made:

- At 700°C, Alloy 709 experienced slight dynamic strain aging with a yield strength of around 180 MPa and an ultimate tensile strength of about 450 MPa.
- Accelerated creep tests at 700 °C showed a brief primary, short secondary, and long tertiary zone.
- Norton plots of the creep tests resulted in a stress exponent of ~6, suggesting the most likely rate-controlling creep mechanism to be dislocation climb. However, further creep test data is needed to unambiguously determine the operating micro-mechanism.
- Ductile transgranular fracture surfaces were observed by SEM with dimple-like features from microvoid coalescence. However, the optical microscopy of the longitudinal cross-section did not reveal any cavitation or cracking away from the fracture tip, implying that most of the damage was concentrated in the immediate vicinity of the fracture tip.
- Although optical microscopy did not show subgrain formation, cross sectional results from the EBSD showed low angle grain boundaries (<15°) forming in the gauge section of the 700°C 165 MPa crept specimen. Orientation maps from the EBSD showed significant grain alignment in the gauge section compared to the grip section.
- TEM results confirms subgrain growth and also shows a decrease in precipitates in the gauge section compared to the grip.
- Thermo-Calc was used to find the phases present and will be used for future creep studies on aged Alloy 709.

4.5 References

[1] T. Sourmail and H. K. D. H. Bhadeshia, “Microstructural evolution in two variants of NF709 at 1023 and 1073 K,” Metall. Mater. Trans. A, vol. 36, no. 1, pp. 23–34, 2005.

[2] P. J. Maziasz et al., “Improved creep-resistance of austenitic stainless steel for compact gas turbine recuperators,” Mater. High Temp., vol. 16, no. 4, pp. 207–212, 1999.

[3] E. Isaac Samuel, B. K. Choudhary, D. P. Rao Palaparti, and M. D. Mathew, “Creep deformation and rupture behaviour of P92 steel at 923 K,” Procedia Eng., vol. 55, pp. 64–69, 2013.

[4] Y. Zhao, J. Zhao, and X. Li, “Microstructural evolution and change in hardness during creep of NF709 austenitic stainless steel,” Acta Metall. Sin. (English Lett., vol. 24, no. 3, pp. 220–224, 2011.

[5] M. Ivanchenko, “Dynamic Strain Aging of Austenitic Stainless Steels and Ni Base Alloys,” AAlto University, 2010.

[6] S. Sham, “Advanced Reactor Concepts Program ARC Materials Development - Accomplishments and Plans,” 2013.

[7] G. Filacchioni, “Tensile and creep behavior of a new family of austenitic alloys: the double stabalized stainless steels,” Mater. Nucl. React. Core Appl., vol. 1, pp. 191–198, 1987.

[8] “Nippon steel material data sheet NF709,” Nippon STEEL SUMITOMO Met. Corp., pp. 10–12, 2013.

[9] S. Monteiro Neves, F. Santos, W. Anacleto, and L. Paulo, “Creep Parameters and Dislocation Substructure in AISI 316 Austenitic Stainless Steel from 600oC to 800oC,” Mater. Res., no. 1, pp. 1–5, 2017.

[10] L. Kloc and J. Fiala, “Viscous creep in metals at intermediate temperatures,” Kov. Mater, vol. 43, no. 2, pp. 105 – 112, 2005.

[11] S. Spiragelli, “Constitutive equation for recovery controlled creep in the austenitic stainless steel X6 CrNiNb 18 11,” La Metall. Ital., vol. 88, no. 8, pp. 530–535, 1996.

[12] K. Milicka, “Dislocation creep of austenitic stainless steels Part 1. Stress and temperature dependences of steady state creep,” Acta Tech., vol. 34, no. 3, pp. 300–318, 1989.

[13] A. S. Alomari, N. Kumar, and K. L. Murty, “Investigation on Creep Mechanisms of Alloy 709,” ASME 2017 Nucl. Forum, p. V009T02A003, 2017.

[14] R. Zauter, F. Petry, H.-J. Christ, and H. Mughrabi, “High temperature creep behaviour and microstructure development of AISI 304L stainless steel,” *Mater. Sci. Eng. A*, vol. 124, no. 2, pp. 125–132, 1990.

[15] C.-C. Hsieh and W. Wu, “Overview of Intermetallic Sigma Phase Precipitation in Stainless Steels,” ISRN Metall., vol. 2012, no. 4, pp. 1–16, 2012.

[16] M. E. Kassner, Fundamentals of Creep in Metals and Alloys Five-Power-Law Creep, Second Edi. Elsevier Ltd., 2008.

[17] O. D. Sherby, R. H. Klundt, and A. K. Miller, “Flow stress, subgrain size and subgrain stability at elevated temperature,” Metal. Trans., vol. 8A, pp. 843–850, 1977.

5. EXPERIMENTAL APPARATUS

5.1. Overview

In order to perform creep-fatigue crack growth and fatigue crack growth experiments at elevated temperature, a sophisticated experimental facility is required. The test specimen must be heated to the desired temperature and held at that temperature for a significant duration of time, the load line displacement of the specimen must be measured accurately to assess the fatigue and creep contributions to crack growth, and the crack length must be measured accurately during this process such that the proper calculations can be made. An experimental testing apparatus has been developed to meet these needs and preliminary experiments have been performed to validate the experimental apparatus.

This chapter summarizes the development and assessment of an experimental testing apparatus developed in the Mechanical Engineering Department at the University of Idaho. The testing apparatus used to perform creep-fatigue crack growth testing of an advanced stainless steel Alloy 709. The experimental testing of this material is an integral part of the DOE-NEUP project “Characterization of Creep-Fatigue Crack Growth in Alloy 709 and Prediction of Service Lives in Nuclear Reactor Components.” The major components of the apparatus include the testing frame, direct current potential drop (DCPD) system, high temperature extensometer, furnace and peripheral components, and data acquisition system. Each major component is reviewed below.

An overview of the experimental testing facility is shown in Figure 5.1. A servo-hydraulic MTS Model 312.21 test frame is outfitted with a TestStar II controller. The TestStar II controller includes a function generator and a number of software packages are available to perform the desired experiments. Testware SX is a program that is used to create the desired testing profile (waveform) for the creep-fatigue crack growth tests. Proportional–integral–derivative (PID) controller settings have been adjusted on the test frame to match the compliance of the system so that the required loads and displacements are met. Loads are measured using an MTS model 661.21 Load cell, the output from which is calibrated and recorded using the TestStar II Controller.

5.2. DCPD System

A direct current potential drop (DCPD) system has been developed in order to provide crack length measurement. This method of crack length measurement is recommended in ASTM E2760 for creep-fatigue crack growth testing. The system consists of a Keithley 2182A nanovoltmeter, a Keithley 2280S-32-6 current supply, and nichrome connecting wires that are spot welded to the specimen.

The DCPD system measures change in crack length by supplying a constant electrical current across the compact tension specimen. Due to electrical resistance in the specimen there is a voltage drop across the specimen that can be measured by a voltmeter as shown by the schematic in Figure 5.2. As a crack propagates the voltage drop increases. Once initial and final crack length are known a correlation can be made between crack length and the measured voltage drop.

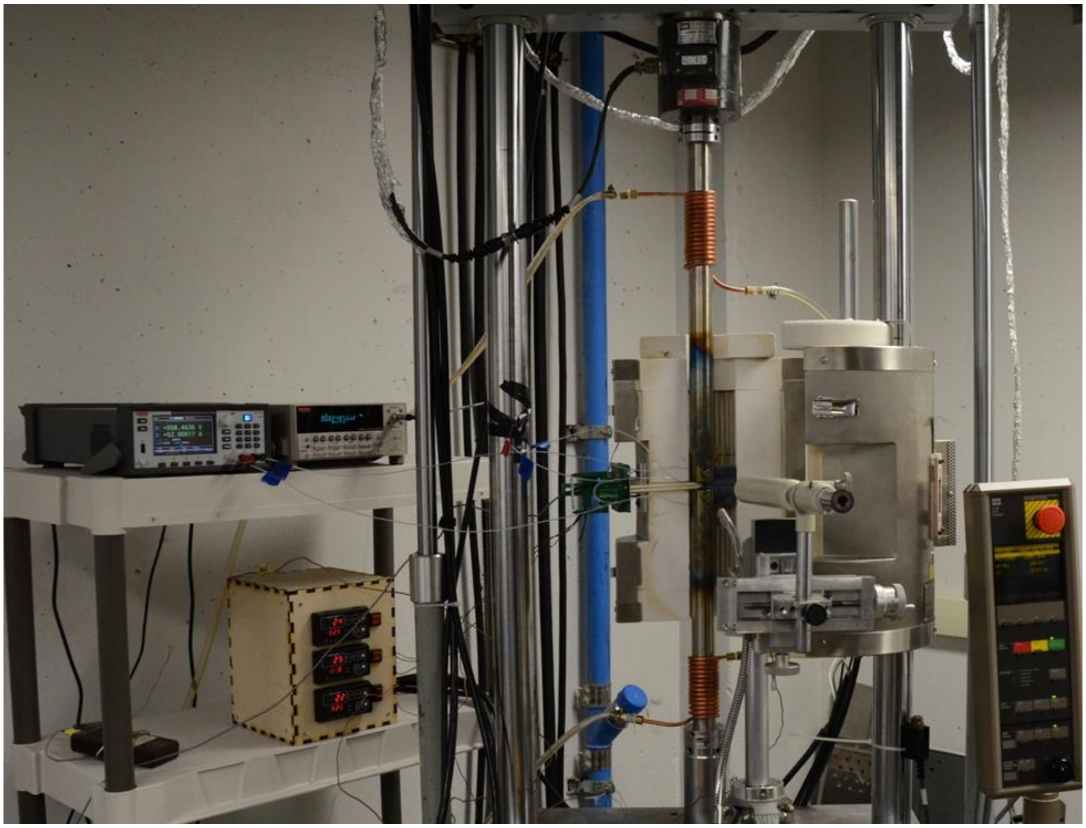

Figure 5.1. Experimental apparatus for creep-fatigue crack growth at elevated temperatures.

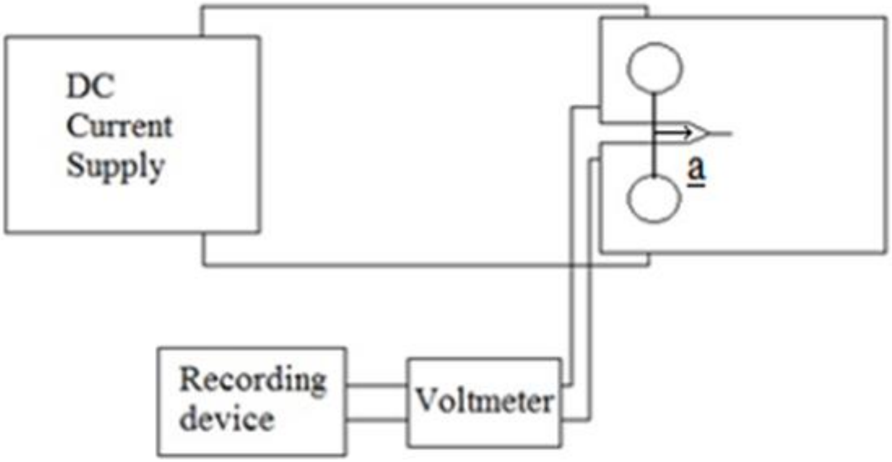

Figure 5.2. Schematic of a DCPD system.

A Keithley 2280S-32-6 current supply was chosen for the DCPD system because it supplies a very stable current source. Verification of the input current at 2 Amps showed a deviation from the set current less than ±0.1 mA. A current input of 2 amps was chosen allowing a suitable voltage output range without causing excessive heating of the wires.
Voltage output from the specimen as part of the DCPD system is measured and recorded using a Keithley 2182A nanovoltmeter, which was chosen for its stable voltage output down to the nanovolt scale. Voltage measurements recorded at room temperature showed there was minimal noise. A typical data set recorded by the nanovoltmeter during a fatigue test is shown in Figure 5.3.

Nichrome wire is used for both the current source and nanovoltmeter on account of its durability and stability at elevated temperature. 26-gauge wire is used for the nanovoltmeter, and 22 gauge wire is used for the current supply as a thicker wire is necessary for the input current. Performance of the DCPD was verified through a system of tests performed on 316 stainless steel. It was determined that a linear relationship was observed between voltage drop and crack length where 1 µV corresponded to approximately 60 µm of crack growth when 2 amps were supplied. Preliminary evaluation of the DCPD system at 625 °C showed a noise level of less than ± 0.15 µV, which correlated to a crack extension of less than ±0.009 mm (well below that suggested in ASTM E2760 of at least ±0.1 mm).

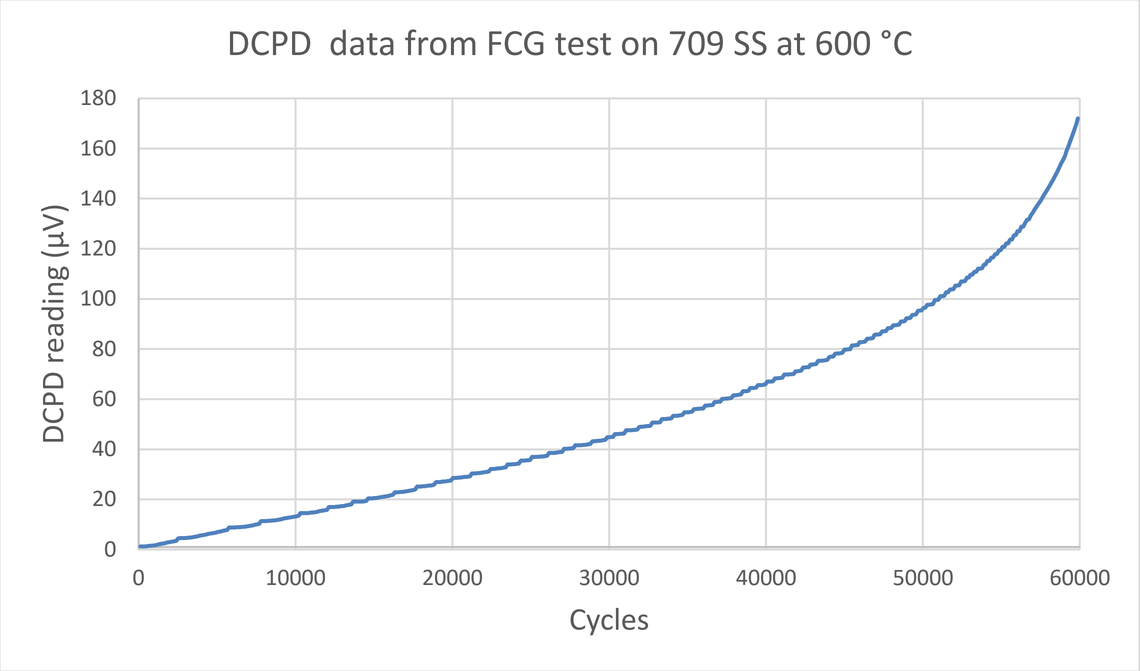

Figure 5.3. DCPD data from a high temperature fatigue crack growth (FCG) test.

5.3. Epsilon 3548COD High Temperature Extensometer

An Epsilon 3548COD-005-025M-ST extensometer was integrated into the system to measure load line displacement of the specimen as well as to confirm crack length during crack growth. The extensometer is positioned within a mounting device located outside of the furnace. The extensometer utilizes 150 mm long ceramic arms which pass through a small opening in the side of the furnace. Excitation voltage is provided by the Epsilon DSCUSB, a device that connects to a desktop computer and is also used for data acquisition.

Initial evaluation of the extensometer showed that noise level increased as temperature increased, from approximately ±0.2 µm at 20 °C to approximately ±3 µm at 700 °C. This was primarily attributed to thermal noise causing expansion and contraction of the ceramic arms, as well as the furnace, which the extensometer was mounted on. Noise level for the extensometer was reduced to roughly ±1.5 µm at 700 °C by mounting the extensometer directly to the load frame column as shown in the right picture of Figure 5.4, and by adjusting the vertical position of the extensometer such that the arms are perpendicular to the load line.

4a 4b

Figure 5.4. Extensometer mounting. (4a) original frame mounting, (4b) modified frame mounting

In order to verify the performance and calibration of both the DCPD system and extensometer, a fatigue crack growth test was performed using both devices. Crack length measured visually by a traveling microscope was compared to crack length calculated by compliance of the specimen measured by the extensometer and crack length measured by the DCPD. Results of this test, presented in Figure 5.5, showed that there is a linear relationship between DCPD reading and crack length.

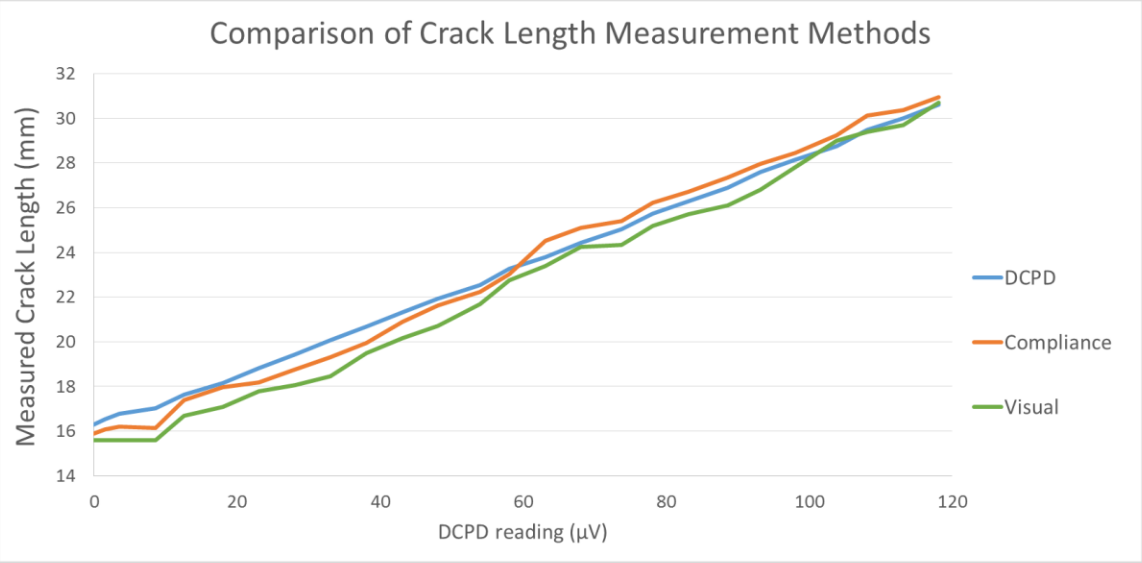

Figure 5.5. Three methods of crack length measurement for a fatigue test.

5.4. Furnace and Temperature Control

An ATS series 3210 three zone split tube furnace, shown in Figure 5.6, was coupled to the MTS test frame. This furnace is capable of operating up to 1200 °C. Tests showed that temperature measurements on a CT specimen in several locations, including above and below the crack plane and near the end of the crack, maintained a temperature of ±2 °C at 625 °C. An existing viewing window on the furnace was expanded by replacing a heating element in order to allow the operator to monitor and observe crack growth of the CT specimen, as the window was originally only 12 mm wide. Specimen grips were machined from Inconel 718 rods, and cooling jackets made of copper tubing were positioned above and below the furnace on the grips to minimize heat conducted to the load cell and linear variable differential transducer (LVDT).

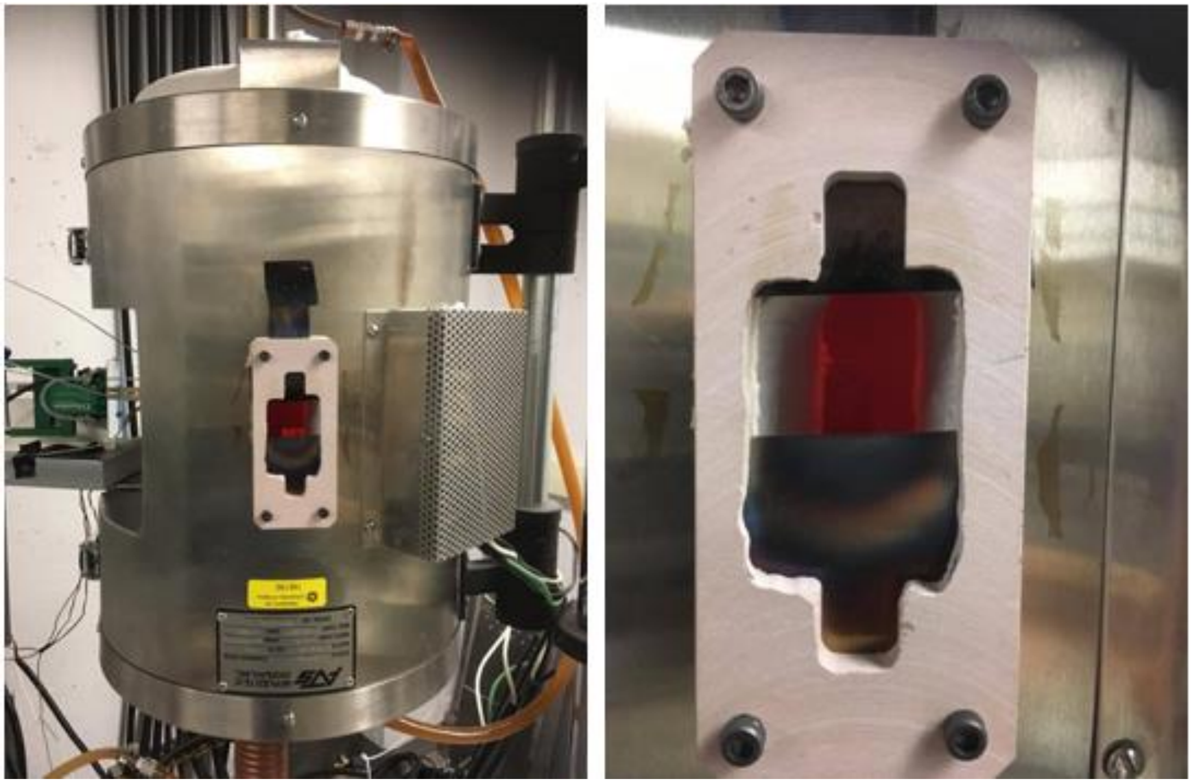

Figure 5.6. ATS furnace with expanded viewing window.

A three-zone temperature control unit was constructed using Watlow Series 981 temperature controllers and Watlow SSR-240-25A-DC1 solid state relays. The temperature in the top and bottom zones of the furnace are controlled using thermocouples located in the walls of the furnace, while the temperature for the middle zone is controlled using a thermocouple spot-welded to the specimen as outlined in ASTM E2760. It was determined that by setting the upper and lower zones of the furnace 75°C below the middle zone where the specimen is located, a constant temperature of the specimen was maintained within ±1 °C of the set point. This also minimized fluctuations in the DCPD and extensometer readings as a result of thermal noise.

5.5. Specimens/Material

The specimen geometry, shown in Figure 5.7, is in accordance with ASTM E2760 for creep-fatigue crack growth testing. The width, W, was chosen at 50 mm. The specimen thickness, B, is 12.5 mm, giving a W/B ratio for the CT specimen to be 4 as recommended in ASTM E2760. Side grooves were machined using a 60° V notch to a depth of 10% of the total width on each side to minimize out of plane cracking as suggested in the standard. However, after a number of tests performed on 316 SS specimens produced asymmetric cracking, the side groove depth was reduced to 4% on each side. This resulted in a more consistent and uniform crack front, as shown in Figure 5.8.

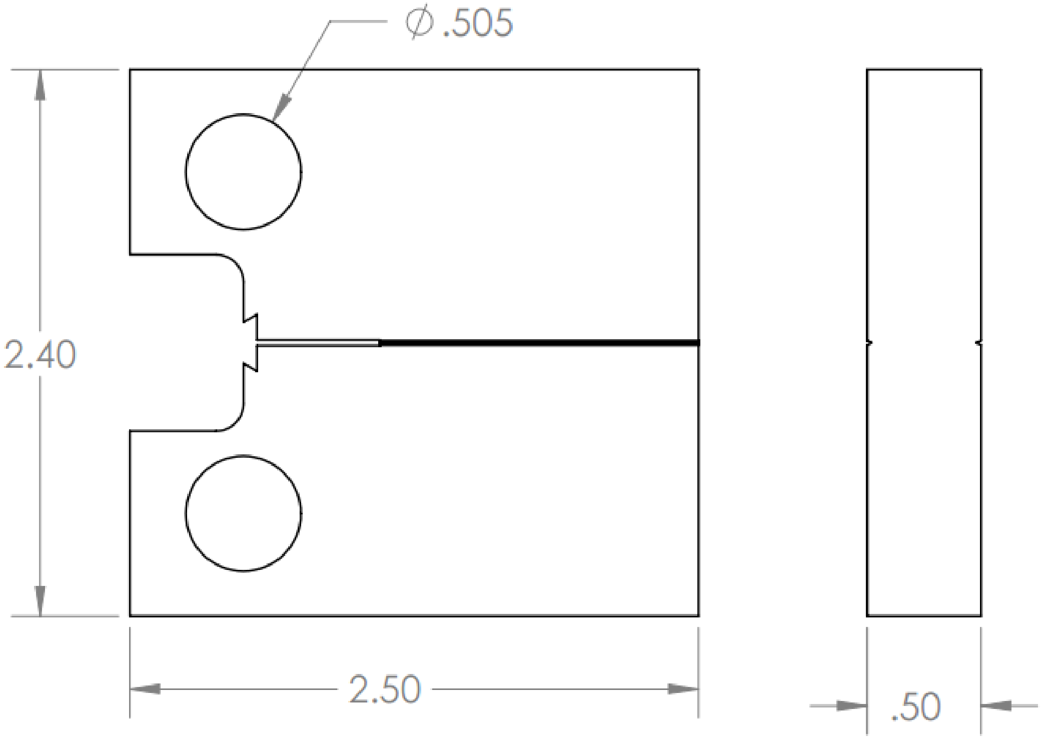

Figure 5.7. Specimen Geometry (All dimensions are in inches).

Three CT specimens were machined from the initial 709 bar, as shown in Figure 5.9. From the second bar, 16 CT specimens were machined, as shown in Figure 5.10. The thickness of the second bar was approximately 30 mm, thus two specimens were machined from the given thickness. It is anticipated that tensile and creep specimens will be machined out of pieces A, B, C, D, and E as shown in the figure.

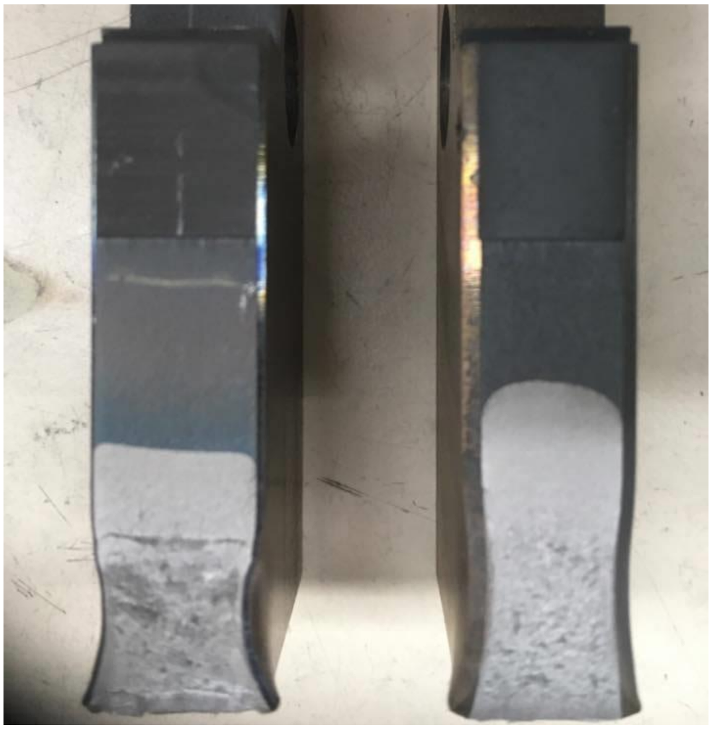

Figure 5.8. Crack front with 4% side groove (left) and 10% side groove (right).

Figure 5.9. First Bar of Alloy 709 provided by ORNL.

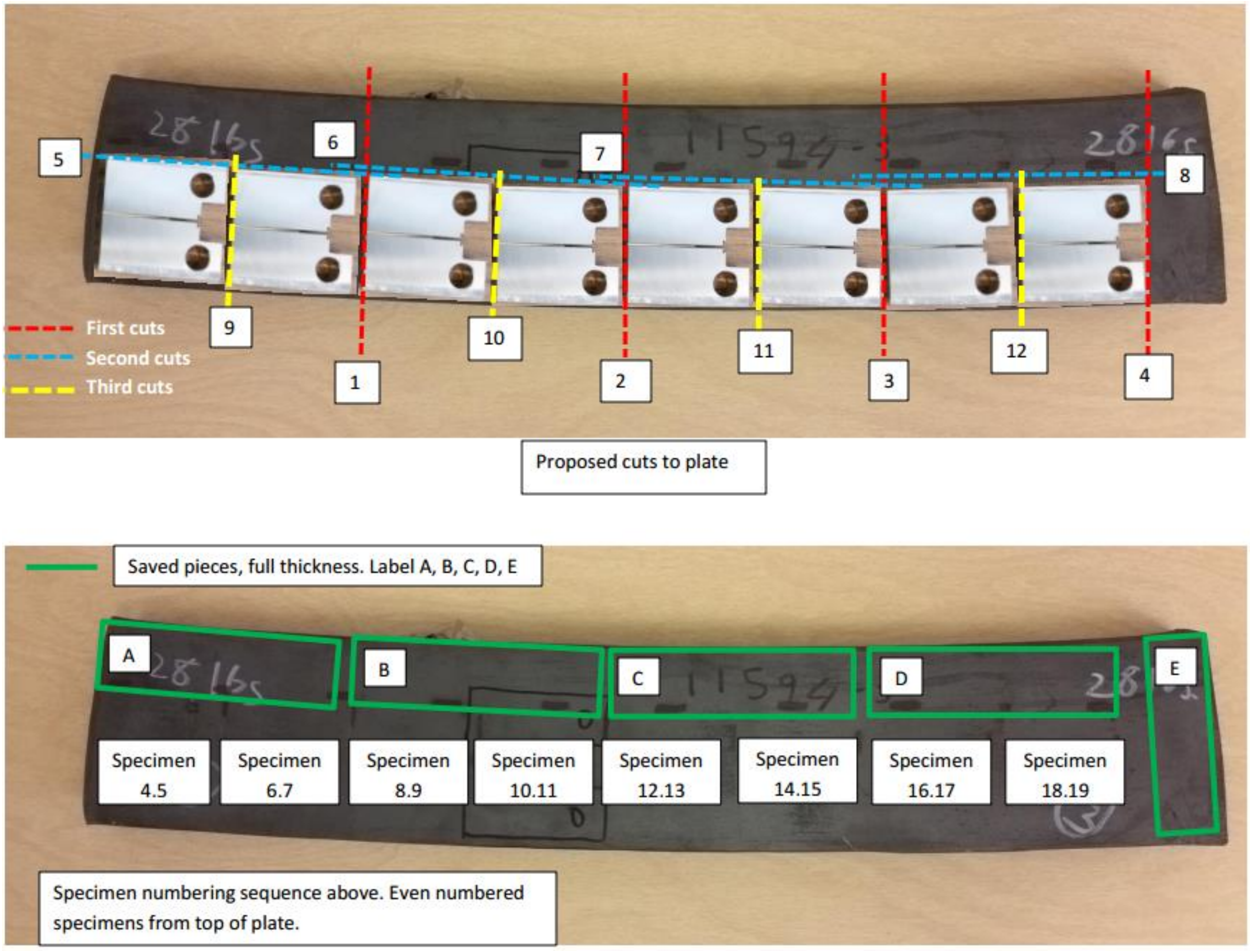

Figure 5.10. Second Bar of Alloy 709 provided by ORNL.

5.6. Data Acquisition

Data output from both the extensometer and the DCPD system are collected by an Asus M32 series desktop. The extensometer output is collected and calibrated by the DSCUSB program provided by Epsilon and streamed into an excel file, along with the time the data are collected. The DSCUSB program also shows the extensometer reading in real time. Using LabVIEW the nanovoltmeter can be programmed to collect up to 1024 data points at a time interval and store this voltage data in its buffer. Once the data is collected in the buffer the LabVIEW program can be used to export the data to an excel file.

5.7. Protocol for performing a typical creep-fatigue crack growth experiment

The following steps summarize the general protocol used to perform a typical creep-fatigue crack growth or fatigue crack growth test.

1. Use etching pen to roughen the area on the specimen where DCPD wires are to be spot welded.
2. Mount the specimen in the test frame such that the notch faces the extensometer.
3. Spot weld the wires onto the appropriate locations on the specimen, use approximately setting 18 for nanovoltmeter, setting 35 for Current Supply, and setting 23 for thermocouple wires.
4. Run pre-crack at room temperature, note that 12 µV is approximately equal to 1 mm of crack growth.
5. Make sure extensometer arms are free to move and not jammed, and that the extensometer is loose in its mounting to prevent damage.
6. Turn on cooling water.
7. Close furnace taking care not to short or damage DCPD wires.
8. Close windows and insulate around load train.
9. Set PID settings to P=15 I=3 D=.015 F=0 for tests with hold times. For tests without hold times use P=1.71 I=.3 D=0 F=0.
10. Flip switches on the temperature control unit to begin heating up system, make sure that the top and bottom zone are set to 75 °C less than the center zone, which should be set at the test temperature.
11. Wait three hours after furnace has reached temperature to begin test.
12. Adjust extensometer so that arms are perpendicular to specimen. Push extensometer forward until it contacts the specimen, back it out about 1 or 2 mm, make sure arms can open and close freely, tighten all mounting screws.
13. Set Interlocks for load at -1000 N and 9999 N. Set Interlocks for LVDT at 1 mm below and 2 mm above wherever LVDT is at when hydraulics are off.
14. Before starting test check to confirm that the DCPD and extensometer are behaving as they should. DCPD shouldn’t have more than about a 150 nV change, and the extensometer shouldn’t have more than about a 10 µm change.
15. Start DCPD in accordance with its own procedure. Set DCPD such that it will complete within a day. Make a note of when DCPD was started. Restart DCPD as needed throughout the test.

16. Check Testware SX procedure to make sure the loads and hold times are correct. If using the function generator make sure enable compensator is on. Execute the Testware SX procedure.
17. Intermittently or constantly run extensometer as needed.
18. After running for four hours check how LVDT compares to where interlocks were set, adjust accordingly.
19. Once test has completed allow the specimen to cool down before running final fracture using function generator at the same loading as was used during the test.

6 CONSTITUTIVE EQUATION OF CREEP DEFORMATION IN ALLOY 709

6.1. Introduction

Alloy 709 is a 20Cr-25Ni austenitic stainless steel that is being considered for structural applications in sodium-cooled fast reactors. In this study, creep tests on Alloy 709 specimens were performed at temperatures of 600 °C and 700 °C under applied stresses in the range of 125 to 250 MPa. Additional creep tests were performed on thermally aged #1 sample (at 650 °C for 3 months) of Alloy 709. A stress exponent (*n*) of 6.7 was found for the tests performed at 600 °C, 5.9 at 700 °C, and 7.6 on the aged #1 crept at 700 °C was obtained from the Norton plots. The stress exponents found are within the range of 5-7 for the dislocation climb creep mechanism, so the threshold stress approach was not necessary to analyze the results. The creep behavior of Alloy 709 was described by the Bird-Mukherjee Dorn equation. Microstructural analyses were carried out for both as-received and crept specimens using optical microscopy, electron backscattered diffraction, and transmission electron microscopy.

Austenitic stainless steels are considered cost-effective materials if they have adequate high temperature oxidation and creep resistance for prolonged duration under service conditions [1]. Alloy 709 is a potential candidate material for structural applications in advanced nuclear reactors, particularly for sodium-cooled fast reactors (SFR). The steel has been down-selected from a list of other high temperature steels because of its superior high temperature properties including elevated temperature oxidation/corrosion resistance, creep strength, sodium compatibility and weldability [1]. A number of creep-resistant austenitic steels have been developed by modifying compositions of the 18/8 austenitic stainless steels. In 1980's, the 20Cr-25Ni based austenitic steel was developed for its creep-resistance in fossil fired power plants [2].

However, Alloy 709 was originally developed by Nippon Steel (Tokyo, Japan), as NF709. This steel has a composition close to ATI 20+25Nb^{TM}. These steels are based on the Fe-20Cr-25Ni (wt%) composition, and the alloy composition is tailored in such a way that the austenitic phase is stabilized. The austenitic phase (close packed structure) is generally considered better for creep resistance compared to BCC ferritic phase (more open structure). The high Ni in Alloy 709 content provides enhanced stability to the steel at elevated temperatures (albeit it makes the steel more expensive) whereas high Cr content provides excellent high temperature corrosion/oxidation resistance. There are only a few creep studies available in the open literature [3, 4]. While it is likely that components will need to serve at temperatures around 550 °C, it is important to understand the creep behavior of this material at different temperatures. However, fundamental information on the creep behavior of the alloy is still sparse.

In this chapter the microstructure of as-received and thermally aged Alloy 709 will be studied. Several creep tests on Alloy 709 at 600 and 700 °C will be considered in determining the creep mechanism of Alloy 709. The creep behavior is mainly studied by using the Bird-Mukherjee-Dorn (BMD) relation. Aged Alloy 709 was also crept at 700 °C and the minimum creep rates are used to compare the results with those of the as-received Alloy 709 and 316SS results.

6.2. Experimental

6.2.1. Material

Three plates of Alloy 709 were analyzed, and the chemical composition is shown in Table 6.5. The plates #1 and #2 were hot-processed (forged + rolled) and annealed at 1100 °C, followed by water quenching. The third plate had an argon-oxygen-decarburization (AOD) melt condition, then was hot-rolled and solution annealed at 1100 °C. It was then water jet cut to remove heat affected zones. The first two plates were then machined into creep specimens with a gauge length of 2.54 cm and a diameter of 0.635 cm. The third plate was sectioned into 1.52 × 1.52 × 10.16 cm sections, then placed in the furnace for a thermal aging of 3 months at 650°C. Post-aging, it was further machined into creep round specimens shown in Figure 6.1.

Table 6.5. The chemical composition of the three plates of Alloy 709.

Element	Plate #1	Plate #2	Plate #3
S	<0.001	0.0006	
C	0.063	0.078	0.07
Mn	0.88	0.9	0.91
Si	0.28	0.39	0.44
P	<0.005	<0.005	0.014
Cr	19.69	19.89	19.93
Ni	25	25.01	24.98
Mo	1.46	1.51	1.51
N	0.14	0.14	0.148
Nb	0.23	0.25	0.26
Ti	<0.01	<0.01	0.04
Cu			0.06
Co			0.02
Al			0.02
B	0.0022	0.0037	0.0045
Fe	52.2448	51.8183	51.5935

6.2.2. Microstructure characterization

Optical microscopy was performed on the as-received, aged #1, and crept sections of Alloy 709 specimens for the characterization of the grain structure. The samples were prepared by hot mounting, grinding and polishing to a 0.05 µm finish, and electro-etching for 6-15 s in 10% by mass oxalic acid. An Olympus PGM-3 light microscope with an attached digital camera was used to examine the microstructure and capture images.

More detailed images were captured using a Zeiss Supra 35 field emission gun scanning electron microscope (SEM) operated at an accelerating voltage of 10-15 kV primarily under secondary imaging mode. Energy dispersive spectroscopy (EDS) was used for identifying chemical compositions for precipitates and bulk material.

Further steps were taken to prepare samples for transmission electron microscopy (TEM) and electron backscatter diffraction (EBSD). The samples were ground and polished down to be less than 100 µm thick and were cut by a Gatan disk punch to obtain 3 mm disks. Then a Fischione twin-jet polisher was used to further reduce the thickness for TEM or remove the mechanical polishing layer for EBSD. A mixture of nitric acid (HNO_3) and methanol (CH_3OH) (1:9 ratio by vol.) was used as the electrolyte and the voltage used was 30 V to 35 V. Dry ice was used to keep temperature of the electrolytic bath close to -40 °C.

A JEOL 2010J transmission electron microscope (TEM) operated at an accelerating voltage of 200 kV was used to identify and study the characteristics of the second phase particles. Also, energy dispersive spectroscopy (EDS) system attached to the TEM was used to carry out compositional analysis.

EBSD was obtained using the same sample preparation process listed above for the TEM samples except for the electro-jet polishing that was done for a shorter duration as a sample perforation is not required for EBSD. The surface- prepared disks were placed in the Zeiss Supra 35 FEG-SEM with the QUASOR^{TM} EBSD system. The sample stage was set at an angle of 70° with a working distance of about 16.5 mm. The SEM was operated at an accelerating voltage of 20 kV and put on high current mode. A binning of 4 pixel × 4 pixel was used in this study to obtain high enough resolution in the EBSD maps created.

Creep tests were performed at 600 °C and 700 °C with applied stresses between 125 and 250 MPa using an Applied Test System (ATS) lever arm (20:1) creep tester. The ATS creep testing system is shown in Figure 6.2. The furnace was set to alarm if there was more than a 1 °C offset. The LVDT used were two Heidenhain ST-12 linear encoders that measured the gauge elongation with an accuracy of ± 0.2 µm.

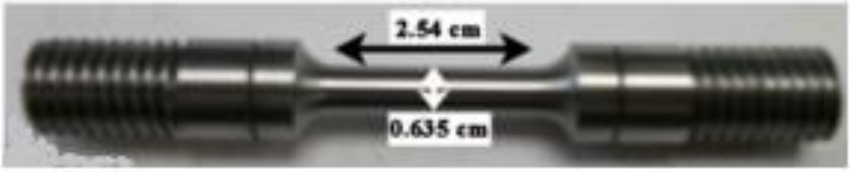

Figure 6.16. Creep test specimen geometry [5].

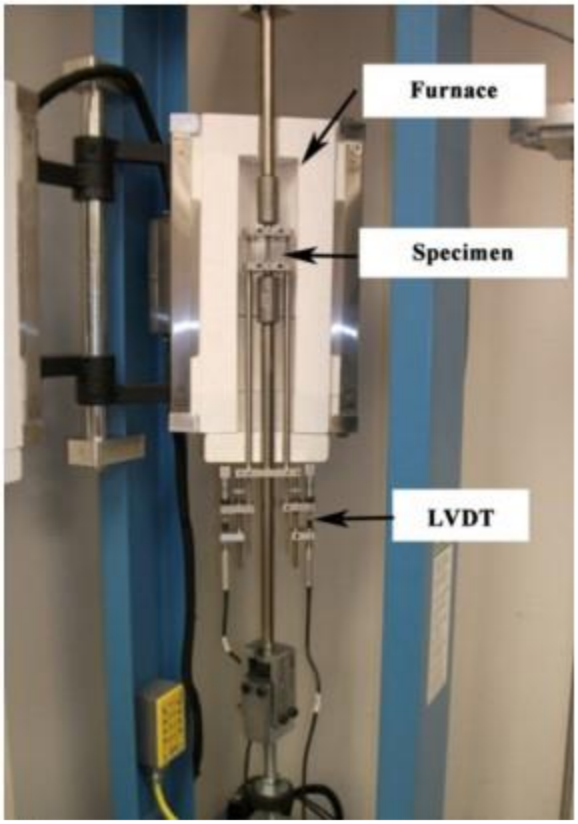

Figure 6.2. Uniaxial tensile creep tester with LVDT axial extensometer.

6.3. Results

6.3.1. Microstructural characteristics

The as-received microstructure of the bulk material is austenite (FCC) with grains sizes consistent on all three orthogonal planes that are 38 ±3 μm for the first plate and 37 ±2 μm for the second plate. The third plate had non-uniform grains with sections of larger grains similar to those found in the first two plates and other sections with much smaller grains. All three of the as-received plates showed the presence of twins.

For Alloy 709, one of the primary strengthening mechanisms comes from precipitation hardening. The as-received material for the first two plates has shown significant amounts of MX precipitates rich in Nb, as shown in Figure 6.3. These MX precipitates are beneficial for hardening the material and preventing dislocations from gliding under creep. M is typically Nb or Ti for Alloy 709 and X is N or C or (N, C) [6]. The specimens that were crept showed a significant increase of precipitate decorations on the grain boundaries.

Figure 6.3. SEM SE image showing Nb rich MX precipitates found in the as-received Alloy 709.

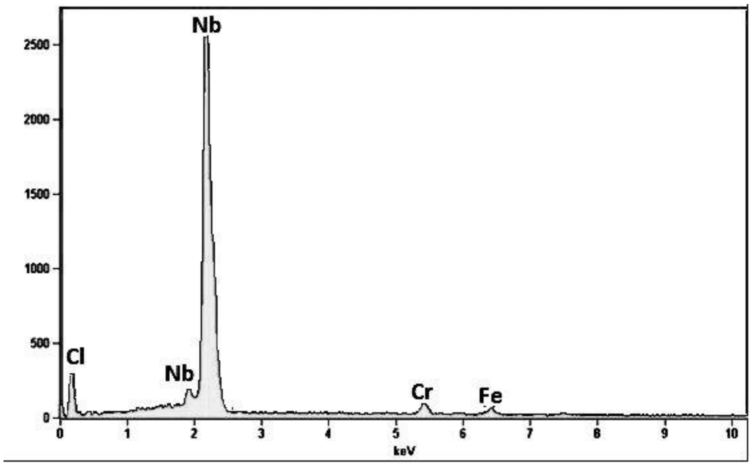

Figure 6.4. EDS spectra of the precipitate (plus marked) in Figure 6.3 showing a large Nb peak indicating it is a Nb rich MX precipitate.

$M_{23}C_6$ is a known precipitate that is often found on the grain boundaries in most stainless steels including NF709[6, 5]. For $M_{23}C_6$, the M typically stands for Cr but other elements like Fe and Mo can be present. In AISI 316 steel $M_{23}C_6$ has been found to have the form of $(Cr_{16}Fe_5Mo_2)C_6$ [7]. This precipitate composition depends heavily on the overall composition of the material and what is available (i.e., what is not already tied into a more stable precipitate). It is known that $M_{23}C_6$ phase dissolves at higher temperature. Given the original state of the as-received Alloy 709 was in solution annealed and quenched condition, $M_{23}C_6$ could not form in the as-received material. But as shown in Figure 6.5, thermally exposed grip part (i.e. without creep deformation) of a creep specimen did evolve to precipitate $M_{23}C_6$ carbide phases.

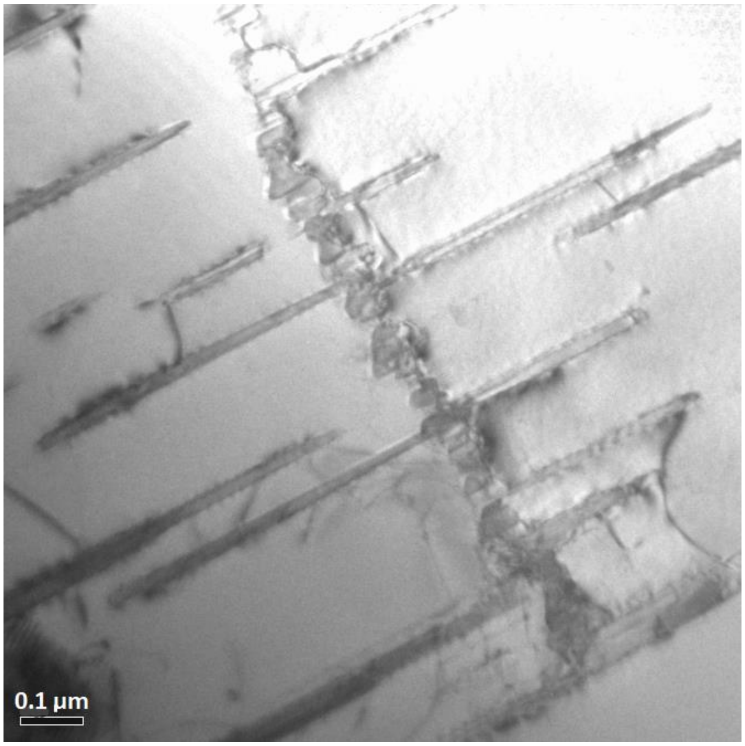

Figure 6.5. $M_{23}C_6$ plates form in the grip region of the 125 MPa crept specimen held at 700 °C for just under 3250 hr.

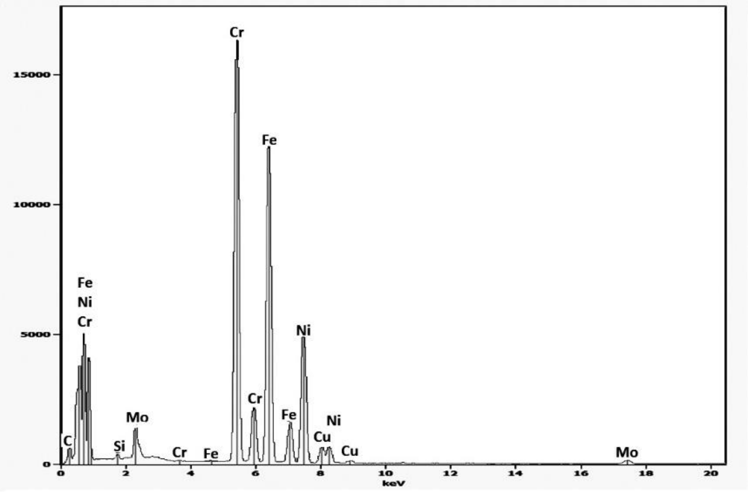

Figure 6.6. EDS spectra of the $M_{23}C_6$ plates shown above with high amounts of C, Cr, Fe, and Ni. Ni most likely present due to Ni in the matrix.

6.3.2. Creep properties

Creep is a time dependent plastic deformation that is generally observed at high homologous temperatures (0.4-0.5T_m or above). Alloy 709 is likely to reach temperatures where creep becomes a dominate mechanism of failure in SFRs. A typical creep curve of as-received specimen of Alloy 709 tested at 700 °C and 165 MPa is shown in Figure 6.7 (a) with the corresponding variation of creep rate versus time shown in Figure 6.7 (b).

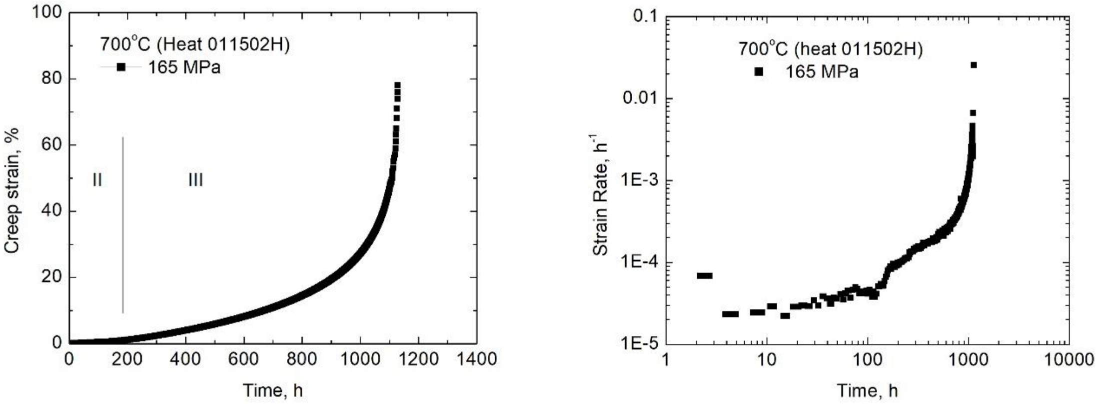

Figure 6.7. (a) Creep strain % with time showing no primary, short secondary (II) and an extended tertiary (III), (b) strain rate with time showing a minimum creep rate of around 4x10^{-5} h^{-1}.

The majority of the creep curves at 700°C showed a very brief primary creep, insignificant secondary and an extended tertiary creep. However, this was no longer the case for stresses at or below 125 MPa at 700°C or for the stresses applied at 600°C.

6.4. Discussion

Thermally-activated diffusion-assisted creep deformation can often be described by the Bird-Mukherjee-Dorn (BMD) equation [5] as

$$\dot{\varepsilon} = A\frac{DEb}{kT}\left(\frac{\sigma}{E}\right)^{n}\left(\frac{b}{d}\right)^{p} \tag{6.1}$$

where $\dot{\varepsilon}$ is the steady state strain rate (or minimum creep rate), σ the applied stress, d the grain diameter, A the material dependent constant depending on the operating mechanism, E the elastic modulus, b the Burgers vector, k the Boltzmann's constant (1.38x10^{-23} J/K) , n is the stress exponent, p is the inverse grain size exponent, and D the diffusivity which is described by the equation:

$$D = D_o exp(-Q/RT) \tag{6.2}$$

where D_o is the pre-exponential constant also known as the frequency factor, Q the appropriate activation energy, R the universal gas constant (8.31 J/K*mol), and T the temperature in kelvin [8]. The BMD equation is a more complex form of the Norton equation used previously for Alloy 709 at 700 °C in chapter 5. The activation energy and diffusivity were not found in this study so values were taken from literature to find the exponents. The creep parameters p, n, and Q are often used to determine the creep mechanism of the material.

$$\frac{\dot{\varepsilon}_m kT}{DEb} = A\left(\frac{\sigma}{E}\right)^n \left(\frac{b}{d}\right)^p \tag{6.3}$$

Comparison of various austenitic stainless steels and Alloy 709 in the framework of such normalization by plotting normalized minimum creep rate against the normalized applied stress. Some studies [3, 9] found stress exponents from the Norton's plots that are higher than the allowable range (5~7) to explain the dislocation climb mainly due to precipitation strengthening or load change creep tests. The larger stress exponents were rationalized by introducing a threshold stress concept due to the added stress introduced by precipitates under creep conditions. Since the data obtained from the monotonic creep tests on Alloy 709 did not result in stress exponents much out of the 5 ~ 7 range the threshold stress approach was determined to not be necessary. It is well known that a stress exponent from 4 to 7 indicates the rate-controlling creep mechanism as dislocation climb. The stress exponents found in this study of Alloy 709 are shown in Figure 6.8. In this study also, we performed a stress change test on Alloy 709 at 600 °C starting at 140 MPa then changing to 125 MPa, back to 140 MPa, then up to 165 MPa.

Monotonic creep tests were completed at 600 °C at 140 MPa, 165 MPa and 198 MPa. The minimum creep rate found in the stress change test resulted in faster creep rates at both 140 and 165 MPa. This in turn resulted in a stress exponent of 10.2 which is similar to the apparent stress exponent (10.3) recorded by Alomari et al. [3]. It appears that the stress change experiments have a tendency to increase the stress exponent value; however the reason for such behavior is not known at this point. The conjecture is that the creep specimen during the stress change test conducted by Alomari et al. [3] on Alloy 709 could have experienced additional microstructural evolution under such conditions [3]. On the other hand, the monotonic creep test data in the present study were obtained from the initial period of creep tests where microstructural evolution may not have fully started.

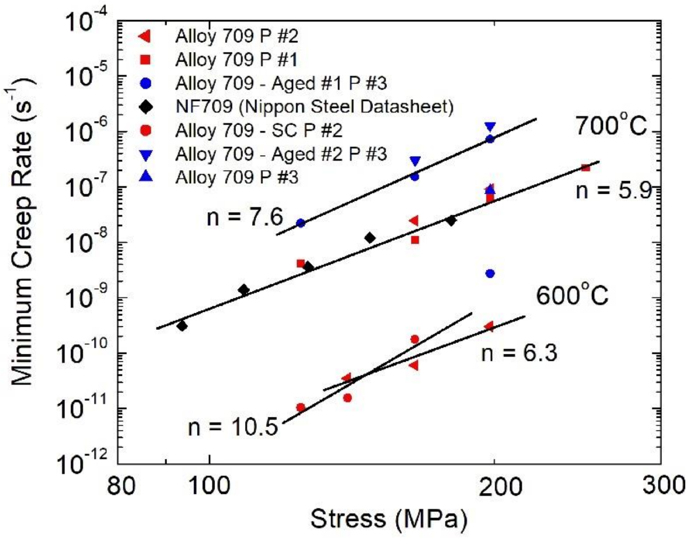

Figure 6.8. Minimum creep rate with the applied stress showing the stress exponents for the various conditions (please note that SC stands for stress change creep test data).

Table 6.6. Parametric dependence of various diffusion-controlled deformation mechanisms [10].

Creep Type	*n*	*p*	*Q*
Nabarro-Herring	1	2	Q_L
Coble	1	3	Q_{GB}
Harper-Dorn	1	0	Q_L
Grain Boundary Sliding	2	2	Q_{GB}
Solute Drag Dislocation Creep	3	0	Q_S
Dislocation Climb Creep	4-7	0	Q_L
Low Temperature Climb Creep	7	0	Q_C

where Q_L is lattice diffusion, Q_{GB} is grain boundary diffusion, Q_C is dislocation core diffusion, and Q_S is solute diffusion.

Since only two temperatures were studied in this investigation, there is not enough data to determine the activation energy of Alloy 709. There is however significant data found in literature that allows a good approximation of the activation energy of Alloy 709. Diffusion in FCC alloys is well documented by Abe et al. [11] giving an activation energy of 284 kJ/mol and a D_o of 1.7×10^{-4} m^2/s for Fe diffusing in Fe-20Cr-25Ni/Nb [11]. A value of the Burgers vector is taken to be 2.5×10^{-10} m. The moduli of elasticity at 600 and 700 °C were found in Nippon Steel's NF709 datasheet to be 1.56×10^{11} Pa and 1.49×10^{11} Pa, respectively [12]. These values were used in this study to assist in finding the mechanism of creep in Alloy 709.

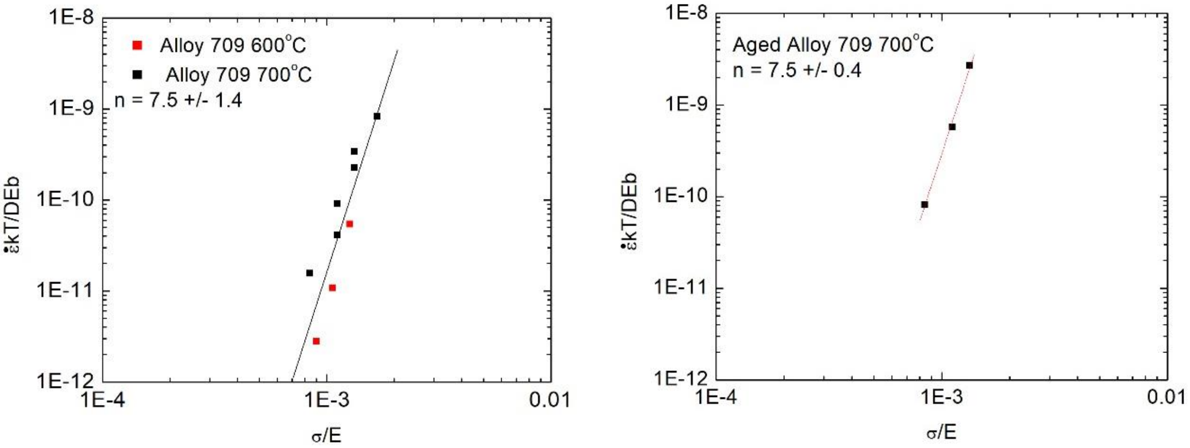

Figure 6.9. BMD plots of the normalized steady state creep rate with the effective stress (a) as-received Alloy 709 crept at 600°C and 700°C and, (b) aged Alloy 709 crept at 700°C.

The BMD normalization of both the aged and as-received Alloy 709 showed a stress exponent of around 7.5. However, the aged Alloy 709 lost creep strength. This suggests that despite aging, the mechanism of creep for Alloy 709 remained in the dislocation climb region of 5 to 7. TEM and optical microscopy are being completed to determine what precipitates or microstructural changes occurred during the aging process. The BMD relation for Alloy 709 is compared with data from variations of 316 SS. For the calculations a D_o of $1.2\text{x}10^{-6}$ m^2/s was used along with an activation energy of 229 kJ/mol [11].

The Burger's vector calculated for Alloy 709 was also used for the 316 SS calculations, the elastic modulus for 316 at 700 °C is not well documented so the one of Alloy 709 at 700 °C was used (1.49×10^{11} Pa). Little variation is observed between Alloy 709 and 316 SS or 316H with this method however Alloy 709 at 600 °C and 700 °C in this study showed slightly better creep strength then the others. The aged Alloy 709 showed worse creep resistance then the 316 counterparts. The stress change test completed by Alomari et al. on Alloy 709 could be experiencing additional precipitation strengthening with the use of stress change tests [3].

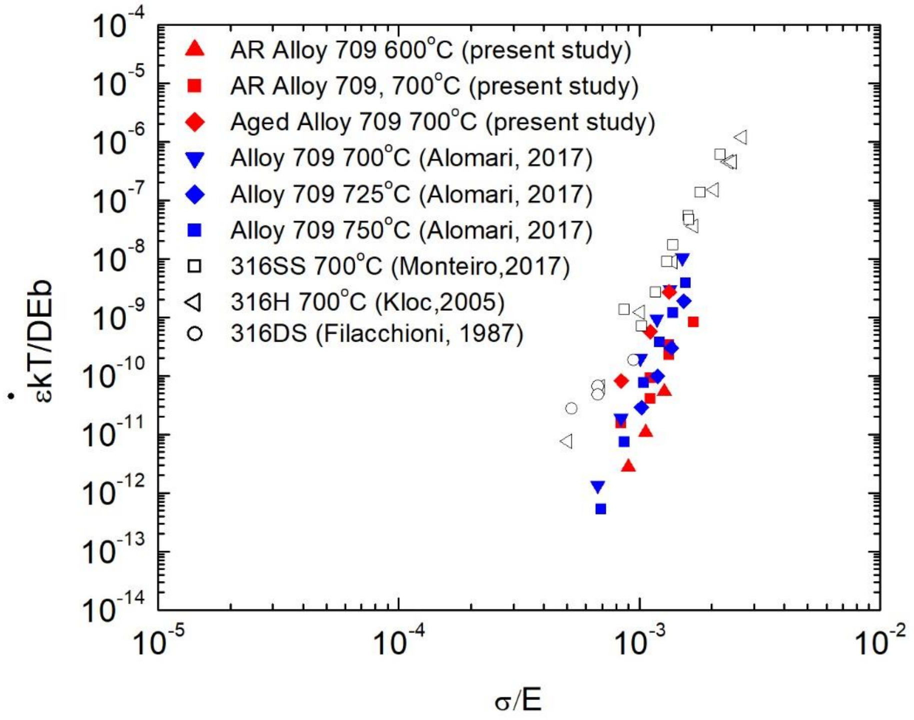

Figure 6.10. Comparison of normalized minimum creep rate with the normalized stress data for different austenitic stainless steels and Alloy 709 [3], [13], [14].

The current results found in this study and the results found by Alomari et al. [3] suggest the creep mechanism of Alloy 709 can be largely described as dislocation climb creep. Thus, the constitutive equation for the as-received Alloy 709 becomes

$$\frac{\dot{\varepsilon}_{ss}kT}{DEb} = 8.3x10^{11}\left(\frac{\sigma}{E}\right)^{7.5\ \pm 1.4} \tag{6.4}$$

6.5. Conclusions

The study presented in this chapter was performed on Alloy 709 to aid in characterizing a potential material for Sodium-cooled Fast Reactors (SFR). Creep tests were performed at 600 °C and 700 °C on as-received Alloy 709. Additional creep tests were completed on aged Alloy 709 at 700 °C. The BMD relation was used to fit the creep tests and resulted in a stress exponent of

7.5 ± 1.4. This alludes to Alloy 709 having a creep mechanism of dislocation climb creep at these temperatures and stresses. This agrees with other studies on Alloy 709 despite not taking the threshold stress approach. Large and fine MX precipitates were observed along $M_{23}C_6$ plates after thermal aging at 700 °C temperatures.

A second batch of aged Alloy 709 (650 °C for 6 months) is to be studied. Potential stress change tests could be studied to determine how a stress change test affects the creep mechanism and life of the material. Additional microstructural analysis is necessary to understand the microstructural effect on the creep properties.

6.6. References

[1] S. Sham, “Advanced Reactor Concepts Program ARC Materials Development - Accomplishments and Plans,” 2013.

[2] Z. Kuboň, Š. Stejskalová, and L. Kander, “Effect of Sigma Phase on Fracture Behavior of Steels and Weld Joints of Components in Power Industry Working at Supercritical Conditions,” Austenitic Stainl. Steels - New Asp., 2017.

[3] A. S. Alomari, N. Kumar, and K. L. Murty, “Investigation on Creep Mechanisms of Alloy 709,” ASME 2017 Nucl. Forum, p. V009T02A003, 2017.

[4] Y. Zhao, J. Zhao, and X. Li, “Microstructural evolution and change in hardness during creep of NF709 austenitic stainless steel,” Acta Metall. Sin. (English Lett., vol. 24, no. 3, pp. 220–224, 2011.

[5] T. Shrestha, M. Basirat, I. Charit, G. P. Potirniche, and K. K. Rink, “Creep rupture behavior of Grade 91 steel,” Mater. Sci. Eng. A, vol. 565, pp. 382–391, 2013.

[6] T. Sourmail and H. K. D. H. Bhadeshia, “Microstructural evolution in two variants of NF709 at 1023 and 1073 K,” Metall. Mater. Trans. A, vol. 36, no. 1, pp. 23–34, 2005.

[7] A. F. Padilha and P. R. Rios, “Decomposition of austenite in austenitic stainless steels,” ISIJ Int., vol. 42, no. 4, pp. 325–327, 2002.

[8] S. McCormick, “Effect of heat treatment and creep deformation on the microstructural characteristics of ATI 20-25+Nb austenitic stainless steel,” University of Idaho, 2015.

[9] T. Shrestha, M. Basirat, I. Charit, G. P. Potirniche, K. K. Rink, and U. Sahaym, “Creep deformation mechanisms in modified 9Cr-1Mo steel,” J. Nucl. Mater., vol. 423, no. 1–3, pp. 110–119, 2012.

[10] I. Charit and K. L. Murty, “Creep behavior of niobium-modified zirconium alloys,” J. Nucl. Mater., vol. 374, no. 3, pp. 354–363, 2008.

[11] F. Abe, T.-U. Kern, and R. Viswanathan, Creep-resistant steels, 1st ed. The Institute of Materials, Minerals, and Mining, 2008.

[12] “Nippon steel material data sheet NF709,” Nippon STEEL SUMITOMO Met. Corp., pp. 10–12, 2013.

[13] L. Kloc and J. Fiala, “Viscous creep in metals at intermediate temperatures,” Kov. Mater, vol. 43, no. 2, pp. 105 – 112, 2005.

[14] S. Monteiro Neves, F. Santos, W. Anacleto, and L. Paulo, “Creep Parameters and Dislocation Substructure in AISI 316 Austenitic Stainless Steel From 600oC to 800oC,” Mater. Res., no. 1, pp. 1–5, 2017.

7 FATIGUE AND CREEP-FATIGUE CRACK GROWTH RESULTS

7.1. Introduction

The power industry is continually growing and pushing the bounds of current structural materials; the nuclear power industry is one such industry. Generation IV reactor designs are expected to maintain a service life of 60 or more years. With the increase in service life, fatigue and creep-fatigue failures are of even greater importance in the design of these modern reactors. Understanding the fatigue and creep-fatigue behavior of the applicable structural materials is paramount for safe design. A recently developed austenitic stainless steel, nominally Fe-25Ni-20Cr (Alloy 709), is a potential candidate material for such applications. To date, Alloy 709 has lacked comprehensive laboratory testing and characterization required for material implementation for structural components. The following report discusses the fatigue crack growth (FCG) and creep-fatigue crack growth (CFCG) testing conducted at various temperatures, load ratios, and hold times. The comprehensive analysis of material property repeatability required comparison between multiple batches of material and aged conditions. Funding for this research was provided by the Department of Energy - Nuclear Engineering University Programs, through the project to “Characterize the Creep-Fatigue Crack Growth in Alloy 709 and Predict Service Life in Nuclear Reactor Components”.

7.2. Nuclear Reactor Materials

Sodium Fast Reactor (SFR) design concepts are under development for Generation IV (Gen IV) nuclear reactors. The primary challenges for Gen IV reactors are: dimensional stability with high thermal stress capacity, high levels of compatibility with heat-transfer media (sodium coolants), and long term stability/reliability, and ease of fabrication [1]. The SFR design concepts utilize liquid sodium metal for primary cooling, requiring continual operating temperatures of 550°C [2], where peak temperatures can extend well above 650°C. Current materials considered for SFR structural applications are austenitic stainless-steels with high temperature resistance and acceptable irradiation doses [3]. Optimal materials selected for the Gen IV SFR designs will require high creep strengths and sodium compatibility at elevated operating temperatures. The Gen IV reactor designs are set to be in operation for maintained service lives of up to 60 years. Within the 60-year service life, structural components are expected to be subjected to long loading periods along with high frequency vibration resulting from pumps and machinery present within the overall design of the reactor [4]. Current materials under consideration for the SFR designs are represented in Figure 7.1 by a property rank chart [5]. As highlighted in this diagram, Alloy 709 is superior in almost all rankings, second only to a high-temperature ultrafine-precipitate-strengthened (HT-UPS) austenitic stainless in the creep category. Overall, Alloy 709 shows promising material properties for SFR reactor designs.

7.3. Fracture Mechanics Background

The importance of fatigue failures and design for fatigue dates back as early as the 1840s with the railway industry and railcar axle failures. Early stress versus life diagrams were developed in the 1860s to characterize a given stress level to the life of a component.

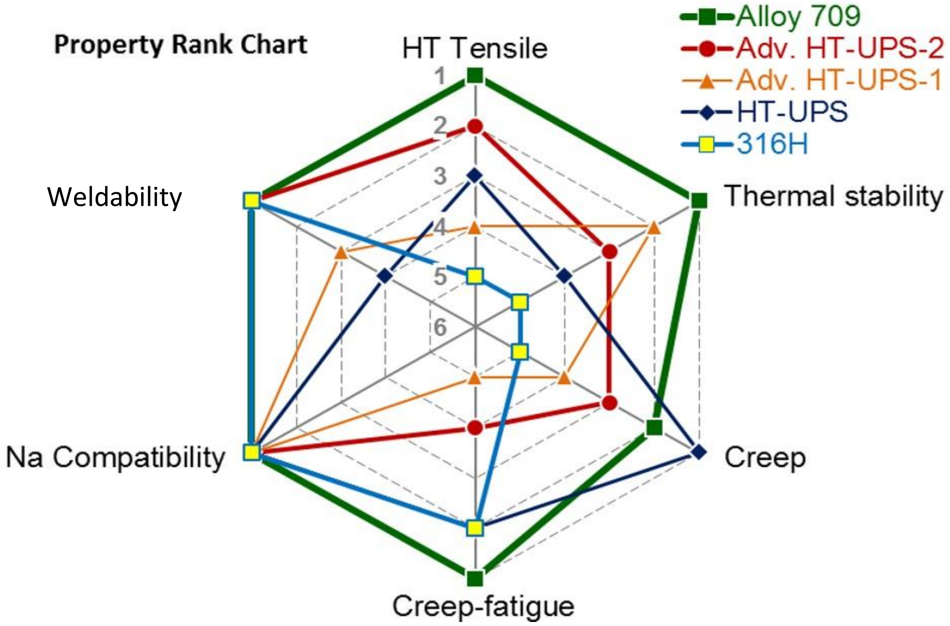

Figure 7.1. Material Considerations for Gen IV SFR designs [5].

Throughout nearly the next decade, numerous tests were conducted around the world investigating the effects of stress concentrations and corrosion effects. It was not until the 1950s that Dr. George Irwin coined the term fracture mechanics. George Irwin and Alan Griffith introduced the stress intensity factor K and the modern principles of fracture mechanics known as Linear Elastic Fracture Mechanics (LEFM) [6]. The loading and extension of cracks is broken down into three modes. Mode 1 is the most common loading case where loading is perpendicular to the crack plane. Modes 2 and 3 result from loading parallel to the crack plane, seen in Figure 7.2. Mode 1 loading is the dominating failure mode experienced under fatigue conditions as the stresses dominate the crack-tip stress field [6].

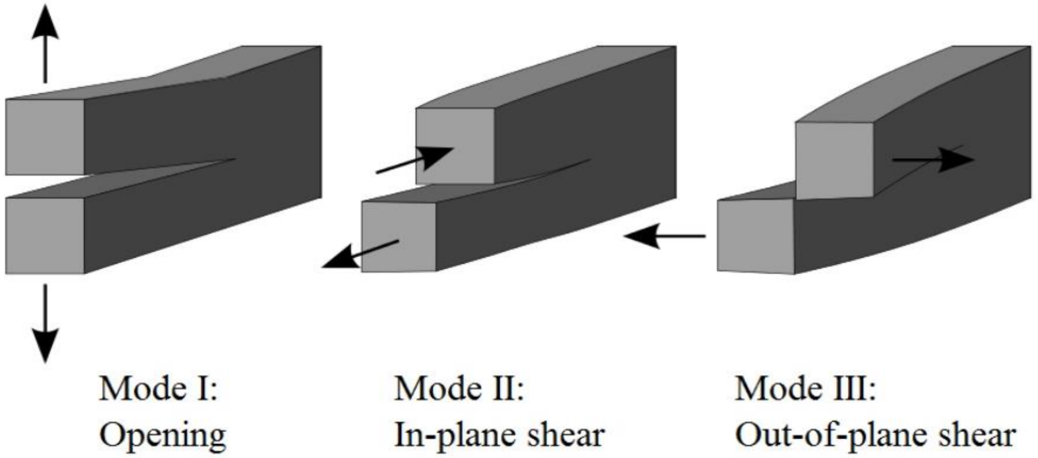

Figure 7.2. Modes of crack extension [6].

The LEFM framework under which crack growth and stresses are characterized has many limitations. The primary qualifying requirement for LEFM characterization regards the size of the plastic zone at the crack tip, requiring the plastic zone to be small in relation to the overall geometry of the specimen. For the standard compact tension, C(T), specimen geometry crack length, a, must satisfy the following condition of [7]

$$(W - a) \geq \left(\frac{4}{\pi}\right)\left(\frac{K_{max}}{\sigma_{YS}}\right)^2 \tag{7.1}$$

where σ_{YS} is the 0.2% offset yield strength at the test temperature, w is the specimen width, a is the crack length and K_{max} is the max stress intensity.

LEFM is based on the idea that at the tip of a sharp crack, there will be some plastic deformation that will cause propagation of a crack through the material. The stress intensity factor K is the fundamental parameter used to characterize the stresses at the crack tip. The general form of the stress intensity factor under Mode 1 loading is of the form of equation (7.2) [6].

$$K = \frac{P}{A_{nom}} \sqrt{\pi a}\, F\left(\frac{a}{w}\right) \tag{7.2}$$

Equation (7.3) is the stress intensity solution for the C(T) geometry used in this study [7]

$$K = \frac{P}{\sqrt{B * B_n}\sqrt{W}} F\left(\frac{a}{W}\right) \tag{7.3}$$

where $F(a/W)$, is

$$F\left(\frac{a}{W}\right) = \frac{(2+\alpha)}{(1-\alpha)^{3/2}}(0.886 + 4.64\alpha - 13.32\alpha^2 + 14.72\alpha^3 - 5.6\alpha^4) \tag{7.4}$$

and $\alpha = a/W$, B is the specimen thickness, B_n is the net specimen thickness, w is the specimen width and P is the applied load. Equations (7.3) and (7.4) are per the American Society for Testing and Materials (ASTM) standard E-647 for the C(T) specimen and accounts for the axial and bending components applied to the specimen as crack length increases.

The standard method for reporting time-independent FCG data is in terms of crack length per cycle, da/dN, as a function of the stress intensity, K, or more commonly, the stress intensity range, ΔK. The stress intensity range is defined as

$$\Delta K = K_{max} - K_{min} \tag{7.5}$$

where K_{max} and K_{min} are the maximum and minimum stress intensities of the load cycle. When reducing raw crack length and cycle data to *da/dN*, ASTM standard E-647 suggest that crack length measurements be made at intervals of no smaller than ten times the crack length measurement precision [8]. The secant method is the recommended technique for calculating *da/dN* on a point by point basis, equation (7.6)

$$(da/dN)_{\bar{a}} = \frac{(a_{i+1} - a_i)}{(N_{i+1} - N_i)} \tag{7.6}$$

This method is common for both FCG and CFCG test data reduction for time-independent crack propagation in metals [7,9]. The C(T) geometry is ideal for fatigue and creep-fatigue crack growth testing to test a large range of stress intensities as ΔK increases quickly with increasing crack length.

Specimen geometry plays a significant role on the loading conditions when determining fracture toughness and mechanical properties of a material. As seen in Figure 7.3, thin specimens will be in a state of plane stress, while an increasing thickness will approach a plane strain condition. This change in stress state is a result of the transition from a triaxial state of stress to a primarily uniaxial state of stress.

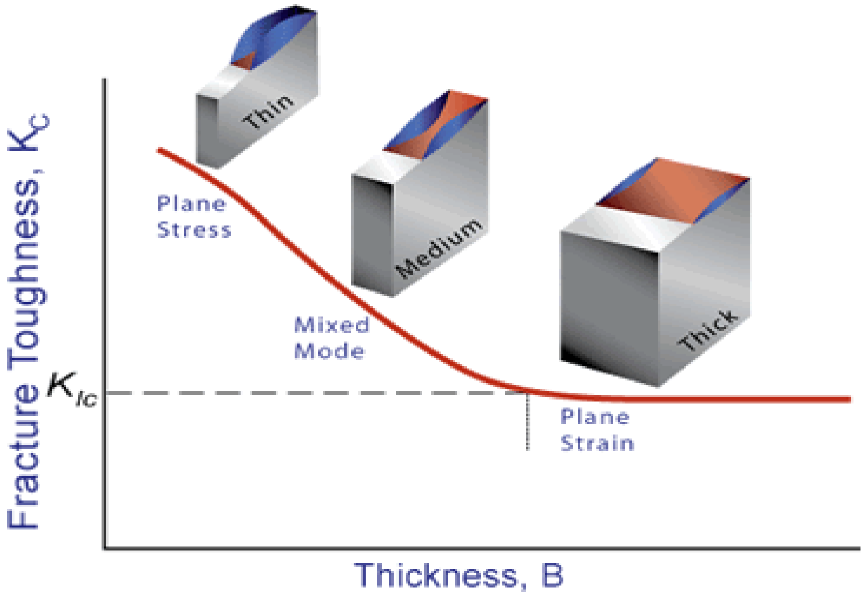

Figure 7.3. Plane Stress vs. Plane Strain loading conditions

7.4. Elevated Temperature Fatigue Crack Growth Testing (FCG)

Elevated temperature testing of metallic materials is critical for numerous modern applications in the power generation industry. Servohydraulic systems are the most common method for testing fatigue properties of materials [6]. Servohydraulic systems are preferred to most other load frame systems due to their versatility, precision and frequency capabilities. A typical servohydraulic system utilizes a proportional servo valve to direct high-pressure fluid to a ram with a feedback control system utilizing either load or displacement feedback. This feedback system provides the capability to attain accurate and repeatable loadings on specimens and is used widely for FCG testing applications [10]. Modern test systems have the capability to run high-cycle fatigue tests at frequencies greater than 15Hz. To fully understand the mechanical characteristics of a material at elevated temperatures, tests must be run at the elevated temperatures to characterize the mechanical properties under the tested conditions. The test method for determining crack growth rates in materials at elevated temperatures is outlined in ASTM standard E-647 [7]. This standard provides specimen geometry requirements and measurement techniques that are widely accepted. At elevated temperatures, special care must be taken to ensure the environmental testing conditions are maintained throughout the length of a test. The ASTM standards specify temperature variation to remain within ±3°C of the setpoint throughout the length of the testing window. Crack length measurement can be conducted using Crack Opening Displacement (COD) compliance, visual measurement or potential drop (PD) systems [11,12]. Crack growth rates under FCG conditions, as early as the 1980s has shown to change with temperature [13]. Sadananda showed that temperature increases in an air environment had the effect of increasing the crack growth rate of a material for a given stress intensity. This was also seen within a vacuum environment. Furthermore, Sadananda showed that the effect on crack growth rates by temperature is pronounced at crack growth rates on the order of 10^{-5} mm/cycle and below, and that the effect is diminished at higher crack growth rates. These results were found with Type 316 stainless steel specimens in both air and vacuum [13]. The driving factor for the crack growth rate change, as a result of increasing temperature, can be attributed to the decrease in the material's elastic modulus at the given temperature and increased surface oxidation[14].

7.4.1. Loading Induced Crack Closure

A crack propagates through a material when the driving force at the crack tip is above a minimum level. When a crack is present in a material, there will be a stress intensity, K_{open}, at which the crack opens. When the stress intensity drops below the K_{open} stress level, or sometimes slightly lower, the crack will close. Loading that does not reach the opening stress of the crack tends not to propagate the crack through the given material. Because K_{open} is often greater than K_{min} the effective stress range that drives the crack is not ΔK but rather ΔK_{eff} defined by $K_{max} - K_{op}$ [6]. The loading ratio, R, is the ratio of minimum load to maximum load, P_{min}/P_{max}, or in terms of stress intensity, K_{min}/K_{max}. The *R*-ratio is the common method in FCG testing to characterize loading. At higher stress ratios ($\approx R>0.5$), crack closure is limited, i.e. the minimum stress, K_{min}, is equal to or greater than the opening stress, K_{open}, for the material. At lower load ratios, crack closure is more prevalent. In terms of *da/dN vs.* ΔK, crack closure will manifest as a shift along the ΔK axis. Higher *R*-ratios had increased crack growth rates compared to lower *R*-ratios at the same stress intensity ranges. However, if crack growth rates are plotted against ΔK_{eff}, the *R*-ratio curves will collapse onto one another (low *R*-ratio curves would shift onto the highest *R*-ratio curve where no closure is present).

7.4.2. Creep Brittle vs. Creep Ductile material

Creep crack growth of metals and metal alloys is characterized in one of two ways, as creep-ductile or creep-brittle. Creep-ductile materials accumulate creep deformation ahead of the crack tip at a rate faster than the crack propagates. In these materials, a time dependent parameter such as C^* or $C(t)_{avg}$ is favored to characterize the stress at the crack tip. Many high-temperature alloys such as stainless-steel behave in a creep-ductile manner. Creep-brittle materials accumulate creep strains slower or near the same rate as the rate of crack extension. In this case, the stress field at the crack tip can be described using a time-independent parameter such as ΔK [15]. Creep-ductile materials will see much higher creep rates than creep-brittle materials due to the increased size of the creep zone over the cyclic plastic zone [16]. As hold time is increased, the creep zone size at the crack tip will continue to increase faster than the cyclic plastic zone and crack extension rates, resulting in gross plastic deformation of the material and increased crack growth rates. The increased crack growth rate can be broken down into two primary components, a time-independent and a time-dependent crack growth rate.

$$\left(\frac{da}{dN}\right)_{total} = \left(\frac{da}{dN}\right)_{cycle} + \left(\frac{da}{dN}\right)_{time} \tag{7.7}$$

where $(da/dN)_{\text{time}}$ is relative to the hold time of the cycle and is often described as da/dt [17].

At low hold times, it is possible for the creep zone to remain smaller than the cyclic plastic zone and the resulting crack growth rates will not be affected by the hold time [18]. In this case, a creep-ductile material will behave similarly to a creep-brittle material until the hold time is long enough to increase the creep zone size over the cyclic plastic zone.

7.5. Elevated Temperature Creep-Fatigue Crack Growth Testing (CFCG)

CFCG testing, is similar procedurally to FCG testing aside from some modifications. Servohydraulic systems are used to generate the required loading waveform and loading accuracy. CFCG results can be reported in the same manner as FCG data, with da/dN as a function of K or ΔK, although primarily only with creep-brittle materials. When reported in this fashion, the creep effect of the material will manifest in much the same way as temperature effects. For a given temperature, Narasimhachary showed that an increase in hold time translated to an increase in crack growth rate per cycle [17]. More commonly, creep-ductile materials are characterized for CFCG in terms of crack extension per unit time, da/dt, and $(C_t)_{avg}$.

This characterization is time dependent rather than cycle dependent. This characterization accounts for crack growth during the hold period of a cycle. *$(C_t)_{avg}$* calculation is a function of the load and load-line displacement measured during the hold period. However, load-line displacements during hold times are often small with relation to the displacement resolution; thus, an analytical approach is preferred [17]. The analytical approach for *$(C_t)_{avg}$* is:

$$(C_t)_{avg} = (C_t)_{ssc} + C^*(t) \tag{7.8}$$

where the small scale creep $(C_t)_{ssc}$, is

$$(C_t)_{ssc} = \frac{2\alpha\beta(1-\nu^2)}{E} F_{cr}(\theta, n) \frac{\Delta K^4}{W} \left(\frac{F'}{F}\right) (EA)^{\frac{2}{n-1}} t_h^{\frac{n-3}{n-1}} \tag{7.9}$$

where n is the Norton Creep Constant, β = 1/3 [19] and

$$\alpha = \frac{1}{2\pi}\left(\frac{(n+1)^2}{1.38n}\right)^{\frac{2}{n-1}} \tag{7.10}$$

the extensive creep contribution, *C^**, is given by

$$C^*(t) = \frac{A(W-a)h_1(a/W, n)P_{max}}{\left(1.455 * \eta * B_n * (W-a)\right)^{n+1}} * 10^{-6n} \tag{7.11}$$

where

$$\eta = \left(\frac{2a}{W-a}\right)^2 + \left(\frac{4a}{W-a}\right)^{0.5} - \left(\frac{2a}{W-a} + 1\right) \tag{7.12}$$

and h_1 can be found from tabulated values provided in [20].

7.6. Previous Creep-Fatigue Work with Austenitic Stainless-Steels

Austenitic stainless steels and nickel-base alloys have been the materials of choice for high strength and corrosion resistant applications. Austenitic stainless-steel alloys consist primarily of Fe-Cr-Ni. They are favored for reactor internals due to the need for elevated temperature corrosion resistance. Corrosion resistance is a result of the formation of chromium-containing spinels (i.e., chromite or magnesiochromite), that retard corrosion rates within the material [21]. Nickel is the basic substitutional element used for austenite stabilization; while the equilibrium phases, ($M_{23}C_6$, NbC, TiC, etc.) depend on the proportion of the three elements Fe-Cr-Ni. MX, such as NbC or TiC, and $M_{23}C_6$, such as $Cr_{23}C_6$, precipitates provide increased creep resistance by creating boundaries to dislocation motion. When creep resistance is a primary concern, solution heat treatment is used to dissolve precipitates throughout the microstructure. Subsequent precipitation occurs during creep and increases strength. $M_{23}C_6$ typically precipitates, in order of prevalence, on grain boundaries, incoherent and coherent twin boundaries and intragranular sites [22]. The primary concern when dealing with stainless steel alloys for structural components is the fatigue life and creep strength of the alloy. Most austenitic stainless alloys that are compatible for highly corrosive environments are creep-ductile in nature. Due to the creep characteristics, it is critical to understand crack propagation through the material under various loading conditions.

AISI 316 stainless steels has been the base line for which most new high temperature austenitic stainless steels are compared. AISI 316 is an austenitic stainless steel of nominal composition Fe-17Cr-12Ni. 316 is well known for its superior corrosion resistance to austenitic stainless steels such as 304. Previous work by Michel et al. [23] showed 304 and 316 to be sensitive to loading hold time, Figure 7.4a and 2.4b. Hold times as small as six seconds in both 304 and 316 solution annealed stainless steel increased crack growth rates. When hold times were increased to 60 seconds, both 304 and 316 demonstrated increased growth rates over the six second hold. The tests were conducted at a temperature of 593℃ (1100°F) with a trapezoidal waveform. Michel et al. also investigated the effect of prolonged exposure at service conditions on material characteristics. An aged condition of 5000 hours (≈7 months) of prolonged exposure at 593℃ (1100°F) was investigated. It was determined that at temperatures of 593℃ and higher, thermal ageing of the 316 stainless decreased crack growth propagation rates. However, thermal ageing displayed no significant effect on crack growth rates for the other materials investigated: 304, 321 and 348. Also, as temperatures were decreased the effect that the load frequency and load profile had on crack growth rates was decreased.

Both hold time and reduced cyclic frequencies have been observed to increase crack propagation rates at elevated temperatures. The crack growth rates of CFCG loading profiles showed increased crack growth rates over the equivalent frequency FCG load profiles, presented in Figure 7.5 for 316. No difference was observed between FCG and CFCG at equivalent frequencies when tested at lower temperatures. Michel et al. concluded that material behavior and crack growth mechanisms during continuous cycling and hold time at the corresponding frequency were different [23].

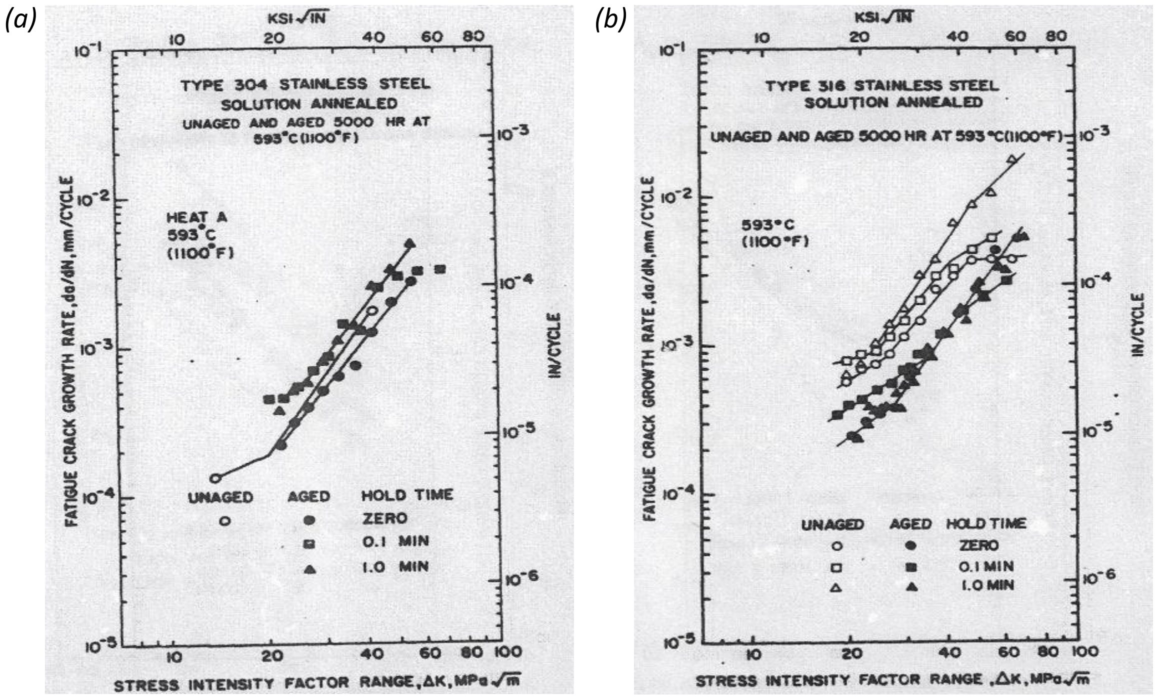

Figure 7.4. 304 and 316 solution annealed stainless steel crack growth rates in as-received and aged conditions [23].

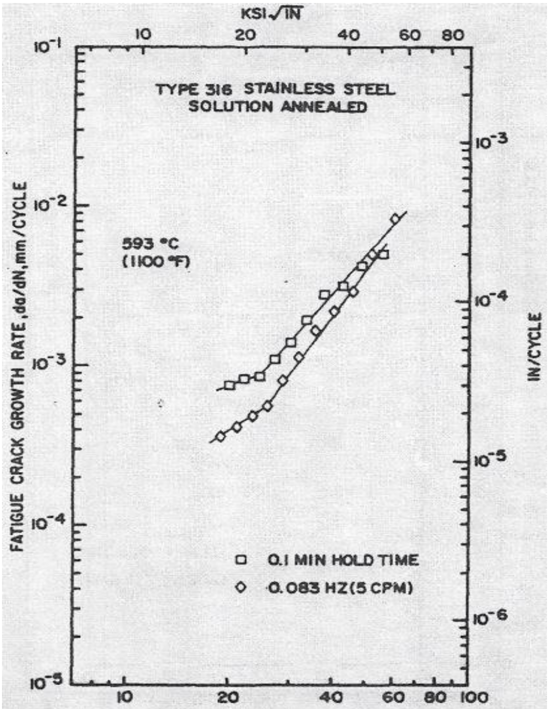

Figure 7.5. 316 solution annealed stainless steel crack growth rates in as-received conditions comparing FCG and CFCG rates [23].

7.7. Experimental Details

7.7.1. Material and Specimen Details

The material of interest for this research was Alloy 709: a solution heat treated austenitic stainless steel with nominal composition of Fe-25Ni-20Cr. Alloy 709 was hot rolled then solution annealed at 1100°C. Solution annealing ensured adequate dispersion of precipitates throughout the material microstructure. All material was received for testing from ORNL. Three separate batches were received and processed in a similar manner; the composition of each batch is shown in Table 7.1. Each batch of material was in the form of a plate. The average grain size was 38 ± 3µm. Batch 3 differed from batches 1 and 2 with increased scatter in grain size with banding of smaller and larger grains within the plate, refer to the batch comparison in section 4.1.3 for further details regarding microstructural differences.

Table 7.1: Material Composition (mass %)

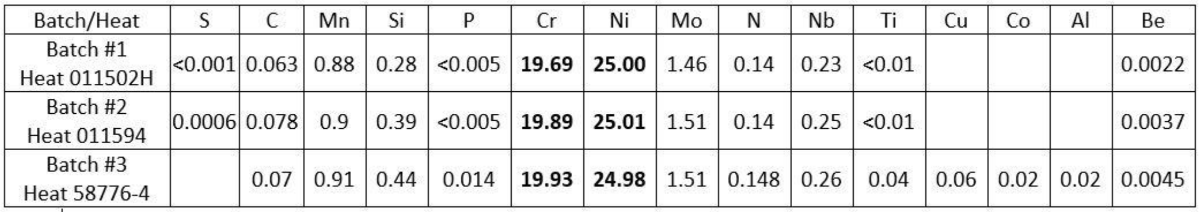

Batch/Heat	S	C	Mn	Si	P	Cr	Ni	Mo	N	Nb	Ti	Cu	Co	Al	Be
Batch #1 Heat 011502H	<0.001	0.063	0.88	0.28	<0.005	**19.69**	**25.00**	1.46	0.14	0.23	<0.01				0.0022
Batch #2 Heat 011594	0.0006	0.078	0.9	0.39	<0.005	**19.89**	**25.01**	1.51	0.14	0.25	<0.01				0.0037
Batch #3 Heat 58776-4		0.07	0.91	0.44	0.014	**19.93**	**24.98**	1.51	0.148	0.26	0.04	0.06	0.02	0.02	0.0045

Specimens were machined from the as-received plates such that the rolling direction was parallel to the crack plane. For plate 3, specimens were oriented such that the crack plane was perpendicular to the striated grain structure. Experimental tests were performed at temperatures of 550°C, 600°C and 700°C. The first batch of material contained three specimens for FCG/CFCG testing, while batch 2 contained 16 and batch 3 contained 48 specimens. Of batch 3, 24 specimens were tested in the as-received condition, while 12 each were used for aged testing at two distinct aging schedules. Specimens were aged at 650°C for three and six months, respectively. The augmented aging times were meant to simulate 25 and 50 years in service at 550°C. Prolonged service life introduces a σ phase in the microstructure which is detrimental to CFCG characteristics. The known physical properties of Alloy 709, in the as-received and aged conditions is outlined in Table 7.2.

Table 7.2: Material Properties of Alloy 709

	25°C As-Received	600°C As-Received	600°C Aged 3 months at 650°C	600°C Aged 6 months at 650°C	700°C As-Received	700°C Aged 3 months at 650°C	700°C Aged 6 months at 650°C
Yield Strength (MPa)	251	206	248	N/A	178	249	N/A
UTS (MPa)	624	558	525	N/A	449	423	N/A

The specimen geometry selected for the FCG and CFCG testing was the standard compact tension type, C(T) geometry, as outlined in ASTM E-647 with W = 50mm and B = 12.7mm and initial notch length a_n=13mm [7]. For CFCG testing, the C(T) specimen geometry was modified with a 4% 60° V-groove on either side of the specimen along the crack plane; the net thickness was reduced to B_n = 11.68mm. The crack plane groove was intended to prevent crack tunneling and out-of-plane crack growth under creep conditions. A 4% notch was used in favor of the standard 10% notch, because 10% was deemed unnecessary.

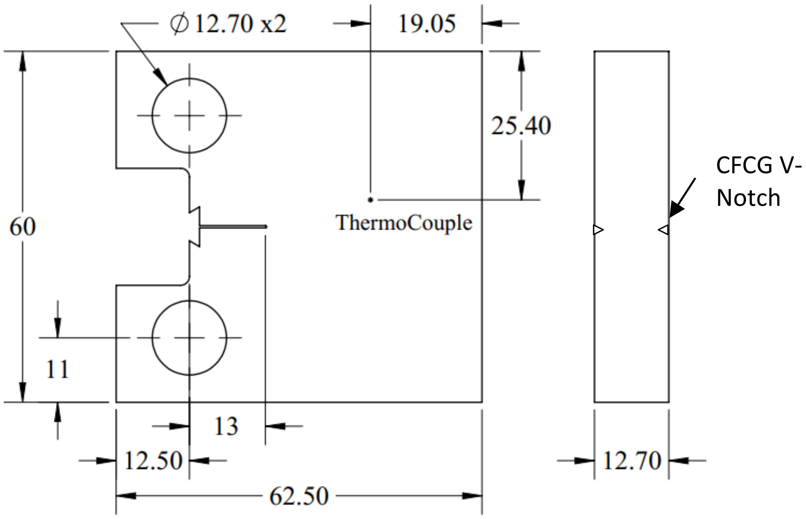

(Measurements in mm)

Figure 7.6: Compact tension C(T) specimen dimensions according to ASTM E-647

For the first two batches of material, the initial notch length was a_n = 16mm. For the 3rd batch, the machined notch length was reduced to 13mm to increase precrack length and ensure a uniform crack front. Specimen notch and extensometer edges were machined using wire electrical discharge machining (EDM) in accordance with the ASTM standards for the C(T) geometry [7]. All specimens were precracked at room temperature to an initial crack length

a_0=18mm. Specimen geometry is outlined in Figure 7.6. The dimensions chosen are in accordance with ASTM Standard 2760 creep-fatigue crack growth testing [9].

Starting ΔK levels were typically around ΔK=20 MPa√m while the tests were terminated at a $\Delta K \approx 45$ MPa√m. A larger range of ΔK values were tested and recorded from a single sample with the development of the Direct Current Potential Drop (DCPD), section 3.5, feedback system that enabled both ΔK controlled increasing and decreasing tests. Utilizing ΔK increasing control, a larger range of ΔK values could be collected for a single specimen. When ΔK decreasing control was utilized, near threshold values were collected. Utilizing ΔK decreasing control, a maximum shedding rate, $c = -0.08\ mm^{-1}$ was used per ASTM standard E-647 [7]. Equation (7.13) is the load control algorithm used for load shedding as a function of the crack length and thus the stress intensity range ΔK.

$$\Delta K_n = \Delta K_0 e^{c(a_n - a_0)} \tag{7.13}$$

ΔK_n and ΔK_0 are the current and next stress intensity ranges respectively; a_n and a_0 are the current and previous crack lengths.

Upon test termination, the specimens were cooled to room temperature and cycled at 5 to 15 Hz until failure. Specimen fracture allowed initial and final crack lengths to be measured using fracture surface beach marks and correlated to the measured PD voltage. Crack length was measured at the end of the pre-crack and at the end of the fatigue or creep-fatigue portions of the test by averaging five measurements equally spaced across the crack front.

7.7.2. Test Frame Retrofit and Verification

As a first step in the research, existing load frames required modification to accommodate temperature-controlled furnaces, high temperature extensometers for COD measurement and DCPD measurement (detailed overview of the DCPD system is explained in Section 3.5). Elevated temperature testing requires the test specimen to be uniform in temperature and maintain a thermal variance of no more than ± 3°C throughout the test duration [24-26]. The furnaces were controlled with Watlow PID temperature controllers (Watlow EZ-Zone®, and Watlow 981 Series); specimen temperature was monitored using K-type thermocouples spot-welded to the specimen above the crack plane on the rear face. The thermocouple location is shown in Figure 7.6. Before any testing, the thermal variance of the specimen was checked at multiple locations to ensure that temperature was uniform across the entire specimen. Two separate test frames were used for all FCG and CFCG testing conducted, as shown in Figure 7.7.

The size of the furnaces and the desired test temperatures required the development of special grips. Due to its high strength at elevated temperatures, grips were machined from Inconel 718. These grips were machined to comply with ASTM E-399 [27] and fit the 12.7mm (0.5in) thick C(T) specimens selected for this testing. The larger of the two frames, Frame 1, was an MTS 312.12 with a load capacity of 100kN (22kips) paired to an MTS TestStar controller with built in *ΔK* control FCG software.

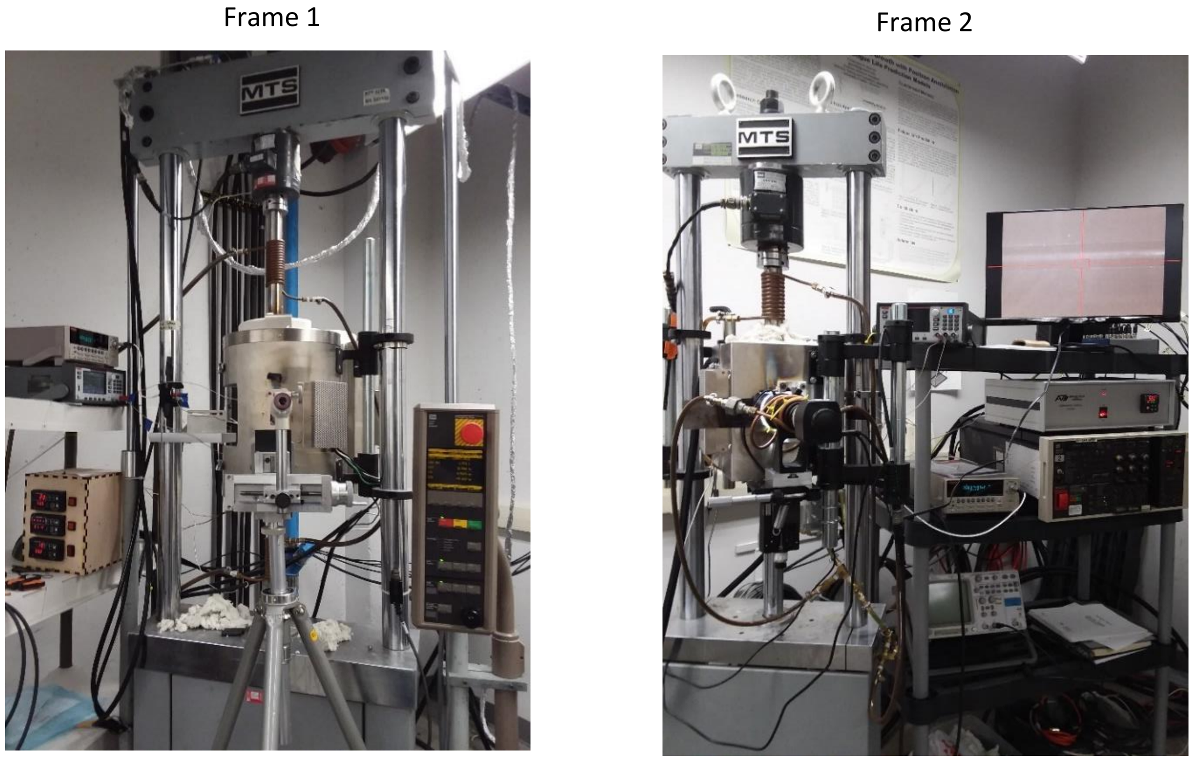

(a) *(b)*

Figure 7.7. Load Frames 1 (a) and 2 (b) with Peripheral Equipment

The FCG software was used for all specimen precrack procedures at room temperature utilizing an MTS 632.02 clip-on extensometer and crack length correlation based on COD as per ASTM E-647.A2 [11]

$$\alpha = \frac{a}{W} = C_0 + C_1 u_x + C_2 {u_x}^2 + C_3 {u_x}^3 + C_4 {u_x}^4 + C_5 {u_x}^5 \qquad (7.14)$$

where

$$u_x = \left\{ \left[\frac{EvB}{P} \right]^{1/2} + 1 \right\}^{-1} \tag{7.15}$$

Table 7.3 outlines the coefficients used for crack length correlation for extensometer mounting at the load line.

The smaller of the frames, Frame 2, was an MTS 312.11 with a maximum load capacity of 27kN (6kips) utilizing an MTS 458.20 MicroConsole with an accompanying MTS 458.91 Micro-profiler. The MTS 458.20 MicroConsole was calibrated to work with the second load frame.

Table 7.3: Compliance coefficients for load line mounted extensometer

C0	C1	C2	C3	C4	C5
1.0002	-4.0632	11.242	-106.04	464.33	-650.68

7.7.3. Loading Conditions and Testing Procedure

The two areas of interest were FCG and CFCG. FCG testing was conducted at load ratios of *R* = 0.1, 0.3, 0.5, and 0.7 utilizing a sinusoidal waveform. *R*-ratio tests were conducted at frequencies of 15Hz. At *R* = 0.1, tests were also conducted at a frequency of 0.01667Hz.

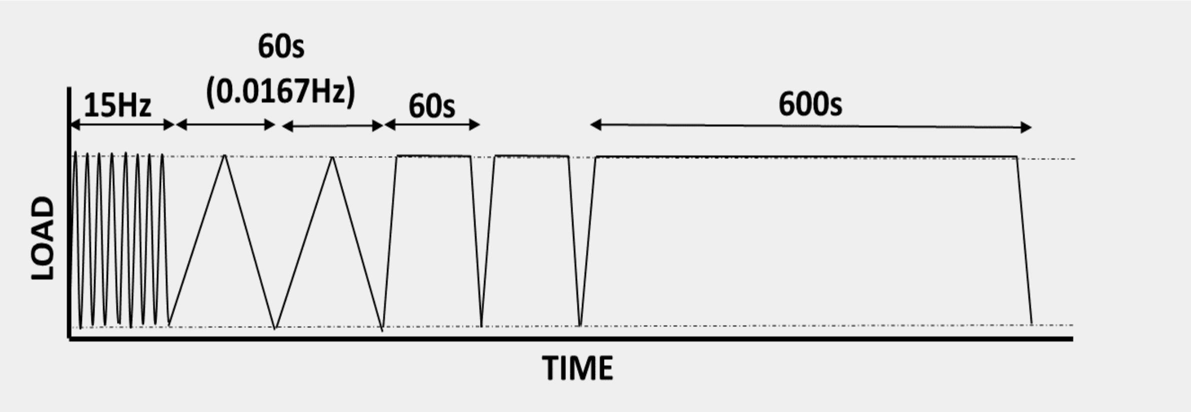

Figure 7.8. Loading waveforms used in FCG and CFCG testing

Throughout the duration of the tests, the minimum and maximum load, loading and unloading compliance, load-line displacement, DCPD voltage, test temperature, and time were monitored and recorded. Visual crack length measurements were also recorded through the furnace window for DCPD measurement validation. Visual measurements were performed using a microscope mounted to a translating stage to monitor crack tip extension. Analog voltages of all measurements were collected at a rate of 5Hz via a LabVIEW interface. The LabVIEW interface was designed specifically to collect data from both load frames independently. The DAQ had true simultaneous sampling with lane independent 16bit converters to reduce signal noise and channel crosstalk. For Frame 2, DCPD and extensometer voltage were also recorded using the NI USB-6341 during testing. After test completion, signal noise was removed using a running average program that was written in Python. Data points were selected at predetermined crack length intervals; ($\Delta a \approx 0.2$mm was typically used) crack length values were used for calculation of crack growth rate and stress intensity factor ΔK.

Frame 1 was integrated more closely to the LabVIEW interface. To conduct ΔK controlled tests, it was desired to have an adequate feedback signal for crack length. Initial testing showed the high temperature extensometer used, an Epsilon E97415, while capable of monitoring crack opening displacement, produced excess noise for the TestStar system to use for crack length feedback at elevated temperature. It was decided to utilize the DCPD system as the feedback/monitoring signal for the TestStar controller. A new sensor was assigned and created within the TestStar software that utilized an input voltage of 0 to 10V calibrated to a crack length of 0 to 50mm. To supply this signal, DCPD voltage was routed through the LabVIEW interface, where it was saved, filtered and then amplified and scaled to produce an output signal to the TestStar controller. This feedback method proved useful in running both ΔK increasing and ΔK decreasing tests. Linear crack length correction was applied to the data after testing based on initial and final crack length measurement from the fracture surface for calculation of ΔK and da/dN.

7.7.4. Modified Long Hold Time CFCG Testing Procedure

Due to the CFCG behavior of this material, a full-length test for a 600s hold time CFCG was unrealistic. It was estimated that a single test (starting at a ΔK = 20 MPa√m, up to a ΔK = 40 MPa√m) would have taken approximately 10 months. Due to time restrictions, a modified testing procedure for 600s hold time was developed. The modified testing procedure started at a ΔK of approximately 25 MPa√m. The crack was grown under the 600s hold time profile until approximately 0.5 mm of crack growth was observed, at which point, the crack was propagated to a predetermined ΔK (typical intervals were between ≈2-4 MPa√m) utilizing a sinusoidal waveform at a frequency of 5 to 10 Hz, after which the 600s hold cycling was repeated. This procedure left obvious beach marks on the surface that could be utilized to confirm intermittent hold time growth rates. These beach marks can be seen in Figure 7.9. This modified testing procedure allowed for various *ΔK* values to be monitored and recorded in a drastically decreased time frame. This test procedure was conducted at temperatures of 600°C and 700°C with batch 2 material and at 700°C with batch 3 as-received, aged 1 and aged 2 material. This modified procedure decreased the testing time to approximately one month for each sample.

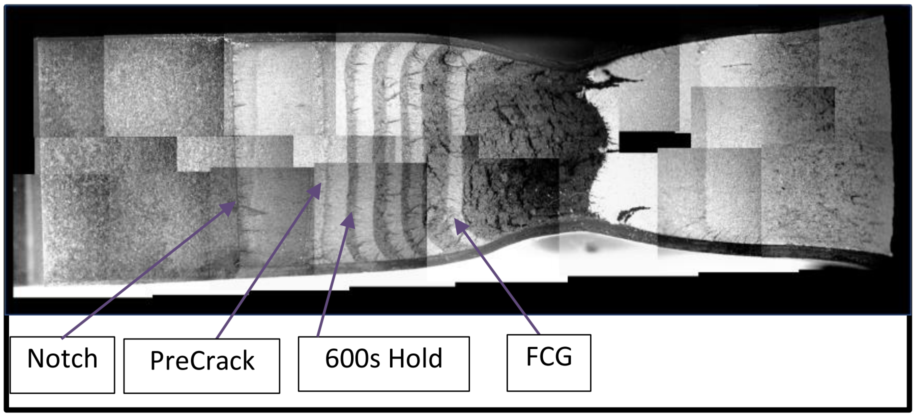

Figure 7.9. Intermittent hold fracture surface mapping

7.7.5. DCPD Measurement Technique

Direct Current Potential Drop (DCPD) is a common method for monitoring crack length propagation in FCG, CFCG, and CCG testing. ASTM E-647.A3 outlines the use of Electric Potential Difference techniques to monitor crack length [12]. For this testing, direct current was used due to relative ease of setup and availability of equipment. Direct current is supplied to the specimen and the voltage across the specimen is measured. The precision current supply used was a Keithley 2280S-32-6 DC Power Supply, while for output voltage measurement, a Keithley 2182A Nanovoltmeter was used. The combined current supply and voltmeter produced a nanovolt resolution of approximately ±2µV, corresponding to a crack length resolution of approximately ±20µm (0.02mm). Current supply and voltmeter wires were attached to the specimen using spot welded Nichrome 60 wires. 22-gauge and 26-gauge wires were used for the supply and measurement, respectively, and spot welded at position A (supply) and B (measurement) as shown in Figure 7.10.

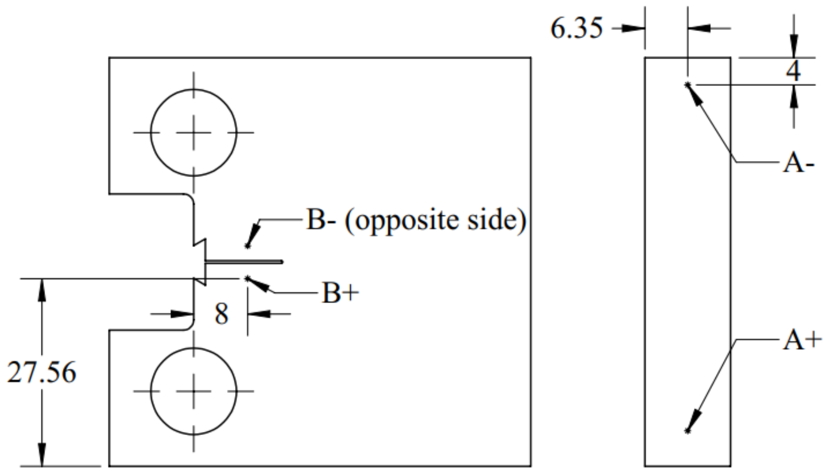

Figure 7.10. DCPD Wire Mounting Locations

A constant current supply of 2 Amps was selected for all tests performed which was sufficient for crack length measurements without voltage measurement error from arcing or crack length shortening. The basis of this DCPD system with numerical analysis and experimental validation is presented in a work of Philip Malmqvist [28].

7.7.6. Microscopy

Optical, Scanning Electron Microscopy (SEM) and Electron Backscatter Diffraction (EBSD) imaging of fracture surfaces, profiles, and microstructure were used to compare material batches, loading and aging effects on Alloy 709. For optical imaging, the specimen surface was hot mounted in an acrylic puck using a PACE Technologies TERAPRESS^{TM} and polished using an ALLIED High Tech Products TWINPREP 3^{TM} polishing wheel and stepping grits to a final grit of 5 micron. After polishing, the surface was electro-etched with oxalic acid at 10% by mass with deionized water for 6 seconds. Optical microscopy was conducted using an Olympus PMG-3 light microscope. For SEM imaging, a Zeiss Supra 35 FEG-SEM fitted with a QUASOR^{TM} EBSD system was used. Images were taken at predetermined ΔK values (steps of $\Delta K = 5$ MPa√m from start of crack growth, i.e. 20 MPa√m, 25 MPa√m, 30 MPa√m) for comparison to other loading conditions. The fracture surface was inspected at various regions across the thickness of the specimen to ensure an accurate representation of the fracture surface at a given ΔK.

EBSD imaging was obtained after grinding the back side of the crack face until the sample was under 200 µm thick. A Gatan disk punch was used to create 3 mm diameter semi-circles that were then ion-milled with argon ions using a PIPS II model 695 machine held at an energy of 4 keV for 5 min, 2 keV for 5 min, and 0.5 keV for 8 min. The surface-prepared disks were placed in the SEM. The sample stage was set at an angle of 70° with a working distance of about 16.5 mm. The SEM was operated at an accelerating voltage of 20 kV and run on high current mode. 4 × 4 pixel binning was used to obtain desired resolution.

7.8. Results and Discussion

7.8.1. Batch Comparison

Due to the small size of the first plate of material, only three specimens were made, thus only three test conditions were performed: FCG(15Hz) at 600℃ and 700℃ and CFCG(60s) at 700℃. These 3 conditions encompass the loading conditions used for comparison between batches. Due to the small quantity of specimens within batch 1, most of the analysis is between plates 2 and 3.

A. Crack Growth Rates

Figure 7.11 presents FCG (left) and CFCG (right) data collected from the three batches of material. Comparison of the three batches showed very little differences for both FCG and CFCG loading conditions. Batch 1 tests for both FCG and CFCG showed similar crack growth rates to batches 2 and 3. The primary difference regarding batch 1 was the slope of the *da/dN vs. ΔK* curve. At both 600℃ and 700℃, the slope of the FCG rate curve for batch 1 was lower compared to batches 2 and 3. For batch 2 and 3, FCG rates overlapped each other substantially; the only difference appearing at low *ΔK* at 600℃. At *ΔK*≈20 MPa√m, batch 1 and 3 growth rates are similar and approximately 25% higher than batch 2. As *ΔK* increased, the fatigue crack growth rates for all three batches, at 600℃, converged at a *ΔK*≈28 MPa√m.

For CFCG, batch 1 was similar to both batch 2 and 3 for a 60s hold time. There was increased scatter with the batch 1 data at lower *ΔK*. Batch 2 and 3 demonstrated similar crack growth rates and were only slightly faster than batch 1, less than 5%. For CFCG tests, an increase in crack growth rate scatter at lower ΔK ranges was observed. As a result, a larger *Δa* was used between data collection for *da/dN* and *ΔK* calculation.

For the batch 1 material, variation in the crack growth rate is inconclusive due to the small quantity of samples. With only one test performed for each loading condition in batch 1, it is not possible to conclude if the retarded crack growth rates were anomalous due to measurement error or otherwise. For crack growth rates in batch 2 and 3 materials, no substantial differences in the crack growth rates were seen. Scatter in batch 1 data at low ΔK values for the CFCG loading is attributed to preliminary tuning with the newly developed DCPD system. Later tests generated more uniform data as use of the DCPD system was improved.

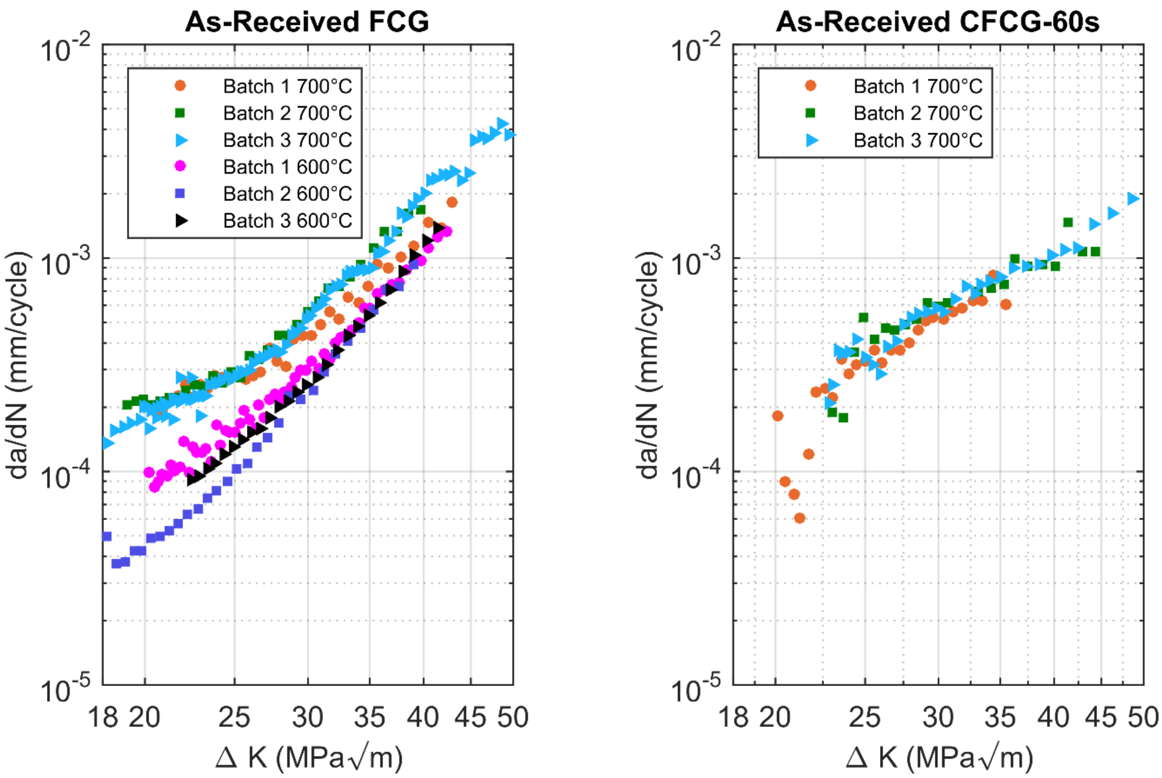

(a) *(b)*

Figure 7.11: Crack growth rates for all batches of material for (a) FCG at a frequency of 15Hz and (b) CFCG with hold time of 60s

B. Fracture Surface

Specimens under both FCG and CFCG conditions showed some differences in the fracture surfaces. Batch 1 and some batch 2 specimens showed the presence of an oxide on the fracture surface. The oxide was seen at temperatures of 600°C and 700°C. Figure 7.12 is a representative image of the oxides formed on the fracture surface of early batch 1 and batch 2 specimens.

The oxide was observed in higher concentration near the mouth of the specimen. Post-test inspection of the fracture surface showed a decrease in oxide presence at longer crack lengths. All batch 1 specimens showed the oxide formation regardless of loading conditions. For batch 2 specimens, only the first five specimens showed an oxide presence on the fracture surface for both the FCG and CFCG profiles.

The oxide observed on the fracture surface of the first specimens tested is most likely attributed to initial burn-in of the new furnaces or improper storage of the specimen surfaces before fractography was completed.

Figure 7.12. Fracture surface oxide formation at 700°C under FCG loading, 1kx magnification

C. Microstructure

The 3 batches of material had small differences in microstructure and chemical composition. Table 7.1 outlines the constituent compositions of the three batches with the most notable differences pertaining to batch 3. Batch 3 showed trace amounts of Copper, Cobalt and Aluminum, while none were identified in batches 1 and 2. Batch 3 also showed no Sulfur content and a small increase in Titanium content. When comparing the microstructure of the plates, plates 1 and 2 showed very similar microstructures with an equiaxed grain structure in all plate directions, with an average grain size of 38±3μm. The equiaxed grain structure from plate 1 is shown in Figure 7.13. This figure was generated from images of all 3 orientations of the grain structure. The grain structure of batch 1 is representative of plate 2 material as well [29].

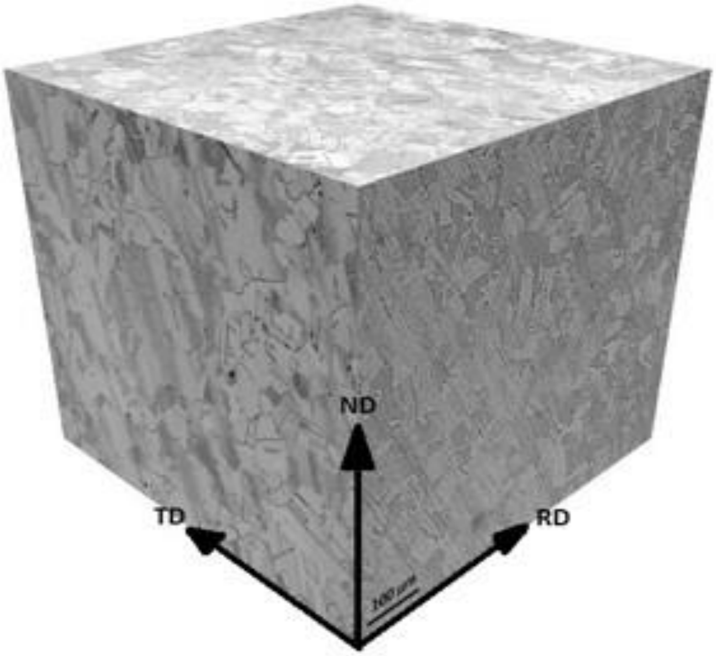

Figure 7.13: Plate 1 Microstructure (Representative of Plate 2)

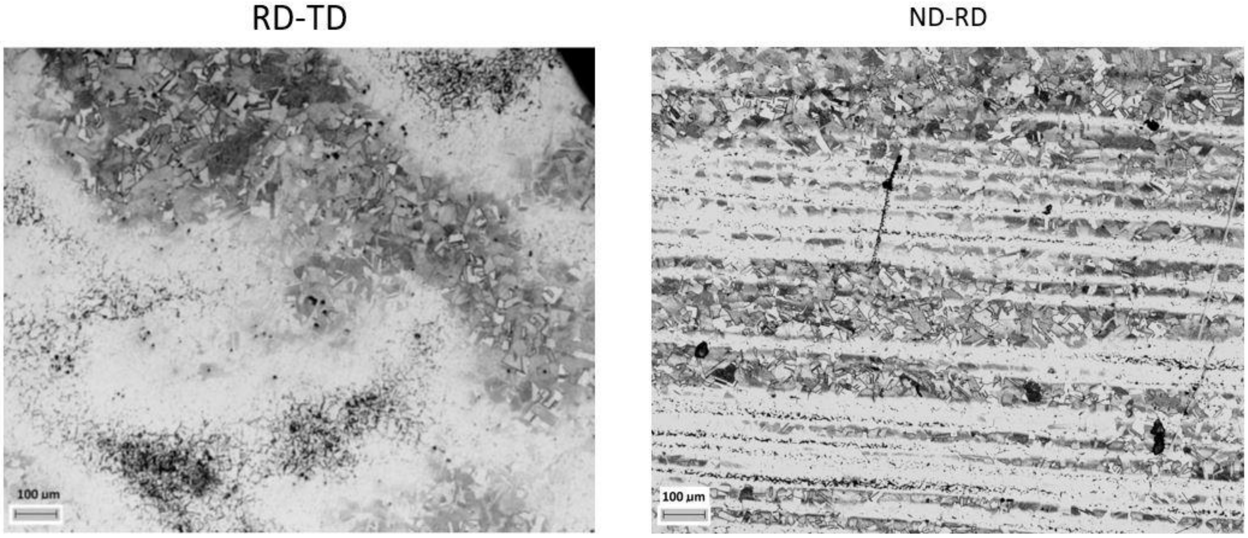

Figure 7.14. Plate 3 Microstructure.

Plate 3 material had microstructural differences from that of plates 1 and 2, Figure 7.14. A varying grain size through the thickness of the plate was observed; most notably, on the normal-rolling directions (ND-RD) plane. The rolling-transverse directions (RD-TD) plane shows the banded structure from on end. For batch 3, there was increased grain size variation compared to batches 1 and 2. The grains size of batch 3 had a larger range of grain sizes with a similar magnitude as plates 1 and 2 at 38±6μm. Specimens were machined from the plate with the crack plane oriented perpendicular to the banded grain structure. With the crack plane perpendicular to the banding, crack growth propagated through an average of the grain sizes.

Since variation in the microstructure of the as-received material was only seen in the third batch of material, it is reasoned that there was an anomaly with the solution annealing process. Since the third plate of material received was also the largest, it is possible that solution annealing was not achieved to the same level as previous plates of material through the full thickness. There was an increase in the presence of additional constituents in the plate 3 material; however, it was still within set specifications for Alloy 709. For batches 1 and 2, $M_{23}C_6$ precipitates were shown to develop in the microstructure to strengthen the material under creep loading [29]. Overall, while the microstructure showed variations in grain size uniformity, the average grain and microstructural characteristics remained similar. Specimens from the third batch were machined from the ND-RD plane of the plate. Machining specimens from the plate in this manner placed the banded grain structure perpendicular to the plane of crack growth; thus, the crack propagated through an average of the grain structure bands.

Crack growth rates of batch 3 for both FCG and CFCG loading profiles presented no differences. The variation in the microstructure did not appear to have any detrimental effects on either FCG or CFCG rates at the conditions tested.

7.8.2. Fatigue/Creep-Fatigue Comparison

For the 3 batches of material, a total of 54 specimens were tested. Of these, 15 were tested under CFCG loading, 10 of them with a 60s hold time and 5 of them with a 600s hold time (intermittent procedure). Under FCG loading, a total of 17 specimens were tested at an R ratio of 0.1 for comparison to CFCG. Of the 17 FCG samples, 2 were tested at low frequency (0.01667 Hz) to simulate equivalent cycle time to the CFCG 60s hold tests. The remaining specimens were tested under various other conditions and are discussed in later sections.

A. Crack Growth Rates (Fatigue/Creep Fatigue Comparison)

Creep-Fatigue crack growth in Alloy 709 showed only minimal effect on crack growth rates at various temperatures. Figure 7.16 shows CFCG and FCG data from Batch 2 material at 600°C and 700°C. At a hold time of 60s and 600°C, crack growth rates showed no difference compared to FCG over the tested range. For the entire test range of *ΔK* there is strong overlap of the CFCG rates as compared to FCG. Likewise, at 600°C, the decreased cycle frequency of 0.01667 Hz had no appreciable effect on the crack growth rates where there is again overlap of the FCG (0.01667 Hz) with regard to the FCG (15 Hz). For both the FCG (0.01667 Hz) and 60s CFCG, the tests were started at a higher *ΔK* in order to minimize overall test time. These results suggest that alloy 709 behaves as a creep-brittle material at temperatures as high as 600°C.

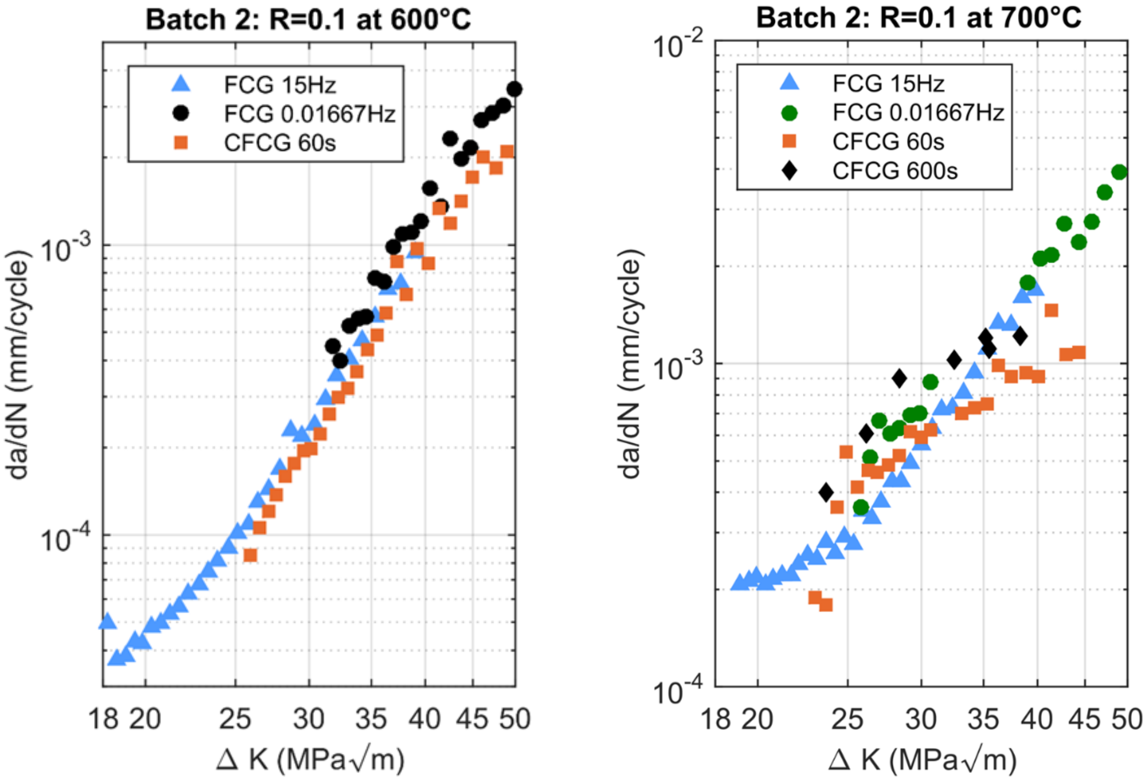

(a) *(b)*

Figure 7.15. Crack growth rates in Batch 2 material at (a) 600°C and (b) 700°C.

At 700°C, crack growth rates showed some distinction between test frequency and hold time. For CFCG with a 60s hold, there is an increase in crack growth rates at low *ΔK* relative to the 700°C FCG rates at 15Hz. However, as *ΔK* increased the crack growth rates began to tail off and crack growth rates became slower relative to the FCG rates. Thus, crack growth rates for the 60s hold CFCG transition from faster than FCG (15 Hz) to slower at a *ΔK*≈30 MPa√m. The rate reduction for the 60s hold is a factor of 2 slower than the FCG (15 Hz) loading profile at a *ΔK*≈45 MPa√m. When the hold time was increased to 600s, there was again an increase in crack growth rates relative to FCG at low *ΔK* that decreased at higher *ΔK*. The crack growth rates of the 600s hold time were greater than the 60s hold times by at most ≈30% over the tested range of ΔK's. The decreased frequency FCG (0.1667 Hz), showed a slight increase in the crack growth rate over the 15 Hz. The 0.1667 Hz loading merge in with the 15 Hz loading by a $\Delta K \approx 35$ MPa√m. The gap in data for this test was due to a computer error that temporarily halted data collection.

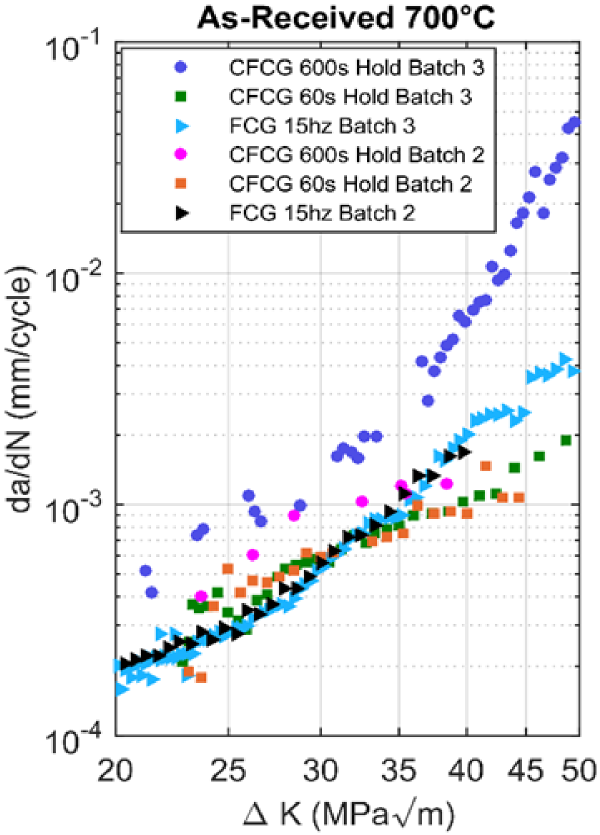

Figure 7.16. FCG and CFCG rates in Batch 2 and 3 material at 700°C

Between FCG and 60s CFCG the difference in crack growth rates is likely attributed to the increase in secondary cracking. At lower stress intensities, secondary cracking was small and did not hinder crack growth. Thus, at lower stress intensities, $\lesssim$25 MPa√m, the crack growth rates are similar or marginally higher between loadings. As the stress level increased, secondary cracking and crack tip blunting was observed. These combine to absorb much of the energy at the tip of the crack to decrease the driving force. The various EBSD scans and fracture surface imaging confirm the increase in depth and severity of the secondary cracking during loading. The decrease in driving force translates into a slower primary crack growth rate with an increase in gross plastic deformation at higher stress levels. This will be discussed in more detail in 4.2.2-4.2.3. Batch 1 and 2 experimental data has shown strong agreement with modeling efforts at the University of Idaho (UI). Modeling of crack growth rates at 700°C for FCG, CFCG (60s and 600s Hold) generate *da/dN vs ΔK* curves similar to the experimental data collected to date [30].

Batch 3 600s hold tests generated different results than the batch 2 tests. For both FCG and CFCG (60s hold), batch 2 and 3 tests coincided well with one another. However, for the 600s hold time, batch 3 material had drastically higher crack growths rates in comparison to batch 2 600s hold CFCG and both batch 2 and 3 60s hold CFCG. With respect to FCG in batches 2 and 3, the 600s hold time demonstrated crack growth rates that were at minimum 2 times as fast. Unlike 60s and 600s tests for batch 2, the crack growth rate did not slow at the higher stress intensities; rather, the slope of the *da/dN vs. ΔK* curve was similar or steeper to the FCG curves.

The increase in crack growth rates of batch 3 over batch 2 material is likely a result of increased proficiency with the intermittent loading procedure; however, batch 2 contained a limited quantity of data for valuable conclusions. The intermittent hold time procedure results for the 600s hold times indicate a net increase in growth rate at all *ΔK*. With crack tip blunting and secondary cracking playing a significant role in the crack growth rates of CFCG it is possible that the intermittent hold procedure created increased crack growth rates during the 600s hold testing intervals. Between CFCG loading cycles, the FCG loading generates a sharp crack tip. If the crack tip blunting plays a significant role in reducing crack growth rates, the sharp crack reformation would likely accelerate the crack growth rate. However, the increased growth rates would appear for a short transient zone where after crack growth rates would stabilize for the tested *ΔK*. From a *ΔK*≈37MPa√m and beyond the tests were conducted as a constant CFCG loading profile without intermittent increases. This suggests that the earlier trend of increased crack growth rates over FCG and CFCG is a result of the 600s hold time and not an artifact of the intermittent hold time procedure. Without running a full length 600s test from start to finish this cannot be verified for the lower *ΔK* values. The increase in crack growth rates *da/dN* for the 600s hold suggests that crack growth rates at temperatures of 700°C are time dependent with crack propagation during the hold period. These results are similar to those from Michel et al with 316 and 304 stainless steels [23], and Saxena with P91 in [17]. The time dependence of Alloy 709 is far lower than results found in these studies for 316, 304 and P91.

B. Fracture Surface (Fatigue/Creep Fatigue Comparison)

Macroscopically, CFCG specimens displayed a much rougher topography than did the FCG samples. Secondary cracking increased overall deformation of the fracture surface. Under CFCG loading profiles, secondary cracking and fracture surface deformation increased with hold time. This increase in topography is especially visible at longer crack length, higher *ΔK*, as seen in Figure 7.17. Both samples shown, under FCG and CFCG utilized constant amplitude loading over the same stress range.

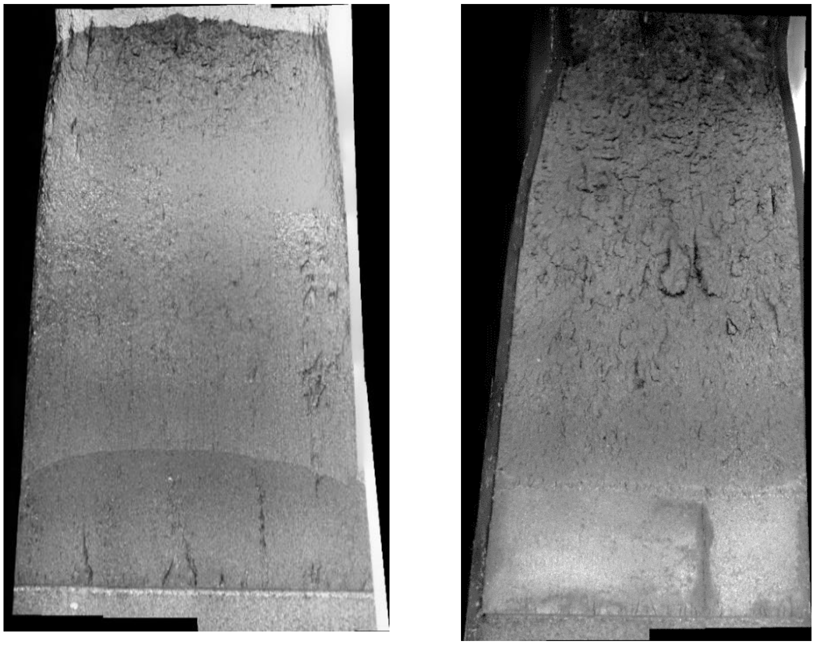

(a) (b)

Figure 7.17: Macroscopic fracture surface, Batch 2 Macroscopic fracture surface at 700°C (a) FCG at a frequency of 15hz, (b) CFCG with hold time of 60s hold.

Comparison of the fracture surfaces between FCG and CFCG with SEM imaging presented numerous surface differences. Fatigue striations were consistently observed at *ΔK* greater than 25MPa√m at all temperatures tested. Additionally, there was significant secondary cracking observed, particularly at higher *ΔK* values. For FCG, the secondary cracking appeared to occur both parallel and perpendicular to the direction of crack growth, Figure 17.18a, while the secondary cracks under CFCG appeared predominantly perpendicular to the direction of crack growth, Figure 7.18b. CFCG showed more pronounced secondary cracking and striations than did the FCG and are more apparent at higher magnifications. Figures 7.18c and 7.18d show

1000x magnification at the higher stress intensity range, *ΔK*≈35MPa√m. These figures further demonstrate the increase in size and depth of the secondary cracking under CFCG conditions.

The low frequency FCG (0.01667Hz) fracture surfaces showed similar striation regions as FCG and CFCG. There was a small increase in the quantity of secondary cracking and fracture surface topography as compared to FCG at 15Hz; however, to a lesser extent than CFCG at equivalent *ΔK*. Figure 4.9 shows striations and secondary cracking of the low frequency FCG in direct comparison to the FCG (15Hz) and CFCG figures previously shown. Crack growth appeared entirely transgranular for all loading conditions.

At 700°C, secondary cracking reduces the driving force at the crack tip and thus reduces the crack growth rate; however, as the hold time increases, the creep zone increases and encompasses the cyclic plastic zone. When fully enveloped within the creep zone, creep crack growth extension occurs during the hold time and secondary cracking from the primary crack plane is insufficient to retard all creep crack extension.

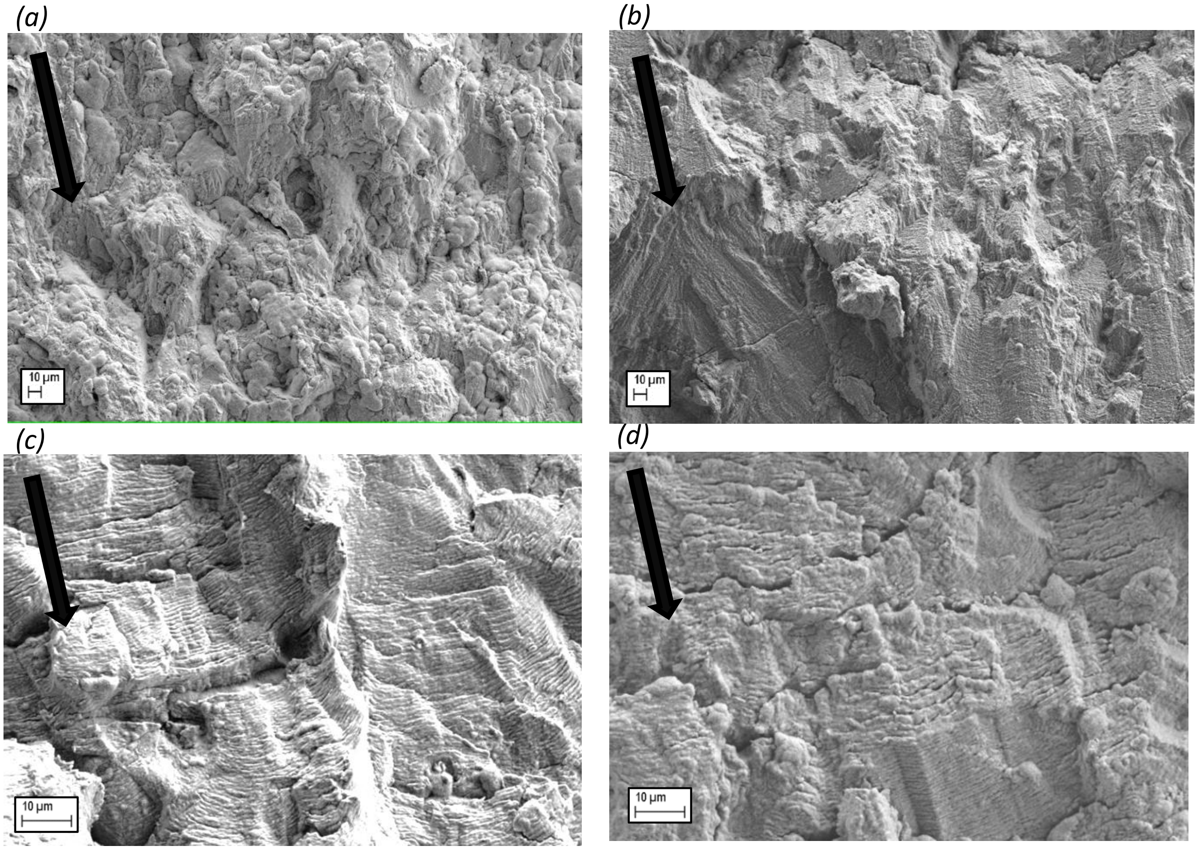

Figure 7.18. (a) FCG, 15Hz, R=0.1 and (b) CFCG 60s hold at 700°C and *ΔK*≈25MPa√m at 250x magnification and (c) FCG, 15Hz, *R*=0.1 and (d) CFCG, 60s hold at 700°C and *ΔK*≈35MPa√m at 1000x magnification

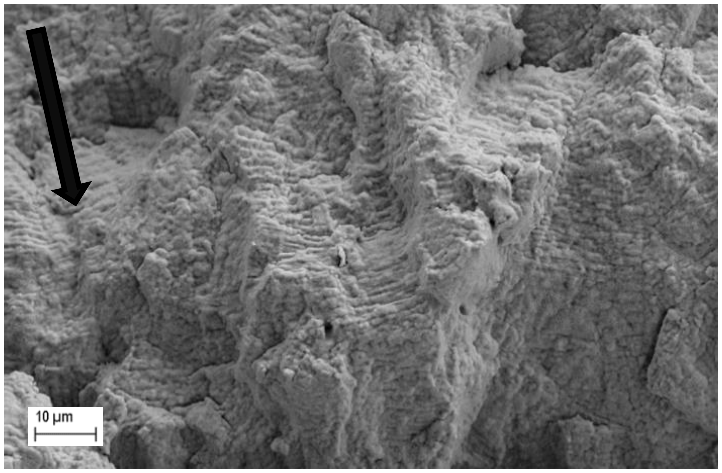

Figure 7.19. FCG (0.01667 Hz) 700℃ , *ΔK*≈35MPa√m, 1000x magnification

C. Microstructure/EBSD Scans (Fatigue/Creep Fatigue Comparison)

Metallography was performed on the specimens' post rupture. The CFCG specimen crack profiles have a significant increase in secondary cracks especially at higher stress intensities. Figure 7.21 shows the crack profile of three separate test conditions at equivalent *ΔK* values of 25 MPa√m. When comparing secondary cracks between FCG and CFCG at this *ΔK*, larger secondary cracks were evident with CFCG loading profiles along with an increase in additional crack branching from the secondary cracks. This was observed for both 60s and 600s CFCG hold times and predominantly at higher stress intensities (≥25MPa√m). All primary and secondary cracks continued to remain transgranular in nature. The final distinction between the crack profiles and surrounding grain structure is the increase in small grain formation from FCG to CFCG. As the hold time increased at a given *ΔK*, there was an increase in secondary grain formation. This can be seen in Figure 7.21 as the hold time is increased. The concentration of grain boundaries is increased in c compared to b, and b compared to a.

EBSD scans confirm this observation, Figure 7.20, which shows grain boundary misorientation maps of the FCG and CFCG specimens. In these maps, the red concentrations represent low angle boundaries, between 2° and 15° and the black lines show the high angle grain boundaries, greater than 15°. The concentration of low angle boundaries is noticeably greater around both the 60s and 600s CFCG main and secondary cracks in comparison to the

FCG cracks. Another important observation from the EBSD maps is confirmation that crack growth is primarily transgranular, where cracks propagated fully across grains for both the

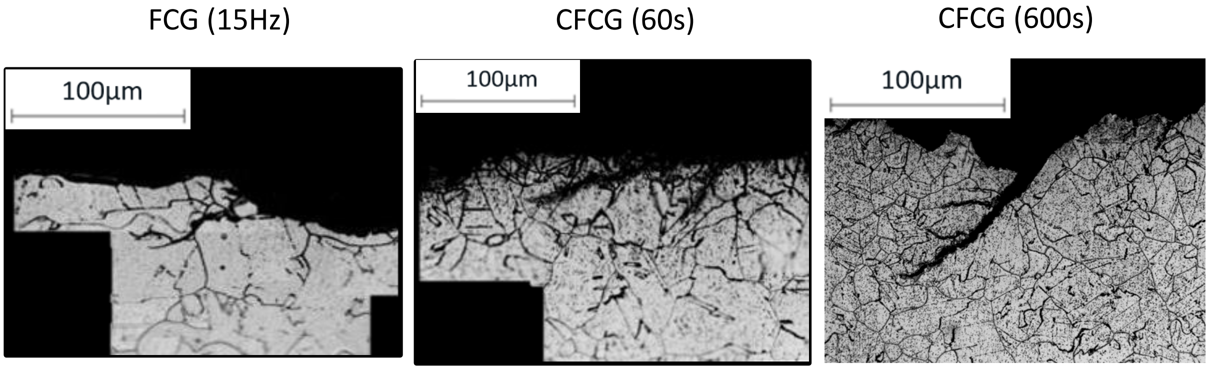

(a) (b) (c)

Figure 7.20. Optical Crack Profiles, left to right, (a) FCG(15 Hz), (b) CFCG(60s hold), and (c) CFCG(600s hold) at a $\Delta K \approx 25 \mathrm{MPa}\sqrt{\mathrm{m}}$

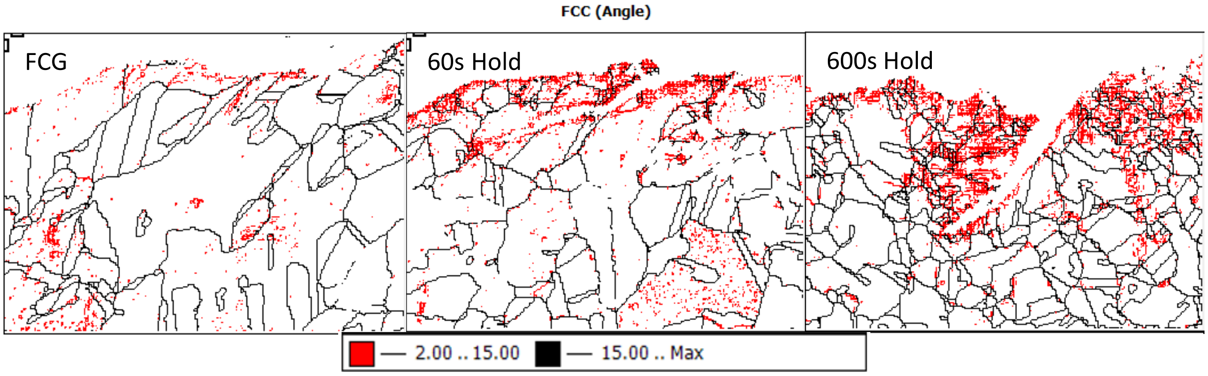

(a) (b) (c)

Figure 7.21. EBSD maps of grain boundary misorientation: (a) FCG (15 Hz), (b) CFCG(60s hold), and (c) CFCG(600s hold) at a $\Delta K \approx 25 \mathrm{MPa}\sqrt{\mathrm{m}}$.

Figure 7.21 quantifies the concentration of the low angle grain boundaries as a percentage of the total boundary angles recorded. From this figure there is a notable increase in the concentration of grain boundaries 4° and less. From FCG to CFCG the percentage of these low angle boundaries increases from ≈23% to ≈35% while there is a near equivalent decrease in higher angle grain boundaries of ≈60° or greater. From the previous EBSD scans, visually there is an increase in low angle boundaries. When quantified into a percentage of total grain boundaries, the increase in low angle boundary concentration is not as noticeable between the 60s and 600s hold times as there is an overall increase in the quantity of grain boundaries resulting from the increased secondary grain formation. As a result, there are many more grain boundaries in the 600s hold time as compared to the 60s hold time both with small angle grain boundaries and large angle boundaries.

Inspecting the fracture surface and crack profiles, the concentration of low angle grain boundaries remains similar and small grain formation increases between the 60s and 600s hold times. The grain boundary orientation maps show a distinct increase in low angle grain boundaries resulting from CFCG loading profile. The low angle grain boundaries are indicative of new, small subgrain formation and dislocation motion. This formation and dislocation motion are a result of cumulative damage at the crack tip. These EBSD images are in line with the crack growth rates; as the hold time is increased there was an increase in fracture surface damage, yet the overall crack growth rates did not show a great increase. Overall, this suggests that the increase in damage at the crack surface is dissipating much of the energy at the crack tip outward from the crack plane rather than forward through the crack plane.

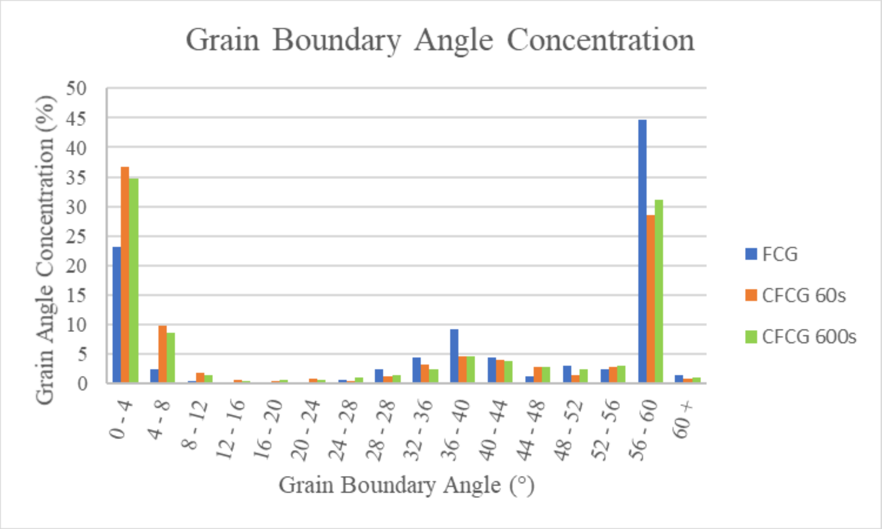

Figure 7.22. Grain boundary angle distribution corresponding to EBSD scans at $\Delta K \approx 25 \mathrm{MPa}\sqrt{\mathrm{m}}$

7.8.3 Material Aging Affects

Material aging affects were investigated for both FCG (R=0.1 only) and CFCG (60s hold) conditions. In the as-received condition, four FCG tests were performed at 700°C and three were performed at 550°C. For 60s hold CFCG as-received, two tests were performed at 700°C and one was run at 550°C. In the aged 1 condition, two FCG tests each were conducted at temperature of 550°C and 700°C, and 60s hold CFCG tests were conducted at temperatures of

550°C and 700°C. Finally, in the aged 2 condition, four tests total were performed, one test at each temperature, 550°C and 700°C, for each loading profile, FCG and 60s hold CFCG.

Crack Growth Rates (Material Aging Affects)

Aged conditions of batch 3 had little effect on crack growth rates. For both FCG and CFCG (60s) at 550°C and 700°C, the data fell within a narrow scatter band with a variance of less than a factor 2 throughout the *ΔK* range. Figure 7.23 presents crack growth data at both 550°C (Figure 4.13a) and 700°C (Figure 4.13b). As seen for both FCG and CFCG, there is only marginal variations in crack growth rate between aged samples without a clear trend for either loading.

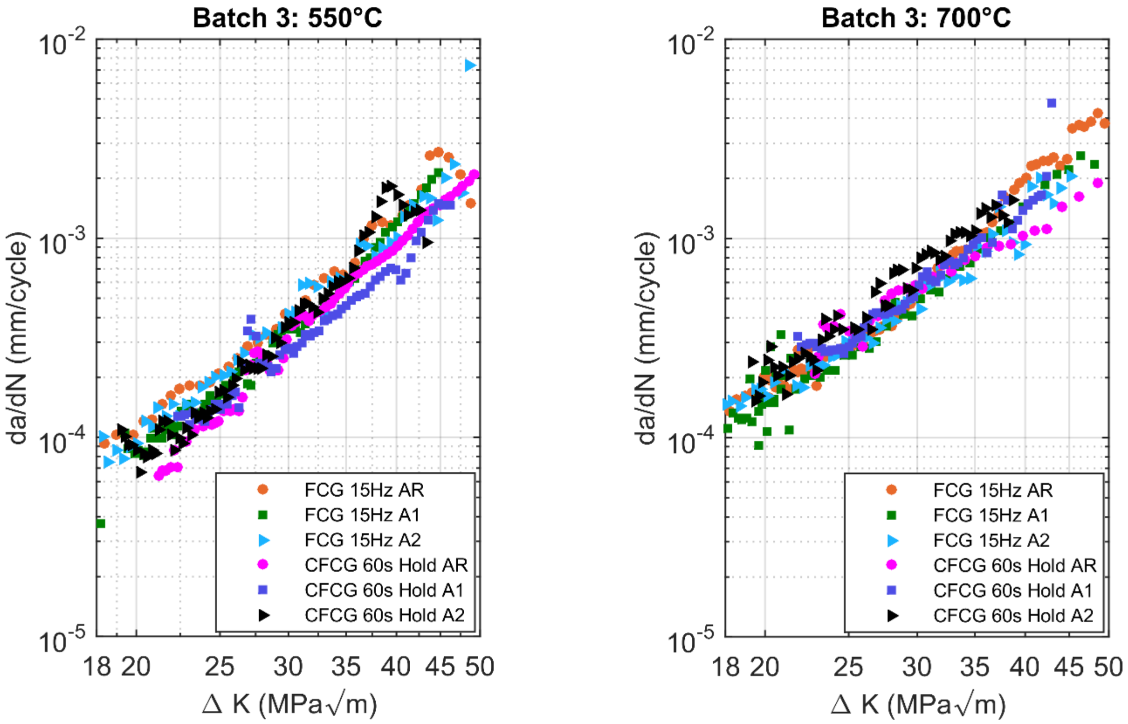

(a) *(b)*

Figure 7.23. Batch 3 aged material comparison, FCG at a 15Hz and CFCG with 60s Hold time: (a) 550°C, (b) 700°C.

For both FCG and CFCG loading the data falls within a narrow band. The ageing schedules, 3 months at 650°C and 6 months at 650°C, predicted an increase in the amount of σ phase into the microstructure. Preliminary analysis by the metallurgical department demonstrated a marked increase in strain rates and an increase in σ phase after aging [29]. σ phase is detrimental to the creep strength of stainless steel alloys. From the creep testing conducted, this appears to be the case [29]. For FCG at the tested *R*-ratio of 0.1 and temperatures of 550°C and

700°C, aging appears to not effect crack growth rates. However, in terms of CFCG (60s Hold) there was an increase in growth rates for the aged 2 condition. The aged 2 condition, at both 550°C and 700°C there was a slight shift in crack growth rates. For both test temperatures, the aged 2 condition crack growth rates were at the upper band of the scatter band for all tests at their respective temperatures. There is an increase in crack growth rate volatility with the aged samples and it is possible that σ phase formation resulted in increased growth rates within sections of the specimen as the aged CFCG tests appeared to have sections of increased scatter for *da/dN*. From a FCG stand point, there is little evidence to support that the aged conditions of the material had any effect on the crack growth rates. In contrast to alloys such as 316, Michel et al. showed a decrease in crack growth rates after ageing by nearly a factor of two [23]. Alloy 709 does not exhibit any significant difference in crack growth rate with thermal ageing. The behavior after thermal ageing of Alloy 709 behaves more closely to alloy 304 which demonstrated no effect in crack growth rates from simulated service life conditions [23].

Comparing FCG fracture surfaces at both 550°C and 700°C there was little observed difference. Figures 7.24 are representative of the fracture surface of the FCG tests in the as-received, aged 1, and aged 2 conditions. All 3 conditions showed similar fracture surface topography, striations and secondary cracking on the fracture surface when compared at equivalent ΔK regions at 700°C.

Furthermore, comparing the aged conditions for FCG at 550°C, the fracture surface topography, striations and secondary cracking were similar between the batches as at 700°C. At both 550°C and 700°C samples displayed striations on the fracture surface that coincided with crack growth rate at any given ΔK; however, secondary cracking was different. At 550°C secondary cracking had a decrease in depth and overall deformation but an increase in quantity. The increased quantity and decreased depth of secondary cracking is likely a result of work hardening at the crack front. As shown by Upadhayay et al, Alloy 709 work hardens at temperatures below 650°C [31]. This work hardening effect lends towards the creep-brittle nature of Alloy 709 at the tested temperatures. The fracture surface of the as-received condition at 550°C FCG loading is presented in Figure 7.25.

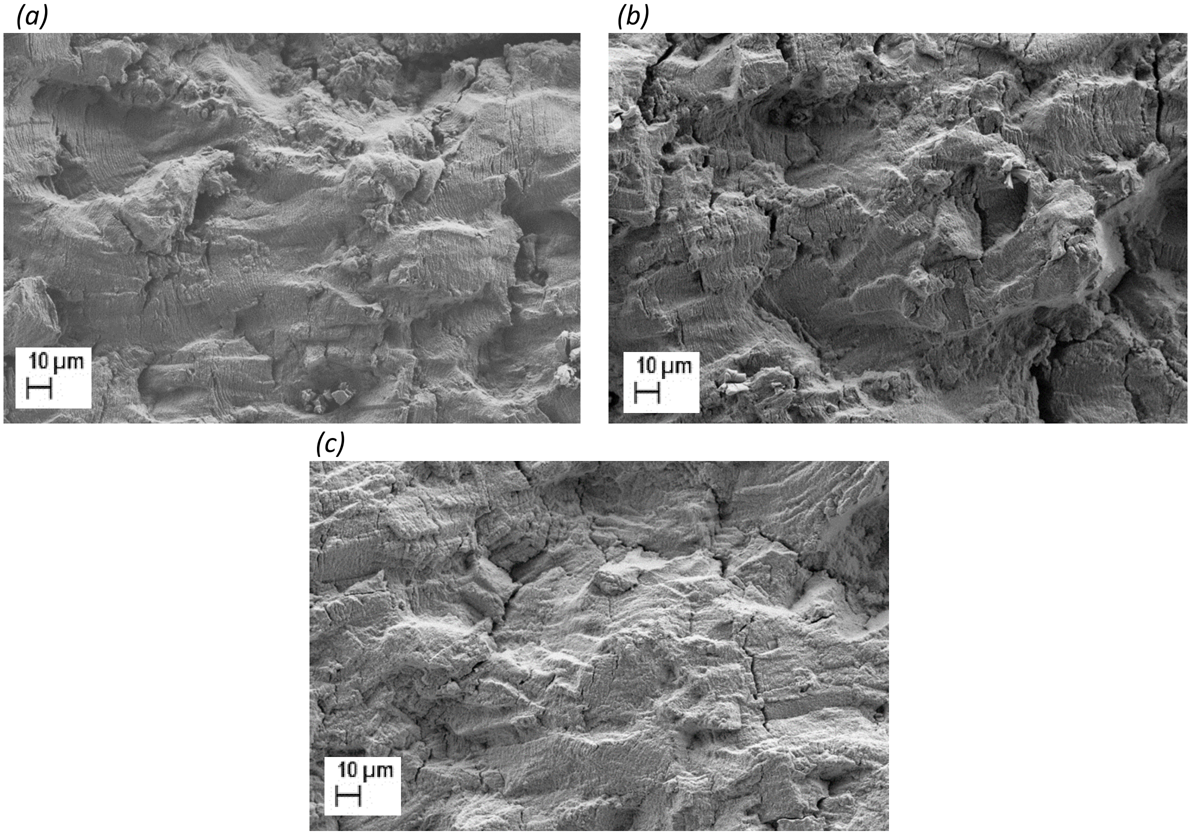

Figure 7.24. FCG 700℃ fracture surfaces, 500x magnification at a $\Delta K \approx 35 \text{MPa}\sqrt{\text{m}}$, crack growth is right to left (a) as-received, (b) aged 1 condition, (c) aged 2 condition.

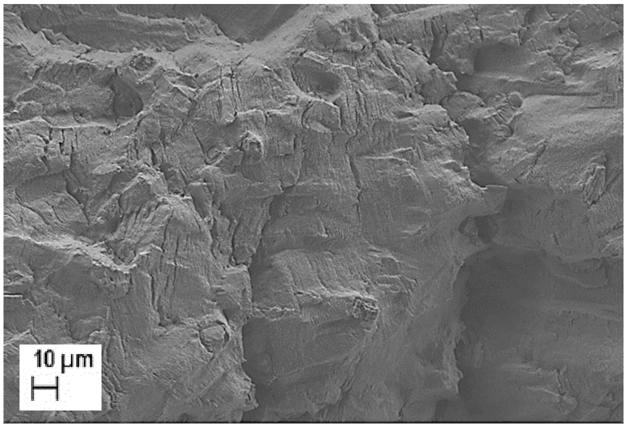

Figure 7.25. FCG 550℃ fracture surface, as-received condition, 500x magnification at a $\Delta K \approx 35 \text{MPa}\sqrt{\text{m}}$, crack growth is right to left

7.8.4. R-Ratio Affects

da/dN vs ΔK curves at 550°C and 700°C for different R-ratio (0.1,0.3,0.5,0.7) are shown in Figure 7.26. These two plots exhibit typical mean stress effects where higher R-ratios have growth rates faster for a given stress intensity range than lower R-ratios. As ΔK increased the R-ratios of 0.1, 0.3, 0.5, and 0.7 converged. As seen in Figure 7.26 a and b, the higher R-ratios of 0.5 and 0.7 exhibited similar crack growth rates, yet faster crack growth rates compared to R-ratios of 0.1 and 0.3. This trend is also shown in Figure 7.26b for a temperature of 700°C. The primary difference at 700°C was a decreased difference between the R-ratio curves of 0.1 and 0.3.

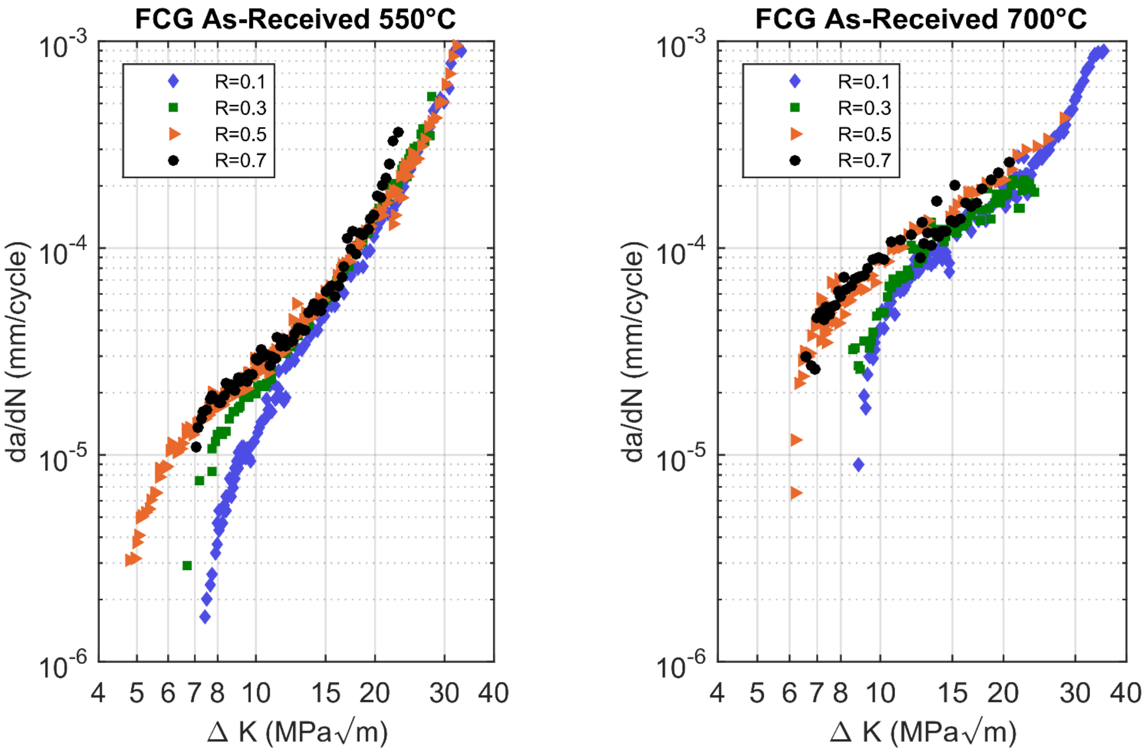

(a) *(b)*

Figure 7.26. FCG at a frequency of 15Hz for Batch 3 material in the As-Received condition at (a) 550°C and (b) 700°C

The R-ratio tests appear to fully merge at a $\Delta K \approx 15$ MPa√m for a temperature of 550°C, Figure 7.26a, and at a $\Delta K \approx 25$ MPa√m for a temperature of 700°C, Figure 7.26b. At 550°C and at all R-ratios, crack growth rates continued to decrease as the stress intensity was decreased in the near threshold region. The slope of the da/dN vs. ΔK curve at 550°C is shallower in the near threshold region than at 700°C. At 700°C crack growth rates decreased rapidly after reaching a crack growth rate of approximately 10^{-5} mm/cycle. The steep slope of the *da/dN* vs. ΔK curve at 700°C was observed at all *R*-ratios. The slope became nearly asymptotic near 10^{-5} mm/cycle, where upon an additional 10^{6} cycles were applied after apparent crack retardation to confirm crack arrest at *R*-ratios of both 0.1 and 0.5. Although crack growth rates of 10^{-7} mm/cycle were not directly achieved due to the rapid arrest of the crack, threshold stress levels for R=0.1 loading at 550°C and 700°C appear to be $\Delta K \approx 7$ MPa√m and $\Delta K \approx 8$ MPa√m respectively. With no apparent crack closure at R=0.7, the ΔK_{eff} threshold stress appears to be $\Delta K_{eff} \approx 4$ MPa√m and $\Delta K_{eff} \approx 6$ MPa√m for 550°C and 700°C respectively.

The data is plotted in terms of ΔK rather than ΔK_{eff}. Higher crack growth rates at low ΔK for *R*-ratios of 0.5 and 0.7 indicate that crack closure is most likely present at *R*-ratios of 0.1 and 0.3. Different *R*-ratios resulted in different crack growth rates in the FCG curves at equivalent ΔK. Growth rates at both 550°C and 700°C showed a decrease in the crack growth rate curves at R=0.1 and R=0.3 relative to R=0.7; however, the difference was less exaggerated between 0.5 and 0.7. At R=0.7, crack closure is likely only present at very low stress intensities or not at all). It is apparent that the R curves merge quickly with one another. At 550°C, all *R* curves merge by $\Delta K \approx 15$ MPa√m and at 700°C the curves merge by $\Delta K \approx 25$ MPa√m. Merging of these curves indicates that crack closure is nearly eliminated at all *R*-ratios at the respective ΔK. As expected the higher *R*-ratios of 0.5 and 0.3 merge more quickly than the *R*-ratio of 0.1. Crack growth data is in strong agreement with current simulation and modeling efforts. Current simulations conducted at the UI utilizing a strip-yield model predict similar opening loads as the experimental results [32]. The modeling efforts are in agreement with previous work from Wang and Blom [33]

7.8.5. Fracture Surfaces (R-ratio Affects)

Fracture surfaces showed differences between *R*-ratio loading profiles. At 700°C, differences in the fracture surface are the most pronounced. As *R*-ratio increased the fracture surface topography and depth of secondary cracking increased. There was an increase in topography and secondary cracking at *R*-ratios of 0.3, 0.5 and 0.7 compared to R=0.1. The differences are most pronounced between R=0.1 and R=0.7 as seen in Figure 7.27. The increase in secondary cracking depth resulted in increased surface topography that is noticeable microscopically, though to a lesser extent than the 60s hold CFCG loading. At a temperature of 550°C the same trend of increased topography and secondary cracking develops although the increase was less pronounced. These images are characteristically similar to the fracture surfaces at 550°C and *R*-ratios of 0.1 and 0.7.

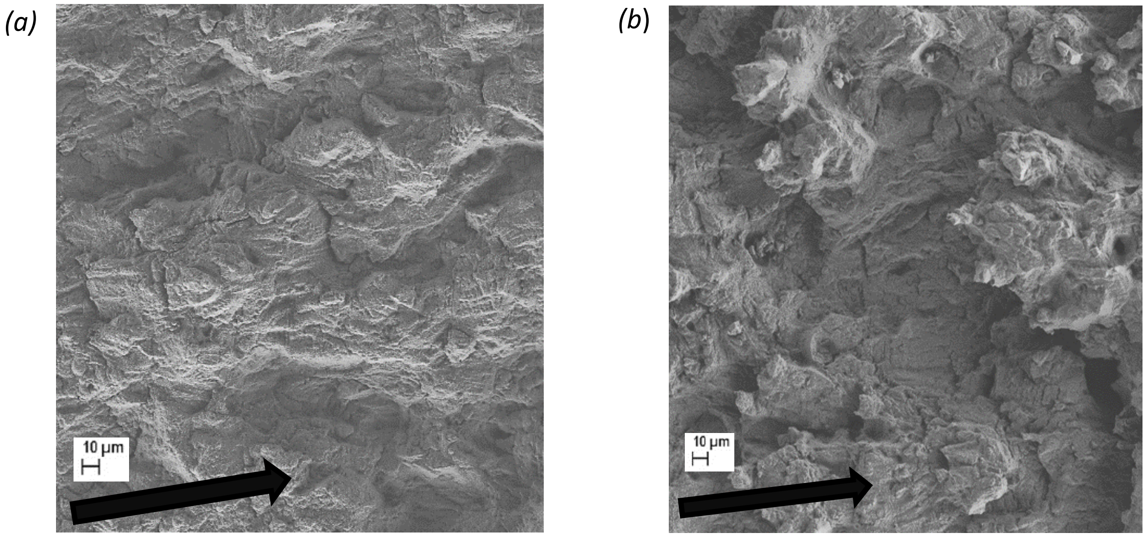

Figure 7.27: Batch 3 As-Received material at 700°C and $\Delta K \approx 25$MPa√m and 250x Magnification (a) FCG R=0.1 and (b) FCG R=0.7

Fracture surfaces differences were a direct result of the increased mean and maximum loads applied to the specimen. Similar to the CFCG loadings, the increased time of crack opening resulted in increased fracture surface topography due to increased secondary cracking prevalence and depth. Analysis of the crack plane utilizing EBSD scans would likely result in similar conclusions to CFCG loading; increased *R*-ratios would result in increased low angle grain boundary concentrations and small grain formation.

7.9. Conclusions

7.9.1. Batch variations

Batch 2 and 3 material exhibited similar crack growth rates as one another under both FCG and CFCG Loading profiles. Batch 1 had crack growth rates that differed from batch 2 and 3, where the da/dN *vs.* ΔK curves for batch 1 had different slopes compared to batches 2 and 3. Batch 3 material had a large variance in grain size and a banded grain structure of smaller and larger grains. Although there were microstructural differences in batch 3, they did not show an appreciable effect on crack growth behavior in Alloy 709. Microstructure of the as-received material for batch 3 was likely a result of a failure in the solution annealing process. Fracture surfaces of both FCG and CFCG between the batches of material were similar except for the presence of an oxide on the early batch 1 and 2 specimens resulting from the new furnace burn in.

7.9.2. Creep-Fatigue Loading Comparisons

CFCG loading with a 60s hold time showed little effect on crack growth rate at 600°C and 700°C. At 600°C there was no effect on crack growth rates with the 60s hold time or slow frequency loading. At 700°C there was a small change in slope of the da/dN *vs* ΔK curves with the 60s hold loading. Batch 2 material yielded insufficient results for analysis of the 600s hold time loading. With batch 3 material, the CFCG 600s hold time showed increased crack growth rates in Alloy 709 when tested using the intermittent hold time procedure. Crack growth behavior for CFCG appeared creep-brittle in nature and was characterized in terms of ΔK. When comparing optical and EBSD micrographs, grain boundary orientation shows a distinct increase in low angle boundary and small grain formation with CFCG loading as compared to the FCG. For 60s hold times, small grain formation and secondary cracking serve to absorb much of the driving force at the crack tip during the hold period of CFCG loading and decreases crack growth rates (da/dN) at ΔK>30MPa√m and 700°C. Crack growth was transgranular for both FCG and CFCG. The 600s hold time CFCG loading showed increased crack growth rates over FCG by, at minimum, a factor of 2.

7.9.3. Material Aging Affects

For both FCG and CFCG (60s Hold) loading profiles, thermal ageing had no substantial effect on crack growth rates. At temperatures of both 550°C and 700°C, da/dN vs. ΔK fell within a narrow scatter band with scatter less than a factor of 2 throughout the full range of ΔK. Alloy 709 reacts to simulated service ageing similar to Alloy 304 when compared to data collected from [23]. Crack growth rates for CFCG at 700°C showed the most volatility in crack growth rates. At both tested temperatures the aged 2 material presented the highest crack growth rates over the as received conditions. Investigating the fracture surfaces between aged specimens showed no difference as a result of ageing regardless of load profile. All fracture surfaces displayed secondary cracking and fracture surface topography consistent with the as received material at the testing temperature.

7.9.4. R-ratio Affects

Alloy 709 displays typical mean stress effects. Crack closure was effectively eliminated by R=0.7 and potentially as low as an R=0.5. The effect of crack closure diminishes with increasing ΔK and the R-ratio curves merge quickly, at a $\Delta K \approx 15$ MPa√m for 550°C and at a $\Delta K \approx 25$ MPa√m for 700°C. The experimental crack growth data generated is in strong agreement with current simulation and modeling efforts, where closure is nearly eliminated by an R-ratio of 0.5. Near threshold data suggests that the threshold ΔK for 550°C is ≈7 MPa√m and at 700°C threshold ΔK is ≈8 MPa√m for an R=0.1. Fracture surface topography and secondary cracking increased with the increased R-ratio loading.

7.10. Recommendations

The results suggest that Alloy 709 has high temperature strength characteristics that are suitable for nuclear reactor applications. Prolonged thermal ageing of the alloy does not appear to affect the crack growth rates under various FCG and CFCG loading conditions. The CFCG loading with 60s hold times appear to have a negligible effect on the crack growth rates. There is some question as to the longer hold time effects on the crack growth rates. Because of the small sample size and of tests at prolonged hold times, it is advisable to, firstly validate the intermittent testing procedure for this alloy, and secondly, perform more CFCG tests at various hold times to investigate the effects of longer hold times. Microstructurally, analysis of microstructural precipitates should be invested with the batch 3 material to verify the mechanisms causing an increase in crack growth rate at longer hold times.

If characterization of crack growth under CFCG conditions by means of $C(t)_{avg}$ is desirable, precise measurement of crack mouth opening would be required. Load line displacement measurement during hold times, if ample resolution could be achieved, would allow accurate characterization of the growth rates as a function of $C(t)_{avg}$. Accurate measurement of load line displacement would remove uncertainty in the C_{ssc} calculations resulting from uncertain Norton constants A and n.

R-ratio testing at elevated temperatures could yield valuable information in terms of ΔK_{eff} if load line displacement measurements had resolution sufficient to record crack opening with respect to load. The capability to measure with sufficient resolution within the testing chamber would require a high temperature extensometer that has a sufficient clipping force at the specimen mouth to ensure proper measurement and in phase comparison to loading. It would be recommended to analyze the crack plane of the R ratio tests utilizing optical microscopy and potentially EBSD scans for comparison between R ratios.

For increased resolution of the crack length measurement, a switching DCPD setup would offer many advantages. Switching DCPD takes a measurement in both the forward current and reversed current directions. By reading a voltage in both the forward and reverse current orientation and averaging the readings, thermal effects are and overall noise from the current signal would be canceled. Along with switched DCPD, digital information from the multimeter should be sent to the computer via digital RS 232 communication. Current analog reading of the voltage from the DCPD system increases noise and precision loss through multiple conversions. Additionally, switched DCPD or an ACPD (Alternating Current Potential Drop) would allow for increased environmental testing under different environments or solutions without sacrificing resolution.

7.11. References

[1] L. Chengliang and Y. Mengjia, “The Challenge of Nuclear Reactor Structural Materials for Generation IV Nuclear Energy Systems,” p. 8.

[2] F. Delage, J. Carmack, C. B. Lee, T. Mizuno, M. Pelletier, and J. Somers, “Status of advanced fuel candidates for Sodium Fast Reactor within the Generation IV International Forum,” *Journal of Nuclear Materials*, vol. 441, no. 1–3, pp. 515–519, Oct. 2013.

[3] G. Koo and J. Lee, “High temperature structural integrity evaluation method and application studies by ASME-NH for the next generation reactor design,” *Journal of Mechanical Science and Technology; Heidelberg*, vol. 20, no. 12, pp. 2061–2078, Dec. 2006.

[4] S. V. Evropin and V. M. Filatov, “Service-life analysis of nuclear reactor elements under high-frequency random loading,” *Atomic Energy; New York*, vol. 113, no. 4, pp. 258–264, Feb. 2013.

[5] "Sodium-cooled Fast Reactor (SFR) Technology and Safety Overview," Washington, DC, 18-Feb-2015.

[6] R. Stephens, A. Fatemi, R. Stephens, and H. Fuchs, *Metal Fatigue in Engineering*, Second. Wiley-Interscience, 2001.

[7] "ASTM E647-95a: Standard Test Method for Fatigue Crack Growth Testing." .

[8] "ASTM E-647.X1: Recommended Data Reduction Techniques." .

[9] "ASTM E2760-10e2: Standard Test Method for Creep-Fatigue Crack Growth Testing." .

[10] "MTS | Test systems, simulation systems and load frames." [Online]. Available: https://www.mts.com/en/products/producttype/test-systems/index.htm. [Accessed: 20-Aug-2018].

[11] "ASTM E-647.A2: Guidelines for Use of Complience to Determine Crack Length." .

[12] "ASTM E-647.A3: Guidelines for Electric Potential Difference Determination of Crack Size." .

[13] K. Sadananda and P. Shahinian, "Effect of Environment on Crack Growth Behavior in Austenitic Stainless Steels under Creep and Fatigue Conditions," NAVAL RESEARCH LAB WASHINGTON DC, NAVAL RESEARCH LAB WASHINGTON DC, Apr. 1979.

[14] K. Sadananda and P. Shahinian, "Prediction of threshold stress intensity for fatigue crack growth using a dislocation model," *Int J Fract*, vol. 13, no. 5, pp. 585–594, Oct. 1977.

[15] B. Hamilton, D. Hall, A. Saxena, and D. McDowell, "Creep Crack Growth Behavior of Aluminum Alloy 2519: Part 1-Experimental Analysis."

[16] M. C. Carroll and L. J. Carroll, "Fatigue and creep–fatigue deformation of an ultra-fine precipitate strengthened advanced austenitic alloy," *Materials Science and Engineering: A*, vol. 556, pp. 864–877, Oct. 2012.

[17] "Crack growth behavior of 9Cr−1Mo (P91) steel under creep–fatigue conditions," *International Journal of Fatigue*, vol. 56, pp. 106–113, Nov. 2013.

[18] A. Saxena, *Nonlinear Fracture Mechanics for Engineers*, First. CRC Press, 1998.

[19] J. L. Bassani, D. E. Hawk, and A. Saxena, "Evaluation of Ct Parameter for Characterizing Creep Crack Growth Rate in the Transient Regime," *Nonlinear Fracture Mechanics: Time-Dependent Fracture Mechanics*, vol. 1, pp. 7–29.

[20] V. Kumar, M. D. German, and C. F. Shih, "Engineering approach for elastic-plastic fracture analysis," General Electric Co., EPRI-NP--1931, 1981.

[21] S. J. Zinkle and G. S. Was, “Materials challenges in nuclear energy,” *Acta Materialia*, vol. 61, no. 3, pp. 735–758, Feb. 2013.

[22] T. Sourmail, “Precipitation in creep resistant austenitic stainless steels,” *Materials Science and Technology*, vol. 17, no. 1, pp. 1–14, Jan. 2001.

[23] D. J. Michel, H. H. Smith, and H. E. Watson, “Effect of Hold-Time on Elevated Temperature Fatigue Crack Propogation in Fast Neutron Irradiated and Unirradiated Type 316 Stainless Steel,” Naval Research Laboratory, Naval Research Laboratory, Washington D.C.

[24] “ASTM E1457-98: Test Method for Measurement of Creep Crack Growth Rates in Metals.” .

[25] “ASTM E466-96: Practice for Conducting Force Controlled Constant Amplitude Axial Fatigue Tests of Metallic Materials.” .

[26] “ASTM E21-92: Elevated Temperature Tension Tests of Metallic Materials.” .

[27] “ASTM E-399.A4: Special Requirements for the Testing of Compact Specimens.” .

[28] P. Malmqvist, “Monitoring of crack growth and crack mouth opening displacement in compact tension specimens at high temperatures,” Karlstads University, 2016.

[29] M. Taylor, “Creep and Microstructural Characterization of Advanced Austenitic Stainless Steel Alloy 709,” Thesis, University of Idaho, 2018.

[30] J. Ramirez, Private Communication.

[31] S. Upadhayay, H. Li, P. Bowen, and A. Rabiei, “A study on tensile properties of Alloy 709 at various temperatures,” *Materials Science and Engineering: A*, vol. 733, pp. 338–349, Aug. 2018.

[32] G. P. Potirniche, “Modeling and Simulation of R-ratio Effects on Alloy 709,” To be Published.

[33] G. S. Wang and A. F. Blom, “Strip model for fatigue crack growth predictions under general load conditions,” *Engineering Fracture Mechanics*, vol. 40, no. 3, pp. 507–533, 1991.

8 THERMODYNAMICS SIMULATIONS OF MICROSTRUCTURE EVOLUTION DURING AGING

8.1. Introduction

The development of novel alloys for service in aggressive environments (high temperature applications, radiation, different chemical atmospheres etc.) is critical for increasing the energy efficiency of the processes used to convert energy. This is true both for fossil fuel power plants and nuclear power plants.

Among the properties required of such materials are their mechanical response, including creep, fatigue, creep-fatigue, fracture toughness etc. In addition to the development of novel materials it is very important to obtain the best possible combination of properties out of the already existing alloys. Because alloys belong to the class of structural materials, their properties (including the ones listed above) could be modified / improved by the application of a thermo-mechanical treatment. It is clearly understood that austenitic steels (to which the recently developed Alloy 709 belongs) cannot be strengthened by a heat treatment. However, such properties as creep, creep-fatigue and creep fatigue crack growth can be manipulated by a single-step, or a cascade of, heat treatments.

One of the goals of the present project was to explore the different thermo-mechanical treatment of Alloy 709 samples to identify the best creep-fatigue performance. This important work cannot be performed on a purely experimental basis because the number of possible treatments starts growing very fast as more parameters are considered. Therefore, a strong need exists in obtaining guidance from high accuracy modeling tools such as Thermo-Calc (thermodynamics and phase equilibria simulation), DICTRA (diffusion modeling), PRISMA (precipitation modeling and construction of CCT and TTT diagrams for the different phases thought to play an important role in the Alloy 709's performance) and density functional theory (DFT) atomistic /electronic structure calculations (especially in those cases when the required thermochemical information is absent).

Yet another powerful tool that starts playing an ever-important role in such studies is data analytics. The largest database on fatigue and creep fatigue of different steels was developed by National Institute of Materials Science (NIMS) of Japan [1], which analyzed using different data analytics approaches [2]. The results, in term of the relative significance of different factors, are presented in Figure 8.1 [2]

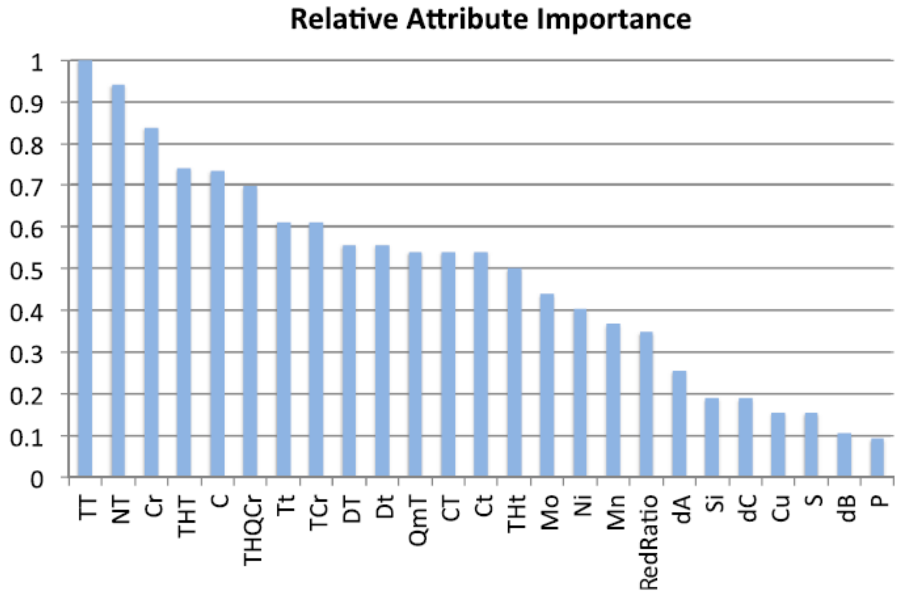

Figure 8.1. The relative importance of different parameters upon the creep fatigue performance of steels [2].

The list of parameters (attributes) included composition, mill product (upstream) features and subsequent processing (heat treatment) parameters. As it turns out, the thermal processing parameters include TT (tempering temperature), NT (normalizing temperature), THT (through-hardening temperature) and other similar parameters. Of all the chemical elements comprising a given steel, the most important were the concentrations of Cr and C.

This example signifies the importance of the scientific basis - thermodynamics and kinetics of phase transformations for the development of proper heat treatments. This report is organized as follows. First, an overview of the modeling tools employed for such purpose is provided. It includes Thermo-Calc, PRISMA, and DFT calculations. Secondly, the obtained results are described and analyzed. Finally, conclusions are made and the list of references is provided.

8.2. Modeling Techniques Used in the Present Report

8.2.1. Thermodynamic Modeling

In this work, an approach developed by Hillert [3], the ThermoCalc and DICTRA software were used for thermodynamic and diffusion calculations, respectively. This choice was relatively simple and straightforward. Indeed, BINGGS works only for binary and some ternary systems, FactSage and PANDAT are standalone thermodynamic platforms that cannot communicate with other existing software platforms. On the other hand, ThermoCalc thermodynamic data can be passed onto the diffusion modeling software, DICTRA, and the data on the mobilities and driving forces from these two codes could be passed onto the microstructure evolution software, MICRESS. Also, several interfaces were developed allowing use of both programs from the environment of Matlab or ASPEN (a computational fluid dynamics simulation software). In other words, there are practically unlimited possibilities for growing a toolbox of useful interdisciplinary applications in the case of ThermoCalc AB software.

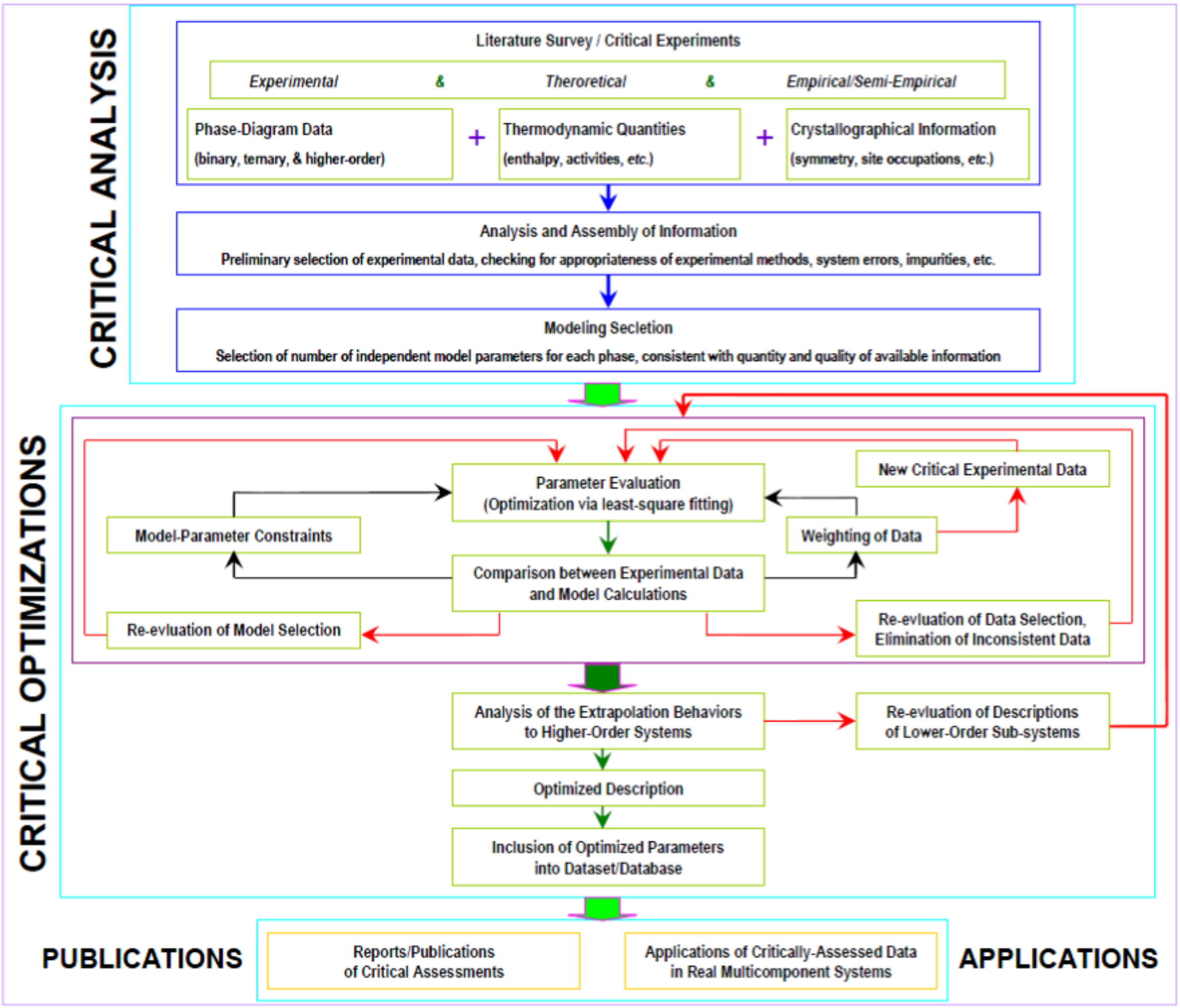

Figure 8.2. The extended CALPHAD approach to calculation of phase equilibria and thermodynamic properties of materials [3 - 8].

The general CALPHAD (stands for CALculation of PHAse Diagrams) approach to self-consistent evaluation of thermodynamic and phase equilibria data was described in the ThermoCalc manual [7]; schematically it is presented in Figure 8.2 [3-9]. The key requirement for successful optimization and assessment is in the presence of the sufficient amount of data on thermodynamic properties of components, intermediate phases, solid solutions, and the liquid phase. This approach was used in the present work, along with thermodynamic databases TTNI8 and TTFE6.

As it follows from Figure 8.2, the process of the database development begins with the collection and critical assessment of existing experimental data both on phase equilibria and thermodynamic properties of materials for a given multi-component system. Then these data are used in the optimization module called PARROT in order to yield a self-consistent description of these two sets of experimental data based on the need to satisfy the fundamental Gibbs equilibrium conditions. After a number of iterations including re-assignments of different weights to the experimental data in order to achieve the best possible description, the problem is solved in the sense that a selected thermodynamic model is parameterized and these data are stored in the database form for further use or development, e.g., increasing the number of components included in a given database.

8.2.2 Precipitation Modeling and Construction of TTT and CCT Diagrams

In order to use thermodynamic information obtained with ThermoCalc (or any other similar computational engine such as PANDAT, FactSage, or MTDATA) it is necessary to consider the kinetics of phase transformations. In modeling, this implies the need to consider different precipitation reactions that may exert a profound influence upon mechanical behavior of materials. For example, it is well established that phases with sharp edges – needles, plates and irregular shapes are detrimental to such properties as creep, creep fatigue and the propagation rate of creep-fatigue cracks [9]. This is why it is important to be able to construct the TTT (time-temperature-transformation and CCT (continuous cooling transformation) diagrams for the precipitation of the phase(s) of interest.

In this project, A sister software of Thermo-Calc called PRISMA was used [10]. Essentially, it represents the precipitation computational engine from PrecipiCalc™, the software developed by QuesTek Innovations, LLC [11]. This engine is built into Thermo-Calc's PRISMA interface to allow for using the well-developed interfaces, and thermodynamic and mobility databases required for these kinetic calculations. According to QuesTek, the input for PrecipiCalc includes:

- Physical quantities such as material compositions, bulk thermodynamics and mobility (TDB files), interfacial properties (such as surface energy and interfacial dissipation) and lattice properties (such as molar volume).
- Thermal cycle, or temperature profile, which defines the thermal history of the material being processed. The thermal cycle can be constant (isothermal), linear cooling (quench) or complicated nonlinear and non-monotonic heat treatments (such as multi-step tempering) [10].

The output of PRISMA includes data on the temporal evolution for [11]:

- Precipitate microstructure — precipitate size distribution, number density and volume fraction, which can be used to construct TTT/CCT diagrams.
- Compositions of matrix and precipitates.
- Driving forces, nucleation rates and critical radii

In the present work, PRISMA was employed for analyzing precipitation of carbide $M_{23}C_6$ and the SIGMA-phase.

8.2.3 DFT Modeling

First-Principles Atomistic Calculations – Structure Optimization

While thermodynamic calculations are very useful for determining the phase composition of a given alloy as a function of temperature, it is possible only in the case if the phase of interest is included into the corresponding thermodynamic database (in our case –TTFE6).

Unfortunately, this is not always the case. One of such important compounds is the so-called **“eta”-phase** was not described in the TTFE6 database used in the present calculations. Neither is it describe in the most up-to-date version, the TTFE9.

Therefore, in a number of cases it becomes important to use some other techniques to obtain the required thermodynamic information (e.g., the enthalpy of formation, the energy of cohesion, etc.). The best way to achieve that is to use the DFT approach [12-18]. It is not our objective here to provide a detailed description of this approach; rather the interested reader is referred to the classical text of Kittel [18]. Below, only the details of the calculation set-up are described as well as the selected values of important parameters.

The formation enthalpy of the Cr_3Ni_2Si compound was determined using first-principles calculations [13, 14] based on DFT. All calculations were performed using the projected augmented wave (PAW) pseudo-potentials implemented in VASP (Vienna Ab-initio Simulation Package) [15, 16] with the GGA-PBE (generalized gradient approximation refined by Perdew, Burke and Ernzerhof) exchange-correlation functional for describing the interactions [17]. Cohesion energies were determined in a similar fashion, including the cohesion energy of the pure elements, Cr; Ni; and Si [12-18]

Table 8.1. Chemical compositions of the 3 batches of Alloy 709.

	Plate #1	Plate #2	Plate #3
Element	Heat 011502H	Heat 011594	Heat 58776-4
S			
C	0.063	0.078	0.07
Mn	0.88	0.9	0.91
Si	0.28	0.39	0.44
P			0.014
Cr	19.69	19.89	19.93
Ni	25	25.01	24.98
Mo	1.46	1.51	1.51
N	0.14	0.14	0.148
Nb	0.23	0.25	0.26
Ti	0.01	0.01	0.04
Cu			0.06
Co			0.02
Al			0.02
B	0.0022	0.0037	0.0045
Fe	52.2448	51.8183	51.5935

8.3. Results and Discussion

8.3.1. Phase composition of 3 Batches of Alloy 709 as Function of Temperature

Three batches of Alloy 709 were obtained from the Oak Ridge National Laboratory. Their compositions are listed in Table 8.1. The goal was to explore whether a limited variation of the alloy chemical composition. For all these cases, the phase composition of these alloys was explored as a function of temperature. This provides valuable information for an alloy designer and for the subsequent development of the most suitable thermo-mechanical treatment. These results provide the types phases and their amounts under equilibrium conditions (i.e. for long durations). Some such results are provided below (Figures 8.3, 8.4 and 8.5).

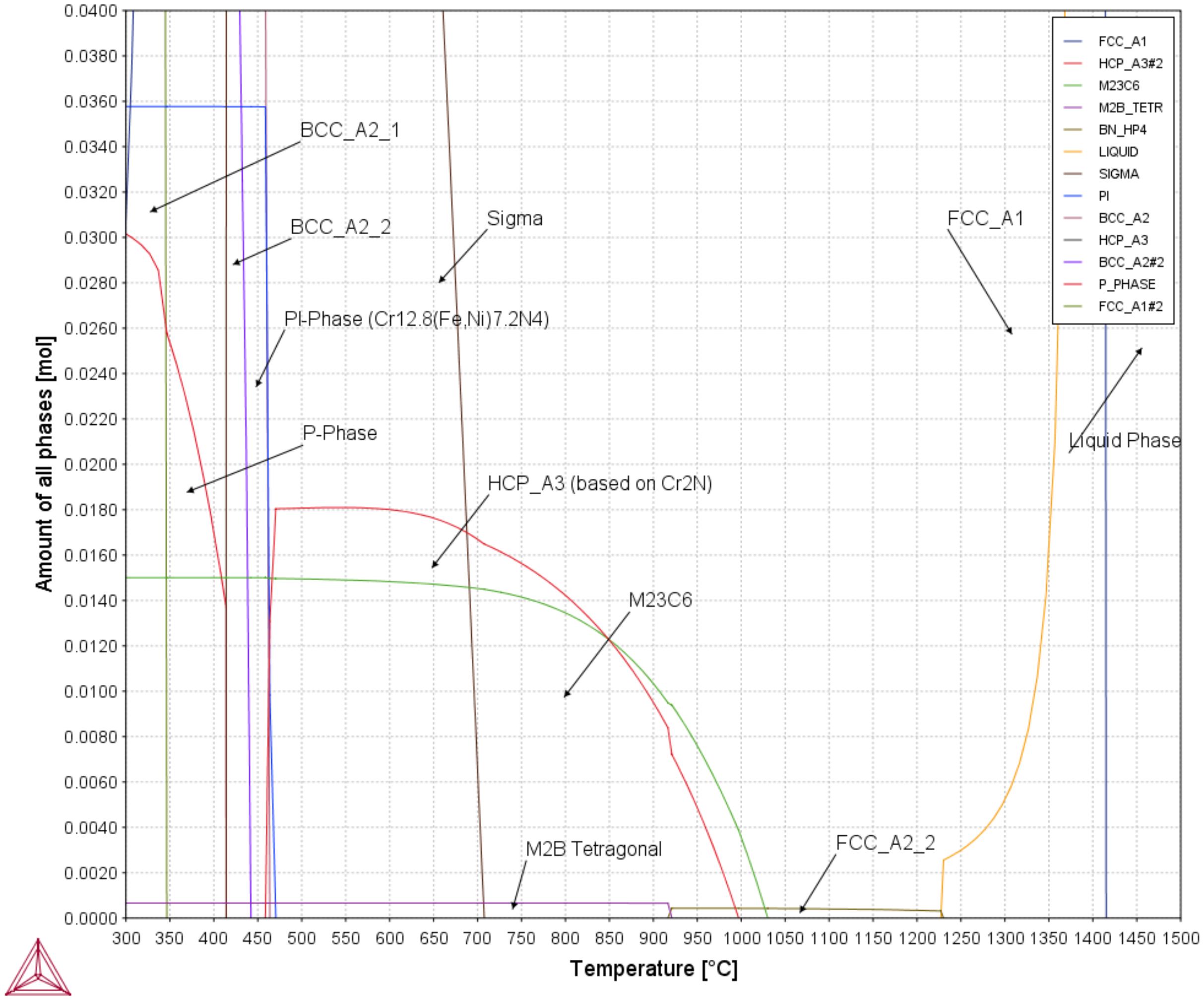

Figure 8.3. Alloy 709, Batch 1 – phase composition as a function of temperature.

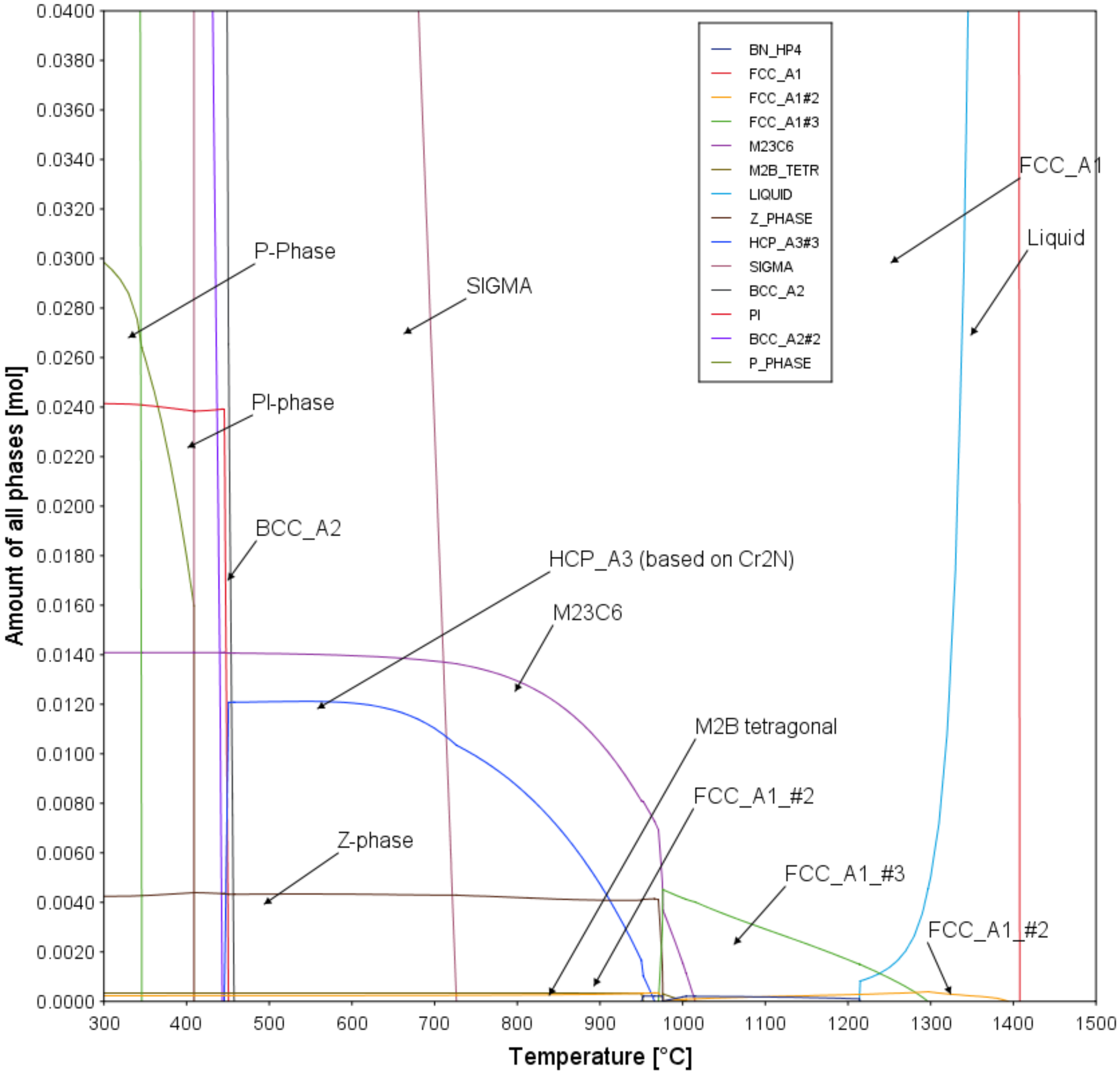

Figure 8.4. Alloy 709, Batch 2 – phase composition as a function of temperature.

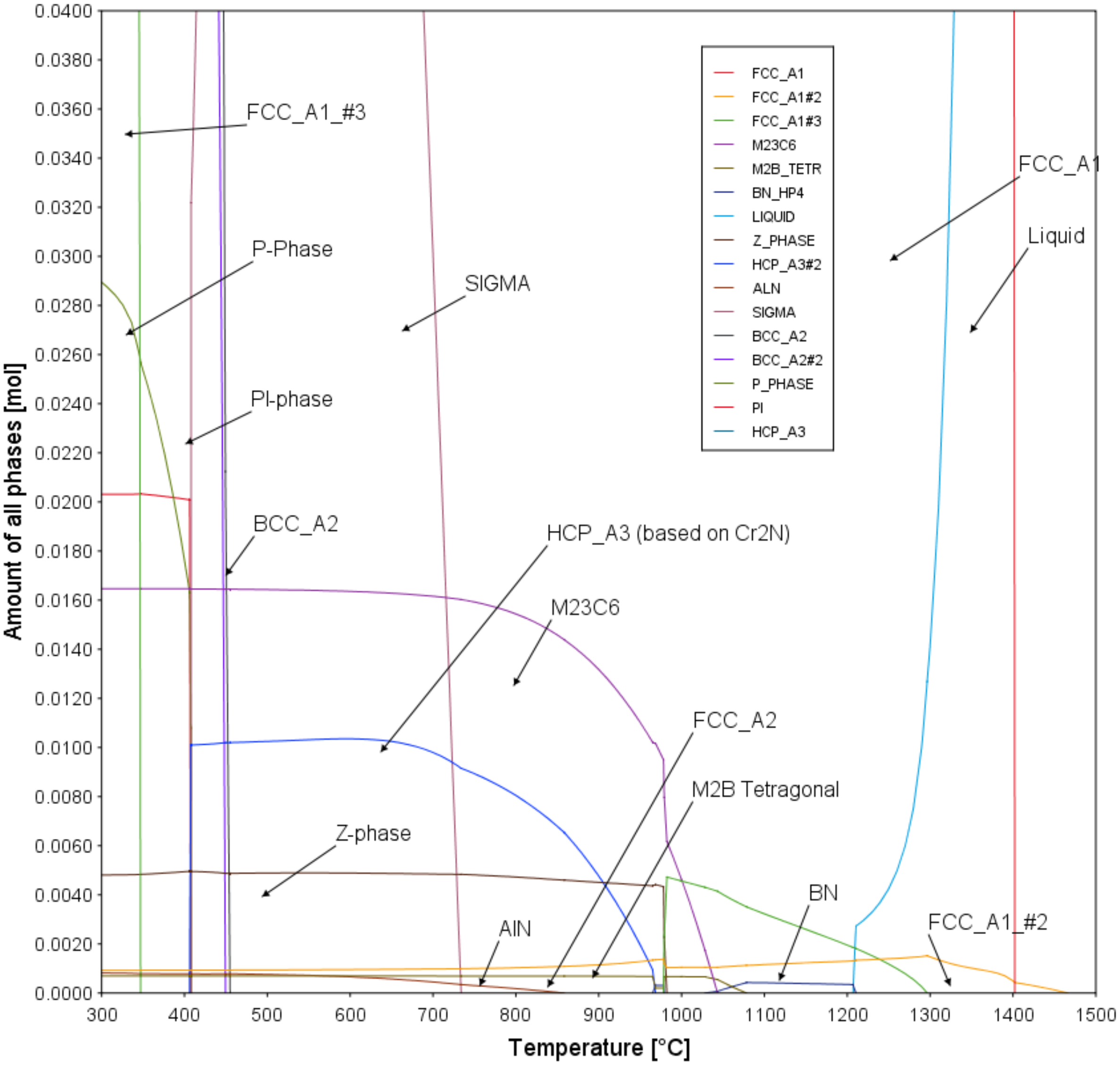

Figure 8.5. Alloy 709, Batch 3 – phase composition as a function of temperature

These figures clearly demonstrate the phase types of all 3 batch alloys as austenitic steels. Also, in addition to the FCC matrix, there are such phases, Sigma, PI-phase, Cr_2N, AlN, M_2B, different carbonitrides of metals, the Z-phase etc. In all cases, understanding of how the phase amounts of a given alloy varies with temperature helps to select the conditions most appropriate for designing the optimal heat treatments for Alloy 709.

At the service temperature of 550°C in Generation IV Sodium-cooled Fast Reactors, the Thermo-Calc results suggest the presence of AlN, M_2B, Z-Phase, $M_{23}C_6$, Cr_2N, and most importantly Sigma phase. For the thermal aging of Alloy 709 it is important replicate the precipitates present and size of the precipitates after several years at service temperatures. Sigma phase is known to be detrimental to the mechanical properties of 20Cr – 25Ni stainless steels so the aging schedule was made to ensure this phase would be present in the alloy similar to 25 and 50 years at 550°C [19]. Aging temperatures over 725°C were ruled out because Sigma phase tend to dissolve into the matrix beyond this temperature. These Thermo-Calc results were confirmed with PRISMA calculations at Colorado School of Mines to replicate the microstructure after aging at 25 and 50 years at 550°C. The two aging schedules carried out were at 650°C for a duration of 2190 and 4380 hours.

Creep, creep-fatigue and fatigue tests are currently being performed on the aged #1 (650°C for 2,190 hours) Alloy 709 along with hardness and microstructural analysis including the precipitate evolution. The results of these ongoing studies will be given in the final report. Aged #2 (650°C for 4,380 hours) Alloy 709 finished its aging schedule just recently and similar tests will be completed to examine the effect of this thermal aging schedule on Alloy 709. It is important to note that this aging schedule takes into account only the thermal effects on the alloy in service conditions, not the mechanical degradations that would occur.

8.3.2 Constructed TTT, CCT diagrams and Precipitate Size Distributions for SIGMA-phase and $M_{23}C_6$ Carbides

Below, we provide the results obtained for the “generic” chemical composition of Alloy 709. There are four kinds of data modeled using the nucleation and growth equations for different precipitates described above in the PrecipiCalc approach:

- TTT-diagram constructed for the precipitation of the SIGMA-phase and carbide $M_{23}C_6$, with M=Fe, Cr;
- CCT- diagram constructed for the precipitation of the SIGMA-phase and the $M_{23}C_6$ carbide (corresponding to the conditions of continuous cooling with different cooling rates);
- Isothermal anneal for different amounts of time;
- Precipitate growth with time for prescribed temperature variation schedule (in our case – isothermal anneal)

To obtain these results, the PRISMA software was employed in conjunction with the thermodynamic and atomic mobility databases TCFE6 and MOBFE1, respectively. The corresponding codes were written for the Thermo-Calc v.2017b general GUI, and the schematic of these four types of calculations is presented below, Figure 8.3.

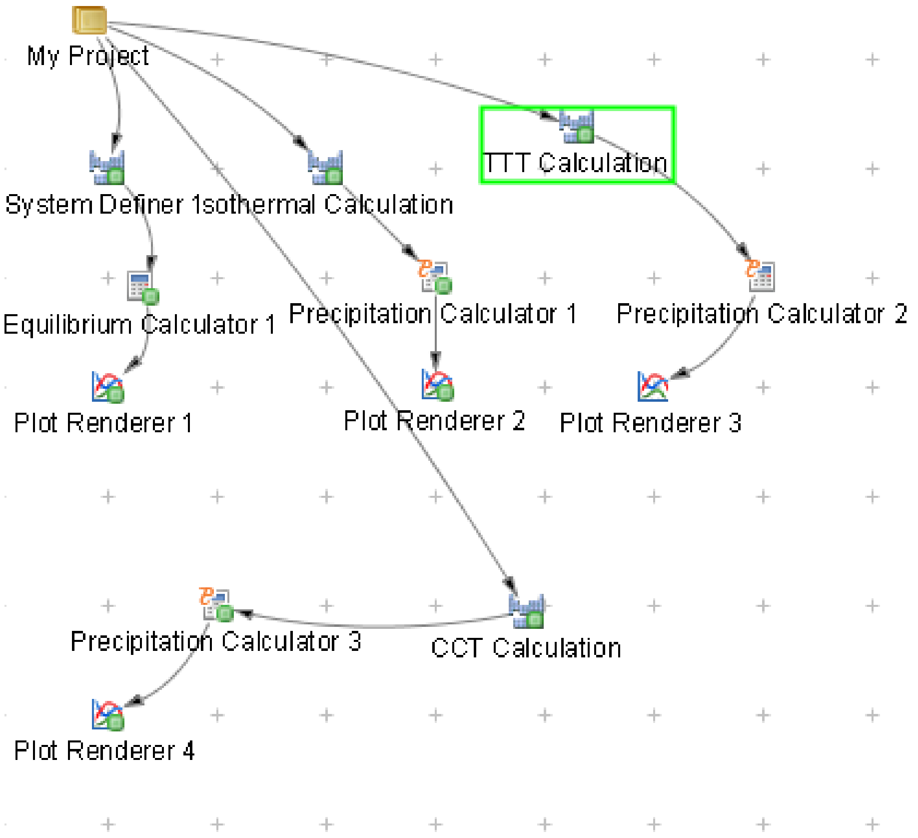

Figure 8.6. Calculation "trees" – four different cases described above: 1- equilibrium calculation (phase composition as a function of temperature); 2- Isothermal anneal calculation; 3 – construction of the TTT diagram for the phases.

To understand the significance of using the latest versions of the TCFE9 and MOBFE4 thermodynamic and mobility databases, we calculated the described results using TCFE6 and MOBFE1 as well. The results for the calculated TTT-diagram, CCT-diagram, and the kinetics of precipitate growth are presented in Figures 8.7 – 8.9.

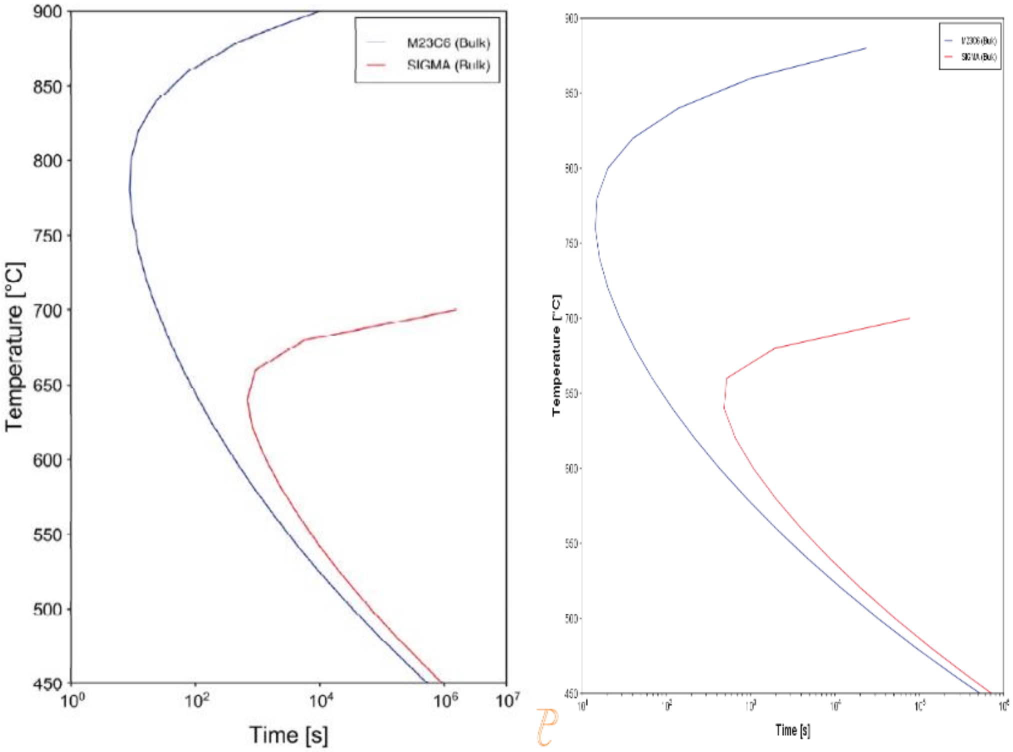

Figure 8.7. TTT-diagrams for $M_{23}C_6$ and SIGMA-phase constructed using TCFE9 and MOBFE4 (left) and TCFE6 and MOBFE1 (right) databases, respectively.

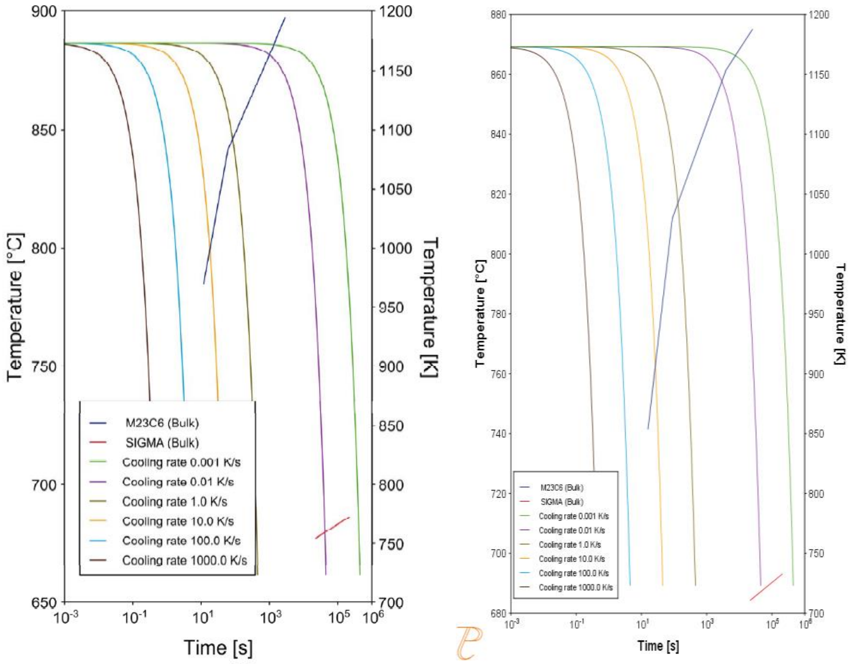

Figure 8.8. Calculation of CCT diagrams for $M_{23}C_6$ and SIGMA-phase: left –with TCFE9 and MOBFE1 databases; right – with TCFE6 and MOBFE1 databases.

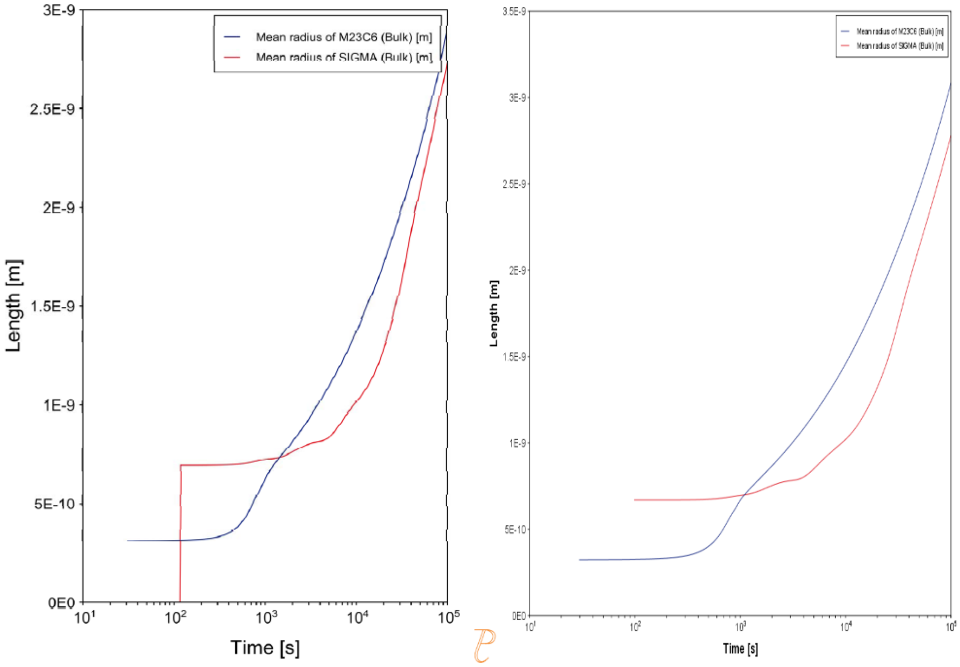

Figure 8.9. Precipitate average size growth as a function of time at 727 °C: left –databases TCFE9 and MOBFE1; right –TCFE6 and MOBFE1.

As can be seen from the obtained results, not much difference was observed when using older databases for thermodynamics and for atomic mobilities. This implies that the results are pretty robust with respect to the introduction of new and improved features or, at least, for this particular system, no significant difference was observed. In particular, the nucleation of the SIGMA phase at 727 °C requires about 100 seconds, while its particles' steep growth commences only after ~10^4 seconds. This provides valuable guidance on avoiding the formation of the undesirable SIGMA-phase in experimental conditions. Currently, further calculations are ongoing to reflect the lower temperature aging conditions where the kinetics of sigma phase formation is very sluggish.

8.3.3 DFT Studies and Results for Sigma-phase

The Wyckoff indices describing the location of the Cr, Ni, and Si atoms are presented in Table 8.2.

Table 8.2. The Wyckoff indices of all atoms in the crystal unit of Cr_3Ni_2Si (or, more precisely, $Cr_{48}Ni_{32}Si_{16}$

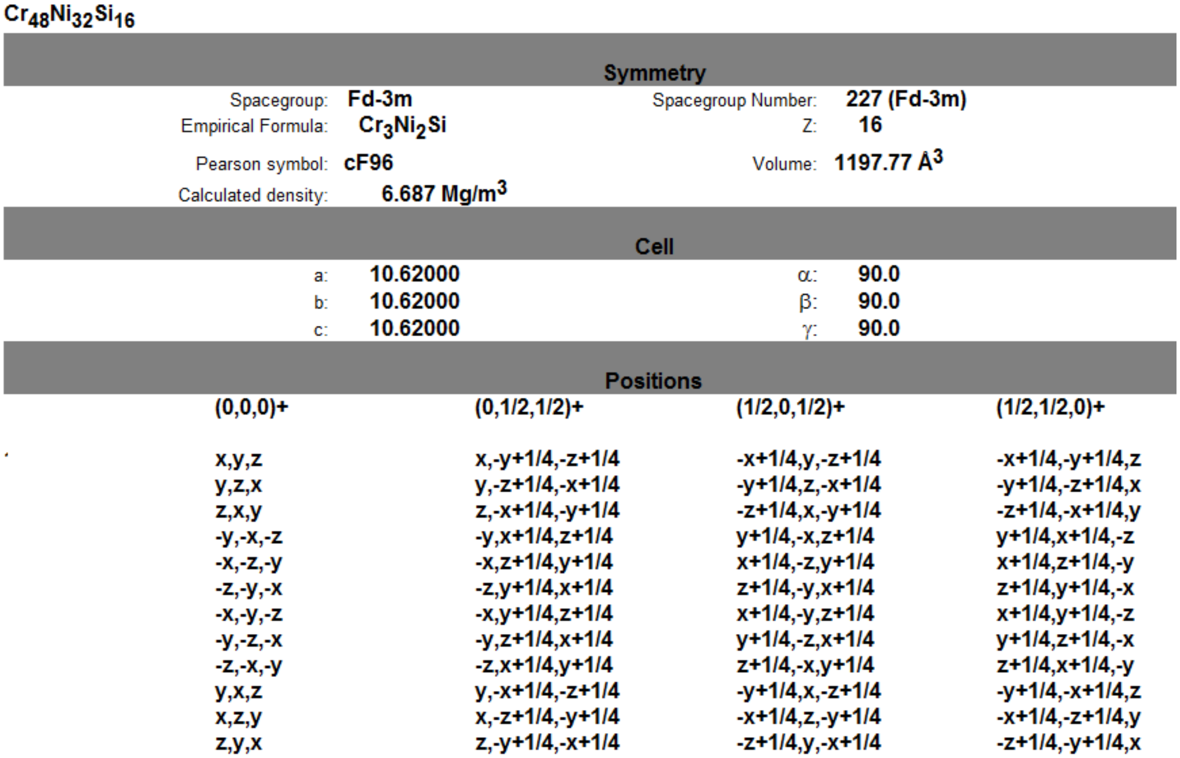

$Cr_{48}Ni_{32}Si_{16}$

Symmetry

Spacegroup:	Fd-3m	Spacegroup Number:	227 (Fd-3m)
Empirical Formula:	Cr_3Ni_2Si	Z:	16
Pearson symbol:	cF96	Volume:	1197.77 $Å^3$
Calculated density:	6.687 Mg/m^3		

Cell

a:	10.62000	α:	90.0
b:	10.62000	β:	90.0
c:	10.62000	γ:	90.0

Positions

(0,0,0)+	(0,1/2,1/2)+	(1/2,0,1/2)+	(1/2,1/2,0)+
x,y,z	x,-y+1/4,-z+1/4	-x+1/4,y,-z+1/4	-x+1/4,-y+1/4,z
y,z,x	y,-z+1/4,-x+1/4	-y+1/4,z,-x+1/4	-y+1/4,-z+1/4,x
z,x,y	z,-x+1/4,-y+1/4	-z+1/4,x,-y+1/4	-z+1/4,-x+1/4,y
-y,-x,-z	-y,x+1/4,z+1/4	y+1/4,-x,z+1/4	y+1/4,x+1/4,-z
-x,-z,-y	-x,z+1/4,y+1/4	x+1/4,-z,y+1/4	x+1/4,z+1/4,-y
-z,-y,-x	-z,y+1/4,x+1/4	z+1/4,-y,x+1/4	z+1/4,y+1/4,-x
-x,-y,-z	-x,y+1/4,z+1/4	x+1/4,-y,z+1/4	x+1/4,y+1/4,-z
-y,-z,-x	-y,z+1/4,x+1/4	y+1/4,-z,x+1/4	y+1/4,z+1/4,-x
-z,-x,-y	-z,x+1/4,y+1/4	z+1/4,-x,y+1/4	z+1/4,x+1/4,-y
y,x,z	y,-x+1/4,-z+1/4	-y+1/4,x,-z+1/4	-y+1/4,-x+1/4,z
x,z,y	x,-z+1/4,-y+1/4	-x+1/4,z,-y+1/4	-x+1/4,-z+1/4,y
z,y,x	z,-y+1/4,-x+1/4	-z+1/4,y,-x+1/4	-z+1/4,-y+1/4,x

The structure of Cr3Ni2Si is based on the paper of Gladyshevskiy (Springer-Landolt crystal structure database) [17]. The structure is Fm-3n, atoms of Cr are in the "f" Wyckoff positions, 32 atoms of Ni are in the "e" positions, and 16 Si are in the "c" positions. The lattice parameter is 10.62 A. The volume of the unit cell; density; positions of all atoms in the crystal lattice of the eta-phase were determined and refined as well.

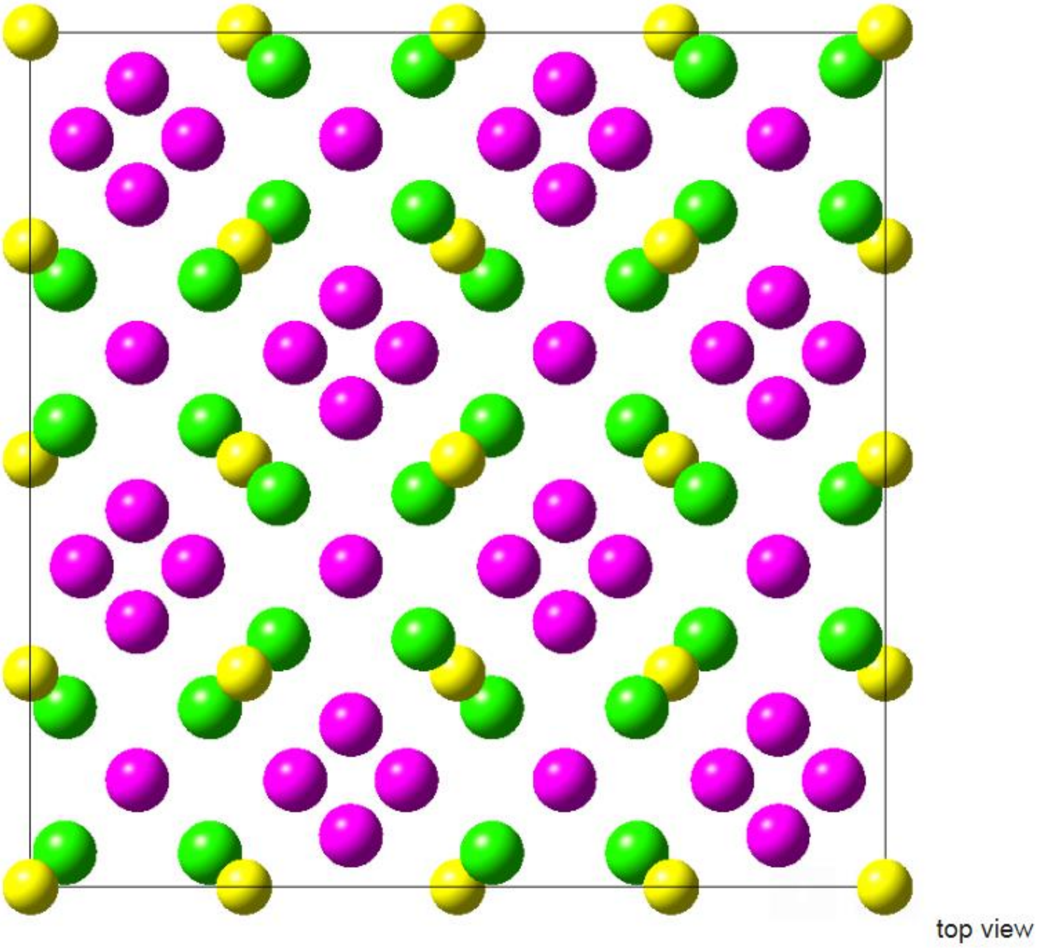

Figure 8.10. Atomic structure of the eta-phase optimized using VASP v.5.4 – top view (yellow – Si; purple – Cr; green –Ni).

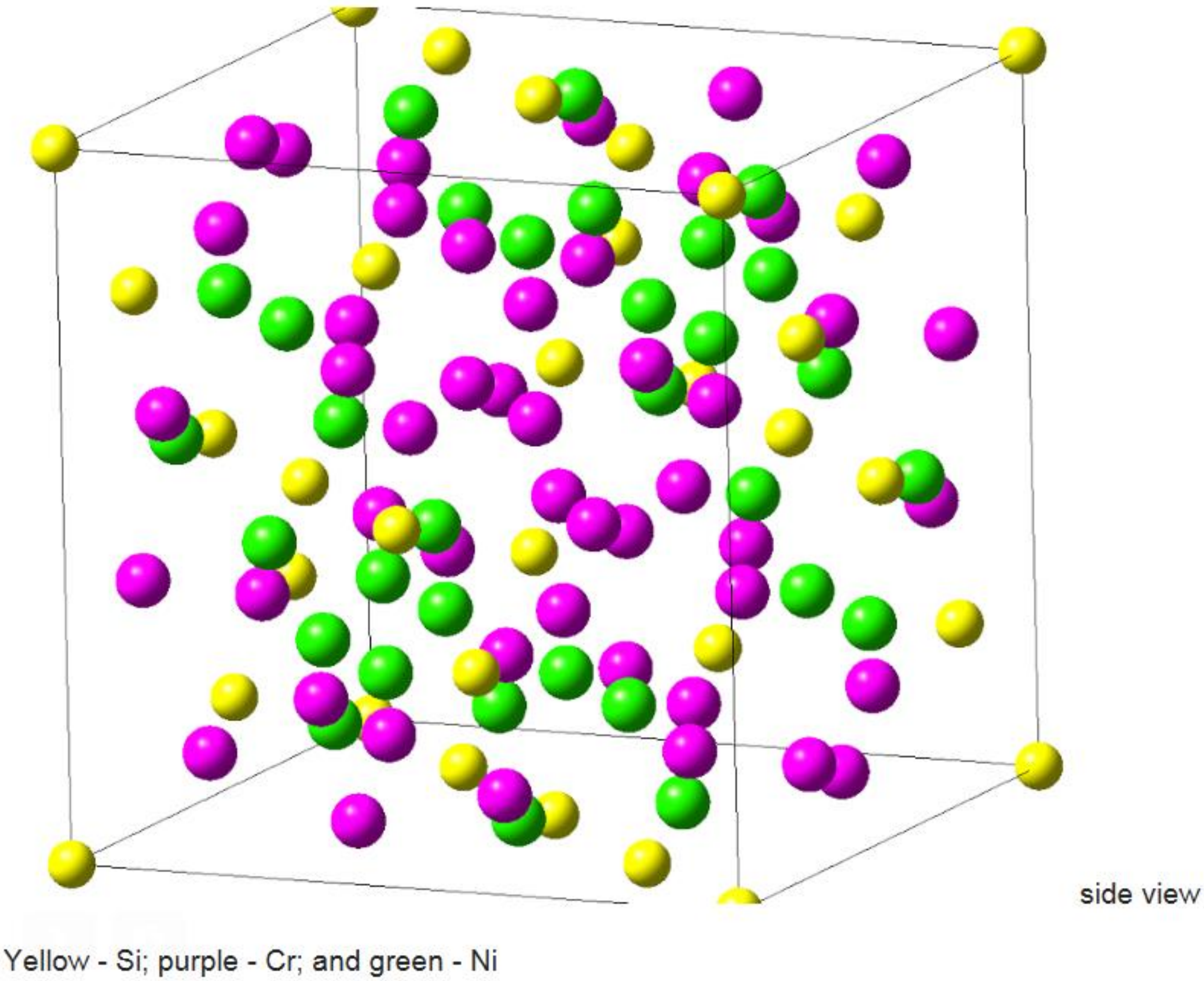

Figure 8.11. Atomic structure of the eta-phase optimized using VASP v.5.4 – side view (3D).

After the structural model of the eta-phase was constructed, VASP v.5.4 was used to optimize it and determine its energy of cohesion and enthalpy of formation.

The enthalpy of formation of a given compound can be defined as the difference in total energy of the compound and the energies of its constituent elements in their stable states [6]. Considering this value in Joules per mole per atom (sometimes called “cohesive energy”), the following formula should be used for calculations [15]

$$\Delta G_{Cr_3Ni_2Si}^{Cohesion} = E(Cr_3Ni_2Si) - \frac{3}{6}E(Cr) - \frac{2}{6}(Ni) - \frac{1}{6}(Si) \tag{8.1}$$

In this equation $\Delta G^{Cohesion}_{Cr_3Ni_2Si}$ stands for the cohesive energy of Cr_3Ni_2Si; E(Cr) is the cohesive energy of chromium; *E*(Ni) is the cohesive energy of nickel, and *E*(Si) is the energy of silicon. By definition, the cohesive energy of a pure element (and any compound) is defined as follows:

Cohesive energy = crystal energy - energy of free atoms

If one needs the enthalpy of formation in Joules per mole, equation (8.1) should be changed by equation (8.2):

$$\Delta H^{f}_{Cr_3Ni_2Si} = E(Cr_3Ni_2Si) - 3E(Cr) - 2E(Ni) - 1E(Si) \tag{8.2}$$

Conducting all calculations using VASP v.5.4 [6, 7] (see above) and equations (8.1) and (8.2) we obtained the following results. All obtained data are presented in Table 8.3.

Table 8.3. Energy of cohesion of the Cr_3Ni_2Si phase

Compound	Cr_3Ni_2Si	Cr	Ni	Si
Cohesion energy, eV/atom, this work	-40.75	-4.12	-4.41	-4.61
Cohesion energy, eV/atom [16]	n/a	-4.10	-4.44	-4.63

8.4. References

[1] NIMS fatigue database, http://mits.nims.go.jp/index_en.html (2018)

[2] A. Agrawal *et al. Integrating Materials and Manufacturing Innovation* 2014, **3**:8. Also see: A. Agraval and A. Choudhary, Perspective: Materials informatics and big data: Realization of the “fourth paradigm” of science in materials science APL Materials **4**, 053208 (2016)

[3] M. Hillert, Phase Equilibria, Phase Diagrams, and Phase Transformations: Their Thermodynamic Basis, 2nd edition, Cambridge University Press, Cambridge (2008).

[4] Z.-K. Liu, First-Principles calculations and CALPHAD Modeling of Thermodynamics, Journal of Phase equilibria and Diffusion, published online 03 September (2009).

[5] H.L. Lukas, S.G. Fries, and Bo Sundman, Computational Thermodynamics (The CALPHAD Method), Cambridge University Press, Cambridge (2007).

[6] N. Saunders and A.P. Miodownik, CALPHAD – Calculation of Phase Diagrams. A Comprehensive Guide, Pergamon, London (1998).

[7] DICTRA Version 25 User's Guide, 2010, Thermo-Calc Software AB, Stockholm, Sweden.

[8] ThermoCalc Classic Version S User's Guide, P. Shi and B. Sundman Editors, ThermoCalc Software AB, Stockholm, Sweden (2010).

[9] G. Potirniche et al., Crack growth testing for fatigue and creep-fatigue loading with short hold time, NEUP Grant # 15-8623 (2016)

[10] PRISMA software, http://www.thermocalc.com/products-services/software/precipitation-module-(tc-prisma)/ (2018)

[11] https://www.questek.com/filebase/src/Articles/PpCTechSheet2013.pdf detailed description of PrecipiCalc™ (2018)

[12] Kresse G, Furthmuller J., ***Phys Rev B*** 1996; 54:11169–86.

[13] Kresse G, Furthmuller J., ***Comput Mater Sci*** 1996; 6:15–50.

[14] Perdew J, Burke K, Ernzerhof M. ***Phys Rev Lett*** 1996; 77:3865–3868.

[15] E.R. Davidson, *Methods in Computational Molecular Physics* edited by G.H.F. Diercksen and S. Wilson Vol. 113 *NATO Advanced Study Institute, Series C,* Plenum, New York (1983) p. 95

[16] M. Methfessel and A. T. Paxton, High-precision sampling for Brillouin-zone integration in metals, Phys. Rev. B 40, 3616 (15 August 1989)

[17] B. Liu, in *Report on Workshop "Numerical Algorithms in Chemistry: Algebraic Methods"* edited by C. Moler and I. Shavitt (Lawrence Berkley Lab. Univ. of California, 1978), p.49

[18] Charles Kittel, *Introduction to Solid State Physics,* 8th edition, Hoboken, NJ, John Wiley & Sons, Inc. (2005)

[19] Sourmail, T. and Bhadeshia, H. K. D. H. (2005) 'Microstructural evolution in two variants of NF709 at 1023 and 1073 K', *Metallurgical and Materials Transactions A*, 36(1), pp. 23–34. doi: 10.1007/s11661-005-0135-y.

[20] Pierre Villars (Chief Editor), PAULING FILE in: Inorganic Solid Phases, Springer Materials (online database), Springer, Heidelberg (ed.) Springer Materials (Cr,Si)3Ni2Si (Cr3Ni2Si) Crystal Structure sd_1006289 (Springer-Verlag GmbH, Heidelberg, © 2016)

8.5. Appendix: Phase composition of Alloy 709 (Batch 1) at different temperatures: 700°C, 800°, and 850°C

Case 1: Alloy 709 at 800°C

Moles	1.00000	
Mass	55.66457	[g]
Temperature	1073.15000	[K]
Total Gibbs Energy	-55873.03611	[J]
Enthalpy	28330.91447	[J]
Volume	7.21272E-6	[m3]

Component	*Mole Fraction*	*Mass Fraction*	*Activity*	*Potential*
B	0.00022	0.00004	2.05299E-6	-1.16854E5
C	0.00311	0.00067	0.00024	-74336.16782
N	0.00596	0.00150	3.08647E-8	-1.54306E5
Mn	0.00405	0.00400	1.87071E-6	-1.17683E5
Mo	0.00870	0.01500	0.00069	-64893.58181
Co	0.00246	0.00260	6.36078E-6	-1.06764E5
Cr	0.21197	0.19800	0.00573	-46052.58786
Ni	0.23797	0.25090	0.00050	-67765.71648
Fe	0.52556	0.52729	0.00284	-52333.96168

Stable Phases

	Moles	*Mass*	*Volume Fraction*	
FCC_A1#1(FCC solid sol'n)	0.97166	54.40981	0.97305	
Composition				
Component	*Mole Fraction*	*Mass Fraction*		
Fe	0.53980	0.53836		
Ni	0.24477	0.25654		
Cr	0.19969	0.18542		
Mo	0.00730	0.01250		
Mn		0.00409		
Co		0.00266		
N		0.00039		
C		0.00004		
B		9.57117E-8		
		Mass	*Volume Fraction*	
HCP_A3#2 (Cr_2N)		0.57856	0.01409	
Composition				
Component		*Mass Fraction*		
Cr		0.83281		
N		0.10737		
Mo		0.04828		
Fe		0.00727		
C	0.00995	0.00294		
Ni	0.00070	0.00101		
Mn	0.00023	0.00030		

Co	5.55769E-6	8.05181E-6		
B	2.24803E-8	5.97459E-9		

	Moles	*Mass*	*Volume Fraction*	
M23C6#1 (Fe, Cr)$_{23}$C$_6$	0.01345	0.64157	0.01221	
Composition				
Component	*Mole Fraction*	*Mass Fraction*		
Cr	0.62941	0.68616		
Mo	0.08270	0.16636		
Fe	0.07172	0.08397		
C	0.20689	0.05210		
Ni	0.00908	0.01117		
Co	0.00010	0.00012		
Mn	0.00010	0.00012		
B	4.00565E-6	9.07949E-7		
N	0.00000	0.00000		

	Moles	*Mass*	*Volume Fraction*	
M2B_TETR#1(boride M$_2$B)	0.00066	0.03463	0.00066	
Composition				
Component	*Mole Fraction*	*Mass Fraction*		
Mo	0.31336	0.57584		
Cr	0.31681	0.31553		
B	0.33300	0.06896		
Fe	0.03187	0.03409		
Ni	0.00497	0.00559		
Co	0.00000	0.00000		
Mn	0.00000	0.00000		

N	0.00000	0.00000		
C	0.00000	0.00000		

Case 2: Alloy 709 at 850°C

Moles	1.00000	
Mass	55.66457	[g]
Temperature	1123.15000	[K]
Total Gibbs Energy	-59836.08518	[J]
Enthalpy	30076.76967	[J]
Volume	7.22971E-6	[m3]

Component	*Mole Fraction*	*Mass Fraction*	*Activity*	*Potential*
B	0.00022	0.00004	4.10421E-6	-1.15829E5
C	0.00311	0.00067	0.00042	-72544.56507
N	0.00596	0.00150	6.37595E-8	-1.54721E5
Mn	0.00405	0.00400	1.82538E-6	-1.23396E5
Mo	0.00870	0.01500	0.00057	-69765.61432
Co	0.00246	0.00260	5.61438E-6	-1.12903E5
Cr	0.21197	0.19800	0.00468	-50105.62127
Ni	0.23797	0.25090	0.00046	-71754.14137
Fe	0.52556	0.52729	0.00241	-56286.86674

Stable Phases

	Moles	*Mass*	*Volume Fraction*	
FCC_A1#1(FCC solid soln.)	0.97483	54.55153	0.97616	
Composition				
Component	*Mole Fraction*	*Mass Fraction*		

Fe	0.53796	0.53688		
Ni	0.24395	0.25585		
Cr	0.20120	0.18694		
Mo	0.00755	0.01295		
Mn	0.00415	0.00408		
Co	0.00252	0.00265		
N	0.00227	0.00057		
C	0.00039	0.00008		
B	1.15716E-6	2.23553E-7		
	Moles	*Mass*	*Volume Fraction*	
HCP_A3#2	0.01225	0.49663	0.01209	
Composition				
Component	*Mole Fraction*	*Mass Fraction*		
Cr	0.65247	0.83653		
N	0.30572	0.10559		
Mo	0.01680	0.03974		
Fe	0.00863	0.01188		
C	0.01514	0.00448		
Ni	0.00102	0.00148		
Mn	0.00022	0.00030		
Co	8.61970E-6	0.00001		
B	5.36430E-8	1.42997E-8		
	Moles	*Mass*	*Volume Fraction*	
M23C6#1 (Fe,Cr)$_{23}$C$_6$	0.01226	0.58232	0.01109	
Composition				
Component	*Mole Fraction*	*Mass Fraction*		

Cr	0.62248	0.68168		
Mo	0.07650	0.15457		
Fe	0.08239	0.09691		
C	0.20688	0.05234		
Ni	0.01146	0.01416		
Mn	0.00015	0.00018		
Co	0.00013	0.00016		
B	0.00001	2.67535E-6		
N	0.00000	0.00000		
	Moles	*Mass*	*Volume Fraction*	
M2B_TETR#1(M_2B)	0.00066	0.03409	0.00066	
Composition				
Component	*Mole Fraction*	*Mass Fraction*		
Mo	0.29798	0.55434		
Cr	0.32306	0.32572		
B	0.33300	0.06981		
Fe	0.03955	0.04283		
Ni	0.00642	0.00731		
Co	0.00000	0.00000		
Mn	0.00000	0.00000		
N	0.00000	0.00000		

Case 3:Alloy 709 at 1050°C

Quantities

Temperature	1050.00000	[°C]

System		
Moles	1.00000	
Mass	55.66457	[g]
Temperature	1323.15000	[K]
Total Gibbs Energy	-76472.75357	[J]
Enthalpy	37563.66218	[J]
Volume	7.29860E-6	[m3]

Component	*Mole Fraction*	*Mass Fraction*	*Activity*	*Potential*
B	0.00022	0.00004	0.00002	-1.17450E5
C	0.00311	0.00067	0.00172	-70030.14492
N	0.00596	0.00150	4.41272E-7	-1.60989E5
Mn	0.00405	0.00400	1.55710E-6	-1.47117E5
Mo	0.00870	0.01500	0.00028	-89826.82831
Co	0.00246	0.00260	3.48607E-6	-1.38251E5
Cr	0.21197	0.19800	0.00230	-66847.08142
Ni	0.23797	0.25090	0.00032	-88430.05665
Fe	0.52556	0.52729	0.00132	-72948.52020

Stable Phases

	Moles	*Mass*	*Volume Fraction*
BN_HP4#1	0.00042	0.00521	0.00033
Composition			
Component	*Mole Fraction*	*Mass Fraction*	
N	0.50000	0.56439	
B	0.50000	0.43561	
Fe	0.00000	0.00000	
Ni	0.00000	0.00000	

Cr	0.00000	0.00000		
Co	0.00000	0.00000		
Mo	0.00000	0.00000		
Mn	0.00000	0.00000		
C	0.00000	0.00000		
	Moles	*Mass*	*Volume Fraction*	
FCC_A1#1	0.99958	55.65936	0.99967	
Composition				
Component	*Mole Fraction*	*Mass Fraction*		
Fe	0.52579	0.52734		
Ni	0.23807	0.25092		
Cr	0.21206	0.19802		
Mo	0.00871	0.01500		
Mn	0.00405	0.00400		
Co	0.00246	0.00260		
N	0.00575	0.00145		
C	0.00311	0.00067		
B	0.00001	2.19201E-6		

9 FINITE ELEMENT MODELING OF CREEP-FATIGUE CRACK GROWTH

9.1. Introduction

Finite element simulations are performed to predict plasticity-induced crack closure and creep-fatigue crack growth rates in two heat-resistant steels, austenitic 20Cr-25Ni (Alloy 709) steel and martensitic 9Cr-1Mo (modified 1Cr-9Mo) steel. In a creep-fatigue cycle, the total crack growth rate is usually computed by the addition of the fatigue crack growth rate during cyclic loading and creep crack growth rate during the hold time. Two-dimensional finite element analyses of compact tension specimens are performed to simulate crack growth under cyclic and time-dependent loading conditions, with the consideration of the elastic-plastic-creep deformation of the material at the crack tip. The simulations quantify the effect of hold time on opening load induced by the combined action of plasticity-induced crack closure and creep-induced stress relaxation at the crack tip. It is shown that increasing hold time during a creep-fatigue cycle results in a decrease of crack-tip opening load, thus increasing crack growth rate during ulterior cyclic loading. Experimental results of creep-fatigue crack growth rates in Alloy 709 are presented. The finite element simulations produce predictions of creep-fatigue crack growth rates that are in agreement with experimental values for both Alloy 709 and modified 9Cr-1Mo steels.

The design and development of the next generation of power plants require innovative structural materials able to withstand higher temperatures and pressures. These new operating conditions place increased load and temperature burdens for longer periods of time on the performance of structural materials [1]. Furthermore, representative operational cycles of energy systems entail periods of start-up, continuous operation at high temperatures and shut-down periods [2,3]. These service characteristics lead to crack growth under a combination of creep and fatigue loads. Consequently, predictive computational models for creep-fatigue crack growth (CFCG) behavior able to incorporate creep-fatigue interactions at high temperatures are relevant to life assessment and determination of inspection intervals of structural components used in energy systems.

CFCG is one of the most important failure mechanisms in components that experience a combination of high temperature and sustained stresses exposure over extended periods of time. Several experimental and numerical studies have been performed to characterize the CFCG behavior in structural materials [2,4–9]. In these studies, the damage during in-service conditions was reproduced by accelerated laboratory tests through the introduction of different loading waveforms. Triangular or trapezoidal loading waveforms are commonly used in laboratory CFCG testing. These waveforms result in elastic-plastic and creep strains at the crack tip being caused by the cyclic and creep portions of a loading cycle [10]. To predict CFCG rates, fracture mechanics parameters such as ΔK, K_{max}, $C(t)$ and $C(t)_{avg}$ have been used both in experimental and computational studies [11–15].

Fatigue crack growth has been successfully modeled using the effective stress intensity factor range ΔK_{eff} as a crack-tip driving force. The computation of ΔK_{eff} involves the measurement of crack-tip opening stress/load as produced by the plasticity-induced crack closure mechanism. Plasticity-induced crack closure was first studied experimentally by Elber [16], and is an inherent feature of the mechanics of fatigue crack growth. Plasticity-induced crack closure is due to the accumulation of the residual plastically deformed material along the crack surfaces as the crack tip advances. The plastically deformed material behind the crack tip, or plastic wake, causes premature contact during unloading in a fatigue cycle, and retards the crack opening in the subsequent loading, thus reducing ΔK and, implicitly, the crack propagation rate per cycle. Plasticity-induced crack closure has been extensively studied using finite element simulations of fatigue crack growth in two-dimensional models for both plane strain and plane stress cases [17–21]. While there are remarkable finite element studies of fatigue crack growth with the consideration of plasticity-induced crack closure [19,22–26], significantly less attention has been dedicated to this phenomenon in the context of CFCG. Only a few numerical studies of CFCG rates with the consideration of creep-fatigue loading interactions have been published until now [8,27,28]. A few studies were identified in the area of finite element computation of crack-tip opening stresses/loads in the presence of hold (dwell) times in high temperature fatigue crack growth [29–31]. However, predictions of CFCG rates were not undertaken in these studies. Currently, there is a need to better understand and quantify the phenomenon of plasticity-induced crack closure in the presence of creep loading, and to perform CFCG rate predictions. This study addresses these issues by providing a quantitative assessment of the impact of the creep hold time of crack-tip opening loads, and thus producing predictions of CFCG rates for creep-fatigue loading with various hold times.

9.2. Experimental Procedures

9.2.1. Material

In this study, two structural materials are employed, i.e., austenitic stainless-steel Alloy 709 (20Cr-25Ni) and modified 9Cr-1Mo (Grade 91) ferritic-martensitic steel. Experimental tests of CFCG were conducted on Alloy 709 at 600°C and 700°C. On the other hand, the CFCG rates for the modified 9Cr-1Mo at 625°C were taken from Narasimhachary and Saxena [2], and were used to compare to our model predictions. Modified 9Cr-1Mo steel has been extensively used in structural components in ultra-supercritical fossil power generation plants and petrochemical refineries [32].

Alloy 709 is an advanced heat and corrosion-resistant austenitic stainless steel derived from the Nb/Ti stabilized Fe-20Cr-25Ni-1.5Mo-Nb (NF 709) steel. Alloy 709 has shown outstanding performance under creep and creep-fatigue loading, good thermal stability, weldability and tensile properties [33]. Due to its superior creep resistance and reduced production cost compared to the conventional 304 and 316 stainless steels, or nickel-based superalloys, Alloy 709 was down-selected as the ideal candidate for structural applications in sodium fast reactors [34]. Among the targeted applications are reactor pressure vessels, core supports, and primary and secondary piping components.

The fabrication process of Alloy 709 involves hot working (forging and rolling) operations, followed by annealing at 1100°C and water quenching. Three different plates with similar chemical compositions shown in Table 9.1 were obtained from Oak Ridge National Laboratory (ORNL). The initial microstructure of the as-received Alloy 709 consisted of an austenitic matrix with near equiaxed grains with the presence of annealing twins. The grain size did not exhibit any significant differences in three orthogonal planes (RD, TD and ND), and was estimated to be 38 ±3 μm. The EBSD maps of the as-received Alloy 709 shows randomly oriented equiaxed grains with the presence of developed twins, as illustrated in Figure 9.1. Fine MX particles (mainly the NbN type) in the size range of 0.19-0.25 μm were identified in the microstructure. After exposure to long-term aging or creep testing, $M_{23}C_6$ carbides were found at the grain boundaries and twin boundaries. The size and volume fraction of the precipitates is a function of the test temperature and time of exposure. Thermodynamic calculations were performed using Thermo-Calc, and the occurrence of $M_{23}C_6$, MX, Z phase, and the σ phase was predicted, while at 700°C the mole fraction of the σ phase decreases significantly. These particles play an important role on creep deformation and failure, and are expected to influence the CFCG rates, even though a systematic investigation of this effect was not undertaken here. During creep deformation, the particles serve as stress concentration sites nucleating voids. The formation of such voids can reduce the internal cross sections and further exacerbate stress concentrations at those areas regardless of the particles' location. During creep deformation, voids nucleated near grain boundary particles can grow further leading to interlinking and creating cracks along grain boundaries, which can ultimately lead to failure. Relevant microstructural and mechanical characterizations of Alloy 709 and NF709 with discussion on deformation and creep mechanisms can be found in [35–37]. The material properties of the Alloy 709 and modified 9Cr-1Mo used in the study are presented in Table 9.2.

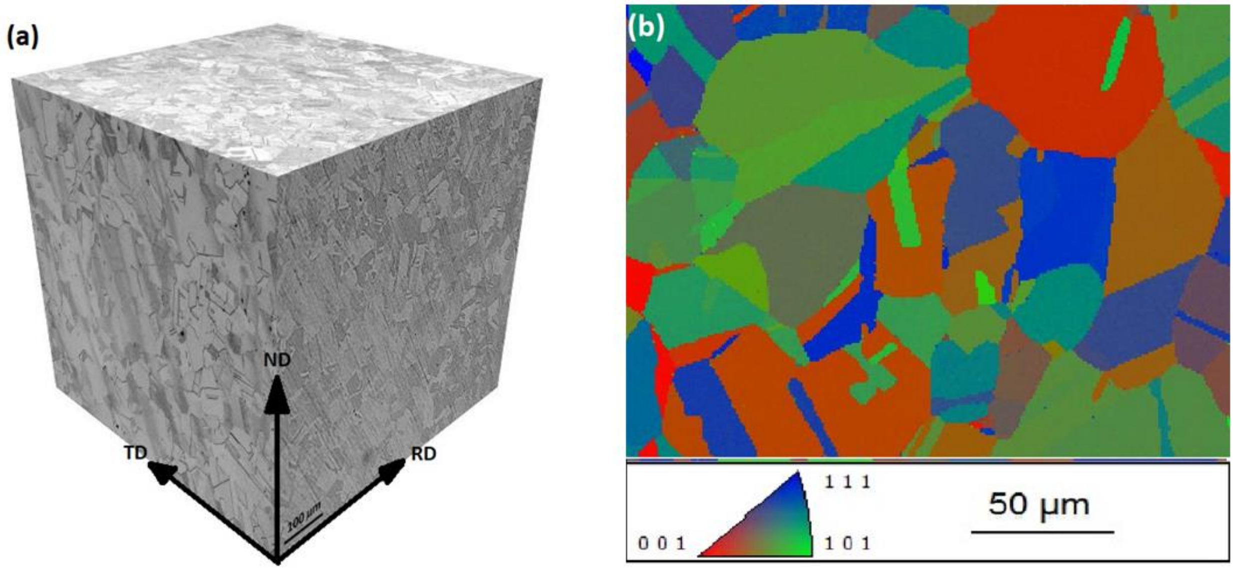

Figure 9.1. Microstructure of the as-received Alloy 709 *(a)* and EBSD inverse pole figure map *(b).*

Table. 9.1. Chemical compositions of the Alloy 709 plates used for creep-fatigue crack growth experiments.

Plate/Heat	**S**	**C**	**Mn**	**Si**	**P**	**Cr**	**Ni**	**Mo**	**N**	**Nb**	**Ti**	**Cu**	**Co**	**Al**	**Be**
Plate #1	<0.001	0.063	0.88	0.28	<0.005	19.69	25.00	1.46	0.14	0.23	<0.01	-	-	-	0.0022
Plate #2	0.0006	0.078	0.9	0.39	<0.005	19.89	25.01	1.51	0.14	0.25	<0.01	-	-	-	0.0037
Plate #3	-	0.07	0.91	0.44	0.014	19.93	24.98	1.51	0.148	0.26	0.04	0.06	0.02	0.02	0.0045

9.2.2. Creep-fatigue crack growth testing

CFCG testing of Alloy 709 was performed in compact tension (CT) specimens at constant amplitude loading and in laboratory air conditions. Study of fracture surfaces revealed no signs of oxidation. The experiments were performed according to the specifications in the ASTM standards E2760-10 and E647-11 [38,39]. The geometry and dimensions of the CT specimens are presented in Figure 9.2 and Table 9.3, respectively. For all specimens, the rolling direction was selected parallel to the crack plane, thus perpendicular to the loading direction. To prevent crack tunneling for CFCG testing, a 60° V-notch was machined in the crack plane on both faces of the specimen, which reduced the nominal thickness of the specimen by 4% on each side. Tests were performed on servo-hydraulic MTS frames at temperatures of 600 and 700°C, and load ratio of $R = 0.1$. Each MTS frame was equipped with a high temperature chamber that ensured a maximum thermal variation of ±3°C during the test duration, and the same temperature within the entire specimen volume. The CT specimens were pre-cracked by fatigue loading at room temperature to an initial crack length normalized by specimen width of $a/W = 0.36$. FCG was performed using a sinusoidal waveform with a frequency of 15 Hz, and CFCG used a trapezoidal waveform with hold times of 60s or 600s. The crack length during testing was measured using the direct current potential drop (DCPD) technique.

Table 9.2. Mechanical properties of modified 9Cr-1Mo and Alloy 709 steels.

Material/ Temperature	**Young's Modulus (GPa)**	**Poisson Ratio**	**Yield Strength (MPa)**	**Tensile Strength (MPa)**	**Norton Creep Constant A $(MPa)^{-n}h^{-1}$**	**Norton Creep Exponent, n**
9Cr-1Mo at 625 ºC [2]	125	0.3	325	344	9.53E-21	8.24
Alloy 709 at 600ºC	156	0.3	191	583	2.83E-22	6.7
Alloy 709 700ºC	149	0.3	178	449	4.9E-18	5.9

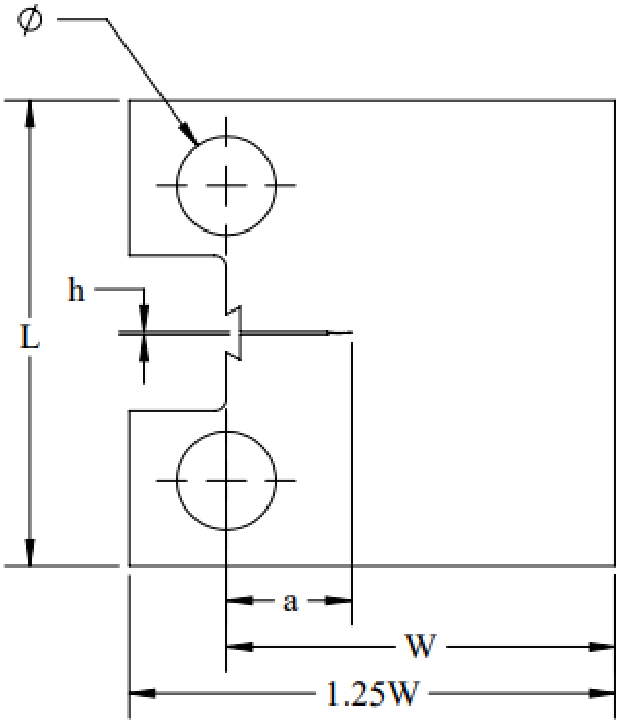

Figure 9.2. Geometry of the CT specimen. Thickness is *B*.

Table 9.3. CT specimen dimensions for each simulated material.

Dimensions [mm]	**Material**		
	9Cr-1Mo (P91)	**Alloy 709**	**316 SS**
L	60	60	60
W	50	50	50
a	20	18	20
h	0.375	0.5	0.375
ϕ	12.5	12.7	12.5
B	12.5	12.7	12.5

9.3. Finite Element Model

9.3.1. Material Modeling

The material model used in the finite element simulations was an elastically-perfectly plastic behavior with the yield stress equal to the actual flow stress of the steel, calculated as the arithmetic average of the yield and flow strengths. The creep behavior was modeled using the strain-hardening version of Norton power law for secondary (steady) state creep as

$$\dot{\bar{\varepsilon}} = A\sigma_e^{\;n} \tag{9.1}$$

The material properties used in the finite element simulations were summarized in Table 9.2.

9.3.2. Two-dimensional finite element mesh and boundary conditions

To simulate CFCG in the finite element method, a two-dimensional CT specimen was generated in the commercial software ABAQUS. Due to the geometrical and loading symmetries, only half of the specimen was modeled and simulated. A typical mesh and boundary conditions used in the simulations of crack growth are shown in Figure 9.3. Four-node quadrilateral elements were used for structured meshing. Reduced integration with hourglass control was employed to prevent shear locking. To capture the forward and reversed plastic zones around the crack tip, areas of increased mesh refinement were placed around the crack tip. The magnified area near the crack-tip region with the largest mesh density is shown in the lower portion of Figure 9.3. The element size in the most refined region was 37 μm for Alloy 709, and 50 μm for the modified 1Cr-Mo steel. These element sizes were chosen after several trial simulations by satisfying the criterion that at least 10 linear elements should be in the forward plastic zone at maximum load, while at least 3 to 4 elements be placed in the reversed plastic zone at minimum load in the cycle [23,40]. These element sizes are in the range of the average grain size of each material, as obtained from microstructural characterization in the case of Alloy 709, and near the minimum size mentioned in [32] for modified 9Cr-1Mo steel.

The boundary conditions applied to the finite element model were symmetry boundary conditions and constrained displacements. All nodes along the crack plane (from the crack tip to the right side of the specimen) were constrained in the vertical direction (*UY=0*). Further, the load point displacement at the center of the pin hole was constrained in the horizontal direction (*UX=0*). In the numerical simulations, the mode I load was applied to a reference point via a multi-point constraint, which transmits the load to the internal nodes of the pin hole. These boundary conditions are shown in Figure 9.3.

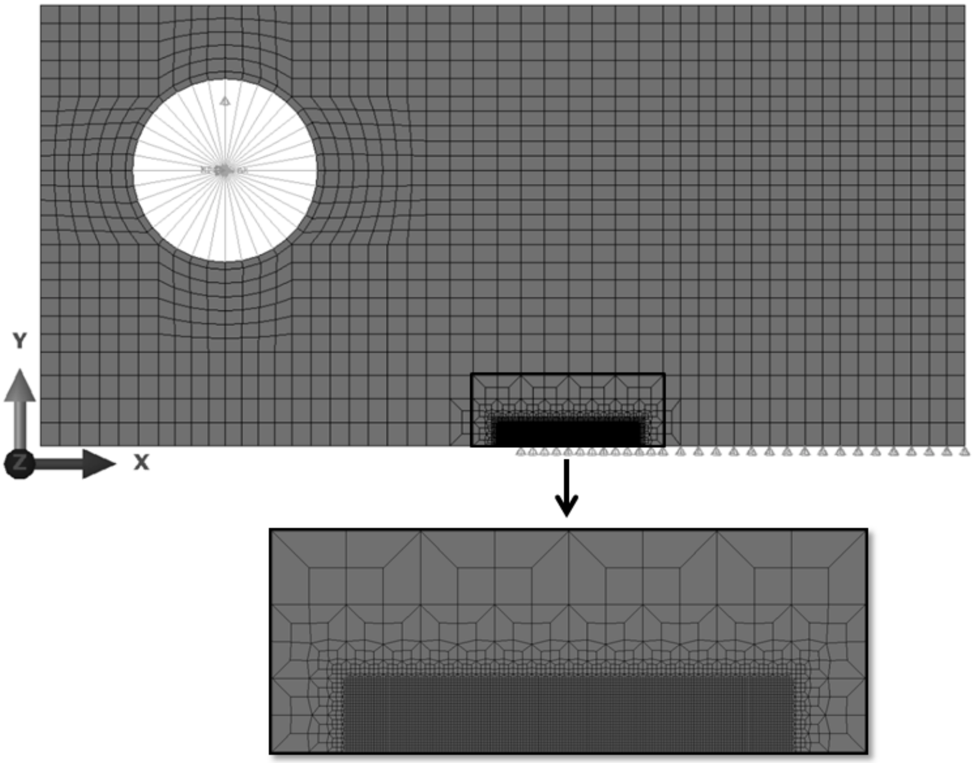

Figure 9.3. Finite element mesh and boundary conditions for the two-dimensional creep-fatigue crack growth simulations.

For an initial crack length of a_0 = 18 mm, the maximum loads applied both experimentally and in the finite element simulations generated an applied stress intensity factor range that varied between ΔK = 19 $MPa\sqrt{m}$ at the onset of the crack growth test to 45 $MPa\sqrt{m}$ toward the end of the testing. However, these values varied slightly from specimen to specimen. The maximum load was kept constant during crack growth, and the increasing ΔK resulted from the increase in crack length.

9.3.3. Load and crack propagation scheme

Creep-fatigue loading was applied to the CT specimens using a trapezoidal waveform, shown in Figure 9.4. The fatigue portion of the cycle includes the loading time L_T, and the unloading time U_T. For the experiments performed on alloy 709 at 600°C and 700°C, $L_T = U_T$ = 0.25s. Loading and unloading times for the test performed on the modified 9Cr-1Mo steel at 625°C steel were $L_T = U_T$ = 2s [3]. In the case of creep-fatigue cycles considered in this study, load hold time t_H ranged from 60s to 600s.

The crack propagation scheme used to simulate and compute plasticity-induced crack closure was the node release method. While this method does not directly produce the actual crack growth increment since the crack is advanced one element per cycle, it is extremely reliable in producing accurate crack-tip opening loads. Once the crack-tip opening load is computed, the effective stress intensity factor ΔK_{eff} is calculated, and the crack growth rate is then inferred. In this node release scheme, the nodes were released at minimum load. Fatigue crack growth was simulated by sequential release of the nodes at the tip of the crack every two applied cycles [41]. The opening loads in the CT specimen were computed using two methods, the node displacement method and the stress method. In the node displacement method, during loading time L_T from the minimum to maximum applied load, the vertical displacements of the nodes in the cracked ligament are constantly monitored. At minimum load some of these node displacements are zero, since the crack is partially closed. The opening load is defined as the remotely applied load at which the last node in the crack plane opens, i.e., its vertical displacement becomes greater than zero. In the stress method, the contact stresses at each node on the crack plane are monitored. When the normal stress in the vertical direction at all monitored nodes becomes zero, it implies that the crack is fully open, and the magnitude of the externally applied load at that moment is recorded as the crack opening load.

Simulations showed that the two methods of computing crack-tip opening loads produce comparable results. The node displacement method was retained due to its practicality. The crack opening load computation is almost always done at the first node immediately behind the crack tip, i.e., no remote closure was observed in these simulations, most likely due to the constant-amplitude loading applied [42]. The procedure is illustrated in Figure 9.4 for the application of one and two cycles before a node release. By performing several simulations, it was observed that releasing the crack-tip node every two cycles at minimum load produced optimum crack opening loads, in agreement with previously published studies. Finally, the contact of the crack surfaces was simulated by introducing a frictionless or penalty function method, both provided in ABAQUS [43]. In this study, both analyses were tested and the penalty function or augmented Lagrange contact algorithm was used, as it was also done in the work of de Matos and Nowell [41].

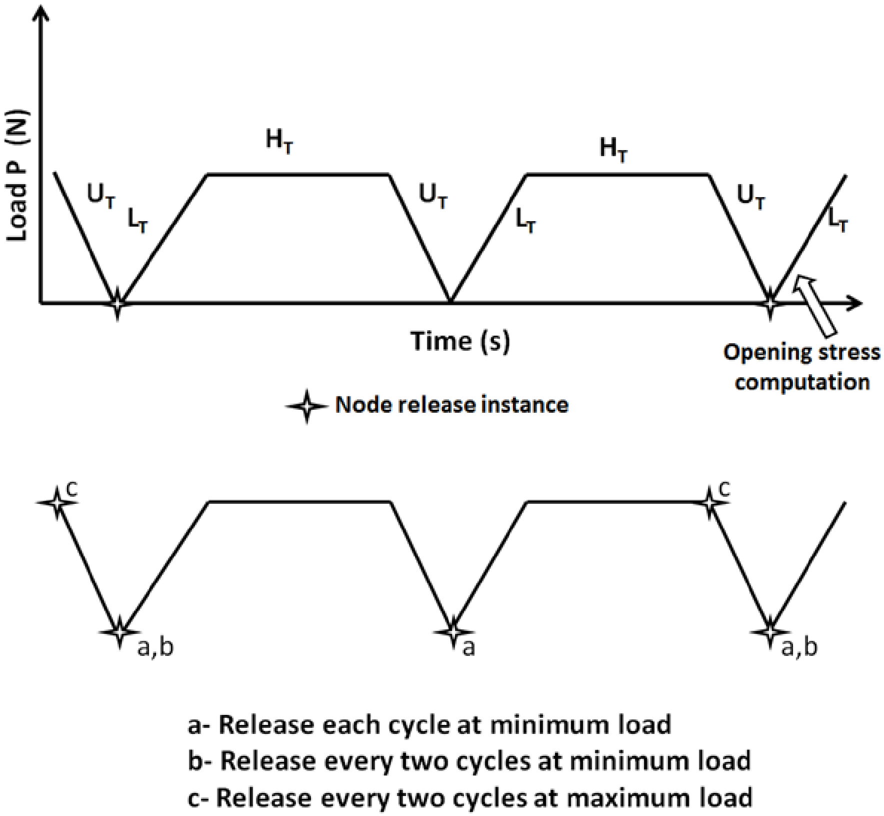

Figure 9.4. Node release schemes tested for the finite element simulations of creep-fatigue crack growth. Method *b* was employed to produce the results in this study.

9.3.4. Model Validation

Prediction of the crack-tip opening loads by the current finite element model were compared to published data from research studies that employed both the finite element method [23] and the strip-yield modelling (SYM) technique [28,44–47] The current modeling predictions were performed using plane stress ($\alpha = 1$) and plane strain ($\alpha = 3$) conditions. The results for both cases are shown in Figure 9.5. The solid line represents the plane stress case, whereas the dashed line is for plane strain. In general, the predictions from the current finite element model are in line with the values from previously published studies. Particularly, an excellent agreement is obtained for the normalized opening loads between this study and the previous ones, when the load ratio R ranged between 0 and 0.8. For load ratios less than 0, the agreement is also good with minor differences between the current model and previous ones. Therefore, it can be concluded that the finite element model and all the computational details are properly setup to simulate crack-tip opening loads caused by plasticity-induced crack closure.

The second validation was performed by comparing the predictions of the current model with the finite element results of Solanki et al. [23].

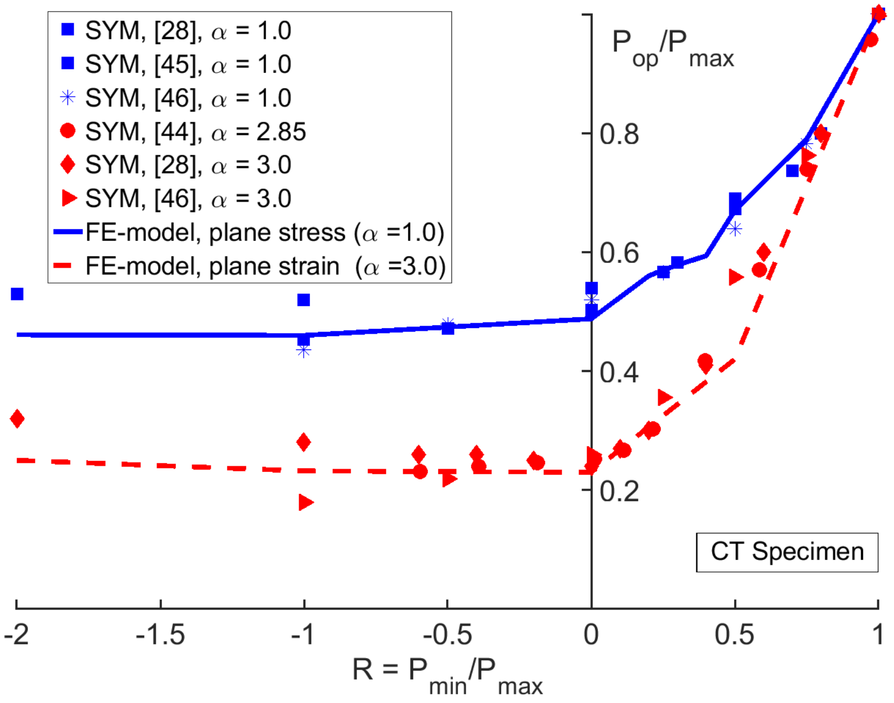

Figure 9.5. Comparison between published data and the current model predictions of normalized opening loads for fatigue crack growth.

Figure 9.6 presents the normalized opening loads as a function of minimum element size at the crack tip normalized by the forward plastic zone size. The predictions of the normalized opening loads levels are in good agreement with the values obtained by Solanki et al. at normalized stress intensity factors of $K_{max}/\sigma_0 = 1.07\sqrt{\text{mm}}$ and $K_{max}/\sigma_0 = 2.21\sqrt{\text{mm}}$, and for two different crack lengths of $a/W = 0.3$ and $a/W = 0.4$. As shown in Figure 9.6, the normalized opening load stabilized at approximately $P_{op}/P_{max} = 0.55$ for $K_{max}/\sigma_0 = 1.07\sqrt{\text{mm}}$, and decreased to $P_{op}/P_{max} = 0.5$ when the maximum stress intensity factor increased to $K_{max}/\sigma_0 = 2.21\sqrt{\text{mm}}$. These opening load values were recorded for meshes with various element sizes at the crack tip, and did not change significantly when the element size was changed. Consequently, for the actual simulations, meshes that used a normalized element size $\Delta a/r_f$ between 0.063 and 0.098 were used to perform the crack growth rate predictions presented in the next section. The approximated forward plastic zone is computed based on the equation,

$$r_f = \frac{1}{2\alpha\pi}\left(\frac{K_{\max}}{\sigma_0}\right)^2 \tag{9.2}$$

Figure 9.7 shows the evolution of the crack opening load with increasing crack length in modified 9Cr-1Mo steel at 625°C. The normalized element size near the crack tip was $\Delta a/r_f$ = 0.063, the applied load ratio R = 0.1 and the maximum applied load P_{max} = 9 kN. The increasing trend of the opening load curve in the initial stage of crack growth is due to the plastic wake build-up.

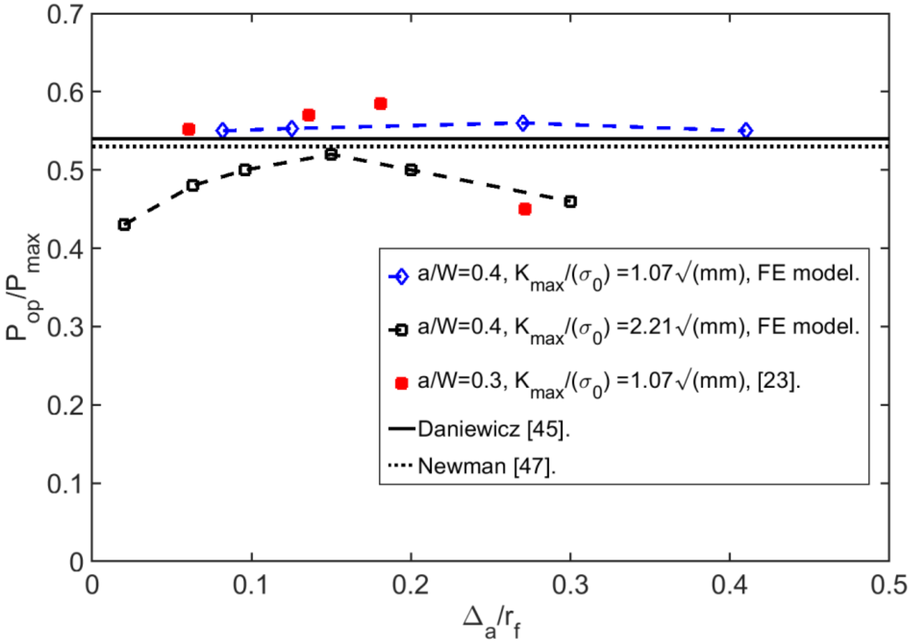

Figure 9.6. Comparison of predicted crack-tip opening loads in this study and the finite element results of Solanki et al. [23] for plane stress. Δa is element size and r_f the plastic zone size.

The normalized opening load eventually stabilizes and does not change noticeably with increasing crack length, due to the stabilization of the plastic wake thickness. The simulations performed using various element sizes and applied loads indicated that the stabilization of the opening load occurs in general after approximately 30 node releases, i.e., 60 cycles of applied load. For the crack growth rate predictions presented in this study, the stabilized values of the crack opening loads were used.

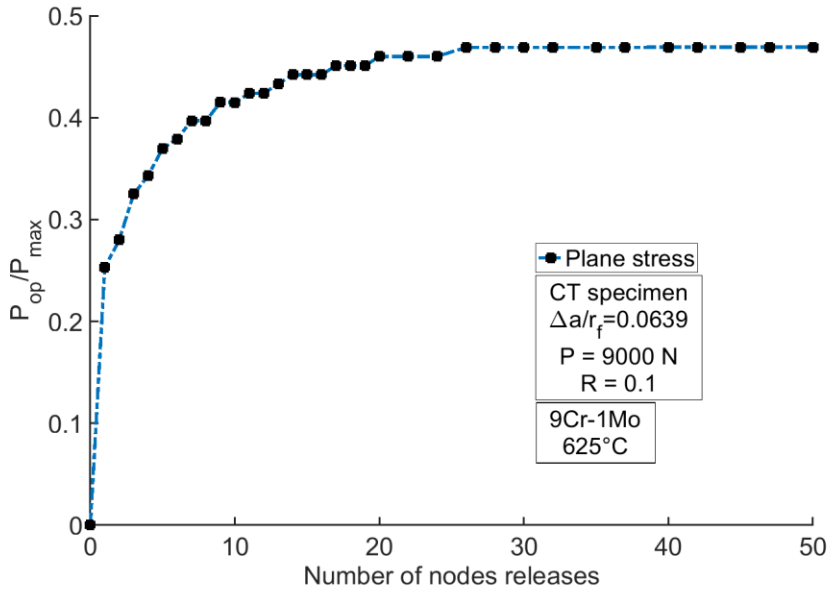

Figure 9.7. Typical evolution of crack-tip opening load as a function of number of node releases.

9.4. Results and Analysis

9.4.1. Prediction of creep-fatigue crack growth rates

Paris et al. [48] proposed a relationship between the fatigue crack growth rate *da/dN* and stress intensity factor range Δ*K*,

$$\frac{da}{dN} = C \cdot \Delta K^{m} \tag{9.3}$$

where *C* and *m* are material parameters. For a CT specimen, the stress intensity factor is defined as,

$$K = \frac{P}{\left(BB_N\right)^{1/2} W^{1/2}} F\left(\frac{a}{W}\right) \tag{9.4}$$

where *F (a/W)* is a geometrical factor which depends on crack length and specimen geometry [38]

$$F\left(\frac{a}{W}\right) = \left[\frac{2+\frac{a}{W}}{(1-\frac{a}{W})^{3/2}}\right]\left(0.886+4.64\left(\frac{a}{W}\right)-13.32\left(\frac{a}{W}\right)^{2}+14.72\left(\frac{a}{W}\right)^{3}-5.6\left(\frac{a}{W}\right)^{4}\right) \tag{9.5}$$

Due to plasticity-induced crack closure, the crack-tip driving force ΔK in equation (9.3) is diminished and is replaced by its effective value ΔK_{eff}. Thus, a fatigue crack growth law widely used to account for the partial closure of the crack at minimum load is [21,49],

$$\frac{da}{dN} = A \cdot (\Delta K_{eff})^{B} \tag{9.6}$$

where during the loading portion of a creep-fatigue cycle, the effective stress intensity factor range is $\Delta K_{eff} = K_{max} - K_{op}$. In this expression, K_{op} is defined as the stress intensity factor at which the crack is completely open. With a simple re-arrangement, ΔK_{eff} in equation (9.6) becomes,

$$\Delta K_{eff} = K_{\max} - K_{op} = K_{\max} \cdot \left(1 - \frac{K_{op}}{K_{\max}}\right) \tag{9.7}$$

The effective stress range ratio or the closure factor can be defined from the above equation in terms of the normalized opening load P_{op}/P_{max},

$$U = \frac{\Delta K_{eff}}{\Delta K} = \frac{\left(1 - \frac{P_{op}}{P_{\max}}\right)}{(1-R)} \tag{9.8}$$

In a creep-fatigue cycle, the total crack growth increment per cycle is generally written as the sum of two contributions, i.e., the cycle-dependent portion $(da/dN)_L$ and the hold portion of the loading waveform $(da/dN)_H$,

$$\left(\frac{da}{dN}\right) = \left(\frac{da}{dN}\right)_L + \left(\frac{da}{dN}\right)_H \tag{9.9}$$

The crack closure effect is taken into account when computing $(da/dN)_L$ using equation (9.6). A key feature of this model that will be described in the next section is that opening load P_{op} depends on the duration of the hold time t_H. Thus, the influence of creep load on fatigue crack growth is made evident and quantified. In part, the influence of t_H on P_{op} highlights some of the load interaction effects on CFCG rates.

The creep crack growth rate is given by the following expression,

$$\left(\frac{da}{dN}\right)_H = \left(\frac{da}{dt}\right)_H \cdot t_H \tag{9.10}$$

where,

$$\left(\frac{da}{dt}\right)_H = A' \cdot K^{B'}{}_{MAX} \tag{9.11}$$

The material constants A, B, A' and B' used in the crack growth Eqns. (6) and (11) are listed in Table 9.4.

Table 9.4. Constants used in the fatigue and creep crack growth laws.

CFCG Constants	A	B	A'	B'
9Cr-1Mo at 625 ºC [9kN]	3.55E-07	2.4	8.0E-8	3.85
9Cr-1Mo at 625 ºC [7.5kN]	3.55E-07	2.5	9.50E-8	3.84
Alloy 709 at 600ºC	9.0E-9	4.26	1.50E-7	3.2
Alloy 709 700ºC	4.60E-7	2.2	1.0E-7	2.9

9.4.2. Crack opening displacements and strain fields

In this section, cumulative plastic and creep strain fields in the crack-tip region are presented for CFCG. The plastic strain fields in the case of CFCG at ΔK between 23 and 30 $MPa\sqrt{m}$ are shown in Figure 9.8. Four different hold times ranging between t_H = 60s and t_H = 600s are presented. Figure 9.8 shows the CFCG simulated for 80 cycles, in which the total crack growth increment was Δa = 1.95 mm. For each hold time, the crack develops a plastic wake of approximately constant thickness throughout the entire crack growth simulation. As expected, the size of the plastic wake behind the crack tip and plastic strain magnitude are the same for all simulations involving different hold times. This confirms that the creep deformation at the crack tip does not affect the plasticity itself. However, due to the time dependent deformation, the longer the applied hold time the larger the crack opening displacements. While the creep strains do not affect directly the plasticity at the crack tip, they increase the crack tip opening displacements at the maximum load in the cycle, and this, in turn, decrease the crack-tip opening load.

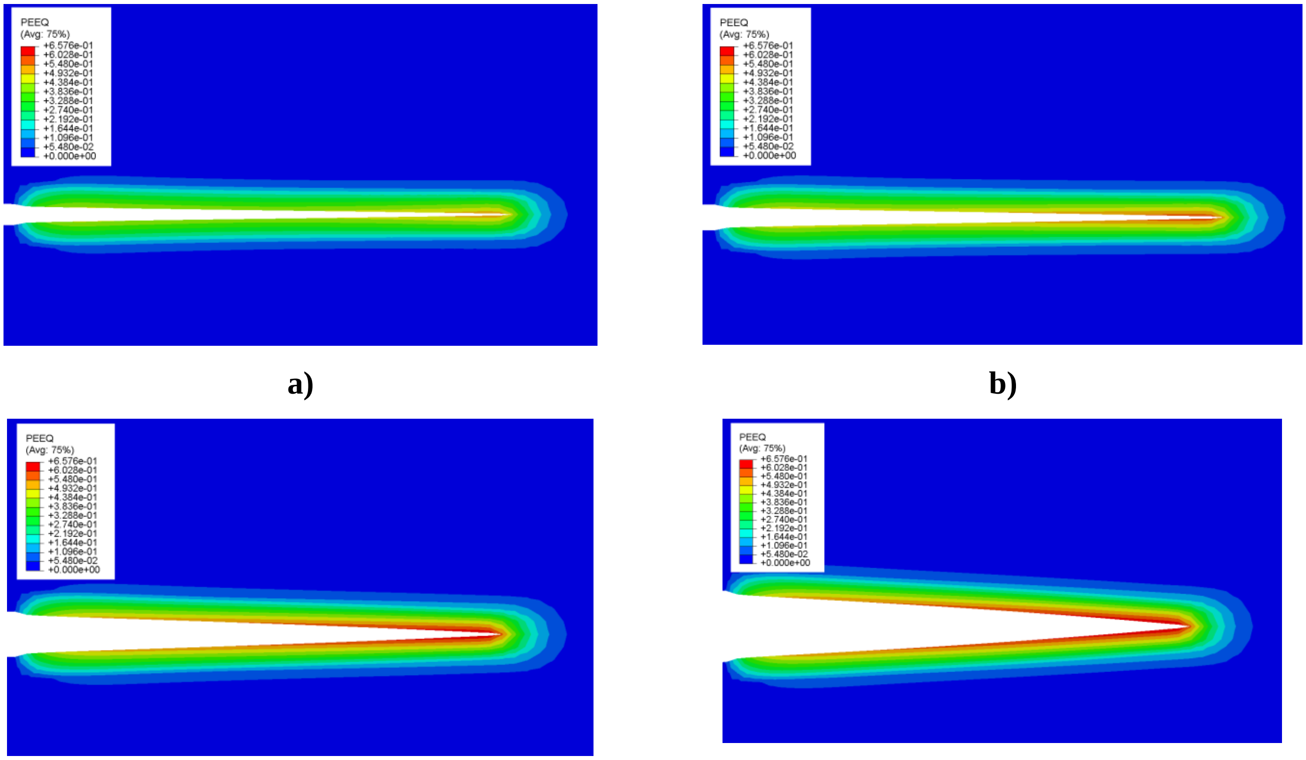

a) **b)**

c) **d)**

Figure 9.8. Equivalent plastic strain fields and crack-tip opening displacements in the near crack-tip region at cycle 80, end of holding for creep-fatigue crack growth with hold times: (a) t_H = 60s, (b) t_H = 100s, (c) t_H = 300s, and (d) t_H = 600s.

Equivalent creep strain fields are presented in Figure 9.9. From this figure, it is observed that with longer hold times, the creep zone size and creep strain magnitude increase in the crack-tip region. This leads to an increased crack opening displacement for the entire crack surface, behind the crack tip. Therefore, for long enough hold times, the crack remains open at minimum load, and the opening load becomes the minimum applied load in the creep-fatigue cycle.

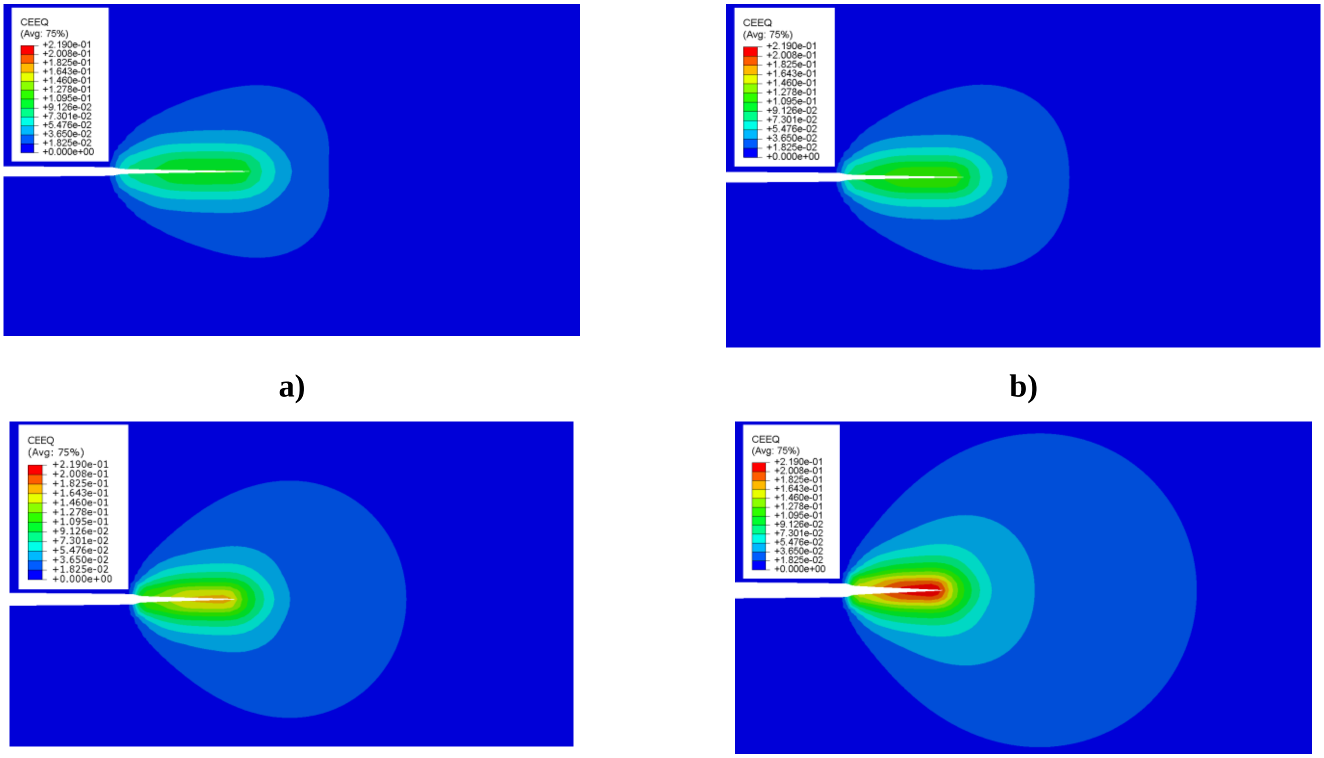

a) **b)**

c) **d)**

Figure 9.8. Equivalent creep strain fields and crack opening displacements in the near crack-tip region at cycle 29, end of holding for creep-fatigue crack growth with hold times: (a) t_H = 60s, (b) t_H = 100s, (c) t_H = 300s, and (d) t_H = 600s.

9.4.3. Stress fields near the crack tip

This section presents the normal stress σ_y variation ahead of the crack tip in the case of a growing crack under fatigue or creep-fatigue loading. The stress distribution is analyzed during cycles 1 and 62, at the end of creep loading and at the end of unloading. The variation of σ_y at the end of the hold time during cycle 1 is shown in Figure 9.10 for FCG and CFCG with different hold times, ranging from t_H = 10s to t_H = 600s. It can be observed that the normal stresses in front of the crack tip decreases as the hold time increases. The extent of the forward plastic zone at the crack tip can be seen from the distribution of the stress ahead of the crack tip for the FCG case (t_H = 0s). Here, the normal stress σ_y, which is the dominant component in the three-dimensional stress state is almost constant for a given distance ahead of the crack tip, and has a value near the flow stress of the material. For the CFCG, the stress magnitude decreases with longer applied hold times, which is the effect of the creep relaxation in front of the crack tip. Figure 9.11 shows the same analysis for the end of hold time at cycle 61. In the case of FCG, the plastic zone size shows a small increase due to the crack becoming longer. For CFCG, the stresses σ_y relaxes even further. The stress relaxation in this case can be observed directly in front of the crack tip whereas each peak stress is lower compared to the similar one in Figure 9.10. Moreover, the stress at a finite distance ahead of the crack tip decreases and the distinction between the stress distributions for creep-fatigue cycles with different hold times is less evident.

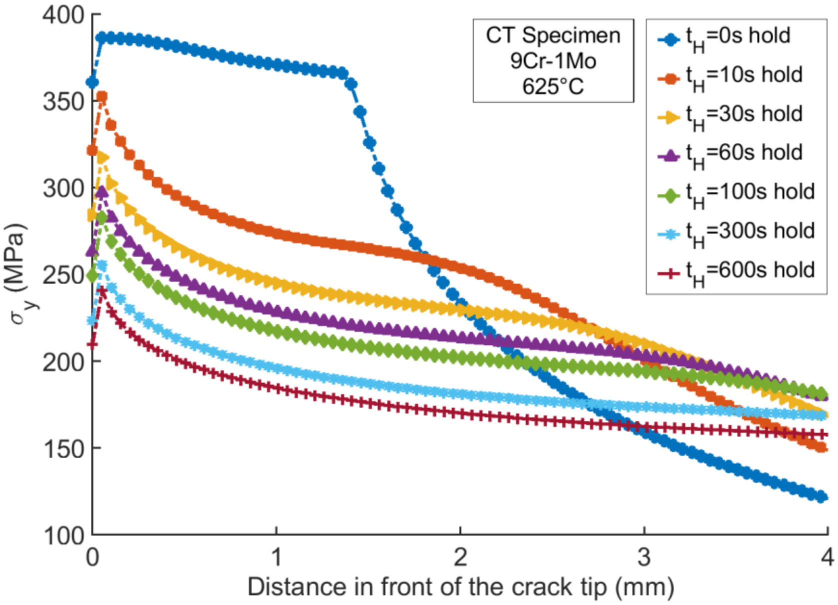

Figure 9.9. Variation of the normal stress σ_y in the crack tip region after holding in cycle 1.

The stresses at the crack tip drop significantly below the yield strength of the material, i.e., below 300 MPa and continue to decrease along the crack path. The normal stresses in front of the crack tip converge to a stabilized value as the applied hold time increases.

In order to understand the effect of hold time on the plasticity-induced crack closure and crack opening loads, we analyze the σ_y distribution at the end of unloading, i.e., at minimum load in the creep-fatigue cycle. The distribution of σ_y stresses at minimum load during cycle 1 and 61 are shown in Figures 9.12 and Figure 9.13, respectively. For clarity, of the six different hold times simulated and shown in Figure 9.11, only four are presented in Figures 9.12-9.13. The compressive axial stresses in front of the crack tip along the crack line are large immediately in front of the crack tip and decrease away from the crack tip. The increasing hold time has the effect of slowing the decrease of the compressive stresses at minimum load away from the crack tip. The stresses drop due to the applied hold time, and become larger than those in the case of no-hold time at distances greater than approximately 1.8 mm in front of the crack tip. As the hold time increases, the difference in the stresses in front of the crack tip becomes larger farther away from the crack tip.

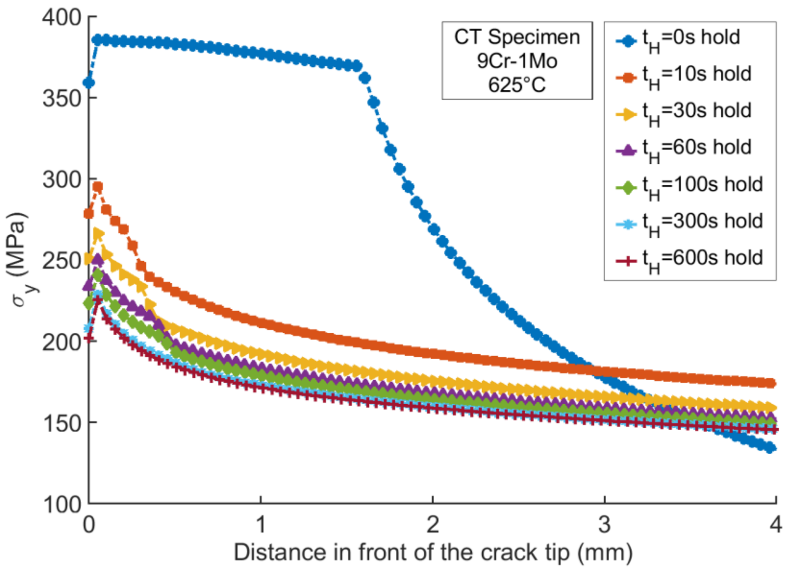

Figure 9.10. Variation of the normal stress σ_y in the near crack tip region after holding in cycle 61.

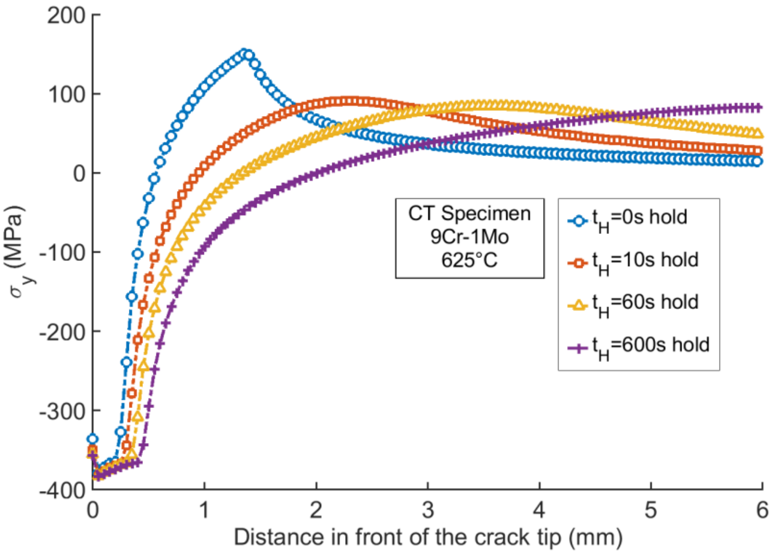

Figure 9.11. Variation of the normal stresses σ_y at minimum load in front of the crack tip after unloading in cycle 1. Crack tip is located at distance $x = 0$.

After 61 cycles of crack growth, the stress distribution ahead of the crack tip at minimum load as a function of hold time is shown in Figure 9.13. The general trend of decreasing compressive stresses is maintained when compared with the stress distribution at cycle 1; however, there is a distinct difference between the fatigue and creep-fatigue loading with different hold times. The compressive axial stresses are higher in the proximity of the crack tip, more specifically in the immediate vicinity of the reversed plastic zone. Farther away from the crack tip, the stress distributions for various hold times are more similar in the case of cycle 61 compared to cycle 1. In conclusion, at minimum load the compressive stress in front of the crack tip relaxes more slowly with increasing hold time. This is related to the tendency of the crack to develop larger opening displacements behind the crack tip, and it will result in a decrease of the plasticity-induced crack closure and the crack-tip opening loads during creep-fatigue loading with larger hold time.

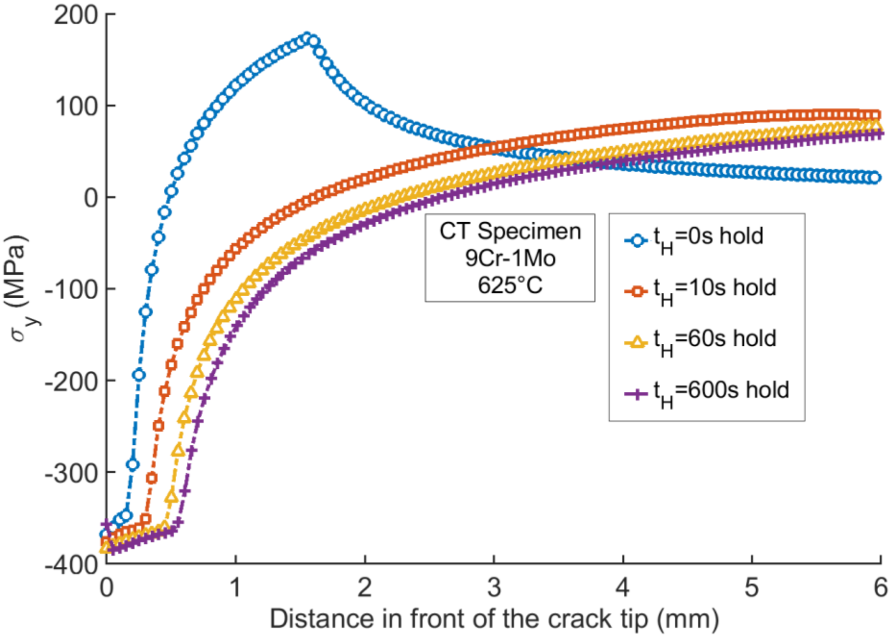

Figure 9.12. Variation of the normal stresses σ_y at minimum load ahead of the crack tip after unloading in cycle 61. Crack tip is located at distance $x = 0$.

9.4.4. Crack opening displacements and contact stresses behind the crack tip

Crack opening displacements (COD) were computed behind the crack tip during FCG and CFCG at maximum and at minimum load in cycle 29. Figure 9.14 shows the COD's at the end of hold time in cycle 29 with different hold times. The COD increases as the hold time increased from t_H = 10s to t_H = 600s. Moreover, the COD in the case of fatigue loading is lower than that in the case of creep-fatigue loading with the lowest applied hold time of t_H = 10s.The COD increase for creep-fatigue loading is the result of flow stress relaxation resulting from the accumulation of creep deformation in the crack plane ahead of the crack tip. This, in turn, affects the crack closing during unloading, resulting is drastic differences in the COD and contact stresses behind the crack tip when the fatigue loading is compared to the creep-fatigue loading case. The COD at minimum load in cycle 29 is shown in Figure 9.15. In the case of fatigue loading, the COD is the lowest for all nodes behind the crack tip, and a portion of the cracked plane is closed at minimum loading. As the hold time increases, the COD at minimum load becomes larger. Moreover, the portion of the cracked plane that is closed at minimum load shortens with increasing hold time. Figure 9.15 shows that for sufficiently large hold times, such as t_H = 300s and t_H = 600s, the crack does not close at minimum load, except for the node immediately behind the crack tip. Consequently, when the reloading occurs in the next cycle, the crack-tip opening load decreases significantly compared to the value recorded from a fatigue cycle when a large portion of crack plane behind the crack tip is closed at minimum load.

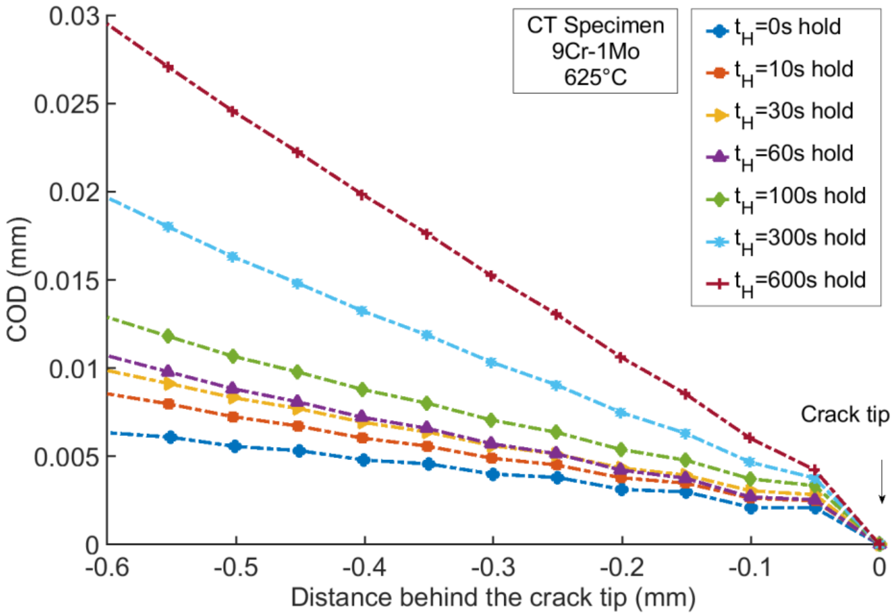

Figure 9.13. Crack opening displacement (COD) in the near crack tip region at the end of hold time during cycle 29.

In the case of creep loading with a sufficiently large hold time, the crack-tip opening load that is computed in the next loading cycle decreases to the minimum applied load. This situation occurs when the crack does not close at all at minimum load in the cycle.

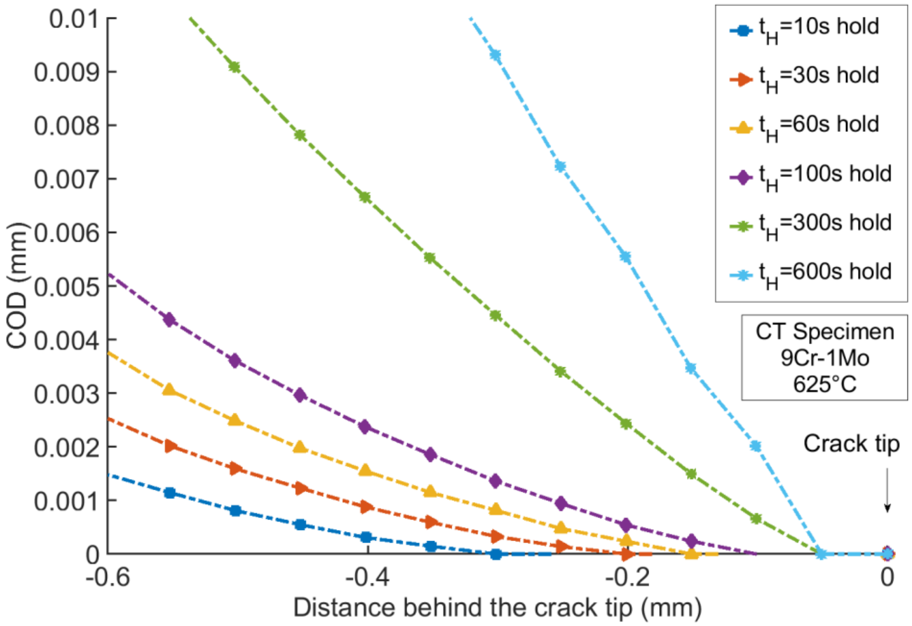

Figure 9.14. Crack opening displacement (COD) in the near crack tip region at minimum load at cycle 29.

In addition to the picture offered by the distribution of the COD at minimum load, the idea of a crack experiencing reduced closure at minimum load with increased hold time can be further understood when the contact stresses between the crack surfaces at minimum load are analyzed. Figure 9.16 shows the contact stresses behind the crack tip after unloading at minimum load in cycle 29. The fatigue loading case shows the largest extent of compressive stresses behind the crack tip, and the magnitude of these stresses decreases in the case of creep-fatigue loading. This can be interpreted as the effect of the increased COD with the added hold time causing the residual plastic deformation on the crack faces to lose its effectiveness in maintaining the crack-tip region closed at minimum load.

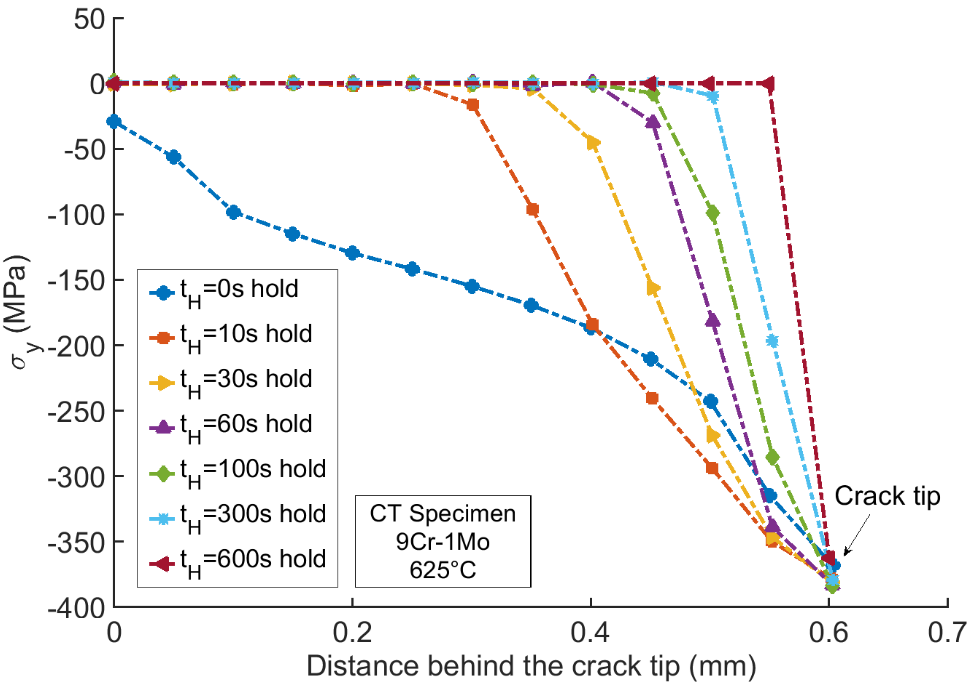

Figure 9.15. Distribution of the normal stresses σ_y at minimum load behind the crack tip at minimum load in cycle 29.

9.4.5. Crack-tip opening loads for creep-fatigue crack growth

In this section, the finite element predictions of crack-tip opening loads are presented for the modified 9Cr-1Mo steel at 625°C. The numerical simulations of CFCG with various hold times were performed for applied ΔK between 23 to 30 $MPa\sqrt{m}$. Figure 9.17 shows the dependence of the stabilized opening load (after 30 cycles of crack growth) as a function of hold time and for different ΔK values. The opening load decreases with longer hold time in the cycle for all tested ΔK levels. This effect should be understood in light of the discussion on the mechanics of crack closure during unloading and crack opening during the subsequent reloading. The effect of hold time on the reduction of the opening is more significant for higher values of ΔK. At higher ΔK values under the same applied load ratio R, K_{max} also increases, which induced larger creep deformation near the crack tip, thus decreasing the opening load.

The variation of the normalized opening load P_{op}/P_{max} as a function of ΔK for the entire crack growth history in the case of modified 9Cr-1Mo steel at 625°C is shown in Figure 9.18. The three different curves on this plot correspond to different hold times, i.e., the fatigue loading case with t_H = 0s, and two creep-fatigue loading cases with t_H = 60s and t_H = 600s.

In the case of fatigue loading, the decreasing trend of the opening load is caused by the increasing ΔK values. As ΔK approaches the value of 38 $MPa\ \sqrt{m}$, the forward plastic zone at the crack tip and the crack surface displacements greatly increase compared to the relatively stabilized thickness of the plastic wake.

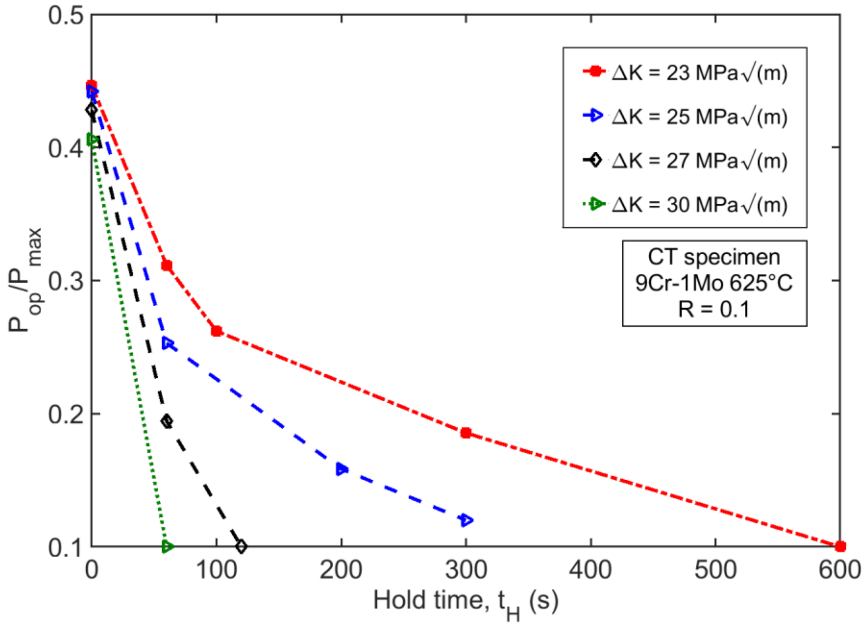

Figure 9.16. Variation of the stabilized crack-tip opening load as a function of hold time at different ΔK values during the crack growth history.

Consequently, the opening load decreases in the final crack growth stage. In the case of creep-fatigue loading with a hold time of t_H = 60s, in addition to the increasing ΔK effect on the plasticity at the crack tip, the larger creep deformation associated with larger K_{max} further enhances the crack surface displacements and decreases the opening load. For creep-fatigue loading with t_H = 600s, the added crack surface displacement caused by creep at K_{max} completely dominates the plastic wake, and the crack becomes fully open at minimum load. In this case, the effect of plasticity-induced crack closure is annihilated by the creep deformation at the crack tip. The opening load plot for fatigue crack growth was curve-fitted using a quadratic function, while the one for creep-fatigue with a hold time of t_H = 60s was curve-fitted with a linear function for the range of ΔK between 19 and 30 $MPa\ \sqrt{m}$. The obtained curve-fitted equations are for fatigue and creep-fatigue 60 and 600s hold, respectively:

$$P_{op} / P_{\max} = -0.0014(\Delta K)^2 + 0.0583(\Delta K) - 0.1446, \text{ for } t_H = 0\text{s} \tag{9.12}$$

$$P_{op} / P_{\max} = -0.0332(\Delta K) + 1.0883, \text{ for } t_H = 60\text{s} \tag{9.13}$$

$$P_{op} / P_{\max} = -0.0438(\Delta K) + 1.1063 \text{, for } t_H = 600\text{s} \tag{9.14}$$

These polynomial functions of opening loads were incorporated in the predictions of the fatigue and creep-fatigue crack propagation rates *da/dN* versus *ΔK*, which are presented in the next section.

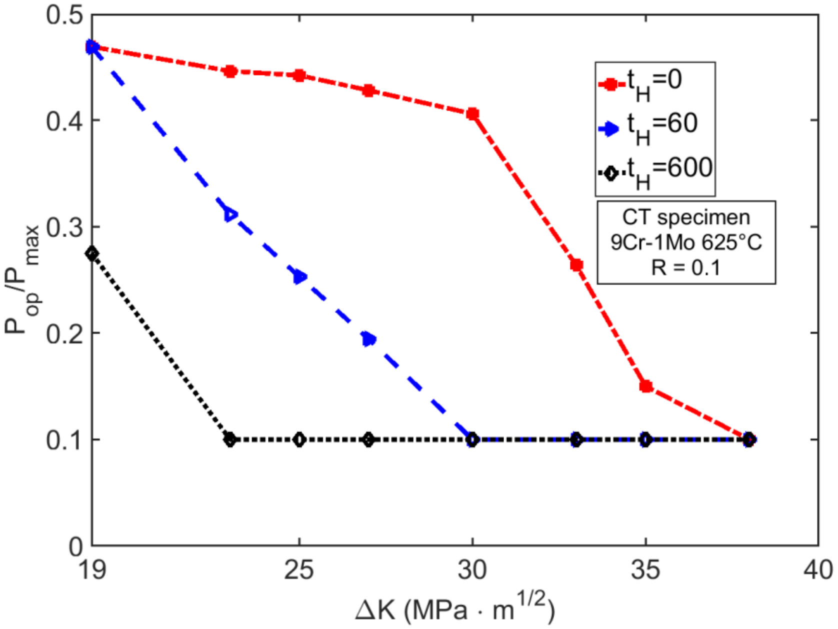

Figure 9.17. Variation of the crack-tip opening loads as a function of ΔK for fatigue and creep-fatigue loading.

9.4.6. Creep-fatigue crack growth rate predictions for modified 9Cr-1Mo steel

In this section, predictions of creep-fatigue crack growth rates for the modified 9Cr-1Mo steel at 625°C are presented. Crack opening loads obtained from the finite element simulations and presented in Figure 9.18, and equations (9.12)-(9.14) were used to compute creep-fatigue crack growth rates. Experimental crack growth rates were retrieved from the study of Narasimhachary and Saxena [2]. The predictions performed with the present finite element model replicate their study by using the same specimen geometry, material properties and applied loading cycle. The material properties and specimen dimensions employed in the finite element simulations were presented in Table 9.2 and Table 9.3, respectively. Narasimhachary and Saxena measured CFCG rates using CT specimens with a width of W = 50 mm, an approximate initial crack length (a/W) = 0.4, applied maximum load of F_{max} = 7.5 kN, and load ratio of R = 0.1. The creep-fatigue cycle used in their experiments had a hold time that was either t_H = 60s or t_H = 600s. Figure 9.19 shows the model prediction for fatigue and creep-fatigue loading with hold times of 60s and 600s when the maximum load in the cycle was $F_{max} = 7.5$ kN. The predictions for fatigue crack growth rates per cycle for 600s hold time show values slightly higher than the experimental ones. This can be explained that the coefficients A and B used in the FCG rate equation were those that were derived from the test that used $F_{max} = 9$ kN The predictions for 60s and 600s hold time when $F_{max} = 9\ kN$ load is applied are shown in Figure 9.20. In this case, the predictions are in good agreement with the experimental data. The corresponding normalized opening loads employed in these computations were given in Figures 9.17 and 9.18.

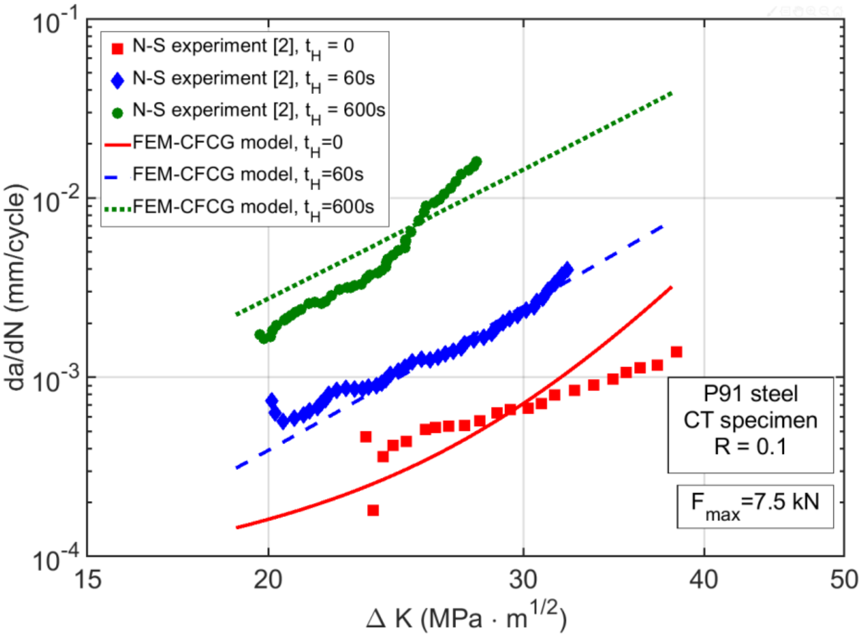

Figure 9.18. Comparison between the current model predictions and the experimental measurements by Narasimhachary and Saxena (N-S) ([2]) for creep-fatigue crack growth rates in modified 9Cr-1Mo steel at 625°C.

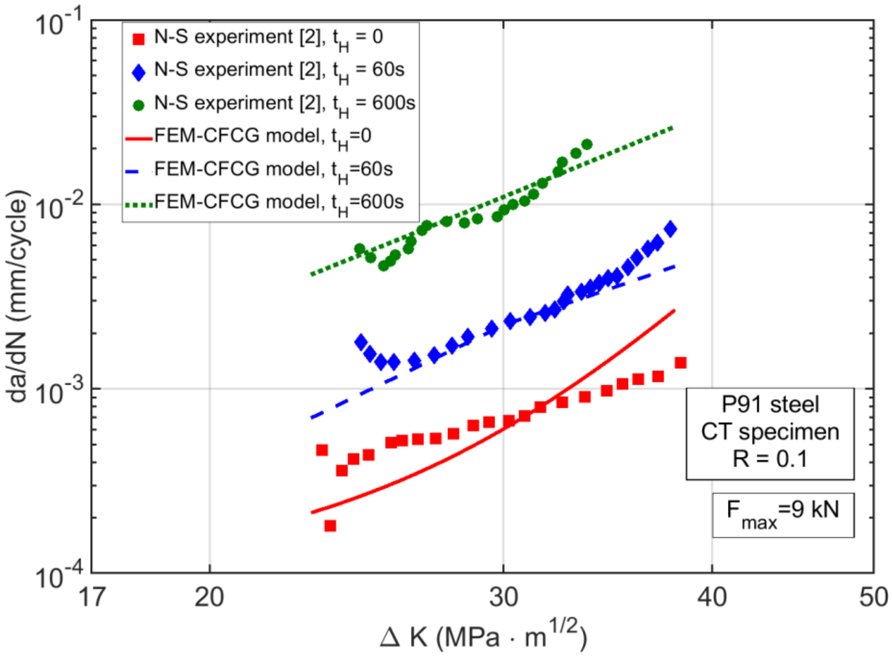

Figure 9.19. Comparison between the current model predictions and the experimental measurements by Narasimhachary and Saxena (N-S) ([2]) of creep-fatigue crack growth rates in modified 9Cr-1Mo steel at 625°C.

9.4.7. Creep-fatigue crack growth rates in Alloy 709.

Experimental tests were performed to measure creep-fatigue crack growth rates in Alloy 709, and these measurements were compared with finite element predictions. The crack growth testing on Alloy 709 was performed at 600 and 700°C in CT specimens loaded at F_{max} = 8.61 kN for pure fatigue and creep fatigue with 60s hold time, whereas F_{max} = 8.33 kN was applied for creep-fatigue with 600s hold time. All testing reported in this work was conducted at a load ratio of R = 0.1. From the performed finite element simulations, the crack-tip opening loads do not change at all with increasing hold times. This implies that alloy 709 exhibits no significant creep deformation during these hold time ranges that could affect the crack opening loads. Therefore, unlike in the case of modified 9Cr-1Mo steel, for Alloy 709 the hold time had no influence on the crack-tip opening load. These predictions of CFCG rates in Alloy 709 are shown in Figure 9.21 and Figure 9.22 for 700°C and 600°C, respectively. Figure 9.21 shows the experimental and simulated crack growth rates for FCG and CFCG with 60s and 600s hold time. In general, the experimental and computational values match, except for crack lengths that result in a ΔK greater than 30 $MPa\ \sqrt{m}$. A method to improve the predicted values for the growth rates for ΔK greater than 30 *MPa* $\sqrt{m}$ is to use a double slope curve for the *da/dN versus* ΔK_{eff} in the Paris regime, which implies the use of two sets of constants *A* and *B* in the fatigue crack growth equation.

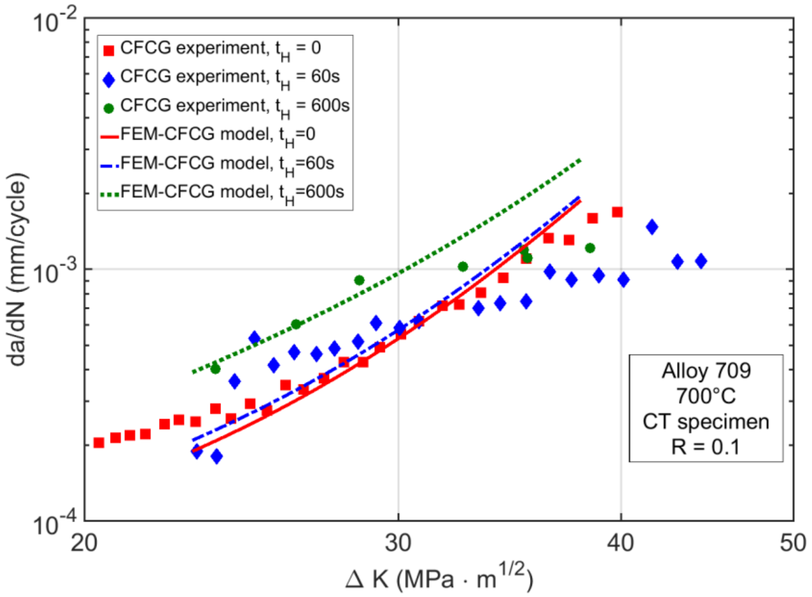

Figure 9.20. Comparison between the experimental measurements and finite element predictions of creep-fatigue crack growth rates in Alloy 709 at 700°C.

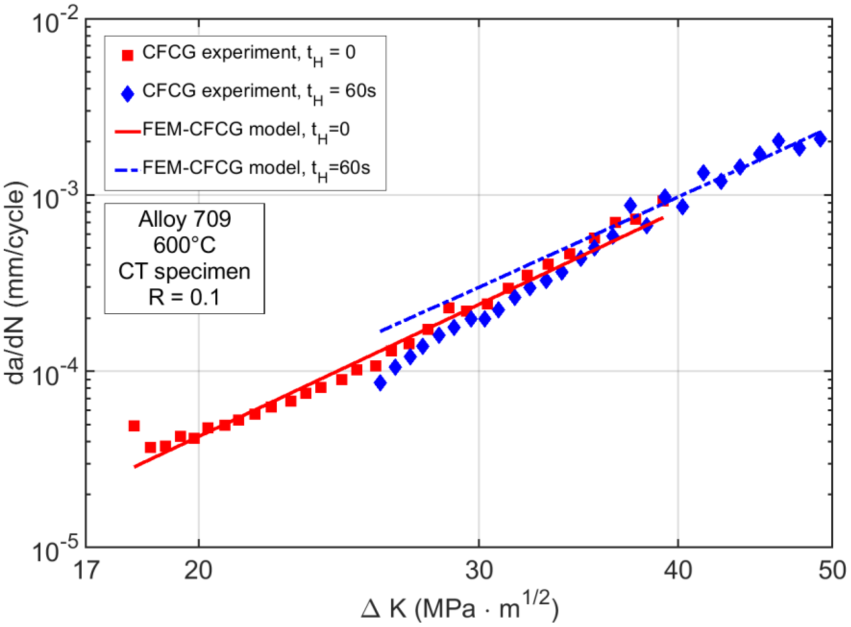

Figure 9.21. Comparison between the experimental measurements and finite element predictions of creep-fatigue crack growth rates in Alloy 709 at 700°C.

Figure 9.22 shows crack growth rates for fatigue and creep-fatigue with a hold time of 60s at 600°C. Experimental tests under creep-fatigue loading with a hold time of 600s at 600°C were not carried out given the excessively long testing time needed. Little variation between the FCG and CFCG rates is observed, both experimentally and computationally. This confirms that the crack-tip opening load does not change any noticeable amount from fatigue to creep-fatigue when a creep hold time of 60s is added to the cycle.

9.5. Conclusions

A two-dimensional finite element model was developed and used to predict crack-tip opening loads and crack growth rates during creep-fatigue loading. Plasticity-induced crack closure was simulated for creep-fatigue loading, and crack-tip opening loads were computed. In the case of modified 9Cr-1Mo steel, the creep deformation occurring in the crack tip region leads to a decrease of the crack-tip opening load with increasing hold time in a creep-fatigue cycle versus a fatigue cycle. Conversely, very little creep deformation occurs near the crack tip in Alloy 709, and the plasticity induced crack closure during fatigue is practically unperturbed for creep-fatigue loading. The simulated crack opening loads were used to compute effective stress intensity factor ranges and predict crack growth rates. The finite element model leads to predictions that are in good agreement with the experimental data for both steels analyzed. The proposed finite element modeling can account for creep-fatigue interactions on creep-fatigue crack growth in alloys at high temperatures, and it can be used reliably to make crack growth rate predictions in structural components at high temperatures.

9.6. References

[1] Zinkle SJ, Was GS. Materials challenges in nuclear energy. Acta Mater 2013;61:735–58. doi:10.1016/j.actamat.2012.11.004.

[2] Narasimhachary SB, Saxena A. Crack growth behavior of 9Cr−1Mo (P91) steel under creep–fatigue conditions. Int J Fatigue 2013;56:106–13. doi:10.1016/J.IJFATIGUE.2013.07.006.

[3] Shlyannikov VN, Tumanov AV, Boychenko NV. A creep stress intensity factor approach to creep–fatigue crack growth. Eng Fract Mech 2015;142:201–19. doi:10.1016/J.ENGFRACMECH.2015.05.056.

[4] Granacher J, Klenk A, Tramer M, Schellenberg G, Mueller F, Ewald J. Creep fatigue crack behavior of two power plant steels. Int J Press Vessel Pip 2001;78:909–20. doi:10.1016/S0308-0161(01)00106-5.

[5] Evans WJ, Jones JP, Williams S. The interactions between fatigue, creep and environmental damage in Ti 6246 and Udimet 720Li. Int J Fatigue 2005;27:1473–84. doi:10.1016/J.IJFATIGUE.2005.06.029.

[6] Ghonem H, Nicholas T, Pineau A. ELEVATED TEMPERATURE FATIGUE CRACK GROWTH IN ALLOY 718—PART II: EFFECTS OF ENVIRONMENTAL AND MATERIAL VARIABLES. Fatigue Fract Eng Mater Struct 2018;16:577–90. doi:10.1111/j.1460-2695.1993.tb00103.x.

[7] Yang H, Bao R, Zhang J, Peng L, Fei B. Creep–fatigue crack growth behaviour of a nickel-based powder metallurgy superalloy under high temperature. Eng Fail Anal 2011;18:1058–66. doi:10.1016/J.ENGFAILANAL.2010.12.025.

[8] Piard A, Gamby D, Carbou C, Mendez J. A numerical simulation of creep–fatigue crack growth in nickel-base superalloys. Eng Fract Mech 2004;71:2299–317. doi:10.1016/J.ENGFRACMECH.2004.02.002.

[9] Hall DE, Hamilton BC, McDowell DL, Saxena A. Creep crack growth behavior of aluminum alloy 2519: part II—numerical analysis. Elev. Temp. Eff. fatigue Fract., ASTM International; 1997.

[10] Yoon KB, Saxena A, Liaw PK. Characterization of creep-fatigue crack growth behavior under trapezoidal waveshape using Ct-parameter. Int J Fatigue 1994;16:235. doi:10.1016/0142-1123(94)90089-2.

[11] Saxena A. Fracture Mechanics Approaches for Characterizing Creep-Fatigue Crack Growth. JSME Int Journal Ser A, Mech Mater Eng 1993;36:1–20. doi:10.1299/jsmea1993.36.1_1.

[12] Saxena A. Nonlinear Fracture Mechanics for Engineers. Taylor & Francis; 1998.

[13] Adefris N, Saxena A, McDowell DL. CREEP-FATIGUE CRACK GROWTH BEHAVIOR IN 1Cr-1Mo-0.25V STEEL. PART II: CRACK GROWTH BEHAVIOR AND MODELS. Fatigue Fract Eng Mater Struct 2018;19:401–11. doi:10.1111/j.1460-2695.1996.tb00977.x.

[14] Adefris N, Saxena A, McDowell DL. CREEP-FATIGUE CRACK GROWTH

BEHAVIOR IN 1Cr-1Mo-0.25V STEELS. PART I: ESTIMATION OF CRACK TIP PARAMETERS. Fatigue Fract Eng Mater Struct 2018;19:387–98. doi:10.1111/j.1460-2695.1996.tb00976.x.

[15] Grover PS, Saxena A. Characterization of creep-fatigue crack growth behavior in 2.25 Cr-1 Mo steel using (Ct)avg. Int J Fract 1995;73:273–86. doi:10.1007/BF00027270.

[16] Wolf E. Fatigue crack closure under cyclic tension. Eng Fract Mech 1970;2:37–45. doi:10.1016/0013-7944(70)90028-7.

[17] Fleck NA. Finite element analysis of plasticity-induced crack closure under plane strain conditions. Eng Fract Mech 1986;25:441–9. doi:10.1016/0013-7944(86)90258-4.

[18] McClung RC, Thacker BH, Roy S. Finite element visualization of fatigue crack closure in plane stress and plane strain. Int J Fract 1991;50:27–49. doi:10.1007/BF00035167.

[19] Pommier S. Plane strain crack closure and cyclic hardening. Eng Fract Mech 2002;69:25–44. doi:10.1016/S0013-7944(01)00061-3.

[20] de Matos PFP, Nowell D. Numerical simulation of plasticity-induced fatigue crack closure with emphasis on the crack growth scheme: 2D and 3D analyses. Eng Fract Mech 2008;75:2087–114. doi:10.1016/J.ENGFRACMECH.2007.10.017.

[21] Lugo M, Daniewicz SR, Newman JC. A mechanics based study of crack closure measurement techniques under constant amplitude loading. Int J Fatigue 2011;33:186–93. doi:10.1016/J.IJFATIGUE.2010.08.004.

[22] Vor K, Gardin C, Sarrazin-Baudoux C, Petit J. Wake length and loading history effects on crack closure of through-thickness long and short cracks in 304L: Part II – 3D numerical simulation. Eng Fract Mech 2013;99:306–23. doi:10.1016/J.ENGFRACMECH.2013.01.014.

[23] Solanki K, Daniewicz S., Newman J. Finite element modeling of plasticity-induced crack closure with emphasis on geometry and mesh refinement effects. Eng Fract Mech 2003;70:1475–89. doi:10.1016/S0013-7944(02)00168-6.

[24] Zapatero J, Moreno B, González-Herrera A. Fatigue crack closure determination by means of finite element analysis. Eng Fract Mech 2008;75:41–57. doi:10.1016/J.ENGFRACMECH.2007.02.020.

[25] GONZALEZ-HERRERA A, ZAPATERO J. Numerical study of the effect of plastic wake on plasticity-induced fatigue crack closure. Fatigue Fract Eng Mater Struct 2009;32:249–

60. doi:10.1111/j.1460-2695.2009.01335.x.

[26] Antunes F V, Camas D, Correia L, Branco R. Finite element meshes for optimal modelling of plasticity induced crack closure. Eng Fract Mech 2015;142:184–200. doi:https://doi.org/10.1016/j.engfracmech.2015.06.007.

[27] Leo Prakash DG, Walsh MJ, Maclachlan D, Korsunsky AM. Crack growth micro-mechanisms in the IN718 alloy under the combined influence of fatigue, creep and oxidation. Int J Fatigue 2009;31:1966–77. doi:10.1016/J.IJFATIGUE.2009.01.023.

[28] Potirniche GP. Modeling of creep-fatigue interaction effects on crack growth at elevated temperatures. MATEC Web Conf 2018;165.

[29] Huseyin S, Wei S. The significance of crack closure under high temperature fatigue crack growth with hold periods. Eng Fract Mech 1989;33:371–88. doi:10.1016/0013-7944(89)90087-8.

[30] Sehitoglu H, Sun W. Modeling of Plane Strain Fatigue Crack Closure. J Eng Mater Technol 1991;113:31–40.

[31] Pommier S. A study of the relationship between variable level fatigue crack growth and the cyclic constitutive behaviour of steel. Int J Fatigue 2001;23:111–8. doi:10.1016/S0142-1123(01)00165-7.

[32] Kalyanasundaram V. Creep, Fatigue and Creep-Fatigue Interactions in Modified 9% Cr - 1% Mo (P91) Steels. Theses and Dissertations. 692. 2013.

[33] Sham S. Advanced Reactor Concepts Program-ARC Materials Development-Accomplishments and Plans 2013. https://www.energy.gov/sites/prod/files/2013/09/f2/ARC-Matls-CrossCut-2013.pdf.

[34] Natesan. K, Zhang. X, Sham. T.-L. and WH. Report on the completion of the procurement of the first heat of alloy 709, ANL-ART-89. Lemont, IL: 2017.

[35] Upadhayay S, Li H, Bowen P, Rabiei A. A study on tensile properties of Alloy 709 at various temperatures. Mater Sci Eng A 2018;733:338–49. doi:10.1016/J.MSEA.2018.06.089.

[36] Kim BK, Tan L, Xu C, Yang Y, Zhang X, Li M. Microstructural evolution of NF709 (20Cr–25Ni–1.5MoNbTiN) under neutron irradiation. J Nucl Mater 2016;470:229–35. doi:10.1016/J.JNUCMAT.2015.12.037.

[37] Sourmail T, Bhadeshia HKDH. Microstructural evolution in two variants of NF709 at

1023 and 1073 K. Metall Mater Trans A 2005;36:23–34. doi:10.1007/s11661-005-0135-y.

[38] ASTM E2760-10: Standard Test Method for Creep-Fatigue Crack Growth Testing, n.d.

[39] ASTM E647-11: Standard test method for measurement of fatigue crack growth rates. ASTM Annual. B. ASTM Stand., Philadelphia: 2011.

[40] Dougherty JD, Padovan J, Srivatsan TS. Fatigue crack propagation and closure behavior of modified 1070 steel: Finite element study. Eng Fract Mech 1997;56:189–212. doi:10.1016/S0013-7944(96)00104-X.

[41] de Matos PFP, Nowell D. Numerical simulation of plasticity-induced fatigue crack closure with emphasis on the crack growth scheme: 2D and 3D analyses. Eng Fract Mech 2008;75:2087–114. doi:10.1016/J.ENGFRACMECH.2007.10.017.

[42] de Matos PFP, Nowell D. Experimental and numerical investigation of thickness effects in plasticity-induced fatigue crack closure. Int J Fatigue 2009;31:1795–804. doi:10.1016/J.IJFATIGUE.2008.12.003.

[43] ABAQUS Analyisis User's Guide 38.1.2, 2016.

[44] Newman JC. Prediction of fatigue crack growth under variable-amplitude and spectrum loading using a closure model. Des. Fatigue Fract. Resist. Struct., ASTM International; 1982.

[45] Daniewicz SR, Collins JA, Houser DR. An elastic-plastic analytical model for predicting fatigue crack growth in arbitrary edge-cracked two-dimensional geometries with residual stress. Int J Fatigue 1994;16:123–33. doi:10.1016/0142-1123(94)90102-3.

[46] Wang G., Blom A. A strip model for fatigue crack growth predictions under general load conditions. Eng Fract Mech 1991;40:507–33. doi:10.1016/0013-7944(91)90148-T.

[47] Newman Jr. J ~C. FASTRAN-2: A fatigue crack growth structural analysis program. NASA STI/Recon Tech Rep N 1992;92.

[48] Paris P, Erdogan F. A Critical Analysis of Crack Propagation Laws. J Basic Eng 1963;85:528–33.

[49] McClung RC, Sehitoglu H. On the finite element analysis of fatigue crack closure—2. Numerical results. Eng Fract Mech 1989;33:253–72. doi:10.1016/0013-7944(89)90028-3.

10 A STRIP-YIELD MODELING TO SIMULATE CREEP-FATIGUE CRACK GROWTH

10.1. Introduction

A strip-yield model was formulated to simulate creep-fatigue crack growth and to quantify the influence of hold time on plasticity-induced crack closure during creep-fatigue crack growth. Creep-fatigue experiments have shown that longer creep hold times result in faster crack growth rates in subsequent fatigue cycles. This model advances the idea that a decrease of plasticity-induced crack closure is experienced by the crack during fatigue loading when a longer hold time is applied each creep-fatigue cycle. Consequently, the crack tip experiences an increase in the effective stress intensity factor range causing faster growth rate during the fatigue loading. The weight function method was used to compute stress intensity factors and surface displacements for cracks embedded in a material experiencing elastic, plastic and creep deformations at elevated temperatures. It is shown that the longer the hold time, the larger the creep deformation and crack opening displacements in the near crack-tip region. In turn, this leads to a decrease in the crack-tip opening stress/load and faster crack growth rates during the subsequent fatigue cycle. The model was used to perform simulations of creep-fatigue crack growth at elevated temperatures in a nickel-base superalloy and AISI 316 austenitic steel.

Failure of structural components by creep-fatigue crack growth occurs when mechanical loading and elevated temperature act concurrently, conditions that are common in power plants, chemical plants and the aerospace industry. Numerous studies have been performed on creep-fatigue crack growth at elevated temperatures. However, understanding the mechanics of crack growth and predicting the measured rates of crack growth during creep-fatigue loading is still an outstanding issue. The most common approach to compute creep-fatigue crack growth rates is to consider the linear summation of the crack growth rates during the fatigue and creep portions of each loading cycle. Oftentimes, models that use this additive rule disregard the interaction effects of the two loading modes. A limited number of models considered this interaction, for instance by adding an extra term to the sum, or by analyzing the crack-tip damage in front of the crack. The load interaction effect on creep-fatigue crack growth implies that the total crack growth rate is greater than the sum of the rates that a crack would experience under only creep or fatigue loading.

Fatigue crack growth in metallic alloys has been comprehensively studied over many decades. For constant amplitude fatigue loading, the Paris-Erdogan power law [1] using the stress intensity factor range ΔK as the input variable is able to predict the crack growth rates for long cracks in metals. To explain the load ratio effect on fatigue crack growth, Elber [2] proposed the concept of effective stress intensity factor ΔK_{eff}, which replaced ΔK in the Paris-Erdogan law and can explain crack acceleration and deceleration during variable amplitude loading. ΔK_{eff} values were computed by quantifying the plasticity-induced crack closure through the concept of crack-tip opening stress (S_{op}).

The influence of creep loading on S_{op} is a topic that has been almost entirely overlooked by the creep-fatigue community. The only previously published research on this topic was found to be that of Sehitoglu and Sun [3]. They employed two-dimensional finite element simulations to study the effect of load hold time on S_{op} in a cracked plate subjected to uniform tension loading. Sehitoglu and Sun showed that increasing hold time leads to larger *COD* and lower S_{op} values. Most recently, J. Ramirez et al. [4] performed a systematic study of the effect of hold time on S_{op} using two-dimensional and three-dimensional finite element simulations.

A computational approach that has been used effectively to characterize the plasticity-induced crack closure is strip-yield modeling. This technique has its source in the theoretical developments of Dugdale [5] and Barenblatt [6], who used a superposition of two elastic solutions to solve the problem of a crack embedded in an elastic-plastic region. Their approach was implemented in several computational models to simulate growing fatigue cracks. These computational strip-yield models have been used successfully to compute crack-tip opening stresses S_{op} caused by plasticity-induced crack closure under constant or variable amplitude loading. One of the first strip-yield models was that of Newman [7]. A main feature of the Newman model was that in order to deal with various test specimens, he used an equivalent center-crack simulation specimen and the K-equivalency principle for the computation of K and *COD* in other specimen types. Using Newman's modeling framework, other strip-yield models have been proposed for fatigue crack growth. Nowadays, the standard methodology involves using integrals of weight functions instead of the K-equivalency principle to compute K and *COD* values for different specimens. Strip-yield models have been developed for fatigue crack growth [8-11], thermomechanical fatigue crack growth [12] and creep crack growth [13]. To date, there are no strip-yield models developed for creep-fatigue crack growth.

In this paper, a Strip-Yield Model for Creep-Fatigue Crack Growth (SYM-CFCG) was developed using the weight function method. Creep-fatigue crack growth rates were computed by summing the growth rates during the creep and fatigue portions of each loading cycle. The loading interaction effects on crack growth rates were accounted for by modeling the decrease of S_{op} with longer hold times. A key feature of this model is the computation of S_{op} values for cracked specimens loaded with creep-fatigue loading. The geometries analyzed were the middle-tension test (MT), single-edge notch test (SENT), double-edge notch tension (DENT) and compact-tension test (CT) specimens. SYM-CFCG was used to compute crack growth rates in a nickel-base superalloy and austenitic 316 stainless steel.

10.2. Mechanics of Crack Opening/Closing during Creep-Fatigue Loading

A typical creep-fatigue load cycle is illustrated in Figure 10.1. The loading segments *A*-*B* and *C*-*D* represent the fatigue or cyclic portion of the cycle, and *B*-*C* the creep or hold time. The total crack growth during *A*-*D* is the sum of the crack growth during *A*-*B* and *B*-*C*. The main assertion of this study is that the hold time t_H during *B*-*C* affects the crack growth increment in the subsequent fatigue cycle, i.e., during *D*-*E*. This effect is a contributor to the commonly known load interaction effect on crack growth during creep-fatigue loading. For instance, this effect was observed and described in the case of creep-fatigue crack growth in a nickel-base superalloy by Piard et al. [14].

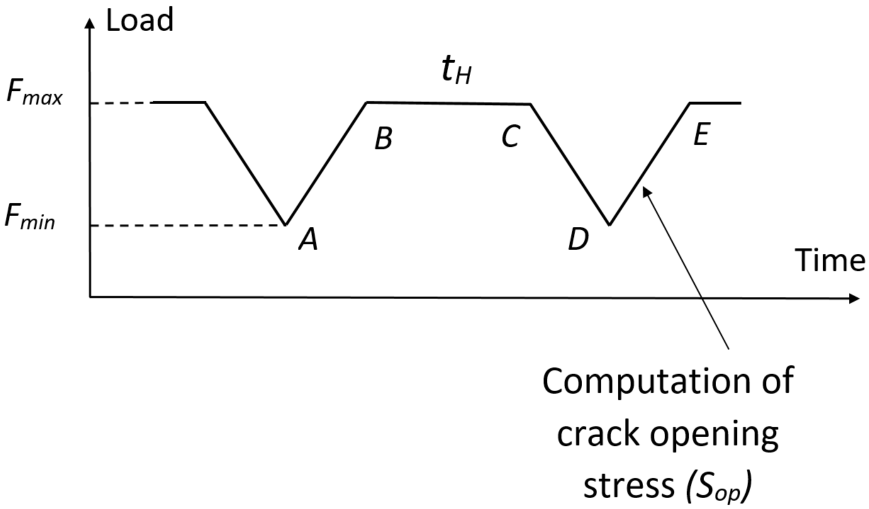

Figure 10.1. A typical creep-fatigue load cycle used in laboratory crack growth testing.

The explanation that is proposed herein for the influence of hold time t_H on fatigue crack growth in the subsequent cycle relies on the concept of plasticity-induced crack closure and the mechanics of crack opening/closing during cyclic loading. Figure 10.2 illustrates a qualitative description of the opening and closing of the crack surfaces at different points in the creep-fatigue cycle. At point B in the creep-fatigue cycle, the crack is loaded under the maximum stress. Therefore, the crack surfaces undergo a certain amount of crack opening *COD*.

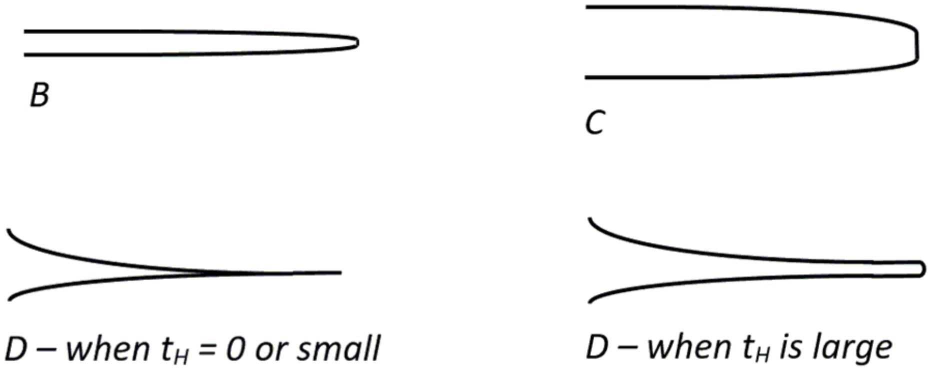

Figure 10.2. Profiles of crack opening/closing displacements during a creep-fatigue cycle.

As a result of the accumulated creep strains at the end of t_H, at point *C* in the cycle, the *COD* further increases compared to its value at point *B*. The amount of this additional increase in *COD* is proportional to t_H. Upon unloading, the crack surfaces may end up partially or totally closed depending on the magnitude of t_H. When t_H is zero (fatigue loading) or small, the crack surfaces will be at least partially closed at minimum applied load (point *D* in the cycle). When t_H is big enough, the large *COD* induced during the hold time will prevent the crack from completely (or partially) closing at minimum load. In effect, for large enough values of t_H, the crack starts the new fatigue cycle *D-E* fully open. In this case, the effect of plasticity-induced crack closure is nullified by the additional *COD* acquired by the crack during the hold time. In turn, this leads to a drop in the opening stress to $S_{op} = S_{min}$ and maximizes the crack tip driving force during the fatigue cycle, i.e., $\Delta K_{eff} = \Delta K$. This phenomenon is expressed as

$$\left(\frac{da}{dN}\right)_{D-E} = f_1\left(S_{op},\ldots\right), \text{ and } \left(S_{op}\right)_{D-E} \propto 1/t_H \qquad (10.1)$$

The above considerations are supported by the previous finite element simulation results in [3-4]. Further experimental studies are needed to establish a quantitative relationship between S_{op} and t_H.

10.3. Strip-yield Modeling of Creep-Fatigue Crack Growth

10.3.1. Modified Dugdale-Barenblatt model for plasticity and creep at the crack tip

Considering a cracked specimen subjected to mechanical loads at elevated temperatures, under cyclic and steady loads (Figure 10.1), the material around the crack tip will experience instantaneous plastic strains and creep strains that accumulate over hold time t_H. A schematic of the plastic and creep zones at the crack tip is illustrated in the first picture of Figure 10.3 for a cracked component subjected to a remote stress S.

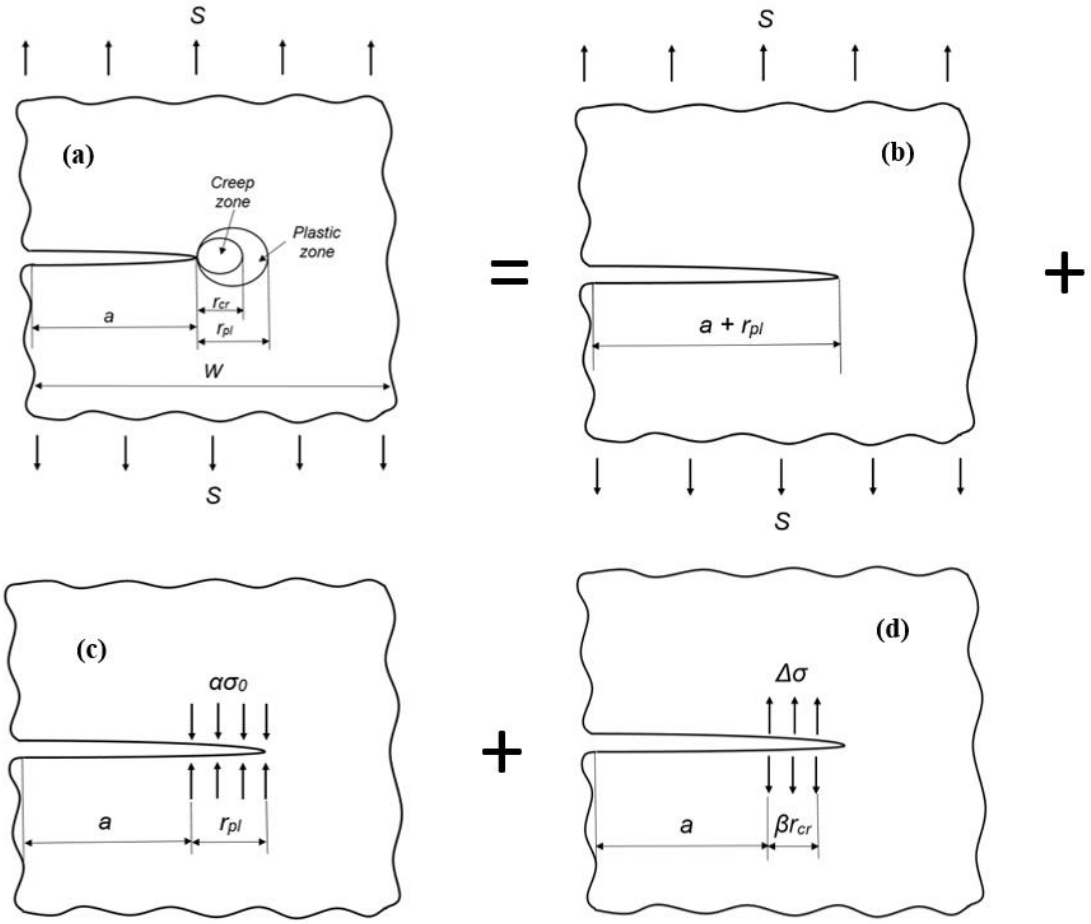

Figure 10.3. Plastic and creep deformations at the crack tip, and the superposition principle applied to three elastic loading cases.

The crack problem illustrated in first schematic of Figure 10.3 is replaced by a superposition of three simplified loading cases of the cracked component undergoing elastic deformations. First, the physical crack of length a is replaced by a fictitious crack of length $d = a + r_{pl}$, where r_{pl} is the plastic zone size at the physical crack tip. Second, the combination of remotely applied load, plasticity and creep zones at the crack tip is replaced by the linear superposition of three elastic cases. These cases consider the elastic specimen with fictitious crack length d loaded as follows: *(i)* the remotely applied load S, *(ii)* a compressive segment load acting in the plastic zone equal to the flow stress $\alpha\sigma_0 = \alpha(S_y + S_{ut})/2$, and *(iii)* a tensile segment load $\Delta\sigma$, on the crack plane representing the stress relaxation due to creep strain accumulation. Here, α *is* the constraint factor ($\alpha = 1$ for plane stress, and $\alpha = 3$ for plane strain), S_y the yield strength and S_{ut} the ultimate strength of the material. The compressive segment load is applied on the entire plastic zone, while the tensile segment load is applied only on the corrected creep zone size by the factor β. If t_h is long enough causing the corrected creep zone to exceed the plastic zone, the application of $\Delta\sigma$ is then limited to the extent of the plastic zone, i.e., the corrected creep zone cannot exceed the plastic zone size.

10.3.2. Crack-tip plastic zone size

The plastic zone size r_{pl} is computed from the condition that the stress intensity factor at the tip of the fictitious crack with length $d = a + r_{pl}$ is zero,

$$K_{IS} + K_{I\sigma_0} = 0, \tag{10.2}$$

where K_{IS} is the stress intensity factor created by the remote loading S, and $K_{I\sigma_0}$ is the stress intensity factor due to the flow stress σ_0 in the plastic zone. Plastic zone size r_{pl} is computed by solving equation (10.2). The stress intensity factors are computed using the weight function method and the following formula

$$K_I = f\, S\sqrt{\pi d}\ , \tag{10.3}$$

where f is a non-dimensional geometrical factor that depends on the specimen type and geometry. Appendix A presents the formulas for f, K_{IS} and $K_{I\sigma_0}$ for two of the specimen types used in this study. Equation (10.2) was solved for r_{pl} using the bisection method, and the integrals in K_{IS} and $K_{I\sigma_0}$ were computed using the 10-point Gauss quadrature.

10.3.3. Crack-tip creep zone size and stress relaxation during creep hold time

While the plastic zone computed in Section 3.2 develops instantaneously as the material yields under the applied load, the creep zone at the crack tip initiates and grows steadily during the hold time. The size of the crack-tip creep zone was computed using the formula introduced by Riedel and Rice [15]

$$r_{cr}(\theta,t) = \frac{1}{2\pi}\left(\frac{K_I}{E}\right)^2 \left[\frac{(n+1)^2 E^n Bt}{2n\alpha_n^{n+1}}\right]^{\frac{2}{n-1}} F_{cr}(\theta), \tag{10.4}$$

where K_I is mode I stress intensity factor, n and B are the stress exponent and coefficient in Norton creep law, respectively, θ is angle and t is time. The parameter $F_{cr}(\theta)$ was considered for $\theta = 90°$, and its values as a function of n for the plane stress and plane strain cases were given by Riedel and Rice, and are presented in Table 10.2. The variable α_n is calculated as

$$\alpha_n = \left(\frac{n+1}{n}\frac{\pi}{I_n}\right)^{\frac{1}{n+1}} \quad \text{for plane stress,}$$

$$\alpha_n = \left[\frac{n+1}{n}\frac{\pi\left(1-\upsilon^2\right)}{I_n}\right]^{\frac{1}{n+1}} \quad \text{for plane strain.} \tag{10.5}$$

The value of I_n was given by Hutchinson [16], and is presented in Table 10.1. When n had a value other than those shown in Table 10.1, linear interpolation was performed to obtain I_n.

Table 10.1. I_n factor for the computation of the creep zone size [16].

I_n				
n	3	5	9	13
Plane stress	3.86	3.41	3.03	2.87
Plane strain	5.51	5.01	4.60	4.40

Table 10.2. F_{cr} factor for the computation of the creep zone size [15].

$F_{cr}(\theta=90°)$			
n	3	5	13
Plane stress	0.25	0.32	0.38
Plane strain	0.55	0.5	0.3

Creep deformation causes stress relaxation in the near crack tip region. According to an equation introduced by Riedel [17], the stress components relax proportionally to $(1/t)^{1/(n+1)}$. The Riedel formula cannot be directly applied directly, as it refers to the stress tensor components in the multiaxial stress state at the crack tip. For the uniaxial stress case of the strip yield model, the variation of the segment stress in the creep zone was taken as

$$\Delta\sigma = \sigma_0\left[1-\left(\frac{t_0}{t}\right)^{\frac{1}{n+1}}\right], \tag{10.6}$$

where t is time, t_0 is a time constant taken as $t_0 = 10^{-3}$ hours (3.6 seconds) for all simulations in this study. This equation preserves the Riedel format of flow stress relaxation, and no creep strains accumulate if $t_H \leq 3.6$s.

The actual stress relaxation is considered to occur not only within the creep zone of size r_{cr}, but also over an extended region ahead of the crack tip, i.e., the corrected creep zone size, which is computed as βr_{cr}. For all simulations in this study, the correction factor β was chosen as 3.5 for the nickel-base superalloy, and 3.0 for the 316 stainless steel. When the corrected creep zone reached and exceeded the size of the plastic zone, it was limited to the size of plastic zone. Therefore, a limited impact of the correction factor is considered in this model. The correction factor β for the creep zone size was chosen from parametric studies that identified the value that best fits the resulting creep-fatigue crack growth rates for the loading waveform with the smallest considered hold time. Then, this value was kept constant for all other creep-fatigue simulations with different hold times.

10.3.4. Meshing of the crack plane and crack advance

The superposition approach illustrated in Figure 10.3 is implemented using the strip-yield modeling framework introduced by Newman [7]. Prior to the onset of crack growth, the crack plane, including both the crack surface and plastic zone, is meshed using 15 one-dimensional elements, of which 10 are assigned to the plastic zone ahead of the physical crack tip and 5 to the cracked surface behind the crack tip. These elements exhibit an elastic-plastic-creep behavior, experiencing stress and elongation during each loading cycle. Figure 10.4 shows the elements in the crack plane mesh. Each element *i* has a given width w_i and length (L_i). The initial element widths w_i in the crack-tip plastic zone and crack surface behind the crack tip are given in Table 10.3.

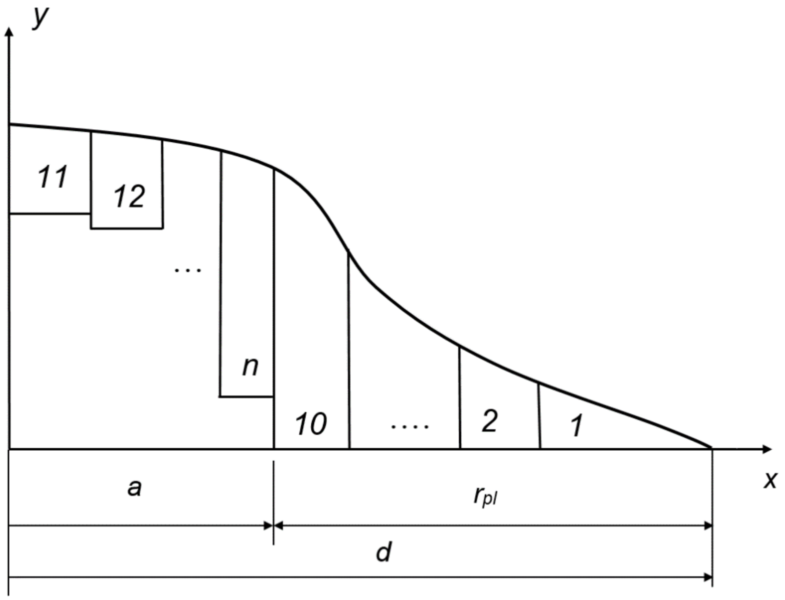

Figure 10.4. Crack-plane mesh.

The crack plane mesh changes during crack advance by two processes, namely the element creation and element deletion by lumping. After the plastic zone size r_{pl} is calculated at maximum load in the creep-fatigue cycle, the physical crack length *a* is increased by a fraction ρ of the plastic zone size, ρr_{pl}. In this study, $\rho = 0.05$ was chosen for all simulations, which is the same as the value used by Newman [7]. Simulations were also performed with different ρ values, and they indicated that $\rho = 0.05$ is the optimum fraction of the plastic zone for the crack growth increment to produce similar results with established literature data on opening stresses for fatigue crack growth. After the crack length is increased by the crack growth increment, $a = a +$

ρr_{pl}, the plastic zone size is recalculated and re-meshed using the element widths presented in the Table 10.3. As the crack tip advances, element 10, which used to be part of the plastic zone mesh, becomes a part of the crack surface behind the crack tip.

Table 10.3. Element widths for the initial mesh of the crack plane. w_i is the element width, and r_{pl} is the plastic zone size.

Element #	**Normalized element size in the plastic zone** $\left(w_i/r_{pl}\right)$	**Normalized element size in the cracked surface** $w_i/\left(r_{pl}a_i\right)$
1	0.3	0.3
2	0.2	0.2
3	0.15	0.15
4	0.12	0.12
5	0.09	0.09
6	0.06	–
7	0.04	–
8	0.02	–
9	0.01	–
10	0.01	–

With each loading cycle, the number of elements in the crack surface mesh increases, because new elements are added to it. To preserve computational efficiency, element lumping in the crack surface mesh occurs whenever the total number of elements in the crack plane, including the plastic zone and crack surface, exceeds a prescribed value, which for all studies was set at 35 elements, which is the same range as the number of elements (20-30) used by Newman [7]. Whenever lumping occurs, elements 11 and 12, which are located the farthest from the crack tip, are lumped into one element, so that the new element 11 will have the following coordinate, width, length and stress, respectively

$$x_{11} = \frac{x_{12} + \frac{w_{12}}{2}}{2} \,, \; w_{11} = w_{11} + w_{12} \,, \; L_{11} = \frac{L_{11} w_{11} + L_{12} w_{12}}{w_{11} + w_{12}} \,, \; \sigma_{11} = \frac{\sigma_{11} w_{11} + \sigma_{12} w_{12}}{w_{11} + w_{12}} \,. \tag{10.7}$$

10.3.5. Crack surface displacements and element lengths at maximum load in the cycle

Crack surface displacements are the result of two types of applied loads, i.e., the remote stresses at the boundaries of the specimen, and the segment loading applied in the crack plane. These applied loads are illustrated in Figure 10.3. For the crack of length $d = a + r_{pl}$, the crack surface displacement in the vertical direction y at a point x on the crack plane is defined as $u(d,x)$. From Figure 10.3, by superposition,

$$u(d,x) = u(d,x,S) + u(d,x,\sigma_0) + u(d,x,\Delta\sigma), \tag{10.8}$$

where, $u(d,x,S)$ is the crack surface displacement at location x caused by a remote stress S, while $u(d,x,\sigma_0)$ and $u(d,x,\Delta\sigma)$ are the crack surface displacements at x caused by the local segment loading σ_0 and $\Delta\sigma$, respectively. The displacements in the above equation are computed using the weight function method. According to Wu and Carlsson [18], the crack surface displacement in the normalized form at location x is given by

$$u(d,x,\sigma) = \frac{\sigma}{E'}\int_{a_0}^{d}\left[f(\xi)\sqrt{\pi\xi}\right]\cdot m(\xi,x)\,d\xi\,. \tag{10.9}$$

where $m(d,x)$ is the weight function for a crack of length d subjected to a stress σ. The Wu and Carlsson weight functions have different forms for the center-crack versus edge-crack specimens. For a center-crack specimen, the above equation is

$$u(d,x,\sigma) = \frac{\sigma}{E'}\int_{a_0}^{d} f(s)\sum_{i=1}^{I}\beta_i(s)\left[1-\left(\frac{x}{s}\right)^2\right]^{i-\frac{3}{2}} ds\,, \tag{10.10}$$

and for an edge crack specimen is

$$u(d,x,\sigma) = \frac{\sigma}{E'\sqrt{2}}\int_{a_0}^{d} f(\xi)\sum_{i=1}^{I}\beta_i(\xi)\left(1-\frac{x}{\xi}\right)^{i-\frac{3}{2}} d\xi\,, \tag{10.11}$$

where I is an index that depends on the specimen type. The lower integration limit a_0 is defined according to the loading mode of the crack. When the entire crack surface is loaded by a stress σ, e.g., the case of remotely applied loading, then $a_0 = x$. In the case of segment load σ on the crack surface between x_1 and x_2, the lower integration limit $a_0 = \max(x_1,x)$. The factors β_i are given in Appendix B, the crack surface displacements for remote loading in Appendix C, and those for segment loading in Appendices D and E.

Once the crack surface displacements u_i are computed at maximum load, the lengths for the plastic zone elements are set to these values, i.e., $L_i = u_i$ for $i = 1,2,\ldots,10$. In the first cycle of the creep-fatigue simulation, the lengths of the elements in the physical crack surface are all set to zero. For ulterior cycles, these lengths are the ones computed in the previous cycle, unless a new element 11 is created by crack extension and lumping. The length of the new element 11 resulting from the lumping process is given in equation (10.7).

10.3.6. Contact stresses and new element lengths at minimum load

Upon unloading, stresses are computed for the elements in the plastic zone and crack surface. At minimum load, the stress in each element j is computed by solving the following compatibility equation

$$u_i = L_i = u\left(d, x_i, S_{\min}\right) + \sum_{j=1}^{n} u\left(d, x_i, x_j, \sigma_j\right), \tag{10.12}$$

where $u(d,x_i,S_{min})$ is the displacement created at element i by remotely applied stress S_{min} and $u(d,x_i, x_j,\sigma_j)$ is the displacement at element i created by a segment load σ_j applied at element j of coordinate x_j. This situation is illustrated in Figure 10.5.

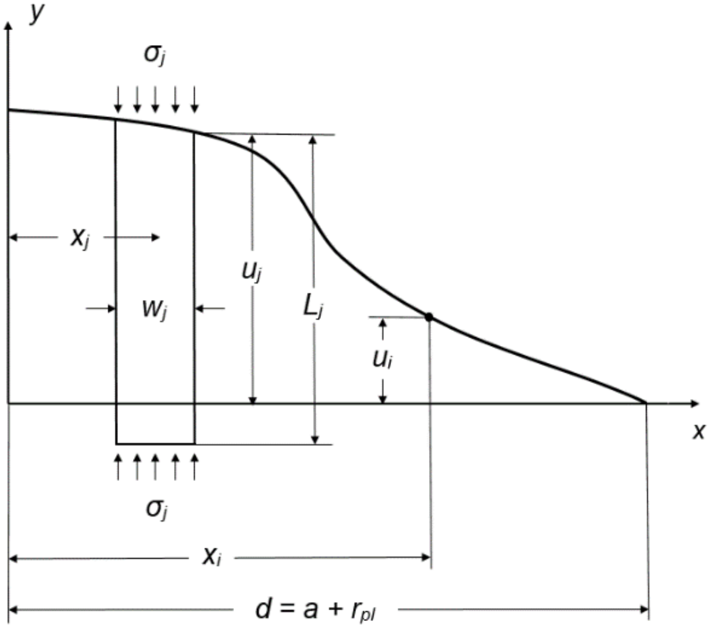

Figure 10.5. Crack surface displacement at point i created by the stress in element j.

From the above equation, element stresses σ_j are computed using a Gauss-Seidel method with constraints, as described in [7]. These constraints are defined for the plastic zone and crack surface elements as follows. For the plastic zone elements, (a) if $\sigma_j \leq -\sigma_0$, then $\sigma_j = -\sigma_0$, and (b) if $\sigma_j \geq \alpha\sigma_0$, then $\sigma_j = \alpha\sigma_0$. For the elements on the crack surface, (a) if $\sigma_j \geq 0$, then $\sigma_j = 0$, and (b) if $\sigma_j \leq -\sigma_0$, then $\sigma_j = -\sigma_0$. After element stresses are calculated at minimum load, element lengths are recalculated for each of the elements that are yielded (tension or compression) at this point in the cycle. New lengths for yielded elements are computed according to the procedure described in Section 3.5 and using the new stress distribution computed at minimum load. This is done according to the following equation only for the elements for which $\sigma_i = -\sigma_0$ when $S = S_{min}$,

$$L_i = u\left(d, x_i\right) = u\left(d, x_i, S_{\min}\right) + \sum_{j=1}^{n} u\left(d, x_i, \sigma_j\left(x_j\right)\right). \tag{10.13}$$

10.3.7. Computation of crack-tip opening stresses

Crack-tip opening stress S_{op} (or load F_{op} in the case of compact tension specimens) is the key variable in this model because it determines the variation of the crack growth rates under creep-fatigue loading with various hold times. Two methods have been used in this study to compute S_{op}, namely, the stress intensity and the crack surface displacement methods.

The first method of computing the crack-tip opening stress requires that K_I from the application of the remote stress increment $\Delta S = S_{op} - S_{min}$ equals K_I created by the contact stresses on the crack surface at minimum load,

$$K_{I\left(S_{op} - S_{\min}\right)} + \sum_{j=11}^{n} K_{I\sigma_j} = 0, \tag{10.14}$$

where $K_{I\left(S_{op} - S_{\min}\right)}$ is the mode I stress intensity factor created on the physical crack length a by the stress increment $S_{op} - S_{min}$, and $K_{I\sigma_j}$ is the stress intensity created by the stress σ_j at element j on the crack surface (not including the plastic zone). This equation was solved for S_{op} using the bisection method.

The second method uses a condition on the crack surface displacements described by Daniewicz et al. [10]. Assuming the stress distribution in the crack surface elements at minimum load, the opening stress S_{op} is the remote stress that fully opens the crack at each element i on the crack surface. This condition is written as

$$u\left(a, x_i, S_{op} - S_{\min}\right) + \sum_{j=11}^{n} u\left(a, x_i, \sigma_j\left(x_j\right)\right) = 0\,. \tag{10.15}$$

S_{op} is computed from the above equation using the bisection method. The crack surface displacements u in the above equation caused by either remote loading $S_{op} - S_{min}$ or local segment loading σ_j are determined according to the formulas described in Appendices C, D and E.

Simulations were performed using the two methods for computing S_{op}, and similar results were obtained, with small discrepancies. The crack surface displacement method yielded the closest values to the previously published results on crack opening stresses for fatigue crack growth. Consequently, this method has been used throughout this study to produce predictions of S_{op} and estimate creep-fatigue crack growth rates.

10.3.8. Computation of crack growth rates

To compute crack growth rates, one calculates the number of cycles dN required to growth the crack by an increment da. The calculation of da was described in section 3.4. The crack growth rate per cycle during a creep-fatigue cycle is computed as

$$\left(\frac{da}{dN}\right) = \left(\frac{da}{dN}\right)_{fat} + \left(\frac{da}{dN}\right)_{cr}, \tag{10.16}$$

where $(da/dN)_{fat}$ is the fatigue crack growth rate per cycle during the increasing portion of the loading, and $(da/dN)_{cr}$ is the creep crack growth rate per cycle during the holding portion of the loading. The fatigue crack growth rate equation is

$$\left(\frac{da}{dN}\right)_{fat} = C \cdot \Delta K_{eff}^{m}, \tag{10.17}$$

where C and m are material constants, and $\Delta K_{eff} = K_{max} - K_{min}$ is the effective stress intensity factor range. The crack growth rate for creep is

$$\left(\frac{da}{dN}\right)_{cr} = C' \cdot K_{\max}^{m'} \cdot t_H, \tag{10.18}$$

where C' and m' are material constants, and t is time. Using these equations, the number of creep-fatigue cycles needed to grow the crack by da is

$$dN = \frac{da}{C \cdot \Delta K_{eff}^{m} + C' \cdot K_{\max}^{m'} \cdot t_H}. \tag{10.19}$$

10.4. Model Verification

The model verification was performed by comparing predicted crack-tip opening stresses for fatigue crack growth with established results from other studies that used either the strip-yield or finite element modeling methods. The verification was performed for all specimen types, MT, SENT, DENT and CT. Plasticity-induced crack closure for fatigue crack growth has been thoroughly studied in the last several decades. It is well known that the crack-tip opening stress during fatigue crack growth increases from the minimum stress in the cycle at the onset of crack growth to some stabilized value during steady crack growth. The most important portion of the fatigue life from the standpoint of plasticity-induced crack closure is the steady crack growth when the crack-tip opening stress stabilizes or vary little from one cycle to another. The results included in this section include only stabilized values of the opening stresses, after a certain number of cycles. The results are presented for values of applied stresses to flow stress, thus they can be applied to any material of interest.

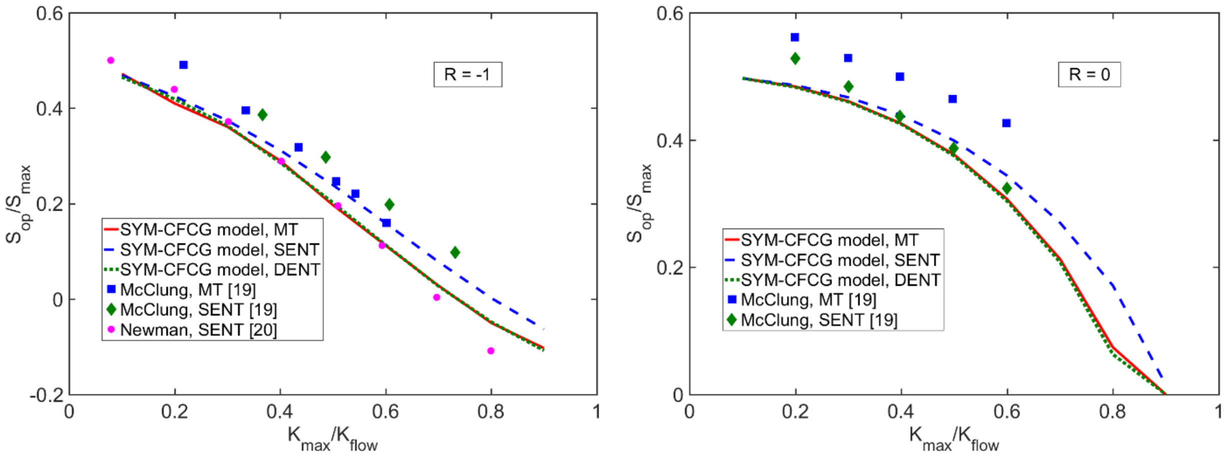

(a) **(b)**

Figure 10.6. Comparison between the predictions of the SYM-CFCG model, strip-yield modeling [20] and finite element simulations [19] of crack-tip opening stresses for fatigue crack growth in the MT, SENT and DENT specimens, plane stress ($\alpha = 1$) for two load ratios: (a) $R = -1$, and (b) $R = 0$.

Figure 10.6 presents a comparison of the opening stresses for the MT, SENT and DENT specimens, at load ratios of $R = -1$ and $R = 0$, and ratios of K_{max}/K_0 between 0.1 and 0.7. All simulations were performed in plane stress conditions. The initial crack length to specimen width ratio in all simulations was *a/W* = 0.1. The results from the SYM-CFCG model are compared with the results from finite element modeling by McClung [19] and strip-yield modeling by Newman [20]. In all cases, the agreement between the three models is good, with small discrepancies between the strip-yield models and the finite element model in the case or $R = -1$ for ratios of K_{max}/K_0 ranging from 0.2 to 0.45, however, the difference between these models is not significant.

The second verification was performed for the CT specimen. In this case, the SYM-CFCG model predictions are compared with those of the strip-yield modeling by Wang and Blom [9]. Figure 10.7a shows the comparison of the predicted opening force normalized by the maximum applied force, P_{op}/P_{max}, for load ratios ranging from $R = -1$ to $R = 0.8$, and for three constraint factors, $\alpha = 1$ (plane stress), $\alpha = 2$ and $\alpha = 3$ (plane strain). Figure 10.7b presents the comparison of the normalized opening force for three values of the applied maximum force in plane stress case. In this case, the maximum applied force in the fatigue cycle is normalized by the force that would cause the net flow stress σ_0 in the uncracked section of the specimen. In all cases, the agreement between the SYM-CFCG and the Wang and Blom models is satisfactory, with only slight differences for the load ratio of $R = -1$. Any difference in predicted S_{op} values between the two models is likely caused by the different weight functions used in each of them.

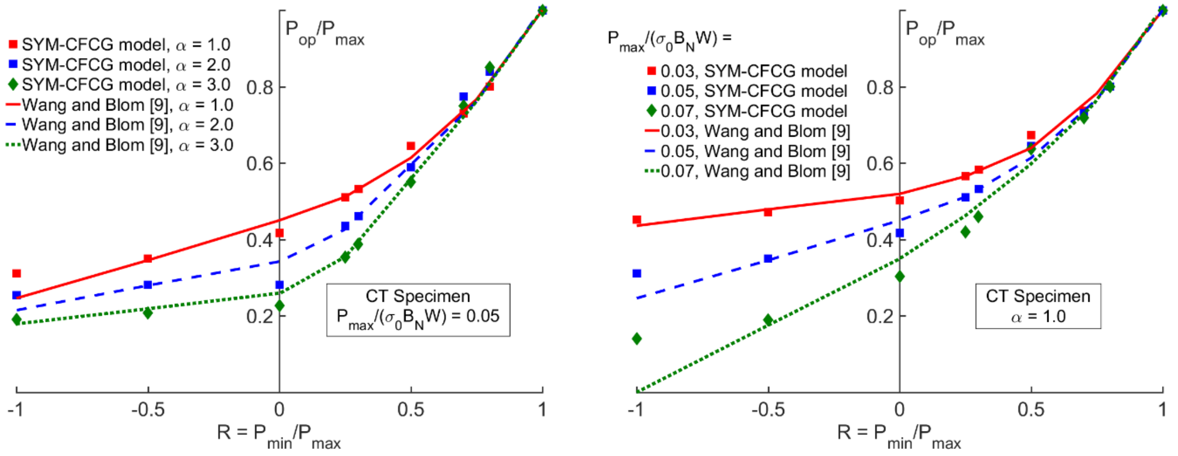

(a) **(b)**

Figure 10.7. Comparison between the predictions of the SYM-CFCG and strip-yield modeling [9] of crack tip opening stresses in CT specimens for: (a) three constraint factors, and (b) three values of maximum applied loads in plane stress. σ_0 is flow stress, B_N thickness and *W* width.

10.5. Results and Discussion

This section presents SYM-CFCG model predictions of creep-fatigue crack growth in a nickel-base superalloy and 316 austenitic stainless steel. The experimental data used for comparison with the model predictions was taken from published studies. For each case, the material constants, specimen geometry and loading were the same in SYM-CFCG simulations as those in the respective published studies, whenever data were available. The material constants used for each material are indicated in Table 10.4. The elastic constants, yield and ultimate strengths, and the Norton creep law constants were obtained as described in Sections 5.1 and 5.2 for the nickel-base superalloy and 316 austenitic stainless steel, respectively. Coefficient C and exponent m in the fatigue crack growth law (equation (10.17)) were obtained by performing a parametric study to determine the effective crack growth rate curve (i.e., da/dn vs. ΔK_{eff}) that produced the best fit for the low R-ratio fatigue crack growth rate curve (i.e., da/dn vs. ΔK). The coefficient C' and exponent m' in the creep crack growth law in equation (10.18) were obtained by a curve fit performed on the creep-fatigue test with the lowest hold time greater than zero. For all simulations using SYM-CFCG, the plane stress case ($\alpha = 1.0$) was considered.

10.5.1. Powder metal nickel-base superalloy

Creep-fatigue crack growth simulations were performed in a powder metal nickel-base superalloy (Astroloy) used for gas turbine components, and the model results were compared with the experimental data published by Piard et al. [14]. Piard et al. performed a study to measure crack growth rates during creep-fatigue loading with hold time of 0, 30s, 300s and 1000s in Astroloy SENT specimens at 750°C. The particularly relevant aspect of the Piard et al. study is that they measured the total crack growth rate da/dN in each cycle, as well as the crack growth rates during the cyclic $(da/dN)_{fat}$ and holding $(da/dN)_{cr}$ portions of each cycle. Thus, they were able to clearly identify the dependence of the $(da/dN)_{fat}$ on the duration of hold time t_H. Piard et al. showed that the longer t_H**,** the faster the crack growth rate in the cyclic loading $(da/dN)_{fat}$, undoubtedly highlighting the load interaction effect on creep-fatigue crack growth.

Table 10.4. Material constants used in simulations.

Property	**Material**					
	PM Astroloy	**9Cr-1Mo (P91)**	**2650 AA**	**2650 AA**	**316 SS annealed**	**316 SS 20% cold worked**
T (°C)	750	625	130	175	593	593
E (GPa)	160	125	68	65	153	153
v	0.3	0.3	0.3	0.3	0.32	0.32
S_y (MPa)	910	325.1	372	345	148	364
S_{ut} (MPa)	910	343.7	412	365	435	617
B ($h^{-1}MPa^{-n}$)	$1.01 \cdot 10^{-27}$	$9.53 \cdot 10^{-21}$	$2.88 \cdot 10^{-49}$	$1.47 \cdot 10^{-25}$	$6.35 \cdot 10^{-33}$	$2.79 \cdot 10^{-26}$
n	8.5	8.24	17.7	8.81	11.83	8.76
C	$6.48 \cdot 10^{-8}$	$3.0 \cdot 10^{-8}$	$1.5 \cdot 10^{-10}$	$3.0 \cdot 10^{-10}$	$1.6 \cdot 10^{-5}$	$3.0 \cdot 10^{-5}$
m	3.1	3.0	3.5	3.5	1.5	1.2
C'	$6.5 \cdot 10^{-8}$	$1.0 \cdot 10^{-7}$	$5.0 \cdot 10^{-9}$	$2.0 \cdot 10^{-8}$	$1.5 \cdot 10^{-7}$	$6.5 \cdot 10^{-4}$
m'	3.8	4.0	2.35	2.35	3.7	2.1
β	3.5	1.0	5.0	5.0	3.0	3.0

SYM-CFCG simulations of crack growth under creep-fatigue loading were performed for the specimen and loading conditions studied by Piard et al. Figure 10.8a shows the evolution of the crack-tip opening stress for fatigue (t_H = 0s) and creep-fatigue with t_H = 30s, 300s and 1000s. In the case of fatigue crack growth, the expected evolution of the opening stress is obtained from the SYM-CFCG simulations, with the rapid initial increase of S_{op} due to plastic wake build-up behind the crack tip as the crack starts growing. Then, a relatively stabilized portion of the S_{op} is observed, followed by a rapid decrease in S_{op} as the crack approached the final failure region. The decreasing portion of the curve is due to the crack opening displacements increasing greatly with longer crack length and ΔK approaching the fracture toughness of the material. For most of the fatigue crack growth history, the opening stresses ranged between 0.58-0.5S_{max}. For creep-fatigue crack growth with the three different hold times, the opening stress S_{op} decreased throughout the entire history of crack growth.

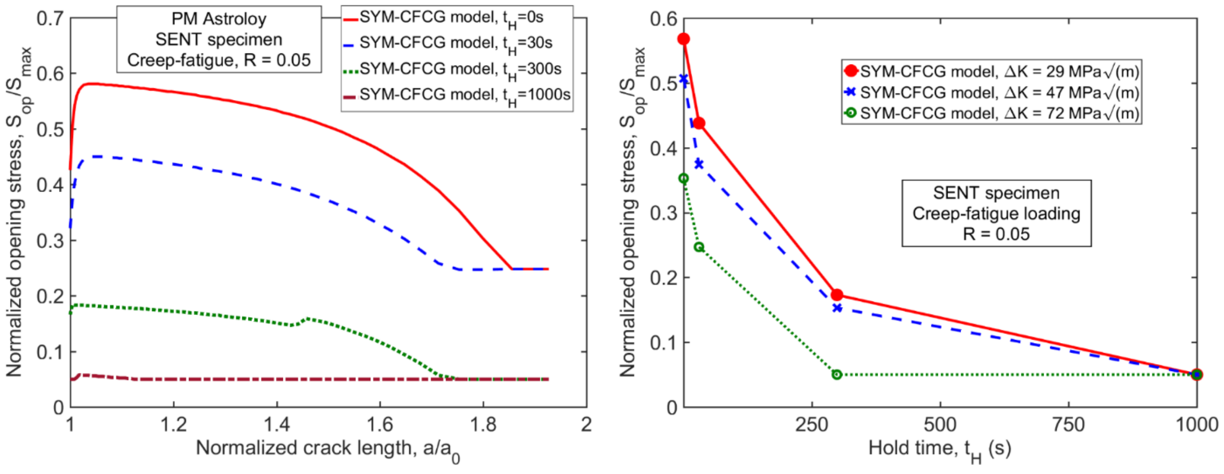

(a) **(b)**

Figure 10.8. (a) Evolution of crack-tip opening stress with crack growth for fatigue and creep-fatigue loading with different hold times in a PM Astroloy material; (b) Variation of peak opening stress as a function of hold time at various stress intensity factor ranges ΔK during the crack growth history in a PM Astroloy material.

Figure 10.8a shows that the longer the hold time, the lower the S_{op}. In the case of the largest simulated hold time of t_H = 1000s, the opening stress drops to the minimum stress, $S_{op} = S_{min} = 0.05S_{max}$, which means that the crack is always open during the creep-fatigue cycle, and the plasticity-induced crack closure is effectively canceled by the additional crack opening incurred during creep holding. In turn, decreasing S_{op} values with longer hold times leads to faster crack growth rates during the cyclic loading, $(da/dN)_{fat}$. The variation of the stabilized (maximum) opening stresses during crack growth with hold time is illustrated in Figure 10.8b. These S_{op} values are reported for three ΔK levels corresponding to the initial phase of crack growth (ΔK = 29 MPa√m), the middle portion of the crack growth life (ΔK = 47 MPa√m), and the final stage of crack growth immediately before the final fracture (ΔK = 72 MPa√m). In all three ΔK cases, the opening stress decreases with hold time, eventually reaching minimum applied load in the cycle at the end of crack growth.

The effect of hold time on opening stresses illustrated in Figure 10.8 can be understood if one analyzes the distribution of *COD* at maximum load and contact stress on the crack surfaces at minimum load. Figure 10.9a shows the *COD* at maximum load in the cycle (point C in Figure 10.1), after the application of the hold time and for the crack length that gives ΔK = 47 MPa√m.

The fictitious crack tip of coordinate $d = a + r_{pl}$ is at a normalized position of $x/d = 1$, and the physical crack tip of coordinate a is at $x/d = 0.96$. For fatigue loading (t_H = 0s), the resulting *COD* is lower than that when the loading includes an additional hold time. The added *COD* is the result of flow stress relaxation and accumulation of creep deformation in the crack plane in front of the crack tip. It can also be observed that the *COD* in the case of creep-fatigue loading with t_H = 1000s is almost twice as large as the one when only fatigue loading is applied.

An analysis of the results shown in Figure 10.9b also enhances the understanding of the creep loading effect on crack-tip opening stresses. This figure shows the variation of the contact stresses between the crack surfaces at minimum load (point D in Figure 10.1). It can be observed that the contact compressive stresses are most significant in the case of fatigue loading, and they diminish with the application of a longer hold time. When t_H = 1000s, the contact stresses behind the physical crack tip become zero, thus the plastic wake behind the crack tip loses completely its effectiveness in closing the crack at minimum load.

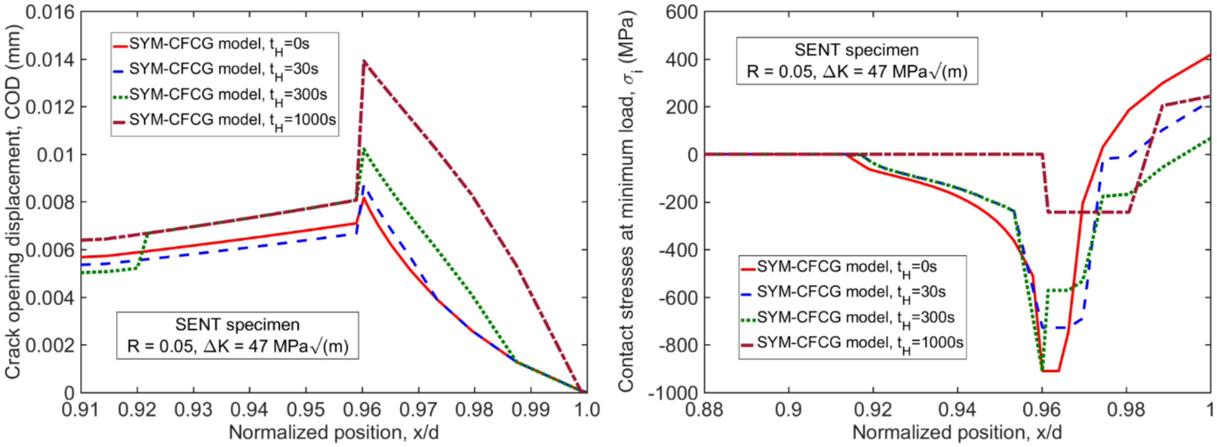

(a) **(b)**

Figure 10.9. Variation in the near crack-tip region of: (a) crack opening displacements at maximum load, and (b) contact stresses between crack surfaces at minimum load. The physical crack length is at a = 26.93 mm (normalized position x/d = 0.96), and the fictitious crack tip is at $d = a + r_{pl}$ = 28.05 mm (normalized position x/d = 1.0).

Using the obtained opening stresses for creep-fatigue loading with different hold times, crack growth rates were computed for the fatigue portion of the cycle and for the total creep-fatigue cycle. Figure 10.10a shows the predictions of $(da/dN)_{fat}$ from the SYM-CFCG model and the comparison with the experimental values of Piard et al. The SYM-CFCG model predicts well most of the data for the four considered hold times. There is some discrepancy between the experimental data and the SYM-CFCG values for the hold time of t_H = 1000s. This could be attributed to some additional damage mechanism at the crack tip that occurs during creep loading, which is not accounted for in this model. An interesting features is the initial drop in the $(da/dN)_{fat}$ curve, which is observed only for fatigue loading.

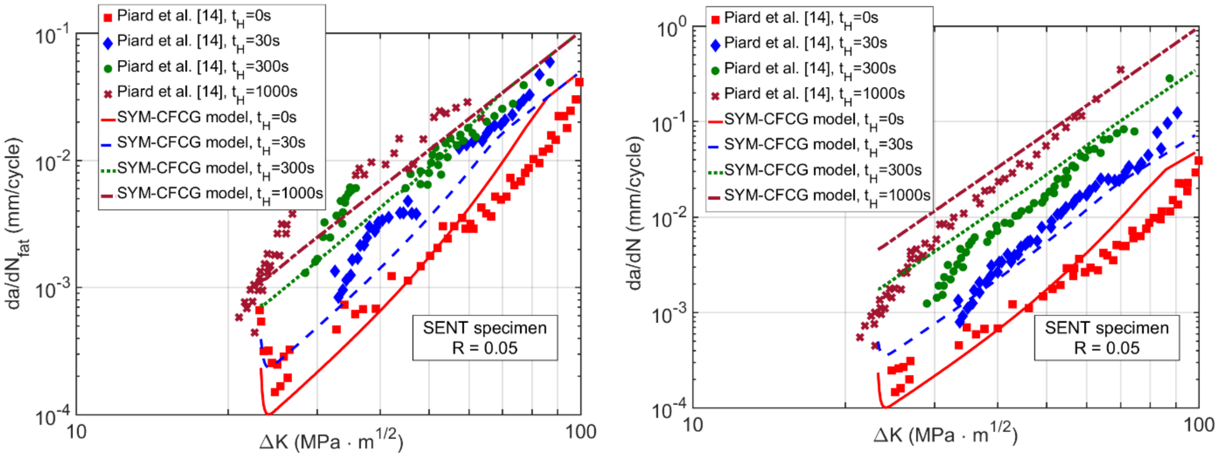

(a) **(b)**

Figure 10.10. Comparison between SYM-CFCG model predictions and experimental measurements of Piard et al. [14] during creep-fatigue loading for: (a) fatigue crack growth rates $(da/dN)_{fat}$, and (b) total crack growth rates da/dN.

The tendency of opening stresses to decrease in the initial phase of crack growth decreases with increasing hold times. This phenomenon is observed in Figure 10.10a in both the experimental data and SYM-CFCG model predictions, and it can be explained by the fact that initially the crack does not have a plastic wake, so the initial crack growth rate is high. As the crack tip advances through the initial crack-tip plastic zone, the crack surfaces develop a plastic wake, which slows down the crack growth rate by some amount. Once the plastic wake reaches a stable thickness, the crack growth rate accelerates again due to the increase in the stress intensity factor range because of crack length increase. While this behavior is particular for fatigue crack growth, in the case of creep-fatigue loading the influence of the plastic wake is diminished, or even eliminated at longer hold times, as a result of the accumulated creep strains and added *COD* during the hold time. Figure 10.10b illustrates the total crack growth rate *da*/*dN*, which includes both the fatigue and creep growth rates as a function of ΔK. The plot presents a comparison between the experimental values and the SYM-CFCG predictions, and good agreement is observed for the four tests performed.

The influence of creep hold time on crack-tip opening stresses produces a load frequency effect for a certain range of frequency values. The load frequency effect for the experiments of Piard et al. and the SYM-CFCG simulations is illustrated in Fig 10.11. In this plot the crack growth rates for the creep $(da/dN)_{cr}$ and fatigue $(da/dN)_{fat}$ are plotted, along with their linear superposition by simply adding the two together. The $(da/dN)_{fat}$ line is computed by the SYM-CFCG model from the fatigue crack growth simulation, when t_H = 0s, thus, it does not depend on frequency. The $(da/dN)_{cr}$ line is the creep crack growth law given in equation (10.18). The dotted line in

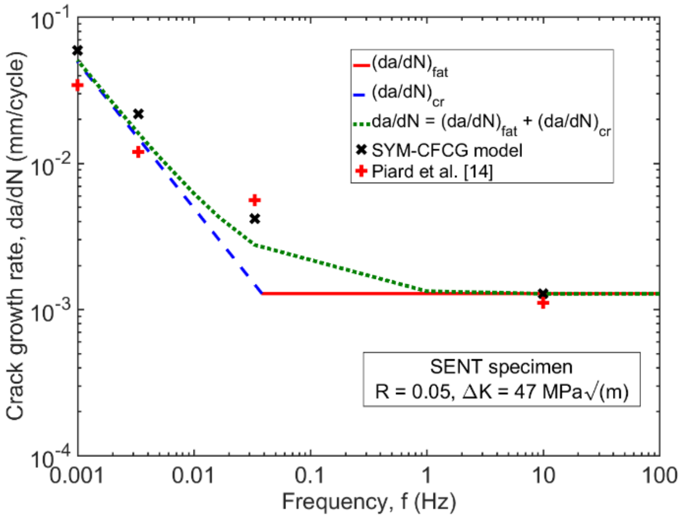

Figure 10.11. Load interaction effect on creep-fatigue crack growth rates for a PM Astroloy material.

Figure 10.11 is the linear superposition of the two crack growth equations, i.e. for $(da/dN)_{fat}$ and $(da/dN)_{cr}$. The SYM-CFCG predictions are also shown in this figure, and one can observe that these predictions are situated consistently higher that the linear summation (dotted) line, which clearly indicates a load frequency effect on the total crack growth rate *da*/*dN* that is captured by the SYM-CFCG model. The most relevant difference is observed for the frequency of f = 0.033 Hz (t_H = 30s). The load frequency effect is less relevant when f = 0.0033 Hz (t_H =

300s) or f = 0.001 Hz (t_H = 1000s), and totally inexistent when f = 10 Hz (t_H = 0s). This can be explained considering that for f = 0.0033 Hz and f = 0.001 Hz creep crack growth is dominant, while for f = 10 Hz fatigue crack growth is the only loading mode. On the same plot, the Piard et al. data are also plotted, and while their data show a strong frequency effect at f = 0.033 Hz, the effect is not visible for other frequencies. This is due mainly to the variability in the experimental data of da/dN versus ΔK at the considered value of ΔK = 47 MPa√m, but the frequency effect is relevant from their experiments as well, if one considers the data in Figure 10.10a.

10.5.2. AISI 316 austenitic stainless steel

Creep-fatigue crack growth in AISI 316 stainless steel was performed by Michel and Smith [21] in SENT specimens and Sadananda and Shahinian [22] in CT specimens at a temperature of T = 593°C, with the material in the annealed and 20% cold worked conditions. The material constants for the 316 stainless steel in the two conditions are presented in Table 10.4. The Young's modulus E values were taken from the British Stainless Steel Association website [23], the yield and ultimate strengths from the American Iron and Steel Institute website [24] and the AKSteel data product bulletin [25], while the Norton creep constants from Monterio et al. [26] study.

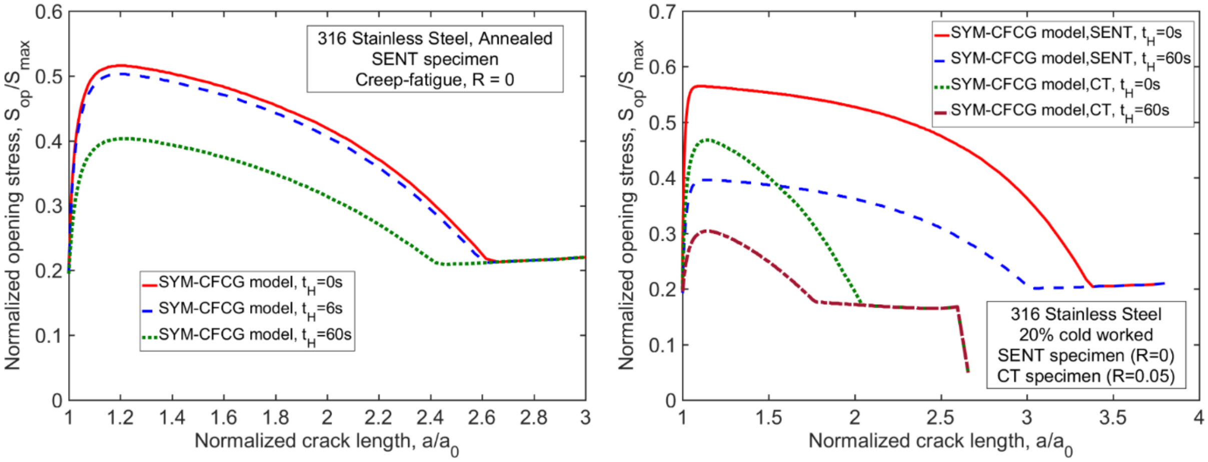

(a) **(b)**

Figure 10.12. Evolution of crack-tip opening stress (SENT)/force (CT) with crack growth for fatigue and creep-fatigue loading with different hold times in AISI 316 stainless steel at 593ºC in: (a) annealed and (b) 20% cold worked conditions.

Figures 10.12a and 10.12b show the evolution of the normalized opening stress/force during creep-fatigue crack growth in the annealed SENT specimens and the 20% cold worked SENT and CT specimens, respectively. At both temperatures, the applied load ratio was $R = 0$ and the hold times were t_h = 0s, 6s and 60s. It can be observed that the opening stress decreases with increasing hold time. The difference in the opening stress curves for t_h = 0s and t_h = 6s is small, however, a significant decrease in the opening stress is recorded when the hold time is increased to t_h = 60s.

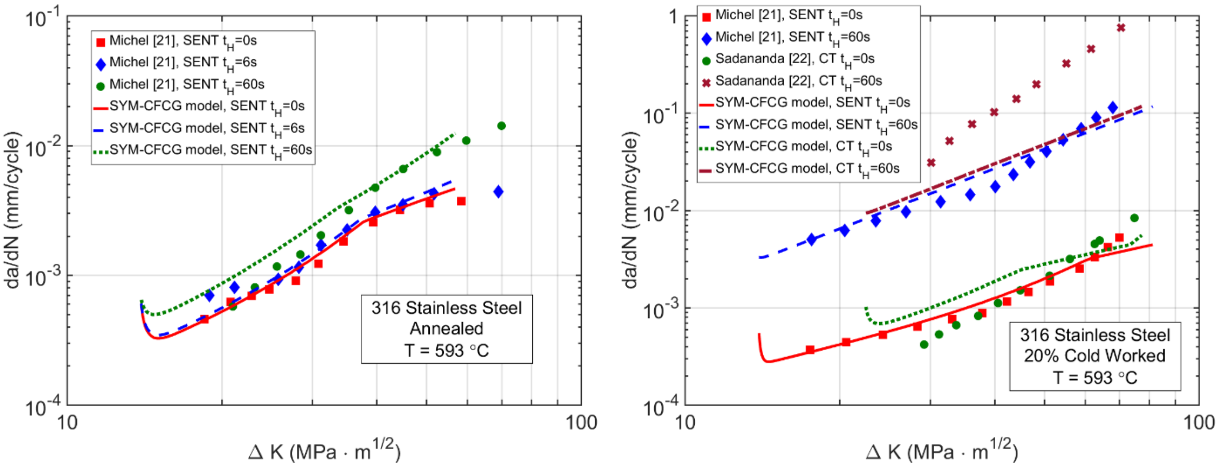

(a) **(b)**

Figure 10.13. Comparison between the SYM-CFCG model predictions and experimental measurements [21-22] of creep-fatigue crack growth rates in AISI 316 stainless steel at 593ºC in: (a) annealed and (b) 20% cold worked conditions.

The SYM-CFCG model predictions of crack growth rates da/dN versus ΔK for both temperatures are shown in Figure 10.13. In Figure 10.13a, it can be observed that because of the small decrease in the opening stress between t_h = 0s and t_h = 6s, the difference in the crack growth rates in these two conditions is very small. However, the predicted crack growth rates for t_h = 60s increases significantly compared with the rates for the other two hold times. Figure 10.13b shows the crack growth rates in the 20% cold worked SENT specimen at a load ratio of $R = 0$, and in the CT specimens at $R = 0.05$. The predictions of crack growth in SENT specimens are compared with the experimental data by Michel and Smith [21], while for the those in CT specimens the predictions are compared with the experimental data by Sadananda and Shahinian[22]. In the case of fatigue crack growth, the match between experimental and simulation data is satisfactory. In the case of creep-fatigue crack growth with t_h = 60s, the predicted values match well the Michel's experimental results, while some discrepancy is recorded with respect to Sadananda's data.

10.5.3 Modified 9Cr-1Mo (P91) martensitic steel

Modified 9Cr-1Mo (P91) steel is used in power plant applications at elevated temperatures, such as heat exchangers and piping. Narasimhachary and Saxena [27] performed experimental tests of creep-fatigue crack growth in CT specimens of P91 material at 625°C under loading with hold times of 0s, 60s and 600s. The SYM-CFCG model was used to perform simulations of the Narasimhachary and Saxena experiments. The same material properties, specimen geometry, loading, initial and final crack lengths were simulated as those in their experiments. The material constants used in the simulations are given in Table 10.4. The three specimens considered for simulations were those with the codes 3-1-8(W) for t_h = 0s, 3-1-2(W) for t_h = 60s and 3-1-3(W) for t_h = 600s, according to Narasimhachary and Saxena specimen code. The load ratio was $R = 0.1$ for all tests.

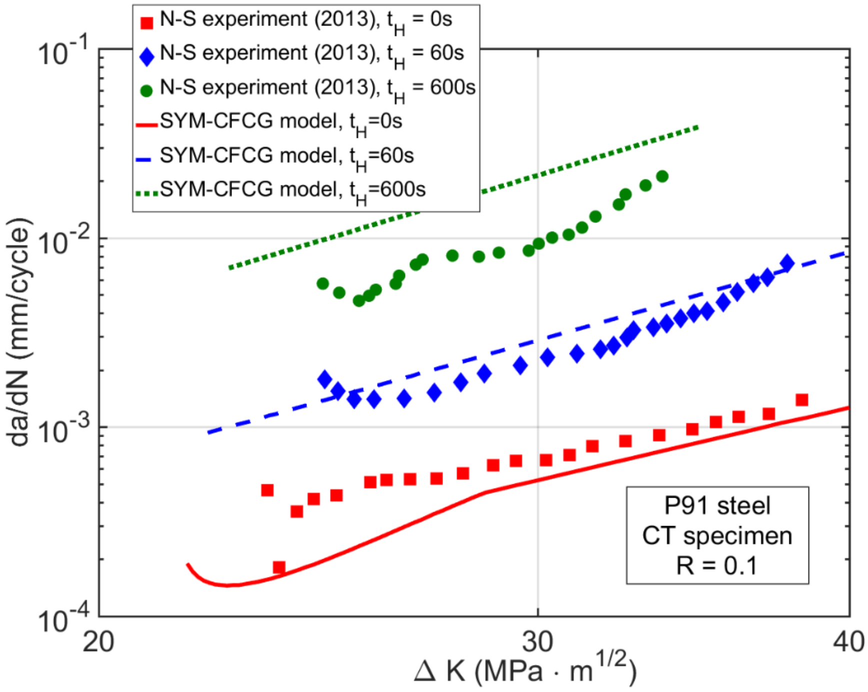

Figure 10.14 Comparison between the SYM-CFCG model predictions and experimental measurements of Narasimhachary and Saxena [27] (N-S) for creep-fatigue crack growth rates in CT specimens of 9Cr-1Mo (P91) steel at 625°C.

In the case of fatigue crack growth (t_h = 0s), the opening force initially increases to a value of approximately 0.33Pmax, and then decreases and stabilizes to 0.22Pmax, after which it drops to the minimum applied force of 0.1Pmax at the end of crack growth. When a hold time of t_h = 60s is added to each fatigue loading cycle, the crack-tip opening force has lower values starting at 0.22Pmax and decreasing sooner to the minimum value of 0.1Pmax. The same trend of decreasing opening force with hold time, but more pronounced, is recorded when a hold time of t_h = 600s is applied. The opening force in this case fluctuates in the range of 0.14-0.16Pmax and drops to 0.1Pmax much sooner in the crack growth history than in the other cases. Figure 10.14 shows the SYM-CFCG model predictions of the total crack growth rate da/dN versus ΔK, and the comparison with the experimental data of Narasimhachary and Saxena. In general, the model predicts well the experimental data, with some over-prediction for the t_h = 600s data.

10.5.4. Aluminum alloy 2650

Al-Cu-Mg aluminum alloy 2650 exhibits enhanced creep resistance, and is used in the aerospace industry in aircraft structures for supersonic flight. Creep-fatigue crack growth at temperatures of 130°C and 175°C was studied by Henaff et al. [28,29] in CT specimens of alloy 2650 at a load ratio of $R = 0.5$. The hold times in their tests ranged between t_H = 0s and t_H = 3000s. Their experiments were simulated using the SYM-CFCG model. The material properties of 2650 aluminum alloy at the two temperatures are presented in Table 10.4. For the Norton creep constants, the data from Djiakovic et al. [30] was used. The variation of the elastic properties with temperature was taken from Robinson et al. [31].

The simulation results for the evolution of normalized opening force with crack growth at the two temperatures are presented in Figure 10.15. In the case of Figure 10.15a, the differences in the opening force between t_h = 0s and t_h = 30s are quite significant. For fatigue crack growth, the crack-tip opening force Pop builds up to a maximum value of approximately 0.68Pmax and then slowly decreases until eventually reaches 0.5Pmax at the end of crack growth near the final fracture. For t_h = 30s, the opening force decreases when compared with the values for t_h = 0s. Toward the end of the crack growth, the two curves follow the same path toward the final failure. When t_h is increased, the opening force decreases for both t_h = 1500s and t_h = 3000s. While the opening force values record an increase from the minimum force of 0.5Pmax for a portion of the crack growth history, they drop to the minimum force toward the end of the crack growth. A similar trend is observed in the Figure 10.15b, which presents the results for the temperature of 175°C. Due to increased creep at this higher temperature, the decrease in the opening force with hold time is more significant. The opening force drops to the minimum applied force of 0.5Pmax for a hold time of t_h = 300s. For even longer hold times, the effect of plasticity-induced crack closure is canceled by the creep deformation in the crack plane, and there are no longer crack-tip opening forces, the crack being completely open at minimum load.

The predictions of the crack growth rates and comparison with the experimental data of Henaff et al. for the two temperatures are shown in Figure 10.16. In both cases, it can be observed that the model predicts well the increase in the total creep-fatigue crack growth rate with increased hold time and for most of the applied ΔK range.

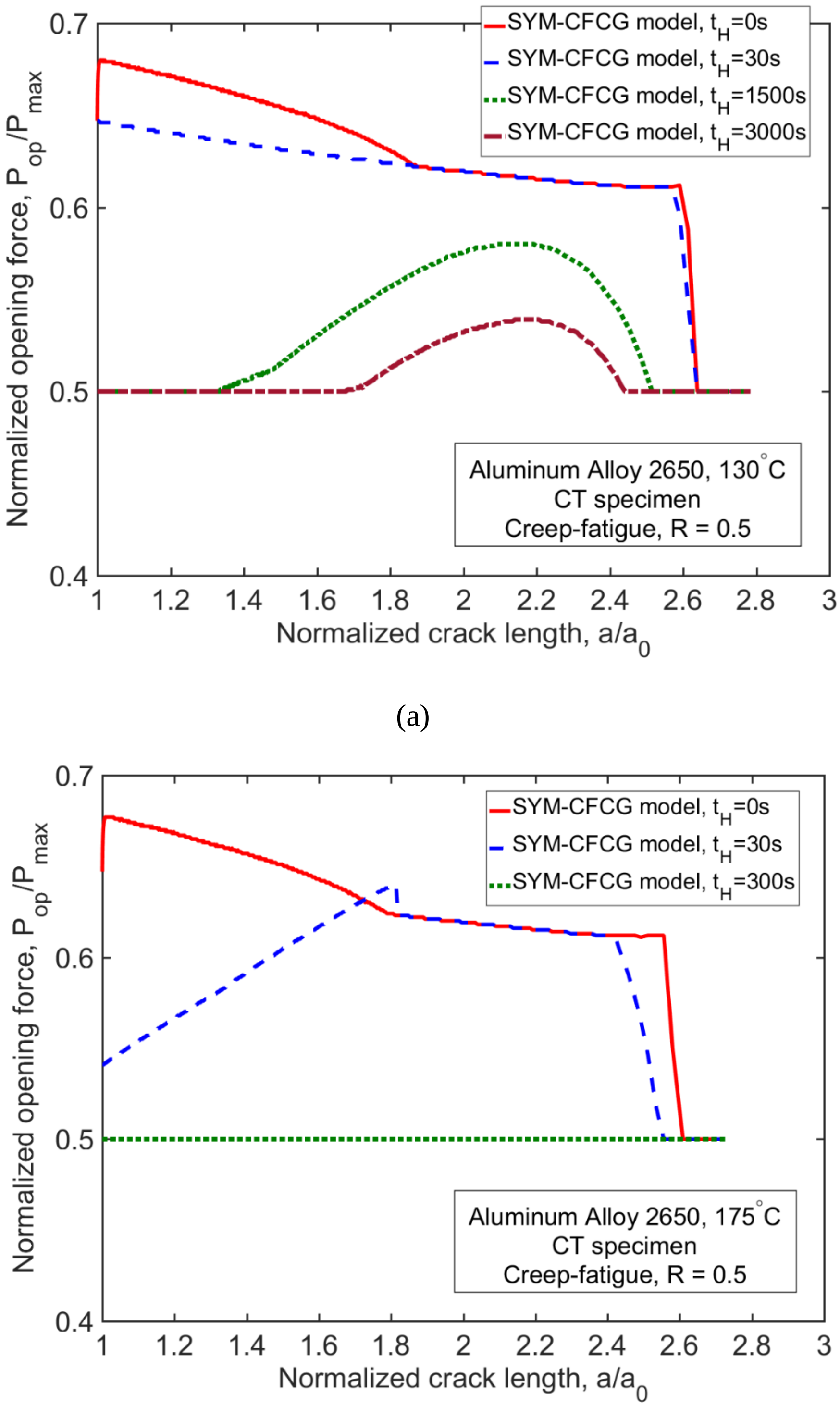

(a)

(b)

Figure 10.15. Evolution of crack-tip opening stress with crack growth for fatigue and creep-fatigue loading with different hold times in 2650 aluminum alloy at: (a) 130°C, and (b) 175°C.

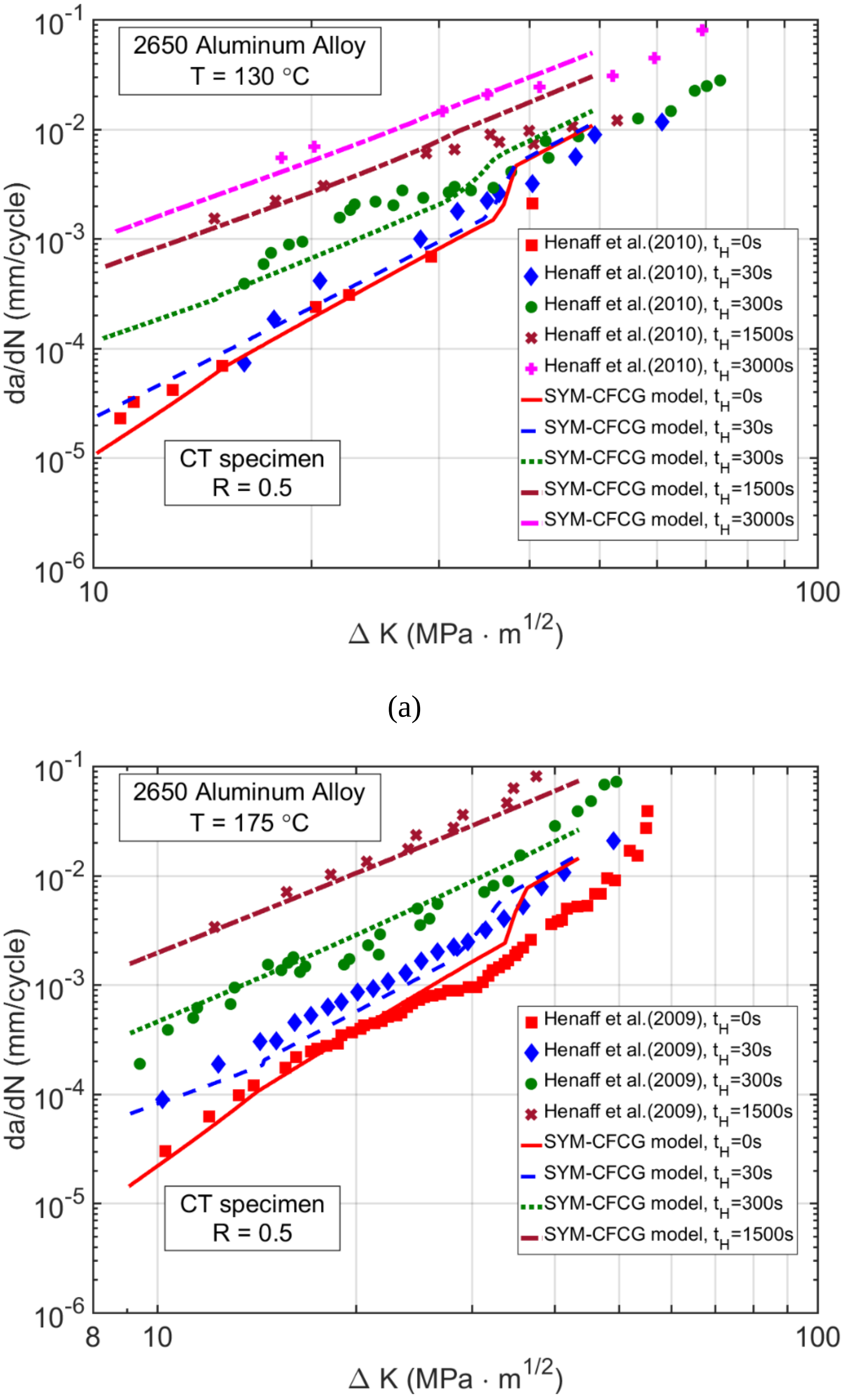

(a)

(b)

Figure 10.16. Comparison between the SYM-CFCG model predictions and experimental measurements of Henaff et al. (29) creep-fatigue crack growth rates in 2650 aluminum alloy at: (a) 130°C, and (b) 175°C.

10.5.5. Alloy 709

Fatigue crack growth predictions were performed in our testing lab on two servo-hydraulic testing frames equipped with elevated temperature chambers. The experimental details of these testing capabilities and specimen geometries were presented in a previous technical report titled “Crack growth testing for fatigue and creep-fatigue loading with short hold time”. In this section, we are concerned with the fatigue crack growth tests performed at temperatures of 550℃ and 700℃ and different load ratios, i.e. $R = 0.1$, $R = 0.3$, $R = 0.5$, and $R = 0.7$. Various maximum load levels were applied in the experimental testing to capture a wide range for the variation of ΔK, i.e., $6\ \text{MPa}\sqrt{\text{m}} \leq \Delta K \leq 40\ \text{MPa}\sqrt{\text{m}}$. The maximum force in the cycle varied from test to test between $F_{max} = 5500$ N to $F_{max} = 19000$ N.

The SYMCFCG predictions used a three-segment *da/dN versus ΔK* curve for each of the temperatures tested. Figure 10.17 shows the schematic of this three-segment curve. The second segment of this curve is the Paris regime.

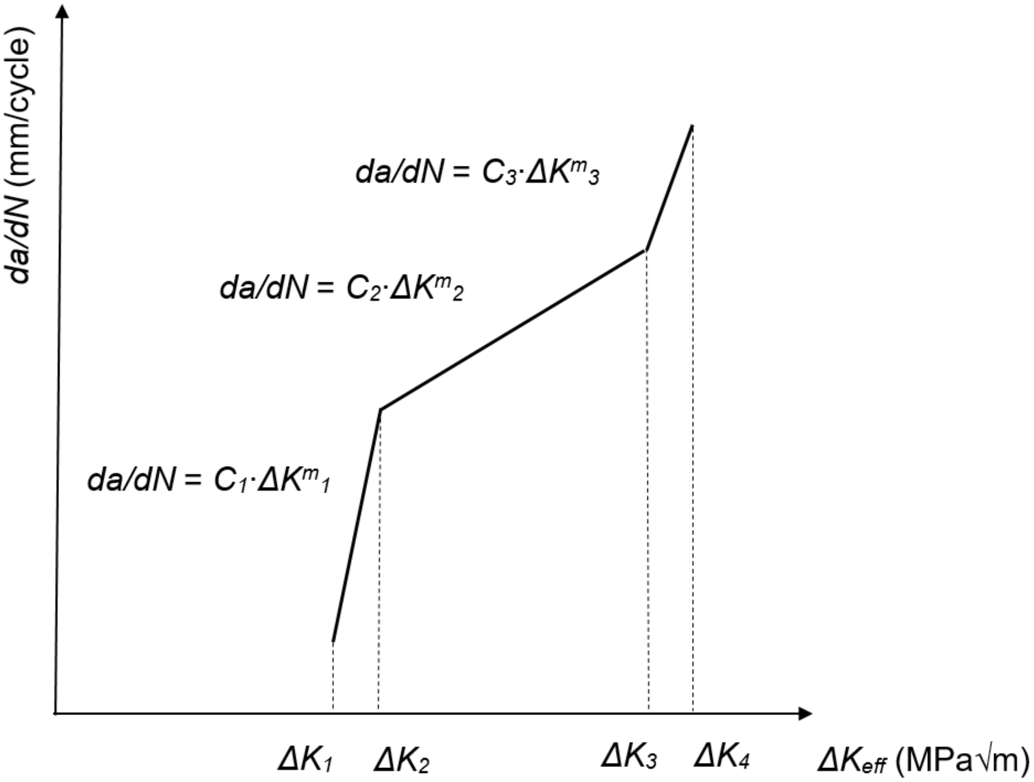

Figure 10.17. A three-segment of the *da/dN* versus *ΔKeff* for alloy 709.

For Alloy 709 at 550°C and 700°C, the set of constants C_i, m_i, and ΔK_i are show in Table 10.5, and the material properties are presented in Table. 10.6. For all simulations the plastic constraint factor used in the crack growth predictions with SYMCFCG was $\alpha = 1.0$, i.e., plane stress conditions were assumed at the crack tip.

Table 10.5. Constants for the *da/dN versus ΔKeff* curve for Alloy 709.

Constant	T = 550°C	T = 700°C
C_1	3.55E-09	1.55E-11
C_2	7.06E-07	2.66E-06
C_3	1.87E-10	4.44E-10
m_1	5.38	8.48
m_2	1.69	1.55
m_3	4.63	4.26
ΔK_1 (MPa√m)	3.5	4.2
ΔK_2 (MPa√m)	4.2	5.7
ΔK_3 (MPa√m)	16.39	25.0
ΔK_4 (MPa√m)	22.7	31

Table 10.6. Material parameters for Alloy 709 at 550°C and 700°C.

Material property	T = 550°C	T = 700°C
Young's modulus E (GPa)	160	149
Poisson's ration v	0.3	0.3
Yield strength S_y (MPa)	197	178
Ultimate strength S_{ut} (MPa)	516	449

The comparison between SYMCFCG prediction and experimental measurements of crack growth rates *da/dN versus ΔK* in the case of fatigue crack growth at 550°C are shown in Figure 10.18. The load ratios tested were $R = 0.1$, $R = 0.3$, $R = 0.5$, and $R = 0.7$. From this figure it can be observed that the experimental and modeling predictions match reasonably well for all load ratios in all three segments of the crack growth rate curve. For any value of ΔK, the $R = 0.7$ produced the largest crack growth rate, while $R = 0.1$ the lowest value of the crack growth rate.

In the case of $R = 0.1$, there is a slight difference between the model simulation and the experimental results for the first and second segments of the *da/dN versus ΔK* curve. From Figure 10.18, one can also observe that the results in the first segment of the *da/dN versus ΔK* curve indicate the value of *ΔK* where the smallest recorded *da/dN* were obtained, which indicates the location of the threshold ΔK_{th} for fatigue crack growth. The threshold is very evident in the case of $R = 0.1$, where the crack growth rate curve is almost vertical at approximately $\Delta K = 8$ MPa√m. While the results shown in Figure 10.18 were obtained using a constant amplitude loading waveform, a load shedding technique was applied on other specimens tested at the same *R* ratios, and the results were shown to be in the same threshold region. The load shedding results are not shown in this figure, but they will be included in the final report.

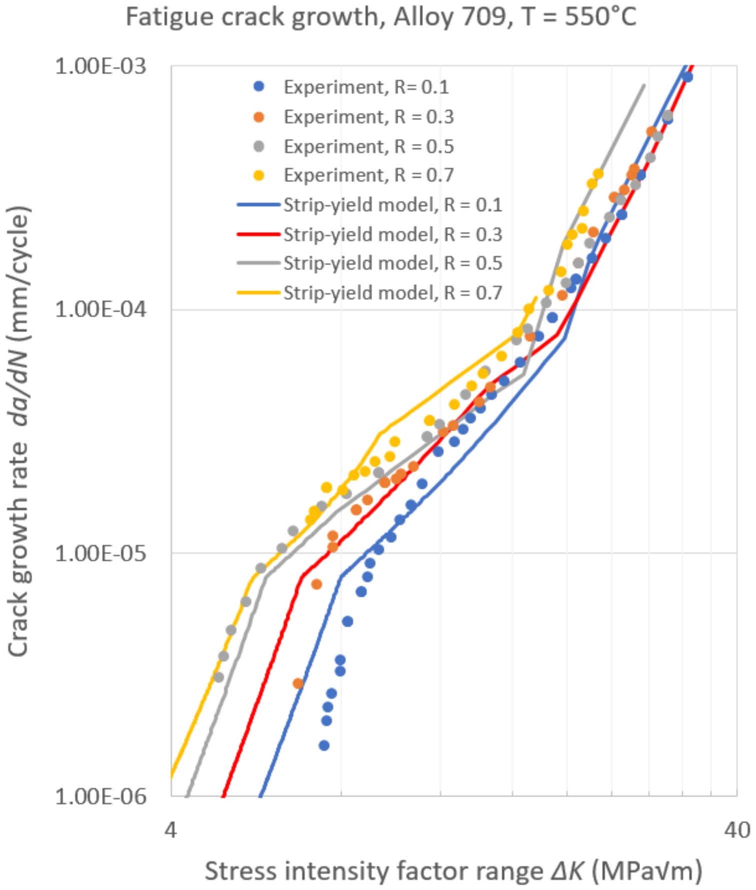

Figure 10.18. Fatigue crack growth rates in Alloy 709 at 550°C

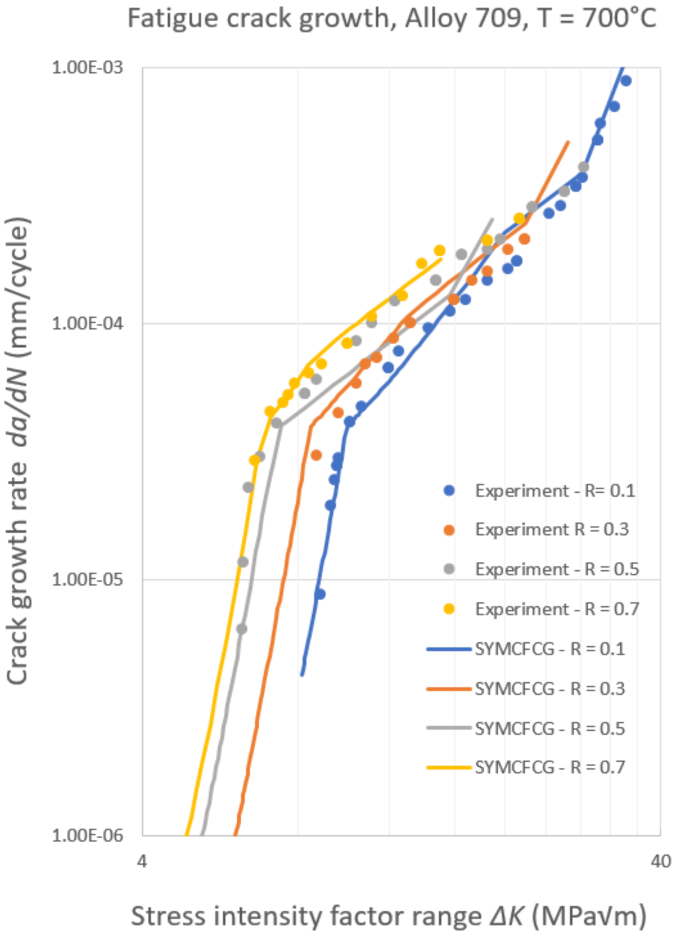

Figure 10.19. Fatigue crack growth rates in Alloy 709 at 700°C

A similar comparison between SYMCFCG prediction and experimental measurements of crack growth rates at 700°C is shown in Figure 10.19. Again, the model is shown to predict well the experimental data for all *R* ratios. The comparison holds for all three segments of the crack growth rate curve, and the threshold is also clearly visible for each load ratio in the case of this temperature.

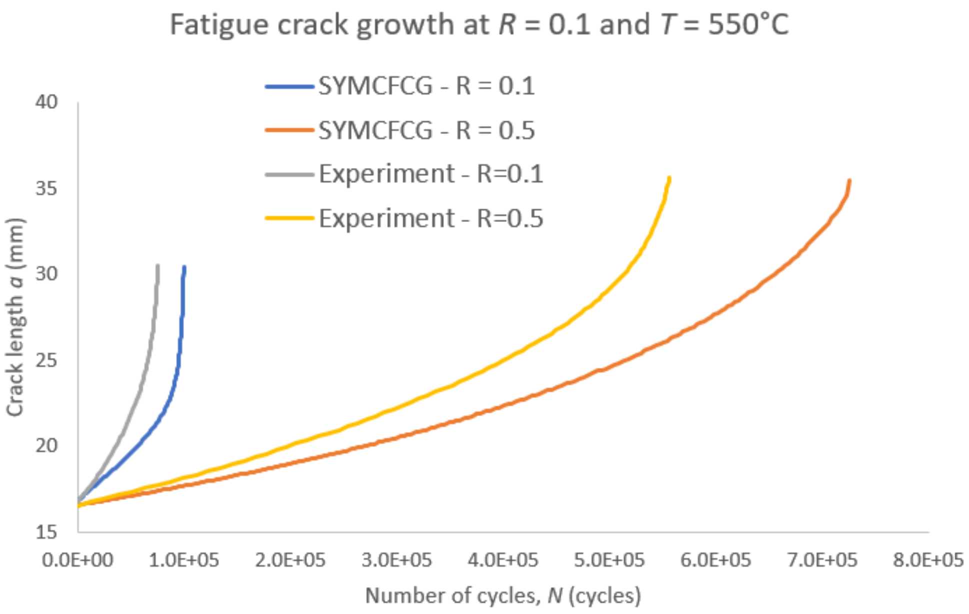

Figure 10.20. Crack length versus number of cycles for fatigue crack growth in Alloy 709 at 550°C.

In addition of the crack growth rates curves, total crack lengths were also measured experimentally and computed with SYMCFCG. Figure 10.20 shows the evolution of the crack length as a function of number of cycles in the case of the fatigue crack growth tests at 550°C. Only cases $R = 0.1$ and $R = 0.5$ are shown in this figure, and the other R-ratios cases involved constant and variable amplitude loading in the same test. In both situations, for $R = 0.1$ and $R = 0.5$ the evolution of crack length versus number of cycles curve has the same trend. In the case of $R = 0.1$, the comparison between the model predictions and experimental results is good, while in the case of $R = 0.5$ some discrepancies are recorded between the experiment and the model predictions. However, the largest difference in the case of $R = 0.5$ toward the final crack length of approximately a = 35 mm is less than 25% between experiment and model predictions. Some of this discrepancy could be further reduced, if simulations are performed with constraints factors larger than $\alpha = 1.0$, given the fact that in some conditions of load for the given C(T) specimen thickness of 12.7 mm, constraint other than plane stress may be encountered. Further study using constraints values of $\alpha = 2.0$ and $\alpha = 3.0$ (plane strain) will be performed, and the results and conclusions will be included in the final report.

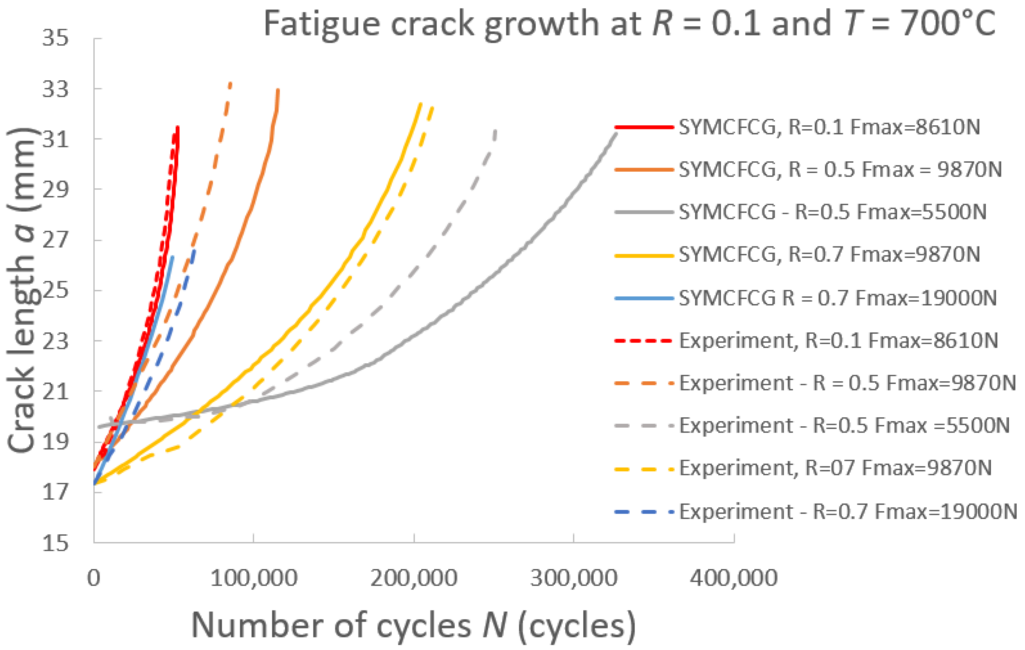

Figure 10.21. Crack length versus number of cycles for fatigue crack growth in Alloy 709 at 700°C.

Figure 10.21 shows the evolution of the crack length as a function of number of cycles in the case of the fatigue crack growth tests at 700°C. In this case, multiple tests were performed for each R-ratio value. For example, for R = 0.7, the test was performed for two values of the maximum force, F_{max} = 9870 N and F_{max} = 19000 N. From Figure 10.21, it can be observed that the comparison between the model predictions and experimental data match very well for R = 0.1 and R = 0.7 with F_{max} = 9870 N. A satisfactory agreement is obtained for R = 0.5 with F_{max} = 8610 N, and for R = 0.7 with F_{max} = 19000 N. The largest discrepancy is recorded for R = 0.5 with F_{max} = 5500 N, however in this case the difference between the model predictions and experimental results is approximately 25%, which for fatigue crack growth is acceptable given the inherent variability of fatigue crack growth data in general. A reason why the model predictions at R = 0.5 with F_{max} = 5500 N deviate the most from the experimental results, is that for such small force level, it would be perhaps more appropriate to use values for the constraint factor larger than α = 1.0, given the fact that the plastic zone size is quite small in this case. More simulations will be performed, and the results for other constraint factors will be included in the final technical report and in upcoming publications. In general, it can be concluded that SYMCFCG predicts well crack length evolution with load ratio and force level for the two tested temperatures, thus it can be used as a reliable flaw evaluation method in service at elevated temperatures.

10.6. Conclusions

A model was proposed to study the influence of creep hold times on fatigue crack growth during creep-fatigue loading. The model was used to perform predictions of creep-fatigue crack growth in two alloys used at elevated temperatures, a nickel-based superalloy and 316 stainless steel. Several cracked geometries commonly used in fatigue and creep-fatigue crack growth testing were used for simulations. The model was numerically implemented using a strip-yield methodology, which included the effect of both plastic and creep deformations at the crack tip. In this methodology, the stress intensity factors and crack opening displacements were computed using the weight function method. It was demonstrated that enhanced creep at the crack tip and the related stress relaxation in the crack-tip plastic zone lead to increased crack opening displacements and diminished compressive stresses for the entire crack surface at minimum load in the cycle. The model results also indicate that increased creep deformation at the crack tip caused by longer hold time leads to a diminishing influence of the plasticity-induced crack closure on the crack growth, thus an acceleration of the crack growth rate during the cyclic portion of a creep-fatigue cycle. For long enough hold times, i.e., up to 3000 seconds for the studied materials, the plasticity-induced crack closure is completely overcome by the creep deformation and the added crack opening displacement induced by creep. In effect, the opening stress drops to the minimum stress in the cycle for longer hold times, which implies that the crack is fully open at minimum load. The comparison between the model predictions and experimental data is satisfactory for most of the testing conditions and materials. The model is also able to predict the loading frequency effect and the synergistic action of creep and fatigue loading on crack growth rates. This approach provides a template for how crack growth predictions can be performed under variable creep-fatigue loading with short to moderate hold times.

10.7. Appendix

Appendix A. Stress intensity factors and the computation of crack-tip plastic zone.

The stress intensity factor *K* for a cracked specimen is computed using a geometrical factor *f*, which is specimen dependent. Moreover, the nominal stress distribution on the crack plane is also a factor in computing *K*. This appendix presents formulas for *K* and *f* for several common fracture specimens. These formulas have been adapted from Wu and Carlsson [18]. They presented their equations by normalizing crack length and specimen width. In this paper, the Wu and Carlsson formulas have been modified to be used with the actual crack length and specimen width dimensions.

For a cracked specimen with a crack length *a* and width *W* subjected to a remote uniform stress *S*, *f* is calculated using the weight function method by

$$f = \int_0^{a/W} \frac{\sigma(xW)}{S} \frac{m(a/W, x/W)}{\sqrt{\pi a/W}} dx, \tag{A1}$$

where $m(a/W,x/W)$ is a weight function, and $\sigma(xW)$ is the nominal stress that would be induced at location *x* in the crack plane by remotely applied stress *S* in the un-cracked specimen. For all specimens except the CT (i.e., the MT, SENT and DENT), the remote stress produces the following nominal stress $\sigma(xW) = S$, while for the CT specimen, the nominal stress is explained below. Substituting specific formulas for $m(a/W,x/W)$ in equation (A1) for each specimen, one obtains the results presented below.

Formulas for *K* are presented for the case of a remotely applied stress *S* and for the case of a segment load in the crack plane $\sigma(xW) = -\sigma_0$ applied between $xW = a_0$ and $xW = a$. In order to apply these formulas to compute the size of the crack-tip plastic zone using the Dugdale-Barenblatt model, one must replace in the *K*-formulas a_0 with *a*, and *a* with $d = a + r_{pl}$.

(a) Single-edge notched tension (SENT)

$$f = \frac{W}{\sqrt{2\pi a}} \int_0^{a/W} \frac{\sigma(xW)}{S} \sum_{i=1}^{5} \beta_i \left(\frac{a}{W}\right)\left(1 - \frac{xW}{a}\right)^{i-\frac{3}{2}} dx, \tag{A2}$$

$$K_{IS} = \frac{SW}{\sqrt{2\pi a}} \int_0^{a/W} \sum_{i=1}^{5} \beta_i \left(\frac{a}{W}\right)\left(1 - \frac{xW}{a}\right)^{i-\frac{3}{2}} dx, \tag{A3}$$

$$K_{I\sigma_0} = \frac{-\sigma_0 W}{\sqrt{2\pi a}} \int_{a_0/W}^{a/W} \sum_{i=1}^{5} \beta_i \left(\frac{a}{W}\right)\left(1 - \frac{xW}{a}\right)^{i-\frac{3}{2}} dx. \tag{A4}$$

(b) Compact-tension (CT) specimen.

$$f = \frac{1}{\sqrt{2\pi a}} \int_0^{a/W} \frac{\sigma(xW)}{S} \sum_{i=1}^{4} \beta_i \left(\frac{a}{W}\right) \left(1 - \frac{xW}{a}\right)^{i-\frac{3}{2}} dx \,. \tag{A5}$$

In the case of a CT specimen, the loading is applied as a concentrated force *P* at the pinhole, which gives a distributed stress in the crack plane as

$$\frac{\sigma(xW)}{S} = b + k\,xW \,, \tag{A6}$$

where $b = 4$ and $k = -6/W$. Then,

$$K_{IS} = \frac{SW}{\sqrt{2\pi a}} \int_0^{a/W} (b + kx) \sum_{i=1}^{4} \beta_i \left(\frac{a}{W}\right) \left(1 - \frac{xW}{a}\right)^{i-\frac{3}{2}} dx \,, \tag{A7}$$

$$K_{I\sigma_0} = \frac{-\sigma_0 W}{\sqrt{2\pi a}} \int_{a_0/W}^{a/W} \sum_{i=1}^{4} \beta_i \left(\frac{a}{W}\right) \left(1 - \frac{xW}{a}\right)^{i-\frac{3}{2}} dx \,. \tag{A8}$$

Appendix B. β-coefficients for the Wu-Carlson weight functions.

In this appendix, for the SENT and CT specimens, *a* is the crack length and *W* is the specimen width. For the MT and DENT specimens, *a* is the crack half-length, and *W* is the specimen half-width. The coefficients β_i used in the Appendices A, C, D and E are adapted from Wu and Carlsson [18] and are as follows.

(a) SENT specimen

$$\beta_1\left(\frac{a}{W}\right) = 2.0 \,, \tag{B1}$$

$$\beta_2\left(\frac{a}{W}\right) = \left[4\frac{a}{W} f_r'\left(\frac{a}{W}\right) + 2 f_r\left(\frac{a}{W}\right) + \frac{3}{2} F_2\left(\frac{a}{W}\right)\right] \Big/ f_r\left(\frac{a}{W}\right) , \tag{B2}$$

$$\beta_3\left(\frac{a}{W}\right) = \left\{\frac{a}{W} F_2'\left(\frac{a}{W}\right) + \frac{1}{2}\left[5F_3\left(\frac{a}{W}\right) - F_2\left(\frac{a}{W}\right)\right]\right\} \Big/ f_r\left(\frac{a}{W}\right) , \tag{B3}$$

$$\beta_4\left(\frac{a}{W}\right) = \left\{\frac{a}{W} F_3'\left(\frac{a}{W}\right) + \frac{1}{2}\left[7F_4\left(\frac{a}{W}\right) - 3F_3\left(\frac{a}{W}\right)\right]\right\} \Big/ f_r\left(\frac{a}{W}\right) , \tag{B4}$$

$$\beta_5\left(\frac{a}{W}\right) = \left[\frac{a}{W} F_4'\left(\frac{a}{W}\right) - \frac{5}{2} F_4\left(\frac{a}{W}\right)\right] \Big/ f_r\left(\frac{a}{W}\right) , \tag{B5}$$

$$f_r\left(\frac{a}{W}\right)=\sum_{i=0}^{7}\frac{\alpha_i\left(a/W\right)^{i-1}}{\left(1-\frac{a}{W}\right)^{\frac{3}{2}}}\,, \tag{B6}$$

with $\alpha_0 = 1.1214$, $\alpha_1 = -1.6349$, $\alpha_2 = 7.3168$, $\alpha_3 = -18.7746$, $\alpha_4 = 31.8028$, $\alpha_5 = -33.2295$, $\alpha_6 = 19.1286$, and $\alpha_7 = -4.6091$. The functions F_i are defined as

$$F_1\left(\frac{a}{W}\right)=4 f_r\left(\frac{a}{W}\right), \tag{B7}$$

$$F_2\left(\frac{a}{W}\right)=\frac{1}{12\sqrt{2}}\left[315\pi\phi\left(\frac{a}{W}\right)-105V_r\left(\frac{a}{W}\right)-208\sqrt{2}\,f_r\left(\frac{a}{W}\right)\right], \tag{B8}$$

$$F_3\left(\frac{a}{W}\right)=\frac{1}{30\sqrt{2}}\left[-1260\pi\phi\left(\frac{a}{W}\right)+525V_r\left(\frac{a}{W}\right)+616\sqrt{2}\,f_r\left(\frac{a}{W}\right)\right], \tag{B9}$$

$$F_4\left(\frac{a}{W}\right)=\sqrt{2}V_r\left(\frac{a}{W}\right)-\left[F_1\left(\frac{a}{W}\right)+F_2\left(\frac{a}{W}\right)+F_3\left(\frac{a}{W}\right)\right], \tag{B10}$$

$$\phi\left(\frac{a}{W}\right)=\frac{1}{\left(a/W\right)^2}\int_0^{a/W} s\left[f_r\left(s\right)\right]^2 ds\,, \tag{B11}$$

$$V_r\left(\frac{a}{W}\right)=\sum_{i=0}^{7}\gamma_i\left(\frac{a}{W}\right)^{i}\Bigg/\left(1-\frac{a}{W}\right)^{2}\,, \tag{B12}$$

with $\gamma_0 = 2.9086$, $\gamma_1 = -5.5749$, $\gamma_2 = 19.572$, $\gamma_3 = -39.0199$, $\gamma_4 = 58.2697$, $\gamma_5 = -54.7124$, $\gamma_6 = 29.4039$, and $\gamma_7 = -6.8949$.

(b) CT specimen.

$$\beta_1\left(\frac{a}{W}\right)=2.0\,, \tag{B13}$$

$$\beta_2\left(\frac{a}{W}\right)=\left[4\frac{a}{W}\,f_r'\left(\frac{a}{W}\right)+2f_r\left(\frac{a}{W}\right)+\frac{3}{2}F_2\left(\frac{a}{W}\right)\right]\Bigg/ f_r\left(\frac{a}{W}\right), \tag*{(B14)}$$

$$\beta_3\left(\frac{a}{W}\right)=\left\{\frac{a}{W}F_2'\left(\frac{a}{W}\right)+\frac{1}{2}\left[5F_3\left(\frac{a}{W}\right)-F_2\left(\frac{a}{W}\right)\right]\right\}\Bigg/ f_r\left(\frac{a}{W}\right), \tag*{(B14)}$$

$$\beta_4\left(\frac{a}{W}\right)=\left\{\frac{a}{W}F_3'\left(\frac{a}{W}\right)-\frac{3}{2}F_3\left(\frac{a}{W}\right)\right\}\Bigg/ f_r\left(\frac{a}{W}\right), \tag{B15}$$

$$F_2\left(\frac{a}{W}\right)=\frac{35\sqrt{2}}{12}\pi\phi\left(\frac{a}{W}\right)-8f_r\left(\frac{a}{W}\right), \tag{B16}$$

$$F_3\left(\frac{a}{W}\right)=\frac{28}{15}f_r\left(\frac{a}{W}\right)-\frac{7\sqrt{2}}{12}\pi\phi\left(\frac{a}{W}\right), \tag{B17}$$

$$\phi\left(\frac{a}{W}\right)=\frac{1}{\left(a/W\right)^2}\int_0^{a/W}s\left[f_r\left(s\right)\right]^2 ds\,, \tag{B18}$$

$$f_r\left(\frac{a}{W}\right)=\sum_{i=0}^{7}\alpha_i\left(\frac{a}{W}\right)^i\Bigg/\left(1-\frac{a}{W}\right)^{3/2}. \tag{B27}$$

The coefficients in the above equation are $\alpha_0 = 1.1214$, $\alpha_1 = 0.0294$, $\alpha_2 = -2.1907$, $\alpha_3 = 3.5511$, $\alpha_4 = 6.2459$, $\alpha_5 = -21.1853$, $\alpha_6 = 20.0463$, and $\alpha_7 = -6.4967$.

Appendix C. Crack surface displacements for specimens loaded under remotely applied loading S.

(a) SENT specimen

$$u\left(a,x,S\right)=\frac{SW}{E'\pi}\int_{x/W}^{a/W}\left[\sum_{i=1}^{5}\frac{\beta_i\left(\xi\right)}{2i-1}\right]\left[\sum_{i=1}^{5}\beta_i\left(\xi\right)\left(1-\frac{x}{W\xi}\right)^{i-\frac{3}{2}}\right]d\xi\,. \tag{C.1}$$

The factors β_i are given in Appendix B(b).

(b) CT specimen

For a CT specimen of width W and thickness B_N, loaded remotely at the pinhole by a concentrated force P, the crack surface displacements are

$$u\left(a,x,\sigma\right)=\frac{\sigma W}{E'\sqrt{2}}\int_{x/W}^{a/W}f\left(\xi\right)\sum_{i=1}^{4}\beta_i\left(\xi\right)\left(1-\frac{x}{W\xi}\right)^{i-\frac{3}{2}}d\xi\ , \tag{C.3}$$

where $\sigma = P/(WB_N)$, and

$$f\left(\xi\right)=bf_c\left(\xi\right)+kf_l\left(\xi\right), \tag{C.4}$$

with $b = 4$, $k = -6/W$ and

$$f_c\left(\xi\right)=\frac{\sqrt{2}}{\pi}\sum_{i=1}^{4}\frac{1}{2i-1}\beta_i\left(\xi\right) \tag{C.5}$$

$$f_l\left(\xi\right)=\frac{\sqrt{2}}{\pi\xi}\sum_{i=1}^{4}\frac{2}{\left(2i-1\right)\left(2i+1\right)}\beta_i\left(\xi\right) \tag{C.6}$$

The factors β_i are given in Appendix B(c).

Appendix D. Crack surface displacements for specimens loaded in the crack plane with a segment load not reaching the crack tip.

The specimen width (or half-width) is W, crack length (or half-length) is a, and the crack surface is loaded by a segment load $\sigma(x) = \sigma$ between x_1 and x_2, where $x_1 < x_2 < a$. Then, with the notation $a_0 = \max(x_1, x)$, the crack surface displacements are as follows (adapted from Wu and Carlsson [18]).

(a) SENT Specimen

$$u(a,x,\sigma)=\frac{\sigma W}{E'\sqrt{2}}\int_{a_0/W}^{a/W} f(\xi)\sum_{i=1}^{5}\beta_i(\xi)\left(1-\frac{x}{W\xi}\right)^{i-\frac{3}{2}} d\xi\,, \tag{D.1}$$

$$f(\xi)=\frac{\sqrt{2}}{\pi}\sum_{i=1}^{5}\left\{\frac{1}{2i-1}\beta_i(\xi)\left[\left(1-\frac{x_1}{W\xi}\right)^{i-\frac{1}{2}}-\left(1-\frac{x_2}{W\xi}\right)^{i-\frac{1}{2}}\right]\right\}. \tag{D.2}$$

(b) CT specimen

$$u(a,x,\sigma)=\frac{\sigma W}{E'\sqrt{2}}\int_{a_0/W}^{a/W} f(\xi)\sum_{i=1}^{4}\beta_i(\xi)\left(1-\frac{x}{W\xi}\right)^{i-\frac{3}{2}} d\xi\,, \tag{D.3}$$

$$f(\xi)=\frac{\sqrt{2}}{\pi}\sum_{i=1}^{4}\left\{\frac{1}{2i-1}\beta_i(\xi)\left[\left(1-\frac{x_1}{W\xi}\right)^{i-\frac{1}{2}}-\left(1-\frac{x_2}{W\xi}\right)^{i-\frac{1}{2}}\right]\right\}. \tag{D.4}$$

Appendix E. Crack surface displacements for specimens loaded in the crack plane with a segment load reaching the crack tip.

In this appendix, the specimen width (or half-width) is W, crack length (or half-length) is a, and the crack surface is loaded by a segment load $\sigma(x) = \sigma$ between x_1 and x_2, where $x_1 < x_2 = a$. Then, with the notation $a_0 = \max(x_1, x)$, the crack surface displacements are the following (adapted from Wu and Carlsson [18]).

(a) SENT specimen

$$u(a,x,\sigma)=\frac{\sigma W}{E'\sqrt{2}}\int_{a_0/W}^{a/W} f(\xi)\sum_{i=1}^{5}\beta_i(\xi)\left(1-\frac{x}{W\xi}\right)^{i-\frac{3}{2}} d\xi\,, \tag{E.1}$$

$$f(\xi)=\frac{\sqrt{2}}{\pi}\sum_{i=1}^{5}\frac{1}{2i-1}\beta_i(\xi)\left(1-\frac{x_1}{W\xi}\right)^{i-\frac{1}{2}}. \tag{E.2}$$

(b) CT specimen

$$u\left(a,x,\sigma\right)=\frac{\sigma W}{E'\sqrt{2}}\int_{a_0/W}^{a/W} f\left(\xi\right)\sum_{i=1}^{4}\beta_i\left(\xi\right)\left(1-\frac{x}{W\xi}\right)^{i-\frac{3}{2}} d\xi\,, \tag{E.3}$$

$$f\left(\xi\right)=\frac{\sqrt{2}}{\pi}\sum_{i=1}^{4}\frac{1}{2i-1}\beta_i\left(\xi\right)\left(1-\frac{x_1}{W\xi}\right)^{i-\frac{1}{2}}. \tag{E.4}$$

10.8. References

[1] Paris, P.C. Erdogan., F. 1963. A critical analysis of crack propagation laws. J. Basic Eng.-T ASME 85, 528-533

[2] Elber, W., 1970. Fatigue crack growth under cyclic tension. Eng. Fract. Mech. 2, 1, 37-45

[3] Sehitoglu H., Sun W., 1989. The significance of crack closure under high temperature fatigue crack growth with hold periods. Eng. Fract. Mech. 33, 3, 371-388

[4] Ramirez, J.; Potirniche, G.P., Pugesek, H., Shaber, N.; Taylor, M, Stephens, R., Charit, I., 2018, Predicting creep-fatigue crack growth rates in Alloy 709 using finite element simulations of plasticity and creep-induced crack closure, MATEC Web of Conferences, 165, 12th International Fatigue Congress, FATIGUE 2018

[5] Dugdale, D.S., 1960. Yielding of steel sheets containing slits. J. Mech. Phys. Solids 8, 2, 100-104

[6] Barenblatt, G.I., 1962. The mathematical theory of equilibrium cracks in brittle fracture. Adv. Appl. Mech. 7, 55–129

[7] Newman Jr., J.C., 1981. A crack-closure model for predicting fatigue crack growth under aircraft spectrum loading, in "Methods and models for predicting fatigue crack growth under random loading, ASTM STP 748, J.B. Chang and C.M. Hudson (Eds.), American Society for Testing and Materials, 53-84

[8] deKoning AU, Liefting G. 1988. Analysis of crack opening behavior by application of a discretized strip yield model, ASTM STP 982, 437—58

[9] Wang, G.S., Blom, A.F., 1991. Strip model for fatigue crack growth predictions under general load conditions. Eng. Fract. Mech. 40, 3, 507-533

[10] Daniewicz, S.R., Collins, J.A., Houser, D.R., 1994. Elastic-plastic analytical model for predicting fatigue crack growth in arbitrary edge-cracked two-dimensional geometries with residual stress. Int. J. Fatigue 16, 2, 123-133

[11] Kim, J.H., Lee, S.B., 2000. Fatigue crack opening stress based on the strip-yield model. Theor. Appl. Fract. Mec. 34, 1, 73-84

[12] Fischer, C., Schweizer, C., Seifert, T., 2015 Assessment of fatigue crack closure under in-phase and out-of-phase thermomechanical fatigue loading using a temperature dependent strip yield model. Int. J. Fatigue 78, 22-30

[13] Potirniche, G.P., 2012. A numerical strip-yield model for the creep crack incubation in steels, ASTM STP 1546, 197-214

[14] Piard, A., Gamby, D., Carbou, C., Mendez, J., 2004. A numerical simulation of creep-fatigue crack growth in nickel-base superalloys. Eng. Fract. Mech. 71, 2299-2317

[15] Riedel, H., Rice, J.R., 1980. Tensile crack in creeping solids, *Fracture Mechanics: Twelfth Conference, ASTM STP 700,* American Society for Testing and Materials, 112-130

[16] Hutchinson, J.W., 1968. Singular behavior at the end of a tensile crack in a hardening material, J. Mech. Phys. Solids, 16, 13-31

[17] Riedel, H., 2000. Fracture at high temperatures, Springer-Verlag, Heidelberg

[18] Wu, X.-R., Carlsson, A. J., 1991. Weight functions and stress intensity factor solutions, Pergamon Press, Oxford, UK

[19] McClung, R.C., 1994. Finite element analysis of specimen geometry effects on fatigue crack closure, Fatigue and Fracture Engineering Materials and Structures, 17(8), 861-872

[20] Newman Jr, JC. Advances in finite element modeling of fatigue crack growth and fracture. Fatigue 02: The Eight International Fatigue Congress Stockholm, Sweden, 2–7 June 2002

[21] Michel, D.J., Smith, H.H., 1976. Effect of hold time on elevated temperature fatigue crack propagation in types 304 and 316 stainless steel. ASME (MPC-3), 391-415

[22] Sadananda, K., Shahinian, P. 1980. Effect of environment on crack growth behavior in austenitic stainless steels under creep and fatigue conditions. Metall. Trans. A 11, 267-276

[23] British Stainless Steel Association, Elevated temperature physical properties of stainless steels, https://www.bssa.org.uk (accessed 13 March 2018)

[24] American Iron and Steel Institute, High-temperature characteristics of stainless steels, A designers' handbook series, No. 9004,

https://www.nickelinstitute.org/~/Media/Files/TechnicalLiterature/High_TemperatureCharacteristicsofStainlessSteel_9004_.pdf (accessed 26 March 2018)

[25] AKSteel, 316/316L stainless steel, product data bulletin, https://www.aksteel.com/sites/default/files/2018-01/316316L201706_2.pdf (accessed 14 April 2018)

[26] Monteiro, S.N., da Luz, F.S., Pinheiro, W. A., Brandao, L. P. M., de Oliveira Braga, F., de Assis, F. S., 2017. Creep parameters and dislocation structure in AISI 316 Austenitic Stainless Steel from 600°C to 800°C. Materials Research, 20, 231-235, DOI: http://dx.doi.org/10.1590/1980-5373-MR-2016-0998

[27] Narasimhachary, S.B., Saxena, A., 2013. Crack growth behavior of 9Cr-1Mo (P91) steel under creep-fatigue conditions. Int. J. Fatigue56, 106-113

[28] Henaff, G., Odemer, G., Benoit, G., Koffi, E., Journet, B., 2009. Prediction of creep-fatigue crack growth rates in inert and active environments in an aluminium alloy. Int. J. Fatigue 31, 11-12, 1943-1951

[29] Henaff, G., Menan F., G., Odemer, G, 2010. Influence of corrosion and creep on intergranular fatigue crack path in 2XXX aluminum alloys, Eng. Fract. Mech. 77, 1975-1988

[30] Đaković, A., Dyson, B.F., Mclean, M., 2005. Damage identification in creep of aluminum alloy 2650-T8. Metalurgija, 243-250

[31] Robinson, J.S., Cudd, R.L., Evans, J.T., 2003. Creep resistant aluminum alloys and their applications. Mater. Sci. Tech. 19, 143-155

11 LIST OF PUBLICATIONS

11.1 Journal Papers

1) G.P. Potirniche and J. Ramirez. Physically-based modeling of creep-fatigue crack growth using a constitutive theory and a strip-yield methodology, *Transactions of the Indian Institute of Metals,* DOI 10.1007/s12666-015-0777-4, Dec. 2015.

2) J. Ramirez, G.P. Potirniche, M. Taylor, H. Pugesek, R. Stephens, I. Charit, The influence of plasticity-induced crack closure on creep-fatigue crack growth in two heat-resistant steels, submitted to *International Journal of Fatigue*, vol. 125, pp. 291-298, Aug. 2019

3) G.P. Potirniche, A crack closure model for predicting crack growth under creep-fatigue loading, *International Journal of Fatigue*, vol. 125, pp. 58-71, Aug. 2019

4) M. Taylor, J. Ramirez, I. Charit, G. Potirniche, R. Stephens, and M.V. Glazoff, "Creep behavior of Alloy 709 at 700°C," Materials Science & Engineering A (under review).

5) M. Taylor, J. Ramirez, I. Charit, G. Potirniche, R. Stephens, and M.V. Glazoff, "Creep mechanisms in Alloy 709: Effect of aging," to be submitted to *Metallurgical and Materials Transactions A.*

6) N. Shaber, R. Stephens , M. Taylor, I. Charit, J. Ramirez, G. P. Potirniche, Microstructural Analysis of Alloy 709 Fatigue and Creep-Fatigue Crack Growth Profiles at 700°C, to be submitted to *Materials Science and Engineering A*

7) N. Shaber, R. Stephens, J. Ramirez, G. P. Potirniche, M. Taylor, I. Charit, H. Pugesek, Fatigue and creep-fatigue crack growth in alloy 709 at elevated temperatures, to be submitted to *Fatigue and Fracture of Engineering Materials and Structures*

8) J. Ramirez, N. Shaber, G. P. Potirniche, R. Stephens, M. Taylor, I. Charit, An experimental and finite element study of load ration effects on the fatigue crack growth in Alloy 709 at 550°C and 700°C, to be submitted to *Engineering Fracture Mechanics*

11.2. Peer-reviewed Conference Publications

1) G.P. Potirniche, Modeling of creep-fatigue interaction effects on crack growth at elevated temperatures, Fatigue 2018, 12th International Fatigue Congress, May 27-June 1, 2018, Poitiers Futuroscope, France, MATEC web of conferences. , 2018, Vol.165, p.05004

2) J.R. Ramirez, G.P. Potirniche, H. Pugesek, N. Shaber, M. Taylor, R. Stephens, I. Charit, Predicting creep-fatigue crack growth rates in Alloy 709 using finite element simulations of plasticity and creep-induced crack closure, Fatigue 2018, 12th International Fatigue Congress, May 27-June 1, 2018, Poitiers Futuroscope, France, MATEC Web of Conferences 165, p. 13005

3) G.P. Potirniche, J.R. Ramirez, Physically-based modeling of creep-fatigue crack growth using a constitutive theory and a strip-yield methodology, 7th International Conference on Creep, Fatigue and Creep-Fatigue Interaction, CF-7, Indira Gandhi Centre for Atomic Research, Kalpakkam, India, January 19-22, 2016

11.3. Presentations at Conferences

1) G.P. Potirniche, A computational strip-yield methodology to explain load interaction effects on creep-fatigue crack growth, Fatigue Damage XII, Hyannis, MA, Sept 16-21, 2018

2) M. Taylor, N. Shaber, J. Ramirez, A. Sittiho, I. Charit, G.P. Potirniche, R. Stephens, M. Glazoff, Characterization of creep-fatigue crack propagation in Alloy 709 at high temperatures using computational simulations and experimental testing, TMS 2019 Annual Meeting and Exhibition, San Antonio, TX, March 10-14, 2019

2) J. Ramirez, G.P. Potirniche, M. Taylor, N. Shaber, I. Charit, R. Stephens, Investigation of load frequency effect on plasticity-induced crack closure during fatigue and creep-fatigue crack growth in steels at high temperatures, TMS 2019 Annual Meeting and Exhibition, San Antonio, TX, March 10-14, 2018

4) N. Shaber, H. Pugesek, J. Ramirez, M. Taylor, R. Stephens, G.P. Potirniche, I. Charit, High temperature strength characterization of alloy 709, TMS 2018, 14th Annual Meeting and Exhibition, March 11-15, 2018, Phoenix, AZ

5) M. Taylor, H. Pugesek, J. Ramirez, N. Shaber, I. Charit, G.P. Potirniche, R. Stephens, High temperature creep behavior of a Fe-20Cr-25Ni based austenitic stainless steel, TMS 2018, 14th Annual Meeting and Exhibition, March 11-15, 2018, Phoenix, AZ

6) J. Ramirez, G.P. Potirniche, H. Pugesek, M. Taylor, R. Stephens, I. Charit, Modeling of creep-fatigue crack growth in steels for high temperature structural applications, TMS 2018, 14th Annual Meeting and Exhibition, March 11-15, 2018, Phoenix, AZ

7) M. Taylor, H. Pugesek, J. Ramirez, I. Charit, I., G.P. Potirniche, R. Stephens R. and M. Glazoff, “High Temperature Creep Behavior of Alloy 709,” Symposium: Materials for Nuclear Energy Applications, Materials Science & Technology 2017 Conference and Exhibition, October 8-12, 2017, Pittsburgh, PA, USA.

12 FINAL QUAD CHART

U.S. DEPARTMENT OF
ENERGY
Nuclear Energy

Characterization of Creep-Fatigue Crack Growth in Alloy 709 and Prediction of Service Lives in Nuclear Reactor Components

OVERVIEW

Purpose:
The project aims to characterize the creep-fatigue crack growth in austenitic stainless steel Alloy 709 by performing experimental tests and developing computational predictive models. The goal is to develop a knowledge base that will help decisions on the adoption of this material for use in nuclear reactor structural components.

Objectives:

- To measure creep-fatigue crack growth rates in Alloy 709 under various creep-fatigue loading in accelerated test conditions.
- To develop computational models to predict creep-fatigue crack growth in A709
- To identify extrapolation rules for creep-fatigue life in components from testing to service conditions.
- To develop and provide a flaw evaluation procedure for creep-fatigue service conditions.

IMPACT

Logical Path:

1. Experimental testing of creep-fatigue crack growth in Compact Tension specimens
    - Specimen manufacturing
    - Microstructure analysis
    - Crack growth testing
    - Post-failure analysis of specimens
2. Thermodynamic simulations to model aging effects in A709
3. Computational modeling
    - Finite element modeling elastic-plastic-creep deformation for growing cracks
    - Strip-yield modeling of crack growth
4. Development of a flaw evaluation methodology

Outcomes:

1. Diagrams for creep-fatigue crack growth rates versus driving forces
2. Computational predictive tools for creep-fatigue life assessment of components
3. A flaw evaluation methodology for monitoring of crack damage evolution

DETAILS

Principal Investigator: Gabriel Potirniche

Institution: University of Idaho

Collaborators: Idaho National Laboratory

Duration: 3 years

Total Funding Level: $799,920

TPOC: Sam Sham, ANL

Federal Manager: Bill Corwin

Workscope: RC-3.2

PICSNE Workpackage #:
DE-NE0008443

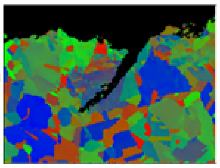

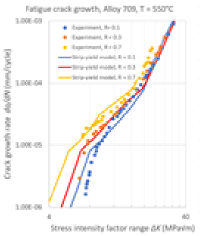

RESULTS

Results:

1. Creep-fatigue crack growth rate data at 550°C and 700°C for as-received and two aged conditions.
2. Uniaxial creep testing on aged samples.
3. Finite element simulation of creep-fatigue crack growth in ABAQUS of crack growth and comparison with experiments.
4. Strip-yield modeling of creep-fatigue crack growth in material at 550°C and 700°C for different load ratios (R = 0.1; 0.3, 0.5 and 0.7)

Accomplishments:

1. Performed fatigue and creep-fatigue crack growth tests at 550, 600 and 700°C for as-received and two aged conditions (aging at 650°C for 3 and 6 months).
2. Performed SEM, TEM and EBSD analysis of the fracture surfaces.
3. Performed finite element and strip-yield modeling simulations of creep-fatigue crack growth.
4. Performed thermodynamics simulations of aging in Alloy 709
5. Performed uniaxial creep tests in Alloy 709 at 550°C, 600°C and 700°C